

AD-A102 679

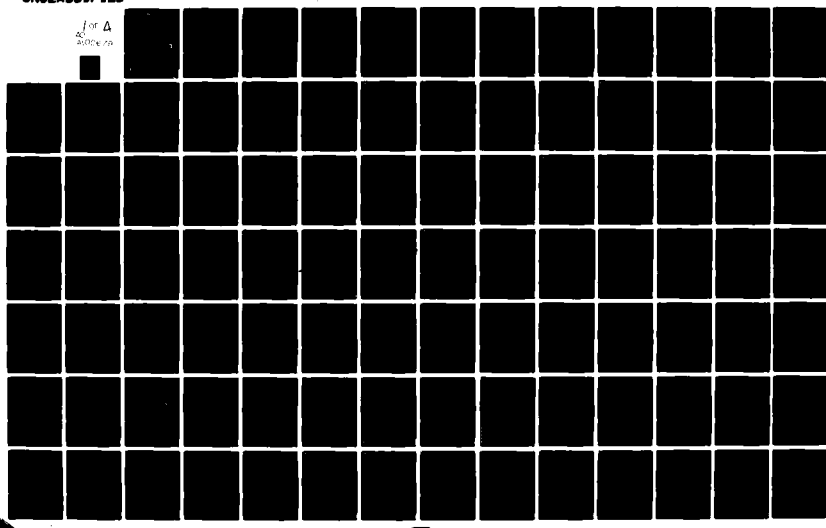
MISSOURI UNIV-ROLLA GRADUATE CENTER FOR CLOUD PHYSICS--ETC F/B 4/2
MARINE FOG STUDIES - FOG SIMULATION PROGRAM.(U)

JUN 81 D R WHITE N00014-75-C-0182

ML

UNCLASSIFIED

For A
as
above



AD A102679

LEVEL

12

REPORT ONR/N00014-75-C0182-0001 new

6
MARINE FOG STUDIES - FOG SIMULATION PROGRAM

10
Daniel R. White
Graduate Center for Cloud Physics Research
University of Missouri-Rolla
Rolla, Missouri 65401

11 Jun 1981

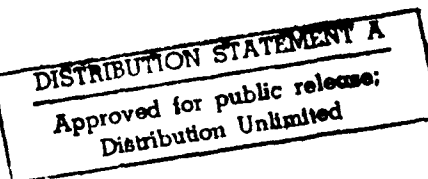


1 FINAL REPORT 15 Sep 74

34 544 20 C

Prepared for:
Office of Naval Research
Department of the Navy
Arlington, VA 22217

Office of Naval Research
Branch Office (Chicago)
536 South Clark Street
Chicago, IL 60605



DTIC FILE COPY

81 7 14 112

SECURITY CLASSIFICATION OF THIS PAGE (When Data Entered)

REPORT DOCUMENTATION PAGE		READ INSTRUCTIONS BEFORE COMPLETING FORM
1. REPORT NUMBER ONR-N00014-75-C0182-0001	2. GOVT ACCESSION NO. <i>AD-A102679</i>	3. RECIPIENT'S CATALOG NUMBER
4. TITLE (and Subtitle) MARINE FOG STUDIES-FOR SIMULATION PROGRAM	5. TYPE OF REPORT & PERIOD COVERED FINAL REPORT 15 Sept. 1974 - 30 June 1980	
7. AUTHOR(s) DANIEL R. WHITE	6. PERFORMING ORG. REPORT NUMBER	
9. PERFORMING ORGANIZATION NAME AND ADDRESS Graduate Center for Cloud Physics Research University of Missouri-Rolla Rolla, Missouri 65401	10. PROGRAM ELEMENT, PROJECT, TASK & WORK PACKAGE NUMBER 123302	
11. CONTROLLING OFFICE NAME AND ADDRESS Office of Naval Research Department of the Navy Arlington, VA 22217	12. REPORT DATE JUNE, 1981	
14. MONITORING AGENCY NAME & ADDRESS (if different from Controlling Office)	13. NUMBER OF PAGES 27	
	15. SECURITY CLASS. (of this report) UNCLASSIFIED	
	15a. DECLASSIFICATION/DOWNGRADING SCHEDULE	
16. DISTRIBUTION STATEMENT (of this Report) Scientific Officer - 1; ONR Branch Office - 1; Naval Research Lab - 6; Defense Documentation Center - 12		
17. DISTRIBUTION ST. (ENT (of this abstract entered in Block 20, if different from Report))		
18. SUPPLEMENTARY FES		
19. KEY WORDS (Continue on reverse side if necessary and identify by block number) Cloud Physics, Expansion Chambers, Fog, Aerosol Generation, Aerosol Characterization		
20. ABSTRACT (Continue on reverse side if necessary and identify by block number) <i>A cooled wall expansion cloud chamber and the supporting equipment and controls was developed and constructed. The purpose was to carry out a series of experiments which simulated the environmental changes occurring in the atmosphere during the formation and early development of clouds and fogs. The experiments were designed to study the microphysics and microchemistry of the processes occurring during this period. While the chamber was constructed and results show that operation of</i>		

of this type chamber is feasible, irreparable malfunctions in the expansion chamber itself stopped work before completion of any of the proposed primary scientific studies. The chamber is designed to provide a true adiabatic environment for a sample of gas with a known vapor content and containing a well characterized aerosol. The chamber can operate between +40°C and -40°C with cooling rates of up to 6°C/min.

Accession For	
NTIS GRA&I	<input checked="" type="checkbox"/>
DTIC TAB	<input type="checkbox"/>
Unannounced	<input type="checkbox"/>
Justification	
By	
Distribution/	
Availability Codes	
Avail and/or Dist	Special
A	

SUMMARY

This project was undertaken in order to study the initial formation and development of clouds and fogs under closely controlled conditions and time scales which approximate those occurring in the natural atmosphere. The purpose was to determine which parameters had significant effects on the formation and development and attempt to measure those parameters. In this way it was hoped to gain additional insight into the factors governing the formation and thereby improve our ability to predict the occurrence of clouds and fogs.

The heart of the system is a cooled wall expansion chamber in which the temperature of the inner wall surface and gas are separately controlled so that they are always equal. In this way a true adiabatic environment is achieved. The chamber was constructed and operational results have shown that this type of chamber is feasible. Due to an early error in assembly procedure failures of some of the thermoelectric modules used for control of the inner wall surface temperature proved irreparable and terminated the useful operation of the chamber before the completion of any of the main scientific experimental program.

Development of supporting equipment includes a transistor thermometer which provides accurate low cost computer compatible temperature measurement, generation and characterization of both salt and silica aerosols, and development of computer control and modeling techniques.

Plan 1

TABLE OF CONTENTS

Summary	1
Introduction	5
Experimental Program	5
Equipment Development	6
Expansion Chamber	6
General Design and Wall Cooling	6
Sample Inlet/Outlet Ports	10
Observation Windows	11
Thermometry	11
Pressure Control and Measurement	12
Control	12
Measurement	13
Assembly and Problems	14
Sample Preparation	16
Optical Sensing Systems	19
Photographic System	19
Transmission System	20
Mie Scattering System	20
Doppler System	21
Aerosol Generation and Characterization	23
Generation	23
Characterization	24
Computer Control, Data Acquisition and Modeling	25
Control and Data Acquisition	25
Modeling	26
Conclusions and Recommendation	27
The Cloud Physics Transistor Thermometer - Characteristics and Preliminary Data	Appendix A
Adaptive Control of a Cloud Simulation Chamber	
Expansion System	Appendix B
Humidifier Calculation	Appendix C
Visible Transmission System - Cloud Simulation Chamber	Appendix D

Progress Made in Generating a Monodisperse Aerosol of Sodium Chloride Using Two Furnaces	Appendix F
Monodisperse Aerosol Generation Efforts	Appendix G
Nucleation Experiments with Monodisperse NaCl Aerosols	Appendix H
Nucleation Experiments on Silica Aerosols	Appendix I
A Computer Data Acquisition and Control System for an Atmospheric Cloud Chamber Facility	Appendix J
A Numerical Cloud Model for the Support of Laboratory Experimentation	Appendix K

INTRODUCTION

The fog simulation studies pursued under this contract were intended to study the microphysics and microchemistry of the initial activation and development of warm clouds and fogs on marine type aerosols. The intent of the studies was to determine the parameters which affect the development of fogs and attempt to determine which parameters might serve to aid in prediction of fogs.

To support these studies a program to construct a cooled wall expansion or cloud simulation chamber was pursued. In addition to the simulation chamber itself the necessary supporting equipment for sample generation, aerosol generation and characterization, drop size measurement, and control and data acquisition was also constructed.

EXPERIMENTAL PROGRAM

The experimental program planned for the simulation chamber under this contract centered on the study of the activation and early growth of water droplets on aerosol particles, particularly sodium chloride particles, under nonfreezing conditions. A series of experiments was developed to carry out these studies. Unfortunately the work had to be terminated prior to the success of any of the main line experiments due to equipment failure (see page 15).

The planned experiments consisted of starting with a simple adiabatic expansion using a monodispersed aerosol which had been characterized as to its activation supersaturation. The intent was to observe the point at which activation occurred and the compare the results of the activation in the simulation chamber with results from the continuous flow thermal diffusion chamber (CFD). This experiment would also serve as a test of the accuracy of the humidifiers in establishing the initial vapor pressure. This experiment was to be done for a range of aerosol activation supersaturations and initial relative humidities.

Once the correlation between the CFD measurements and simulation chamber activation had been established, a series of

experiments was planned to measure the growth rate of the droplets in the 2 to 15 μ diameter size range. It was planned to compare the experimental results with the predictions based on growth models such as that developed by Carstens and Kassner (1968)*. By varying the temperature it should be possible to uncouple and individually determine values for the thermal accommodation and sticking coefficients. In addition to varying the aerosol activation supersaturation, starting temperature and initial relative humidity, it was planned to use a range of expansion rates to vary the growth rate. It was also planned to include a series of experiments in which the growth expansion would be followed by a compression to produce evaporation so that the evaporation process could be studied.

Initially the experiments would utilize monodispersed aerosols, then as experience was gained polydispersed aerosols would be used. The primary requirement for the polydispersed aerosols and clouds was development of a technique to measure the droplet size distribution to test the theory of the broadening of the droplet size distribution due to the growth of larger drops at the expense of smaller unactivated drops after the ambient supersaturation has peaked.

In addition to measurements in the simulation chamber separate studies of the CFD characterization of the aerosols were planned. Also studies of the effects of generation technique on the activation supersaturation as a function of physical dry size.

EQUIPMENT DEVELOPMENT

Expansion Chamber

General Design and Wall Cooling - The cloud simulation chamber is designed as a cooled wall expansion cloud chamber capable of creating environmental conditions similar to those observed in the atmosphere but under controlled laboratory conditions. The

*Carstens, J. C. and J. L. Kassner, Jr., 1968: "Some Aspects of Droplet Growth Theory Applicable to Nuclei Measurements", J. Rech. Atm., 3, 33-39.

chamber developed under this contract and referred to as Proto I was intended to serve as both an operational chamber and an engineering test of the system prior to construction of a large chamber having much longer cloud retention times.

The basic design, shown in Fig. 1, consists of a 10 sided right prism 18 inches in diameter and 24 inches tall with a flat top and bottom. The wall cross section shown in Fig. 2 has the thermoelectric modules (TEM's) clamped between the 1/4 inch aluminum inner wall plate and the 3 inch aluminum heat sink. The heat sink also provides the structural strength of the chamber.

The temperature of the interior surface of the chamber is maintained by circulating a thermostated liquid through passages located in the heat sink. This provides a suitable uniform temperature near the desired initial chamber temperature. The TEM's are then used to pump heat either out of or into the inner wall plate to produce the actual desired chamber temperature. During an expansion the heat pumping of the TEM's is increased so that the interior wall surface of the chamber cools at the required rate. Due to the electrical nature of the TEM's their response to changes in the cooling rate is excellent.

Control of the TEM's started with a single temperature sensor located in the inner wall of the chamber and a single programmable power supply. All 868 TEM's were wired in series and the voltage capability of the system limited cooling rates to approximately $0.3^{\circ}\text{C}/\text{min}$. and maximum temperature changes of 3°C . The temperature uniformity for the 28 thermometers located in the inner wall plates of the chamber was typically 0.4°C or better peak to peak. Major contributing factors to the temperature variations were considered to be slight variations in the cooling capabilities of individual sets of TEM's, differences in the heat sink configuration which caused variations in heat sink temperature that were reflected back into the chamber, and differences in the reverse heat flow once a temperature difference between the inner wall and heat sink was established.

After several intermediate schemes which increased cooling

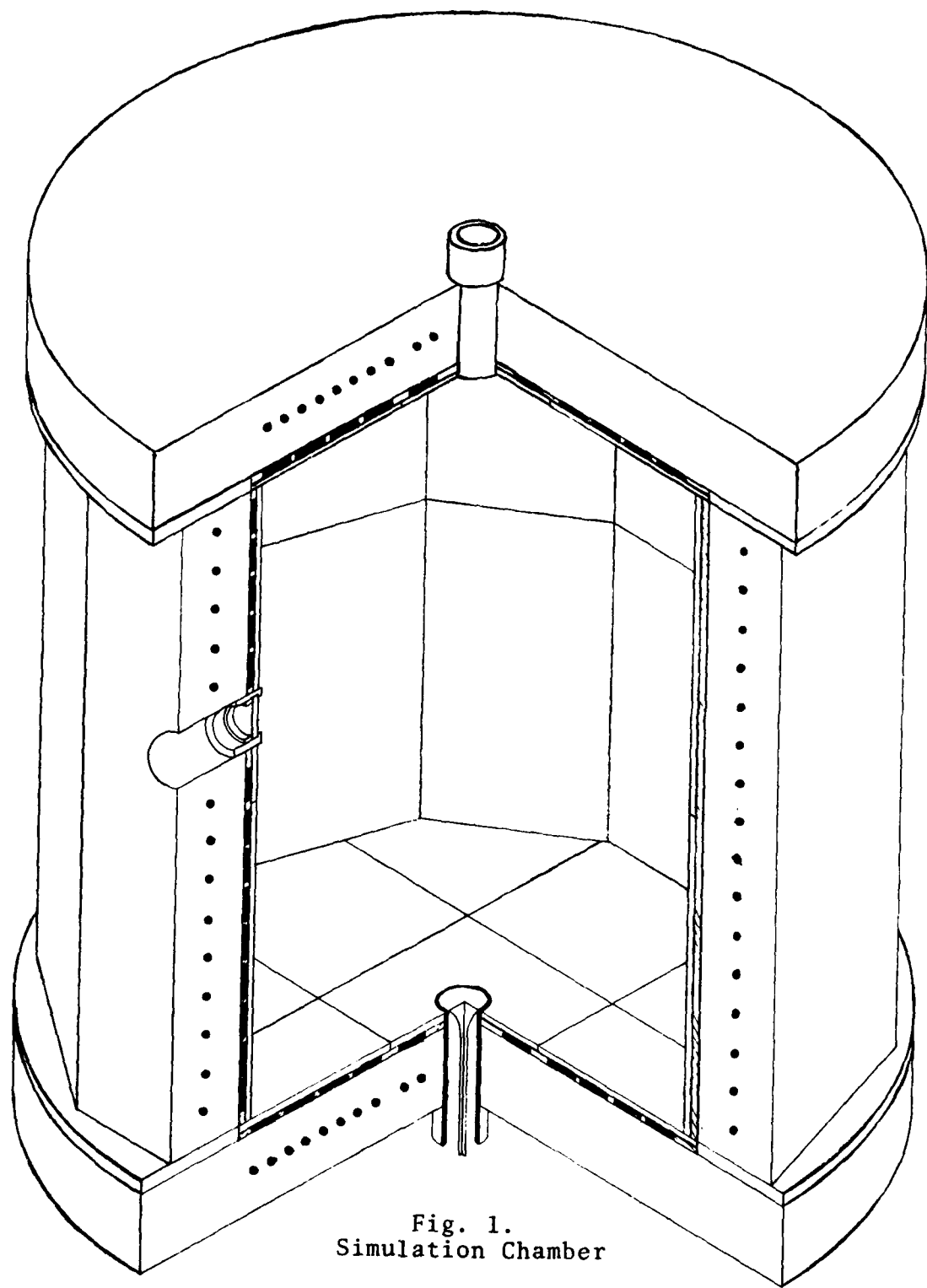


Fig. 1.
Simulation Chamber

0 6
SCALE IN INCHES

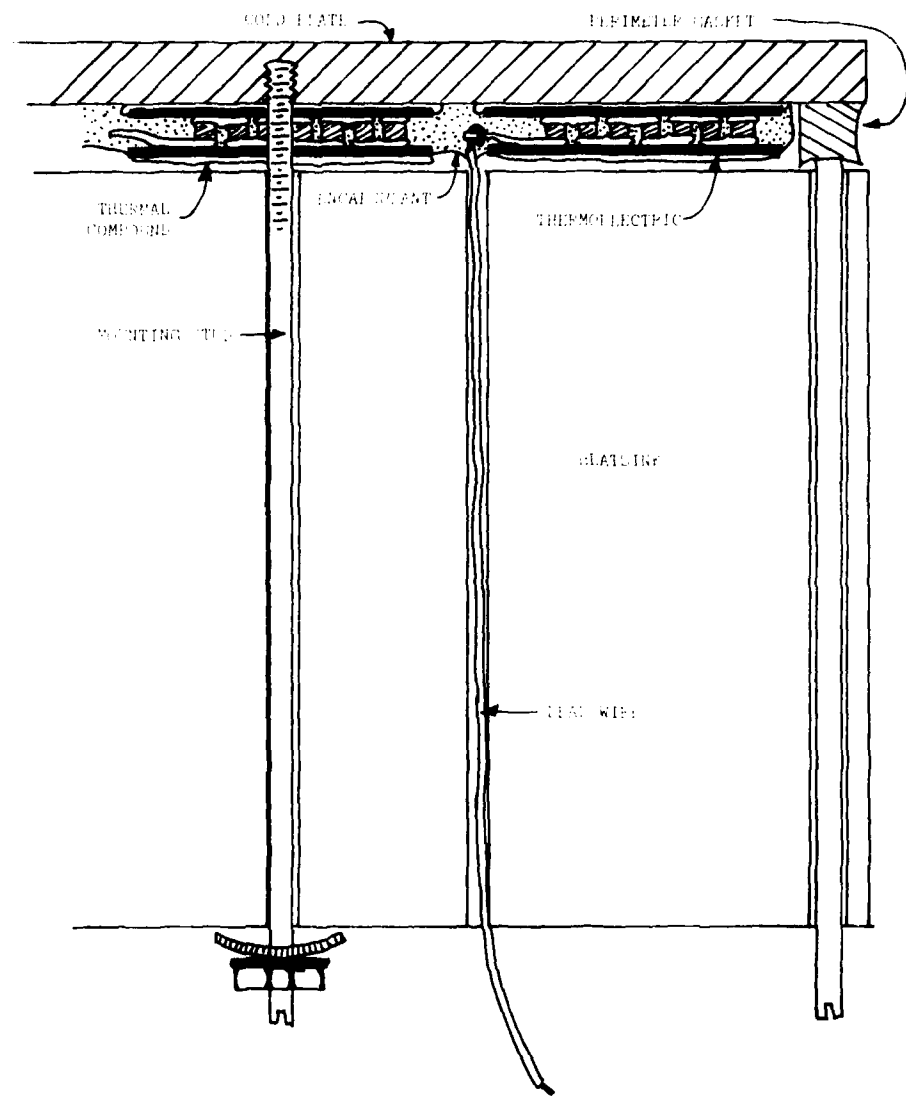


Fig. 2. Cross-section of Simulation Chamber Wall

rate and maximum temperature change but also drastically increased temperature nonuniformities a system of 28 separate programmable power supplies was used. With this system each inner wall thermometer acted as the control sensor for its own control circuit and power supply which powered the TEM's located under the inner wall plate containing that thermometer. In this way the chamber was divided into 28 separate control sections, 2 on each side (upper and lower halves) and 4 on each of the top and bottom.

This system increased the maximum cooling rate to $6^{\circ}\text{C}/\text{min}$. and the maximum temperature change to 25°C while the temperature uniformity of the 28 temperature sensors was typically 0.1°C or better following the initial control transient. The temperature uniformity became worse for large inner wall to heat sink temperature differences (15°C or larger) due to exceeding the cooling capabilities of some of the weaker sections. This latter effect was somewhat dependent on the desired cooling rate.

Sample Inlet/Outlet Ports - The sample to be studied is introduced into the chamber using a flow through flushing technique. The sample enters the chamber through the top port and is removed through the bottom port. Proto I was designed with a single large portion (2 inch diameter) in the center of both the top and bottom plates. The ports were designed to create as much turbulence in the entering gas as possible to enhance mixing within the chamber.

While the single large port in the top and bottom simplified construction it caused temperature anomalies on the surface of the inner wall. Several attempts were made to provide active cooling of valve stem which closed the port and became part of the chamber inner wall, however, these attempts were all unsuccessful.

Part of the difficulty was due to the loss of the cooling of four TEM's for each port. Since the uncooled area was square and the port was circular this resulted in a significant amount of uncooled inner wall plate surrounding the port. This only

enhanced the problem and to a large extent negated attempts to improve the temperature profile by cooling the valve.

Observation Windows - Three observation windows provided adequate optical access to the interior of the chamber for the various optical systems used to observe the drops (see page 19). Each window has a clear aperture of 1.25 inches. However they did cause temperature anomalies on the inner walls similar to those caused by the sample ports. Attempts to actively control the window temperatures were also unsuccessful.

The problem of uncooled inner wall plate surrounding the window was even worse than in the case of the sample ports. The windows were smaller than the ports yet their location in the heat sink still caused the loss of four TEM's. This meant that any attempt to cool the windows had to also deal with the surrounding uncooled inner wall plate.

Thermometry

It became obvious early in the project that temperature measurement would have to be a major consideration. The requirement for a large number (in excess of 60) of stable, rugged, high resolution sensors which were compatible with both analog control and computer data acquisition posed significant problems.

Thermocouples were considered but rejected due to the cost of the associated electronics, their need for frequent recalibration and a constant known reference temperature, and susceptibility to electrical noise. Thermistors pose a problem in that their temperature response is nonlinear which makes interchangeability of sensors difficult when the resolution required is as great as that for this project.

A selection was made to proceed with the development of a thermometer whose sensor is the base to emitter voltage of a transistor whose collector current is held constant. While requiring considerable development (see Appendix A) the results were a small, rugged, stable thermometer with a resolution of 0.001°C and an accuracy of $\pm 0.010^{\circ}\text{C}$ when compared to the calibration standard. System stability with time is good, however,

it is dependent on the specific techniques used in manufacture of the sensor. The system is relatively inexpensive and compatible with both analog control use and digital computer data acquisition.

Pressure Control and Measurement

Control - The pressure within the chamber is controlled by either removing or adding air through a series of small ports located along each of the 10 vertical joints between individual side wall heat sink sections. The external flow resistances are balanced to produce a uniform horizontal radial motion of the gas within the chamber during an expansion or compression.

The external screw driven piston mechanism originally developed to provide pressure control was fine until the system of 28 separate power supplies for the TEM's came on line. It did not have sufficient expansion rate or range to match the new cooling capabilities. It was therefore abandoned in favor of a variable orifice valve approach.

The first design utilized a three way rotary valve operated by a stepping motor (see Appendix B). The valve could provide a variable orifice opening either to a partial vacuum for expansions or to a pressurized tank for compressions. The system utilized a digital control system and was capable of the required expansion rates and range. However the response time of the system was slow enough that small oscillations about the desired pressure were inherent in the design. While small on an absolute scale (less than 0.15 psi peak to peak), they were still large enough to make interpretation of events occurring during the initial period of cloud formation impossible. The primary difficulty being the establishment with sufficient accuracy of the exact instant at which the chamber reached the conditions which the drop activation model being tested predicted drop activation and growth should begin.

The final design abandoned the requirement of having a capability for major recompression and utilized an 8-bit digital valve (Digital Dynamics, Inc., Model #8-8AA1B1BXF1W1-Z) to

provide a variable orifice between the chamber and a vacuum system. Again a digital control scheme was utilized. This time the compatibility of the valve with digital control permitted the use of a far simpler control algorithm so that the response of the system was sufficiently fast to eliminate the oscillations. Deviations of the measured pressure from the desired control pressure typically were less than ± 0.005 psi for all expansion rates up to and exceeding the equivalent of $15^{\circ}\text{C}/\text{min}$. The transient caused by a step change in expansion rate was 2 to 3 seconds in duration for pressure sample and control update rates of once per second.

A single solenoid valve connected to a pressurized tank provides a small compression capability for use when the control is trying to maintain the chamber at a constant pressure.

Measurement - Studies of the effects of errors in pressure measurement on the determination of the required environmental parameters, primarily the gas temperature during the expansion, showed that both the absolute pressure and pressure changes had to be measured with uncertainties of 1 part in 10^4 or better. The absolute pressure measurements did not pose a problem since precision strain gage transducers are available with the required dynamic response which can be calibrated to 1 part in 10^4 . If however, the same absolute pressure transducer is used to measure small (1 to 3 psi) pressure changes at an ambient pressure of 14.7 psi then it must have an accuracy and resolution of better than 1 part in 10^5 for the changes measured to be accurate to 1 part in 10^4 . This exceeds the state of the art for electrical pressure sensors used for dynamic measurements.

Our solution to this problem has been to utilize a differential strain gage pressure transducer with the required range, resolution and accuracy to measure the pressure changes to 1 part in 10^4 . The reference side of the transducer is then connected to the measurement side of a precision dead weight pressure gage operating in the absolute mode and set for a pressure midway between the initial and final pressures of the chamber during

the proposed experiment. Now as long as the piston of the dead weight gage is floating the reference pressure is constant and known to 1 part in 10^4 . Secondary controls have been developed to offset the normal piston sink rate associated with dead weight gages.

During the initial experiment set up the transducer calibration curve is stored in the data acquisition and control computer, this together with the dead weight gage setting which is also stored in the computer is used to calculate the absolute pressure of the chamber everytime the computer reads the pressure transducer output. The results are then stored as well as used in the pressure control as necessary.

The transducer is located immediately adjacent to the exterior wall of the chamber and is connected to the interior of the chamber by a 3/16 inch diameter tube passing through both the heat sink and inner wall.

Assembly and Problems

During the assembly of the inner wall plates, TEM's and individual heat sinks into a unit it was discovered that the location of clamping studs along the edge of the inner wall plates made it impossible to form a gasket seal between the inner wall and heat sink if the gasket material was to be located only along the edge of the inner wall plate. At that time (1969) the thermoelectric manufacturer (Borge-Warner Thermoelectrics) had only limited experience with nonstandard mountings and was strongly recommending, almost insisting, that a clamping stud be located on each side of every TEM. This appeared to preclude the deletion of the edge studs. The solution used was to completely fill the space between the inner wall and the heat sink which contains the TEM's with a flexible silicon potting compound. This technique provided an adequate seal.

As the side wall heat sinks were being assembled it was discovered that the personnel and equipment in the university central machine shop at that time had not held the machining tolerances close enough for the o-ring seals to function as designed.

After extensive tests and trials these joints were sealed with silicon chalking compound.

The one exception was the joint between the top plate and the top of the side wall heat sinks. This could be sealed with a ring of closed pore urethane foam. The foam had an initial thickness of 1/2 inch and was compressed to approximately 1/16 inch during sealing, but it could still conform to the irregularities on the top of the heat sinks. The foam permitted the chamber top to be raised for access to the interior of the chamber, but it had to be replaced each time the chamber was opened and required about 24 hours to form a good seal. The clamping studs had to be retightened several times during this period.

The primary difficulty resulting from the use of the potting and chalking compounds was the loss of the ability to disassemble and then reassemble a part of the chamber. This made repairs extremely difficult if not impossible, and severely restricted the design options permitted for modifications to correct defects as they were discovered. This was particularly true in the case of the temperature anomalies caused by the sample ports and windows.

The use of the potting compound around the thermoelectric modules also led to the eventual failure of the chamber. Initially when the chamber was being operated at low power levels there was no difficulty, however after the 28 individual power supplies were in operation and the power levels were significantly increased we began to experience breaks in the thermoelectric circuits inside the chamber walls. The thermoelectrics were wired with four modules connected in series inside the wall and the leads for each set brought out, therefore each break represented the loss of four modules. Initially we tried to work around the problem, but by January, 1980 we had lost four sets in the bottom plate alone. (It should be noted that the majority of the failures did occur in the top and bottom plates.) These together with the temperature anomalies due to the sample and window ports made it impossible to establish the required quiescent conditions within the chamber.

Several studies were made by introducing 2 μm diameter latex spheres into the chamber and observing their motion with the video camera while various corrective measures were attempted. None of the attempts were successful and it was finally determined that further work with the Proto I chamber would not be of profit.

During disassembly a study of the thermoelectric modules revealed that during the potting operation the potting compound not only surrounded the modules but also completely filled their interior between the individual semiconductor elements. The failure analysis has concluded that once high power operation began the resistance heating of the potting compound inside the modules caused it to expand and mechanically fracture the brittle semiconductor elements of the modules.

Sample Preparation

The chamber is designed to use a flow through purge technique for sample introduction. With a volume of approximately 100 ℓ this requires a flow of 1-5 ℓ/s of air for extended periods if the chamber is to be adequately flushed in a reasonable amount of time (5 to 10 min.). It was determined that the use of dry tank air was not economically feasible and a system to supply clean air with a known water vapor content starting from ambient room air was needed.

The resulting system consists of a blower which provides the driving pressure for air motion throughout the system. This is followed by a coarse filter to remove large dust particles and a refrigeration drier which reduces the dew point of the air to approximately 3°C. A desicent drier unit of silia gel which reduces the moisture content to a point where the frost point is less than -40°C follows next. Two columns of silica gel are in parallel so that one can be baked out while the other is in use. Following the silica gel is a backup freeze drier which also removes many of the organic vapors. The air then passes through a commercial absolute filter to yield a clean dry flow of air.

At this point the air can be diverted directly to the

chamber to provide a clean dry flush to remove any residual aerosol and moisture remaining after an experiment. It also serves as a source for any other use of low pressure clean dry air required in the system.

Once the air has been cleaned and dried the desired vapor content must be established. Due to the uncertainties associated with current techniques for measuring the vapor content of an air stream, it was decided to saturate the air with water vapor at the temperature for which the equilibrium vapor pressure corresponded to the desired vapor pressure.

To accomplish this, arrays of vertical glass rods were mounted in two thick walled aluminum cylinders (Fig. 3). Appropriate manifolding was constructed at the top and bottom of the cylinders so that a continuous stream of thermostated water can be pumped to the top of each cylinder and allowed to flow down over the surface of the rods. The water is collected at the bottom of the cylinders and recycled. The temperature of each cylinder is maintained by a separate closed loop of thermostated fluid circulating through tubes in the outer wall surface.

The two cylinders are arranged in series so that the dry sample air flows through both cylinders. During the entire 72 inch flow path the air is never more than 1/2 inch from a surface of flowing thermostated water (see Appendix C). The temperature of the entire system is maintained by a closed loop analog control based on the temperatures of the moist air leaving the second column, the humidifying water and both cylinder walls. The entire system is heavily insulated.

The system utilizes the transistor thermometers as sensors and has a stability of $\pm 0.005^{\circ}\text{C}$ during steady state operation. The controls are setable to any temperature between 0° and $+40^{\circ}\text{C}$ with a resolution of 0.001°C .

Immediately following the humidifiers are two additional cylinders of similar design. In these cylinders the glass rods are replaced by glass tubes with thermostating fluid flowing through them. The purpose of these cylinders is to raise the temperature of the air from the humidifiers so that the relative humidity is

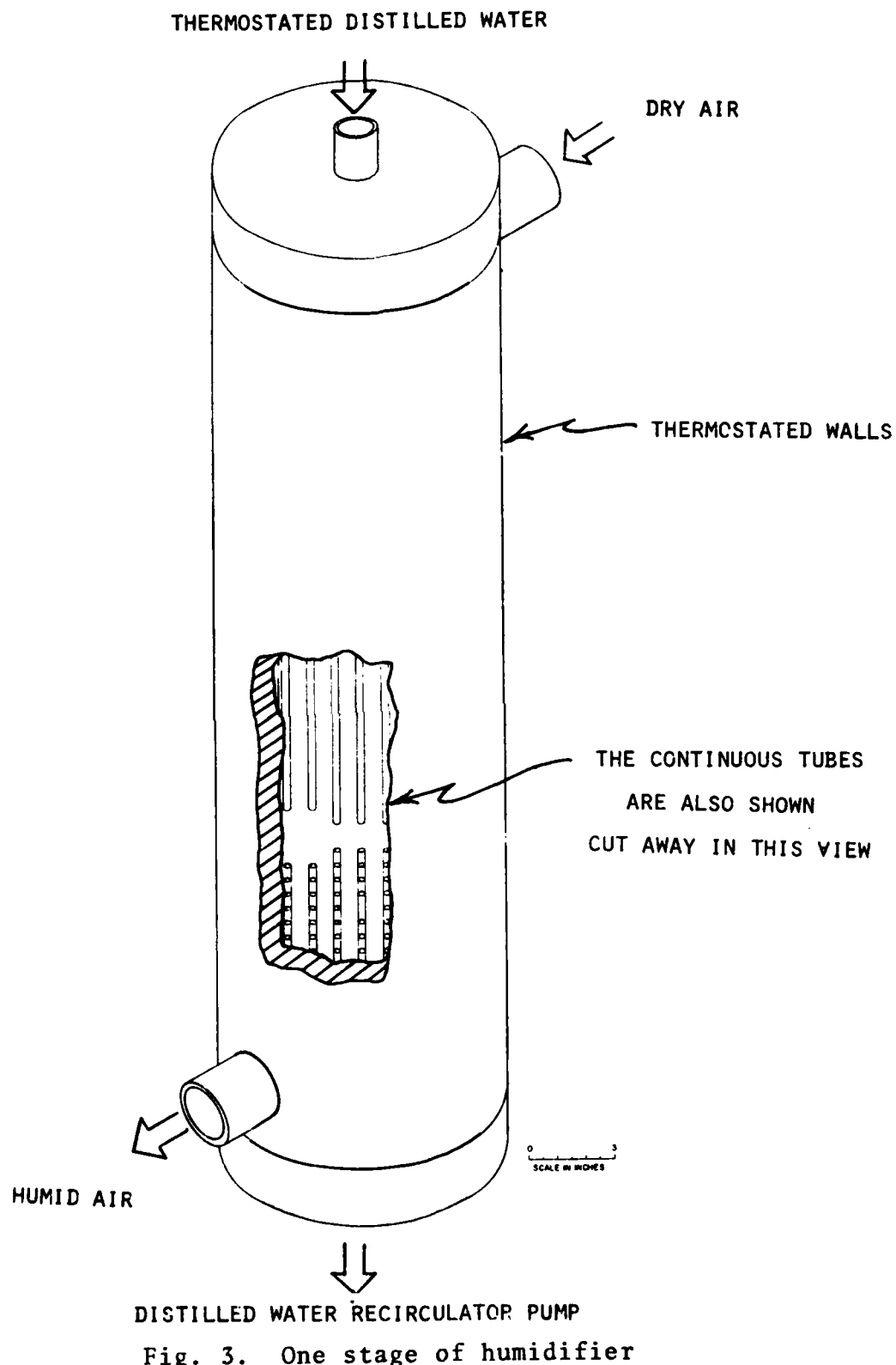


Fig. 3. One stage of humidifier

reduced below saturation. This insured that moisture is not lost due to condensation in the pipes leading to the chamber. Such condensation and later evaporation could destroy our knowledge of the vapor content.

The final step in sample preparation is to add the aerosol to be studied. This is done using a mixing ratio of at least 100 parts of clean moist air to 1 part aerosol laden air. This is to maintain an adequate knowledge of the vapor content. The exact ratio depends on the concentration of the aerosol laden air and the desired final concentration of the sample. At this point the sample is ready to enter the chamber.

Optical Sensing Systems

Four separate but complementary optical systems have been developed to monitor the formation and development of the drops within the chamber. The use of optical techniques was selected to minimize disturbance of the drops during the experiment. All four systems utilize the three observation windows located in a single horizontal plane at relative locations around the chamber of 0° , 72° and 180° .

Photographic System - The photographic system is designed to measure the number of drops per cubic centimeter in the center of the simulation chamber at predetermined times during the course of an experiment. This is accomplished by photographing the drops in a 1.1 cm thick flash beam and counting the number of drops in a calibrated area of the film.

The system utilizes a motorized Nikon 35 mm single lens reflex camera mounted on the 72° window, and a 1.1 cm wide beam of light from a point source xenon flash lamp which enters through the 180° window.

At the predetermined times during experiment a signal from the control computer activates an optically isolated control circuit. The control circuit closes a shutter in front of the photomultiplier tube located at the 0° window to protect it. At the same time it inserts a 45° mirror into the optical path into the chamber and opens the shutter of the camera. When all of

these actions have been completed the flash lamp is fired (1000 joules maximum energy per flash). The system is then returned to its original state until the next control signal from the computer is received.

The camera can hold film for up to 36 pictures at one loading and the flash lamp can be fired with a minimum of five seconds between flashes. These are more than adequate for the projected experimental requirements.

For those times when a direct real time view of the center of the chamber is desirable, such as during the initial set up of a new experiment or when trying to diagnose a malfunction in the chamber, a low light level video camera may be substituted for the photographic camera. During use of the video camera illumination is provided by the same laser beam used for the Mie scattering and Doppler systems.

Transmission System - The transmission or light attenuation system measures the decrease in the intensity of a light beam during a single pass across the chamber due to the presence of a cloud of drops (Appendix D). The source of the beam is a light emitting diode located at the 180° window and the detector is a photodiode located at the 0° window. A small lens focuses the light into a narrow beam prior to entering the chamber. A second detector diode monitors any intensity changes of the source and automatically corrects the signal of the primary detector.

The change in intensity caused by the drops is a function of their size and concentration. In the case of a monodispersed cloud the changes in intensity can be related to the mean drop size if the concentration is determined from photographic data. The system also provides a sensitive means of detecting the onset of cloud formation.

Mie Scattering System - An argon ion laser operating on the 488 nm line serves as the light source for both the Mie scattering and Doppler scattering systems. After being expanded to a diameter of 1 cm the beam is directed into the chamber through the 180°C window. As it enters the chamber an optical wedge bends

the beam up at a 2° angle.

The photomultiplier tube detector is located at the 0° windows, which also has a 2° optical wedge. By limiting the acceptance angle of the photomultiplier tube with appropriate apertures the tube will only accept light scattered through a 4° angle by drops in a small volume ($\sim 5 \text{ cm}^3$) in the center of the chamber.

For a nearly monodispersed drop size distribution the intensity of the scattered light very clearly shows the maxima and minima as a function of size (see Fig. 4) as predicted by the Mie scattering theory (Kerker, 1969)*. By recording the output of the photomultiplier tube as a function of time on a light beam oscilloscope the mean size of the drops as a function of time can be determined by relating drop size to the various maxima and minima.

Doppler System - Before the argon laser beam enters the chamber a beam splitter is used to direct part of the beam around the outside of the chamber. The remainder of the beam passes through the chamber and is scattered through a 4° angle in the vertical plane. After the scattered beam leaves the chamber it is combined with the unscattered beam and the combined beam detected by a photomultiplier tube.

When the chamber is free of convection currents the only motion of the drops will be their terminal fall velocity. Therefore the light scattered from the drops will undergo a doppler shift in frequency which is a function of the fall velocity. The fall velocity is related to the drop radius through Stokes' Law.

At the detector the mixing of the shifted scattered light and the unscattered light sum and difference frequency components result. The difference frequencies are in the audio range. By sampling at a rate of 10 khz with the data acquisition computer a fourier transform can be performed on the signal amplitude as a function of time to obtain the signal power as a function of frequency. The transform can then be used to determine the drop

*Kerker, M., 1969: "The Scattering of Light and Other Electromagnetic Radiation" (Academic Press, New York).

Intensity of Scattered Laser Light

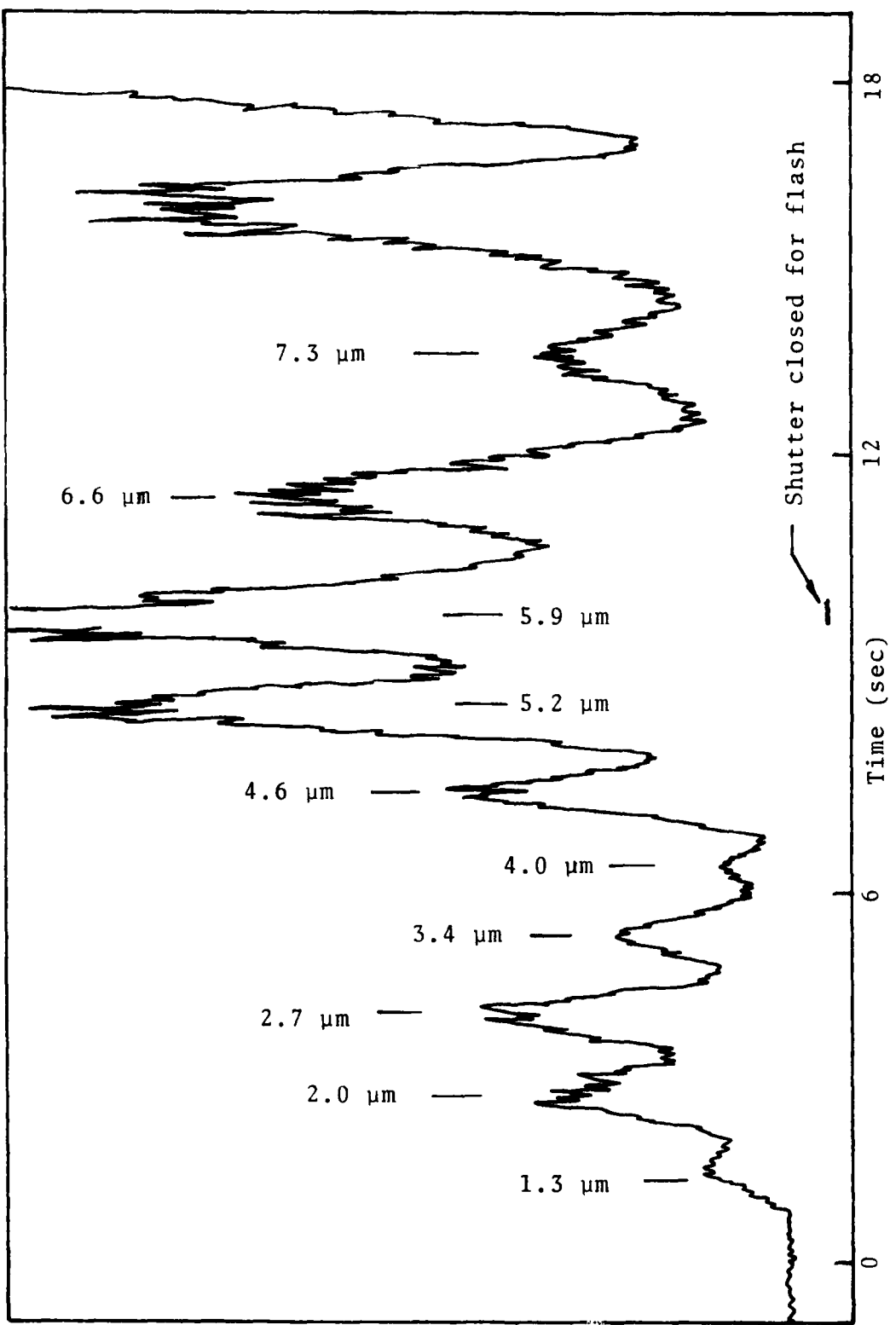


Figure 4. Mie Scattering Signal from a cloud of monodispersed drops as a function of time. Drop radii are shown.

size distribution (see Appendix E).

AEROSOL GENERATION AND CHARACTERIZATION

Generation

One of the predominate aerosols in the marine environment is sodium chloride (NaCl), therefore we have followed a program to develop methods for generating NaCl aerosol in the size range and concentrations required. The size range of primary interest has been between 0.01 μm and 0.05 μm with concentrations up to 10^5 - 10^6 cm^{-3} . Most of our effort has been directed at evaporation - condensation technique using high temperature furnaces (See Appendix E) with a smaller effort directed to methods based on the evaporation of salt solution droplets.

The furnace technique while requiring more equipment has the advantage that it can produce a relatively stable aerosol over a period of hours which permits the use of an aerosol with the same characteristics in several successive experimental expansions over the course of a day's operation. The system is also sufficiently reproducible to allow returning to the use of an aerosol with particular characteristics when required.

In most of the early experiments it was planned to use an aerosol with a nearby monodispersed size distribution. While the size distribution of the aerosol produced by the furnace method cuts off at the large end it does not do so on the small end, therefore the polydispersed aerosol is passed through an Electrostatic Classifier (Thermo Systems, Inc., Model 3071) to select out particles of the required size (see Appendix G). Figure 3G shows a typical result using this procedure.

The second generation method utilizes a standard Collision atomizer to generate droplets of the appropriate salt solution. The droplets are then exposed to a desiccating environment and the water removed by evaporation leaving a small salt particle. The resulting aerosol is polydispersed but can be made monodispersed by use of the Electrostatic Classifier. The size and concentration of the aerosol is dependent on the air flow rate and salt

solution concentration (see Appendix H).

While this technique requires less equipment and can be started on short notice, it requires a source of compressed air and the resulting maximum concentrations are at least an order of magnitude less than those from the furnace method.

Due to its abundance in the atmosphere silica was selected as the next type of aerosol for study. The generation technique developed (Appendix I) involves the hydrolysis of alkyl silicates in alcoholic solutions, in the presence of ammonia which act as a catalyst. The size of the resulting monodispersed spherical particles depends on the chemical concentrations and type of alcohol used. The suspension is then atomized and passed through a heated ceramic tube. As with the salt aerosols the monodispersity and determination of the particle size can be improved by use of the Electrostatic Classifier.

Characterization

Considerable work has been done with the continuous flow thermal diffusion chamber (CFD) in selecting and developing its use as a condensation nucleus counter (Alofs and Carstens, 1976*; Alofs, 1978**; and Alofs et al., 1979***). It was planned that the CFD would be the primary aerosol characterization instrument for use with the simulation chamber. The intention is to provide the same sample to both the simulation chamber and the CFD such that the CFD can determine the activation supersaturation spectrum of the aerosol while the initial turbulence in the simulation chamber is decaying before the state of the expansion.

A comparison of the results from measurements on the salt aerosols generated using either the condensation of salt vapor or evaporation of salt solution technique did not show any effects

*Alofs, D. J. and J. C. Carstens, 1976: "Numerical Simulation of a Widely Used Cloud Nucleus Counter", *J. Appl. Meteor.*, 15, 350-354.

**Alofs, D. J., 1978: "Performance of a Dual Range Cloud Nucleus Counter", *J. Appl. Meteor.*, 17, 1286-1297.

***Alofs, D. J., M. B. Trueblood, D. R. White and V. L. Behr, 1979: "Nucleation Experiments with Monodisperse NaCl Aerosols", *J. Appl. Meteor.*, 18, 1106-1117.

due to type of generator (Appendix H). Electron microscope studies did show a difference in structure but this did not affect the activation characteristics. The electron microscope studies also verified that the dry particle size as determined by the CFD or the Electrostatic Classifier were correct.

Similar studies with the silica aerosols showed agreement between the electron microscope and CFD that the particles were monodisperse and of the correct size.

Studies so far have indicated that the CFD is an effective instrument for characterizing aerosols for use in the simulation chamber experiments.

COMPUTER CONTROL, DATA ACQUISITION AND MODELING

Control and Data Acquisition

With a policy that the capability and versatility of the overall system should be kept as broad as possible coupled with the requirement to read and store over 100 different channels of data from a variety of sensors it was recognized at the beginning of the project that digital control and data acquisition was a must. The heart of the resulting system is a NOVA Model 830 minicomputer with appropriate peripherals (Appendix J).

During an experiment data acquisition and storage represents one of the computer's two primary real time duties. At predetermined times during the experiment, beginning while the sample is entering the chamber and continuing until the chamber is opened for cleaning, the computer reads and stores either all or selected groups of transistor thermometers. Those temperatures useful in guiding the action of the operator are displayed on the CRT terminal and updated as new data is gathered. Also during the experiment the data from the pressure transducer, photomultiplier tube, silicon photodiode, numerous valve position indicators and several flow meters are taken and stored according to a predetermined plan.

The data is available for use as control input during the experiment as well as hard copy output after the experiment for post experiment analysis.

Control is the second primary real time function of the computer. During the expansion the gas and wall temperatures must track each other closely to minimize the wall effects. Because of the slow response time of the walls due to their high thermal mass the wall temperature is made to follow a predetermined time profile. At present the pressure is then controlled to follow a similar time profile which is predetermined based on the nucleation and growth model currently being used. Work is being directed toward being able to perform the model calculations in real time based on sensor data to determine the required pressure, but this is not possible yet.

The computer also initiates the data acquisition programs throughout the experiment as required as well as insuring that all of the air and sample flow directing valves are in their required positions.

Modeling

Direct gas temperature measurements are not practical in a situation where condensation is occurring (Kassner et al., 1968)*. Therefore in order for the control system to maintain the gas temperature equal to the wall temperature a cloud must be used to determine the corresponding pressure. The model must also include the effects of drop growth.

The use of the model for control purposes implies that it can be run in real time on a computer connected to the experimental facility. While a variety of models exist (Cotton, 1975)** they are primarily directed to theoretical studies and not suitable for control purposes.

Considerable effort has been given to developing a computer cloud model which can serve the needs of real time control of the simulation chamber. This would permit the continual

*Kassner, J. L., Jr., J. C. Carstens and L. B. Allen, 1968: "Analysis of the Heat and Vapor Propagation from the Walls of the Nolan, Pollak, and Gardner Type Condensation Nucleus Counter", J. Atmos. Sci., 25, 919-926.

**Cotton, W. R., 1975: "Theoretical Cumulus Dynamics", Rev. Geophys. Space Phys., 13, 419-448.

correction of the profiles to account for the actual liquid water content. Much of the effort has been devoted to streamlining the model to reduce computing time. At present the model can run in real time except for a short interval which occurs just as the cloud begins to form (Appendix K).

Other modifications of the model adapt it for use in determining the proper selection of various parameters during experiment design to enhance the effect under study and during post experiment analysis of the results.

CONCLUSIONS AND RECOMMENDATION

During the period of the contract major portions of the design, development and construction of the cooled wall expansion chamber and supporting equipment has been carried out. In addition, work in the classification and generation of aerosols has been particularly successful. It is unfortunate that the failure of the thermoelectric modules in the simulation chamber force termination of the work with the Proto I chamber before any of the main experiments could be performed. The experience gained in working with the Proto I chamber, even with its temperature anomalies, has shown that construction and operation of this type of chamber is feasible.

While the expansion chamber itself has been disassembled, all of the support equipment remains operational. At present a new chamber similar to Proto I but with the faults corrected is being constructed under separate funding. The new chamber is referred to as Proto II. A taller chamber (2.84 m), designated as Romulus, is also under construction. Work on both chambers is well advanced.

We feel that when one of these chambers becomes operational, the original scientific program, as well as any new areas, should be reviewed and work in those areas of study which have not been addressed by other methods renewed.

APPENDIX A
The CLOUD PHYSICS TRANSISTOR THERMOMETER
Characteristics and Preliminary Data

(Revised on 4/28/76)

Written by
Larry W. Berkbigler
2 September, 1975
University of Missouri-Rolla
Cloud Physics Research Center
Rolla, Missouri 65401

FOREWORD

The thermometer described in this report was developed to satisfy a need for an inexpensive alternative to expensive commercial precision thermometers. The resulting thermometer was quite successful and is currently being considered for a patent by personnel at the Office of Naval Research.

The thermometer was developed with the financial aid of ONR-Themis through grants held by Dr. James L. Kassner, Jr. Much of the original development work was done by Mr. Bruce A. Warren. The concept was further developed and refined by Larry W. Berkbigler and Paul C. Kriegshauser, who jointly compiled the information and data in this report with the computer programming aid of Mrs. Kathryn P. Berkbigler.

TABLE OF CONTENTS

	Page
I. BACKGROUND	1
II. OPERATION	3
A. Measurement Theory	3
B. Circuit Description	4
III. ANALYSIS OF THERMOMETER ERRORS	8
A. Errors Due to Thermometer Nonlinearities	8
B. Errors Due to Instabilities in Circuit Parameters	13
C. Errors Due to Sensor Heat Flows	17
IV. APPLICATION	23
A. Sensor Construction and Application	23
B. Thermometer Calibration and Testing	24
C. Notes on the Cloud Physics Thermometry Systems	30
FIGURES	33
REFERENCES	41
APPENDIX A	42
A Mathematical Model of the Transistor Thermometer	42
APPENDIX B	45
Thermometer Component Parts Description	45
APPENDIX C	46
Specifications of the Revision 2 Transistor Thermometers	46

I. BACKGROUND

Development of the thermometer described in this report was begun in 1972 to satisfy the needs of the Cloud Simulation Chamber facility at the University of Missouri at Rolla, Graduate Center for Cloud Physics Research. The needs were (and are) for high gain electronic thermometers which would be inexpensive, relatively fast, and very accurate over a narrow temperature range (-40°C to +40°C). High gain thermometers were desired because they would decrease costs and errors in the recording and amplifying circuits driven by the thermometers. Low cost thermometers were necessary because a multitude (potentially hundreds) of measurements are required in the facility. A fast response was desired because it decreases the measurement errors during temperature excursions. It was decided that absolute accuracy, though desirable, was less essential than differential accuracy (thermometer to thermometer) and stability over time.

In-house development was necessary because all commercial instruments with sufficient accuracy were prohibitively expensive. Five techniques considered for development were:

1. Converting the change in a temperature sensitive resistance to voltage and amplifying it;
2. Amplifying the voltage output of a thermocouple junction;
3. Converting the resonant frequency change of a crystal to a voltage and amplifying it;
4. Infrared temperature measurement, and;
5. Amplifying the voltage change across a semiconductor junction which is biased with a constant current.

After varying amounts of development these techniques were abandoned because they were insufficiently accurate or too expensive to implement.

The technique which was further developed was first seen in an article written by Robert Pease, in which he described thermometry using transistors as sensors¹. Although the technique is similar to the fifth one mentioned above, it differs in several ways which tend to improve the overall performance. The transistor thermometer does use the base-emitter junction voltage for the temperature-to-voltage conversion, but the sensor's collector current is held constant; the base current can, and does, vary as the sensor temperature changes. The primary advantage of this circuit is that the sensor transistor is in a feedback loop where its gain decreases the overall thermometer sensitivity to the amplifier used as a gain element. This will be illustrated in the next section after the thermometer operation has been explained. Similar thermometers have been mentioned in other journals², but their stability is not sufficient and upon careful reading, one wonders whether they were completely understood by the manufacturer.

II. OPERATION

A. Measurement Theory

The thermometer uses the base-emitter voltage (V_{BE}) of a small signal transistor for the temperature-to-voltage conversion. This voltage is highly predictable according to the equation^{3,4}:

$$V_{BE} = V_{g0} \left(1 - \frac{T}{T_0}\right) + V_{BE0} \left(\frac{T}{T_0}\right) + \frac{mkT}{q} \ln\left(\frac{T_0}{T}\right) + \frac{kT}{q} \ln\left(\frac{I_c}{I_{c0}}\right)$$

or

$$V_{BE} = V_{g0} - T \left[\frac{V_{g0}}{T_0} - \frac{V_{BE0}}{T_0} - \frac{mk}{q} \ln\left(\frac{T_0}{T}\right) - \frac{k}{q} \ln\left(\frac{I_c}{I_{c0}}\right) \right] \quad (1)$$

where

T = temperature ($^{\circ}$ K)

V_{g0} = 1.205 volts (the extrapolated energy-band-gap voltage for silicon at $T=0^{\circ}$ K)

m = a constant determined by transistor type (typically 1.5)

k = 1.38×10^{-23} j/ $^{\circ}$ K (Boltzmann's constant)

q = 1.602×10^{-19} coul (the electronic charge)

V_{BE0} = V_{BE} at some initial collector current I_{c0} and temperature T_0 .

As will be shown later, the thermometer circuit typically biases the sensor transistor at a constant collector current, so (1) becomes

$$V_{BE} = V_{g0} - T \left[\frac{V_{g0}}{T_0} - \frac{V_{BE0}}{T_0} - \frac{mk}{q} \ln\left(\frac{T_0}{T}\right) \right]. \quad (2)$$

The last term in equation (2), being a source of non-linearity, is a basic error in the thermometer even if the circuitry contributed no additional errors. To determine the magnitude of

this error, values of V_{BE} were calculated for various temperatures using this equation. The errors are reasonably small over small ranges; for example, over a 0°C to 25°C range the deviation of this equation from a straight line through the end points is less than 0.016°C .

Referring to (1), one notices that the nonlinearity could be entirely eliminated if the collector current were made to vary with temperature so that the last two terms cancelled. To do this,

$$I_c = \left(\frac{I_{c0}}{T_0}\right) T^m$$

which wouldn't be particularly easy to implement electronically. However, it is easy to make the collector current proportional to absolute temperature. Calculations show that making

$$I_c = \left(\frac{I_{c0}}{T_0}\right) T$$

will decrease the deviation mentioned above from 0.016°C to about 0.005°C . Since this is a significant improvement, the capability of varying the collector current in this fashion has been incorporated as an option into the circuit which is explained in the following section.

B. Circuit Description

A simplified schematic of a thermometer is shown in figure 1. If the circuit is in its active operating region, the collector of Q1 will be held by A1 to very nearly zero volts. Under this condition the collector current of Q1 will be a constant

determined primarily by the positive reference voltage (+REF) and R8. The emitter voltage of Q1 is determined by the negative reference voltage (-REF) and the voltage divider consisting of R1, R2, R3 and R4. This voltage is set by adjusting R1 and R2 until the thermometer output is zero when the sensing transistor is at 0°C. The thermometer output is a multiple of the base voltage of Q1. The value of this multiple is determined by the voltage divider consisting of R5, R6 and R7. The gain of the thermometer is set by bringing the sensor transistor to a known temperature and adjusting R7 until the thermometer output reads correctly. The resistance values shown in the schematics in this report are selected to cause the thermometer output to be zero at 0°C and to have a gain of -0.1v/°C. The voltage divider resistors could be changed to allow the thermometer to have different gains and zero points.

To understand the circuit operation, assume the temperature of Q1 increases. The base current of Q1 will tend to increase (V_{BE} decreases) and, since the transistor gain is several hundred, the collector current will tend to increase several hundred times as much. But any increase in collector current produces a voltage change at the positive input of A1, where it is greatly amplified and fed back to the base of Q1. This feedback keeps the collector current very near its original value by decreasing the base voltage an amount proportional to the transistor temperature change.

Referring to figure 2, one sees many additional components which are not shown on the simplified thermometer schematic. Components R10, R11, R12, R13 and A2 comprise an error reducing circuit which can vary the collector current of Q1 proportionally to the absolute temperature. This "linearizing" option, whose function was explained earlier, is not necessary; but it can significantly reduce thermometer errors, as will be shown in the next section. The circuit inverts the thermometer output to obtain a voltage proportional to temperature. This voltage is impressed on R13 to cause the collector current of Q1 to vary proportionally to temperature.

Capacitors C1-C7 are all included to insure the AC stability of the circuit by 1) shunting EMI signals which would otherwise be rectified by various circuit components to cause apparent DC errors, 2) shunting EMI which would cause AC noise on the thermometer output, and 3) eliminating instabilities caused by the capacitances of long cables which may be used on the thermometer sensor and output. Using these capacitors eliminates, in most cases, the need for careful shielding of the thermometer circuitry. This is done at the expense of greatly limiting the circuit's bandwidth, but even with the capacitors the time constant of the circuit is 1/1000 the thermal time constant of the sensor, which is one second at best. Thus the capacitors do not significantly affect overall thermometer response time.

Ferrite beads L1, L2 and L3 operate in conjunction with C1, C2 and C3 to decouple the sensor cable at high frequencies. The sensor cable is shielded, but the beads were still required to

eliminate errors when there was strong EMI. Resistors R14 and R15 with capacitors C6 and C7 are used to decouple each card of two thermometers from the amplifier power supply.

The gain and zero potentiometers are wirewound for stability and their values were chosen to insure a resolution of one millidegree per wire. A discussion of stability requirements for all circuit components will follow in the section on analysis of thermometer errors due to changes in circuit parameters.

III. ANALYSIS OF THERMOMETER ERRORS

A. Errors Due to Thermometer Nonlinearities

The errors described in this section would occur even if the only change in the state of the thermometer was a change in sensor temperature. They are primarily due to sensor nonlinearities. The effects of ageing and ambient temperature changes are assumed to be zero; these are discussed in the next section. The thermometer performance predicted in this section is the optimum for the chosen circuit configuration and components; it can never quite be achieved.

Figure 3 is a feedback system model for the thermometer of figure 2. This model is used only to illustrate the operation of the thermometer and to assist in calculation of the thermometer circuit's loop gain. As shown, the temperature of the sensor (T_{Q1}) is converted to the voltage V_{BE} according to the relationship stated earlier. This voltage is summed with the emitter voltage (V_E) to yield the base voltage (V_B), which is compared by Q1 to a portion of the thermometer output voltage (V_0/K_2). Any difference is multiplied by the voltage gain of Q1 and appears at the collector (V_C), where it is multiplied by the voltage gain of A1 whose output is the thermometer output (V_0). As in any high gain feedback system, the steady state error in the output is V_0/G , where G is the loop gain. To determine the loop gain for the thermometer one must determine the voltage gains of the sensor, the amplifier, and the feedback voltage divider. The voltage gain of the sensor is

$$A_V = \frac{\Delta V_C}{\Delta V_B} = \frac{R8\Delta I_C}{\Delta V_B} = \frac{R8(\Delta V_B/h_{ie})h_{fe}}{\Delta V_B} = \frac{R8h_{fe}}{h_{ie}}$$

$$= \frac{R8h_{fe}}{m h_{fe} kT/q I_E} = \frac{R8I_E}{m kT/q} \approx 170 \text{ at } 300^\circ K$$

where

I_C = sensor's collector current, 60×10^{-6} A

h_{ie} = dynamic resistance of sensor's base, Ω

h_{fe} = sensor's small signal current gain

I_E = sensor's emitter current, approx. 60×10^{-6} A

$R8$ = sensor's collector load resistance, $10^5 \Omega$.

From the manufacturer's data sheets, the gain of A_1 is seen to be 25,000 or greater; and referring to figure 2,

$$K_2 \approx (R5+R6+R7)/R5 \approx 43.$$

Thus, the loop gain of the circuit is at least

$$G = 25,000 \times 170 / 43 \approx 100,000$$

and the error due to finite loop gain is $V_0/100,000$ or less, which is negligible. This means that the thermometer output will be a multiple (K_2) of V_B which is just offset from V_{BE} which is proportional to temperature. Thus the thermometer output will be proportional to temperature with negligible error due to finite circuit gain.

The preceding discussion allows construction of a more useful model for the mathematical description of thermometer operation and errors. The model is shown in figure 4 and developed in appendix A. It is based on the premise that the circuit loop gain is high enough so the output voltage will become whatever value is necessary to cause V_C to be zero and I_C

to thus assume a value determined by +REF, R8, and possibly R13.

The model accurately predicts thermometer errors due to some component drifts and also predicts linearity errors fairly accurately. Many simulations were run using calibration points of 0°C and 25°C. Figure 5 summarizes the results of these runs and compares them to the experimental data for corresponding thermometers. The experimental data was obtained by measuring the temperature of an aluminum block with a Hewlett-Packard Model 2801A Quartz Thermometer and with transistor thermometers which had been calibrated to agree with the Quartz Thermometer at 0°C and 25°C. The temperature of the block was varied and the difference between the Quartz Thermometer and transistor thermometers was noted at five degree intervals.

The discrepancies between the experimental and model deviations are difficult to explain. There are three likely possibilities which will be discussed. They are 1) errors due to Quartz Thermometer nonlinearities, 2) errors caused by experimental apparatus and procedure, and 3) errors due to model or circuit deficiencies.

Part of the discrepancy between experimental and model data is certainly due to the nonlinearity of the Quartz Thermometer. Although precise data on its errors is unavailable, that which can be found shows that the deviations of the Quartz Thermometer from true temperature are in a direction opposite from those of the Transistor Thermometer. Thus the Transistor Thermometer errors are not as great as experimental data indicates, but it

doesn't seem likely that errors in the Quartz Thermometer could account for all of the discrepancies between experimental and model data.

There are undoubtedly errors in the experimental data due to deficiencies in the apparatus, as illustrated by the fact that, for different runs, the deviation between the Transistor and Quartz Thermometers at 15°C varied as much as 0.006°C . The aluminum block used in the test had temperature gradients in it which may have contributed to the variations, and the problems of heat flow down the thermometers' sensor cables couldn't be entirely eliminated. However, the fact that all thermometers were zeroed in an ice bath, and remained within $\pm 0.002^{\circ}\text{C}$ when inserted into the aluminum block at 0°C was some indication of validity. It would be desirable to perform a more rigorous linearity check at some future date, but the expense of such a test in terms of time and materials could be great. The linearity experiments described above have errors of less than $\pm 0.005^{\circ}\text{C}$ in the deviation data due to experimental deficiencies.

The model is quite simple and has been checked experimentally where possible. For example, the model assumes a constant value of I_C for the basic thermometer; this was verified experimentally. The model also predicts precisely the effects of variations in the reference voltages. It seems that the model accurately predicts circuit operation, so if there is any error in the model it probably comes from the $V_{BE}(T)$ equation. In one reference³, there is some mention of the possibility of errors

in the $V_{BE}(T)$ equation, but the magnitudes of the errors is not considered. To check circuit operation, the sensor V_{BE} was carefully measured during a linearity check; the thermometer output was found to display precisely the same nonlinearity as V_{BE} . Thus, the circuit is apparently not contributing to the nonlinearity.

Two additional points should be noted in this section. One is that thermometers using sensors of the same type (typically 2N5089) always tracked within a millidegree. In all linearity tests, 2 or 3 transistor thermometers were compared to the Quartz Thermometer in each experiment. Although the transistor thermometers differed from the Quartz Thermometer by varying amounts in different experiments, the Transistor Thermometers always agreed among themselves, even when the sensors were manufactured by different companies. This is a very important point because, in many applications, the absolute accuracy of the thermometers is far less important than the differential accuracy. Since the Transistor Thermometers agree very well, their differential accuracy can be extremely high; it is limited only by sensor construction and application, which will be discussed later.

The second important point is that the optional linearizing circuitry significantly reduces thermometer error, as shown in figure 5. The Cloud Physics thermometers do not employ this option because it doesn't improve the differential measurements for which these thermometers are used. Only one

linearizing circuit transfer function was tested; others could be implemented by changing R13, or by making the linearizing circuit nonlinear and connecting R13 to the junction of R4 and R2.

B. Errors Due to Instabilities in Circuit Parameters

The errors described in this section could occur even if the sensor temperature remained constant. They are caused by many diverse phenomena; the list is undoubtedly incomplete, for every time someone feels that all errors are understood, another new one crops up.

Before considering specific errors, it might be wise to consider briefly the causes of the errors. The most notable offenders are time, temperature, noise, and humidity. Time is probably the hardest to detect, for it is difficult to accelerate its effects reliably. All critical components were chosen with time stability in mind. The best overall indicator of success is the fact that several thermometers have operated continuously for four months with drifts of less than $\pm 0.005^{\circ}\text{C}$ from all causes. Since the beginning of that test a new model of the thermometer has been developed which is expected to be more stable. Ambient temperature changes will cause errors, but they are fairly easy to isolate and diminish; they will be considered in detail during the following discussions. Noise is another elusive cause of error since it may come and go, and has many sources which can disturb the sensitive thermometer. Sources that have caused problems include the sensor, circuit loading, radio stations, and motors. The respective cures were to use

a lower noise sensor, improve circuit compensation, bypass high impedance points, and add ferrite beads to the sensor cable and an EMI filter to the AC power line. Humidity has not been a problem so far because special precautions were taken and because the thermometers are not exposed to humidities greater than 60%, but experience indicates that it could cause significant errors. For example, a change in the leakage around R3 (see figure 2) of 2×10^9 ohms will cause an error of one millidegree. It is important to clean all soldered points thoroughly if the thermometers will be used in high humidity environments.

The sensor is the most important component, obviously, and the most sensitive to humidity. A great deal of time was spent trying to find a low-noise sensor which was unaffected by humidity; this was necessary because the sensors often monitor humid air or water temperatures, and because they are inserted into water during calibration. Many transistor types (such as G.E. #2N2712, 2N6002, 2N6008, and Fairchild #2N5963) are sensitive to moisture. If they remain immersed in water between tests, the thermometers' outputs typically drift several hundredths of a degree in a negative direction during the first week and continue indefinitely in the same direction at a slower pace. However, some transistor types (such as National #2N5089 and Motorola #2N5089) are completely unaffected by immersion for at least six to seven days; some have been immersed in water varying between 0°C and 25°C for four months with no trend in their drifts. Such performance is not typical, though, because most 2N5089 sensors begin after one to three weeks to cause their thermometers' outputs to drift slowly negative.

The reason for the drifts in most transistors is not completely resolved, but the probable explanation is that water permeates the package and attacks the chip. Motorola and National might either use a better chip passivation process or a better epoxy package. Many coverings and sealers were tested, but none would seal the leaky transistor types; water is apparently very permeant. In any case, the 2N5089 solves the problem nicely, since it is also a low noise transistor. A low noise sensor is desirable because a sensor with much low-frequency noise, such as some G.E. 2N2712 transistors which were previously used, can cause the millidegree digit of the readout to flicker. The long-term errors in the low-frequency noise region are greater, so random drifts of several millidegrees can be observed over periods of days. The type 2N5089 was tested and found to have a typical RMS noise level about a factor of five below that of the type 2N2712, so that its noise is not observable. It should be mentioned that the low-frequency noise levels varied by as much as 4 to 1 for sensors of the same type.

The negative reference must be extremely stable for low thermometer drift; the thermometer sensitivity to this voltage is one millidegree/0.05 mv. or one millidegree/3.5 ppm. In other words, the thermometer output will drift one millidegree for a change of only 3.5 parts per million on the negative reference. The positive reference is less critical, for the thermometer sensitivity to that supply is only one millidegree/0.33 mv. or one millidegree/55 ppm. Sensitivity to the +15V power supply is less than one millidegree for a +5% variation.

The most critical resistors in the circuit are those comprising the emitter voltage divider, or R1, R2, R3 and R4. The thermometer sensitivity to differences in drifts of R3 and R4 is

approximately one millidegree/4.2 ppm. The sensitivity to the zero potentiometer is only about one millidegree/330 ppm. The thermometer sensitivity to the collector current sensing resistor, R8, is one millidegree/55 ppm. The thermometer sensitivity to differences in the drifts of the base voltage divider resistors (R5, R6 and R7) is $V_0 \times 1$ millidegree/100 ppm, where V_0 is the output voltage. Thus, when the output voltage is two volts (20°C), the sensitivity is one millidegree/50 ppm. The sensitivity to the gain potentiometer is about 1/9 that of the overall base voltage divider, or $V_0 \times 1$ millidegree/990 ppm. Thermometer sensitivity to the linearizing components will not be considered, except to mention that the sensitivity to any resistor in that part of the circuit is less than or equal to the sensitivity to the base voltage divider resistors. The exact sensitivities to those components depends upon how much gain is used in the circuit, and whether the non-inverting thermometer output is used. Resistors R9, R11, R14 and R15 are the only non-critical resistors in the circuit.

The capacitors in the circuit need not have close tolerances on their value ($\pm 20\%$ is sufficient) but they should have low leakages. Capacitor C1 is especially critical, for a change of six nanoamps in its leakage will cause a one millidegree shift in indicated temperature.

The amplifier A1 need not be fancy; the effects of its drifts are decreased primarily because, in this circuit configuration, the amplifier does not directly amplify the sensor's signal. For example, an input offset voltage drift increases the sensor

collector current just as would a shift in the positive reference. Thus, the sensitivity to drift of the A1 input offset voltage is only one millidegree/0.33 mv. A drift in the amplifier's input offset current changes the sensor collector current by the amount of the drift, so that sensitivity is only one millidegree/3.3 na, which is also the thermometer sensitivity to changes in sensor collector current.

The connections to the thermometer must also be given consideration to insure stability. The thermometer sensitivity to resistance changes in the sensor's emitter lead is one millidegree/0.04 ohm, and the sensitivity to changes in the negative reference path is about one millidegree/0.03 ohm. Therefore, all connections should be clean and preferably gold plated. Special care must be taken to avoid errors due to changes in ground currents or changes in reference currents. It is very important that any thermometer be adjusted or, preferably, recalibrated if its cable length is to be changed, for the indicated temperature decreases about 2.36 millidegrees for each additional foot of cable. It has also been shown that changing the temperature of a 30-foot sensor cable (Belden #8643) by one degree Celsius will shift the thermometer output 0.2 millidegree, due only to the change in cable resistance. It is very important that there be no electrical or mechanical leakage in the cable or connectors.

C. Errors Due to Sensor Heat Flows

The errors caused by heat flows in the sensor are difficult to quantify because they depend greatly on the application and probe design. To eliminate some confusion, only the probe which

is currently in use at Cloud Physics will be considered quantitatively. This probe is sketched in figure 6 and its construction is outlined in the next section. Before the errors in the probe can be estimated there are three sets of thermal impedances which must be analyzed.

The first is the thermal resistance from the sensor junction to the outside probe surface (θ_{JS}). This was measured by increasing the power dissipated by a probe inserted over 1- $\frac{1}{4}$ " into an ice bath (see calibration notes) and noting the resulting junction temperature rise. Under these conditions, θ_{JS} was approximately 60°C/W. There is actually little apparent improvement in θ_{JS} as a probe is inserted more than about $\frac{1}{2}$ " into a material because the surface area doesn't increase appreciably. However, as a probe is removed to shallower depths, the apparent θ_{JS} will increase as the surrounded surface area decreases. Thus, a sensor inserted only $\frac{1}{4}$ " into a material which is at least a moderately good heat conductor, such as water, will have an apparent θ_{JS} of approximately 100°C/W.

The second important thermal resistance is that from the probe surface to the measured surface, or θ_{SS} . For materials which are moderately good heat conductors, the heat conducted into (or from) the sensor will not cause significant temperature gradients in the material so the measured surface is representative of the material's temperature. The sensor is usually mounted in a hole which is 0.204" in diameter, and any voids are filled with thermally conductive grease. It has been shown that, with the sensor mounted $\frac{1}{4}$ " deep, the value of θ_{SS} is less than 5°C/W;

and if it is mounted 1" deep, the θ_{SS} is less than 2°C/W .

The last thermal resistance is that of the connections to the sensor. The thermal resistance of the wires is $5000^{\circ}\text{C/W-in}$, and that of the teflon sheath is $135,000^{\circ}\text{C/W-in}$; thus the parallel combination of sensor connections has a thermal resistance of approximately $5000^{\circ}\text{C/W-in}$.

One error due to heat flow in the sensor is caused by internal heat generation. The sensor generates 36 microwatts; this heat flowing from the transistor chip to the measured surface causes a temperature difference between the two. This heat flows through θ_{JS} and θ_{SS} . Using the preceding thermal resistances, one can show the temperature difference to be 2.2 millidegrees for a sensor in a 1" deep hole or an ice bath, and 3.8 millidegrees for a sensor in a $\frac{1}{4}$ " deep hole. These errors are small and nearly constant. They are thus partially or totally removed during calibration.

Another error due to heat flow considerations is the sensor time constant. The sensor response to an instantaneous surface temperature change, such as sudden immersion in an ice bath, has a two second time constant. Thus, in 20 seconds the error is less than $1/20,000$ of the temperature change. The sensor time constant varies inversely with the amount of surface area affected, since this causes an apparent change in θ_{JS} . Thus, if the sensor is mounted in a $\frac{1}{4}$ " deep hole, the time constant will be nearly four seconds. The time constant of a sensor in a particular mounting configuration is constant and

fairly predictable, so this error is not terribly serious; it can even be decreased by compensation, if necessary.

The most serious error is caused by heat flow down the leads connected to the sensor. This heat flow, although relatively small, could cause significant errors if precautions aren't taken. The amount of heat flow is relatively easy to compute, but the errors caused by it are difficult to predict. For example, if the connecting leads are heated 2" from the sensor to a temperature 20°C above the sensor, the heat flow would be two milliwatts. If all this heat went to the chip, and then through the θ_{JS} , the error would be about 0.2°C for a sensor mounted in a $\frac{1}{4}$ " deep hole. However, a 0.015°C error is experimentally observed under these conditions. The reason for the discrepancy is the invalid assumption that all the heat flowing in the wires reaches the chip. Actually, most of the heat flows from the leads to the epoxy package surface; it is thus shunted around the chip. Additionally, since the base and emitter leads are connected to the chip with one mil bond wires, they have a relatively high thermal resistance path between them and the chip. To accurately predict the errors, a model of the sensor which has five thermal resistances would be needed. Since some of them are difficult to quantify and would vary with each mounting configuration, it is easier to experimentally determine an equivalent θ_{JS} , called $\theta_{JS'}$. To use $\theta_{JS'}$, one calculates the heat flow (Q) in the probe leads and assumes it all flows to the junction and through $\theta_{JS'}$ to the sensor surface. The error is thus $Q \times \theta_{JS'}$. To experimentally determine the value of $\theta_{JS'}$,

one raises or lowers the temperature of the probe leads to a known temperature at a known distance from the sensor (possibly with a crushed ice pack in a plastic bag) and notes the change in indicated temperature. From this data, values for \dot{Q} and θ_{JS} , can be calculated. Values for θ_{JS} , have been determined to be $7^{\circ}\text{C}/\text{W}$ for a $\frac{1}{4}$ " deep hole, and $0.75^{\circ}\text{C}/\text{W}$ for a 1" deep hole. Thus, if there is a 20°C temperature difference across the connection between the sensor and cable, the above parameters predict a 0.007°C error for a sensor mounted $\frac{1}{4}$ " deep and a 0.001°C error for a sensor mounted 1" deep. These errors are quite small, but this accuracy can be attained if the teflon tube is insulated from changes in ambient temperature.

The preceding data and calculations were for a particular probe type, but variations are currently being developed for specific uses. One possible variant is shown on the inset in figure 6. That probe is designed to be mounted in 1" deep holes where it is expected to further reduce the errors previously mentioned. It has the transistor case extended with very high thermal conductivity epoxy. This is expected to reduce to insignificance the error due to heat flow down the leads. The epoxy may decrease θ_{JS} slightly, but it is not expected to affect the time constant significantly. Another variation is similar to the basic probe, but with much of the epoxy package sanded off. It boasts a one second time constant because it has a lower θ_{JS} ; it is designed to be mounted on a surface, or possibly in a slot. Other variations have been considered for applications where temperatures of materials with poor heat

conductivities need to be measured. Those probes would minimize heat transfer to the sensor.

IV. APPLICATION

A. Sensor Construction and Application

Since the sensor can easily contribute the most error to the thermometer, it should be carefully designed and applied. Figure 6 is a sketch of the construction of the most commonly used probe. As mentioned before, the sensor is a type 2N5089 epoxy transistor whose leads have been cut to about 1/16". The connections are made with enameled copper wire; the collector lead is #42 AWG and the other two leads are #40 AWG. The wire is enclosed in a 4" length of #28 thin walled teflon tubing which has been etched about $\frac{1}{2}$ " up on the ends. One end of the tubing is attached to the sensor with epoxy and the other end is overlapped with a piece of shrinkable tubing which also covers the splices and the end of the cable. All soldering to the transistor leads should be done quickly with a clean hot iron, for if the sensor is overheated, it may be affected by moisture when it is used.

When the thermometer is mounted, all gaps between it and the measured surface should be filled with heat conductive grease. If the hole in which the transistor is mounted is less than 1" deep, the teflon tube should be insulated from direct contact with undesired materials and air currents.

An epoxy packaged sensor was used because it has desirable properties; it is nonconducting, has a small heat capacity, has a short time constant, and can be altered by sanding. The epoxy package has one major shortcoming; it is vulnerable to environmental stresses, as mentioned earlier. The 2N5089 sensor is

quite immune to moisture for short periods of time if it is only used over a short range. The exact range limits are unknown, but some sensors have been cycled numerous times between +60°C and -40°C without failure. All sensors which have been heated to 100°C have failed, and all taken much below -40°C have failed. Some sensors have failed at moderate temperatures; it appears that those failures were due to poor workmanship during construction, for the bond between the transistor package and the epoxy which holds the sheath was broken. Water then leaked to the leads and, apparently, up the package to the chip. During probe construction, the strength of this bond can be assured by cleaning all flux from the area and flushing the transistor and tube with a cleaning solvent. The "failures" in preceding discussion are characterized by an immediate sensitivity to water, very similar to that described earlier for sensors like the 2N2712.

A metal can hermetically-sealed transistor would eliminate all leakage worries, and it could greatly extend the range and reliability of the sensor, if its shortcomings could be tolerated. The connections would still need to be insulated, and sensor would probably be larger and have a longer time constant.

B. Thermometer Calibration and Testing

The Transistor Thermometer must be calibrated very carefully or its overall accuracy will be limited by calibration errors. In principle, the thermometer can be calibrated at any two temperatures, but practical considerations limit the choices. For example, the resolution of the thermometer is limited to about one millidegree by sensor noise, and the range is limited by the sensor's operating range. Calibration is very much facilitated if one calibration temperature is chosen to cause

the thermometer output voltage to be zero, for then the zero and gain adjustments are nearly independent. The greatest calibration problem is that of insuring that the transistor thermometer and the reference thermometer are at the same temperature. That may sound obvious, but, even for good thermal conductors, temperature gradients of millidegrees can occur because of incredibly small heat flows. Any calibration facility must be checked carefully for gradients, because they often change with changes in room temperature; if they do, thermometers calibrated on different days may not track one another.

The thermometers used in Cloud Physics are calibrated at 0°C and approximately 25°C . The reference thermometer is a Hewlett-Packard Model 2801A quartz thermometer; calibration is performed using an ice bath and an aluminum block at room temperature.

The ice bath, which is used to zero all thermometers, has been found to be a very consistent and stable 0°C medium. It is made using distilled water and ice made from distilled water; all materials in contact with the bath should also be reasonably free from contaminants. A small amount of contamination will only cause the temperature of the bath to shift a few millidegrees. Using tap water for the ice and water may cause an error of several more millidegrees, so it is best to keep the

bath as pure as reasonably possible. The ice baths are generally constructed as follows:⁵

- 1) Crush the distilled water ice with an ice crusher (may be a blender attachment).
- 2) Pulverize the ice in a blender, adding distilled water as necessary.
- 3) Fill a large dewar flask (1 quart or larger) with the ice, adding only enough distilled water to fill the spaces between the ice.

Baths constructed as explained above should not vary more than ± 1 millidegree from bath to bath.

There is no provision for heating or cooling the aluminum block which is used for gain calibration. The block, sketched in figure 7, is well insulated and is allowed to "float" around room temperature. Because there is no appreciable heat flow in the block, gradients are negligible and the temperature of the block changes very slowly. The necessity for negligible gradients is obvious, but the need for slow temperature changes is more subtle. The primary reason is that the time constants of the quartz thermometer and transistor thermometer probes are 12 seconds and two seconds respectively. If the temperature of the block changes at a rate of 0.1 millidegree/second, the temperatures of the thermometers will be approximately one millidegree different due to the different time constants; a greater rate of temperature change causes a greater temperature difference. Another reason slow temperature changes are desirable is that, if the block changes temperature slowly, it will smooth out small

and rapid variations in room temperature. The block shown in figure 7 drifts 0.01 millidegree per second for every degree of difference between the block temperature and ambient temperature.

Prior to calibration, one should check all references to insure precise tracking of all thermometers. If the voltage references have drifted, they should be readjusted to their correct values.

It is also a very good idea to keep three or more transistor thermometers as references for use during calibration. These should be inserted into the ice bath to insure that it is a good bath. If the bath is good, the quartz thermometer should be adjusted to read 0°C while its probe is at rest in the bath. Previous data shows that the quartz thermometer's zero drift can be several millidegrees per week, but the gain is very stable. Thus, the quartz thermometer should be zeroed before it is used as a room temperature reference for transistor thermometer gain calibration.

From the above discussion one can see that, in terms of millidegrees, there is no single absolutely trustworthy reference. The ice bath is most reliable, but it can become contaminated; the quartz thermometer has stable gain, but its zero drifts; the transistor thermometers are stable, but they need to be checked, too. Thus, during calibration, one compares all references; if anomalies turn up, he must use his best judgement to determine which reference is in error.

The following steps are used to calibrate and check the thermometers with 2N5089 sensors.

- 1) Check the transistor thermometer voltage references and readjust them if necessary.
- 2) Make an ice bath as described earlier.
- 3) Check the ice bath for contamination by inserting the reference transistor thermometer probes at least 1- $\frac{1}{2}$ " into the center of the ice. The thermometers should indicate that the bath is within the desired accuracy of 0°C.
- 4) Insert the quartz thermometer probe into the ice bath and readjust the quartz thermometer if necessary, as discussed earlier. Be certain that all objects inserted into the ice bath are reasonably clean.
- 5) Be sure that all thermometers are installed in each rock from which any thermometers are to be calibrated. R2 should be installed on all thermometers; it should be a short for uncalibrated thermometers. The system should have warmed up long enough to be stable.
- 6) Insert up to eight thermometer probes at least 1- $\frac{1}{2}$ " into the center of the ice bath.
- 7) Turn the zero potentiometers to their midpoints. Change R2 to cause the indicated temperature to be within one degree of zero. Decreasing R2 by 100 ohms increases the indicated temperature by about 2.3°C. The range of the zero pot is about 2.9°C.

- 8) After waiting 15 minutes or more for R2 to cool, jiggle the probes and adjust the zero potentiometers for an indicated temperature of 0°C. Shake the probes again, tamp the ice and recheck the indicated temperatures.
- 9) Insert the transistor and quartz thermometer probes into their holes in the gain calibration block; insure that the holes are full of water when the probes are inserted.
- 10) Allow the sensors and the block to stabilize for at least 10 minutes (or longer if water was added), then adjust the thermometers' gain potentiometers to cause the indicated temperatures to agree with a corrected quartz thermometer reading. The corrections are shown in figure 8; they compensate for the nonlinearity of the transistor thermometers so that all thermometers will track one another despite their having been calibrated at different sensor temperatures.
- 11) Insert the transistor probes into the ice bath again to recheck the zeroes. Although there is little interaction between the zero and gain if the preceding calibration sequence is used, it is wise to double-check the zero. If the zero is readjusted in this step, the thermometer gain must also be readjusted as in steps 9 and 10.

The following are checks of thermometer operation and reliability.

- 12) To check for electrical leakage between the sensors and water, one can dip into the ice bath a clip lead connected to the -15 volt amplifier power supply. The indicated temperatures of probes in the ice bath will change less than a millidegree for good probes.
- 13) To check sensor immunity to humidity, leave the sensors in the ice bath after calibration is complete. Recheck the zeros about an hour later; the thermometers should not have drifted. A sensor may be vulnerable to moisture even when there is no electrical leakage.
- 14) To check overall circuit operation, one can monitor the sensor emitter voltage as the sensor is cycled between 0°C and room temperature. The voltage should change less than 20 microvolts. This test can detect defective sensors, leaky cables, defective amplifiers, etc. Measure the voltage carefully to avoid seeing apparent errors which are really due to ground currents.

C. Notes on the Cloud Physics Thermometry Systems

The transistor thermometers are widely used at Cloud Physics. There are three racks in use with various experimental facilities and one cabinet containing eleven racks of 16 thermometers for use with a cloud simulation chamber. The three individual racks contain five, six, and seven thermometers; these racks are completely self-contained, for each has its own reference supplies which are derived from its amplifier power supply.

The 176 thermometer cabinet was carefully planned to eliminate errors from ground currents and other loading effects. One pair of reference supplies feeds all thermometers, so there will be no differential errors due to reference supply drifts. The reference supplies are designed to be extremely stable, despite the fact that the negative reference supplies 300 milliamps. Each rack of 16 thermometers is individually wired to the reference points (GND, +REF, -REF) in the cabinet; all temperature measurements and calibrations are made using the point ground in each rack. The thermometers are not used or calibrated unless each thermometer is in the rack and carrying its proper current from the negative reference. All thermometer sensors are insulated and the thermometers' outputs go only to differential input devices. These measures, along with the fact that the thermometer cabinet ground is connected to the external system ground at only one point, should eliminate all errors due to circulating ground currents.

The thermometer design has been revised twice since the original eight units were made. The first revision (mid 1974) included the following modifications:

- 1) Designing a more sophisticated circuit board to eliminate the R.F. pickup and ground problems associated with the original model.
- 2) Gold plating the connectors on the new circuit board to eliminate errors due to contact resistance.
- 3) Stabilizing the AC characteristics of the circuit to eliminate oscillations which occurred in the original

model anytime its output was connected to a cable.

- 4) Changing the zero adjustment circuitry to permit an adjustment resolution of approximately one millidegree, rather than the ten millidegree resolution of the original model.

The second revision (early 1975) included the following changes:

- 1) Designing a more compact circuit board which contained two thermometers in the space previously occupied by one.
- 2) Employing a new sensor type in a radically modified probe design, which decreased errors due to sensor heat flows and sensor noise.
- 3) Adding a linearizing option to the circuit board.
- 4) Changing the zero adjustment circuitry to decrease the thermometer sensitivity to changes in potentiometer contact resistance. Used a 10K potentiometer rather than 100 ohm units.

A list of components used in the thermometer is included in appendix B.

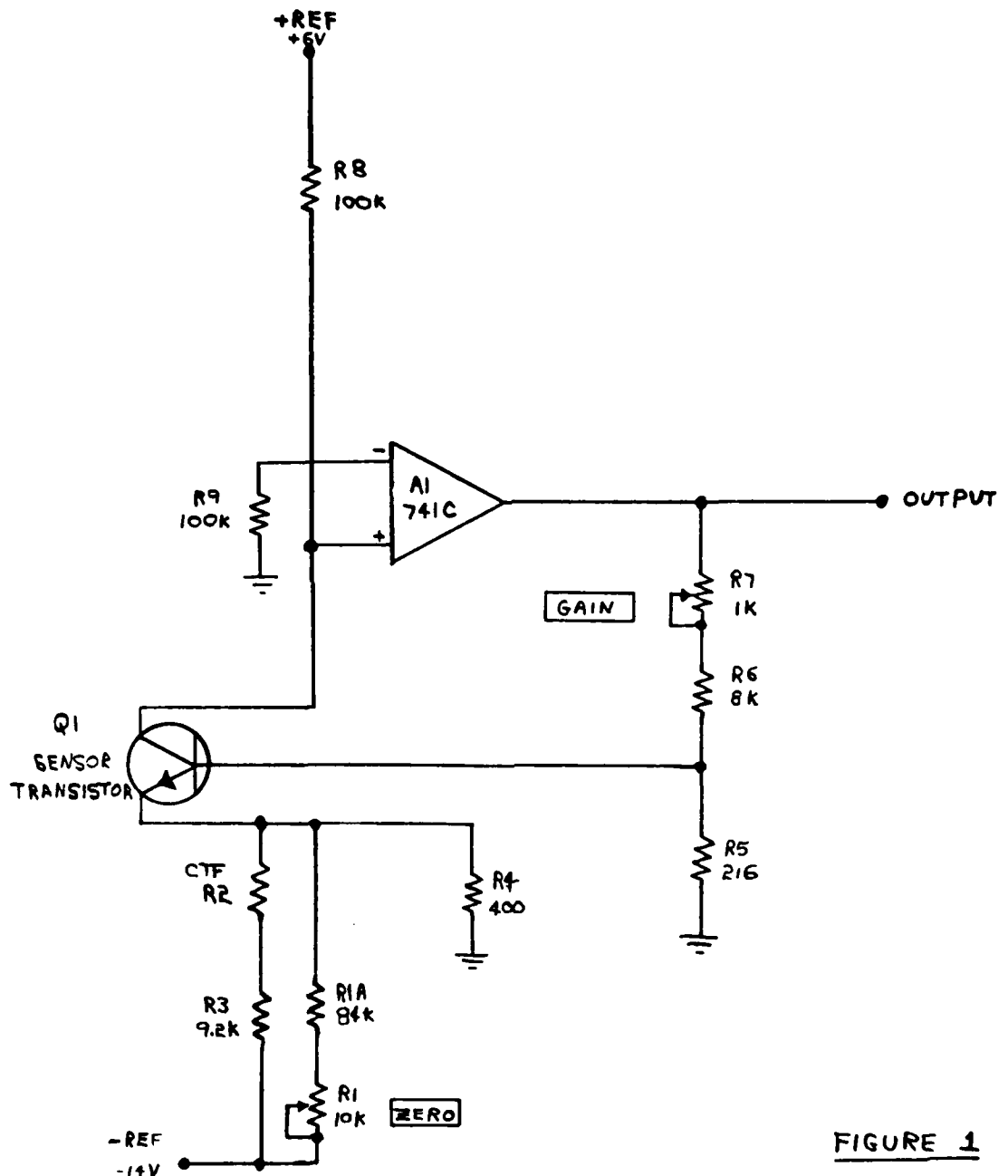
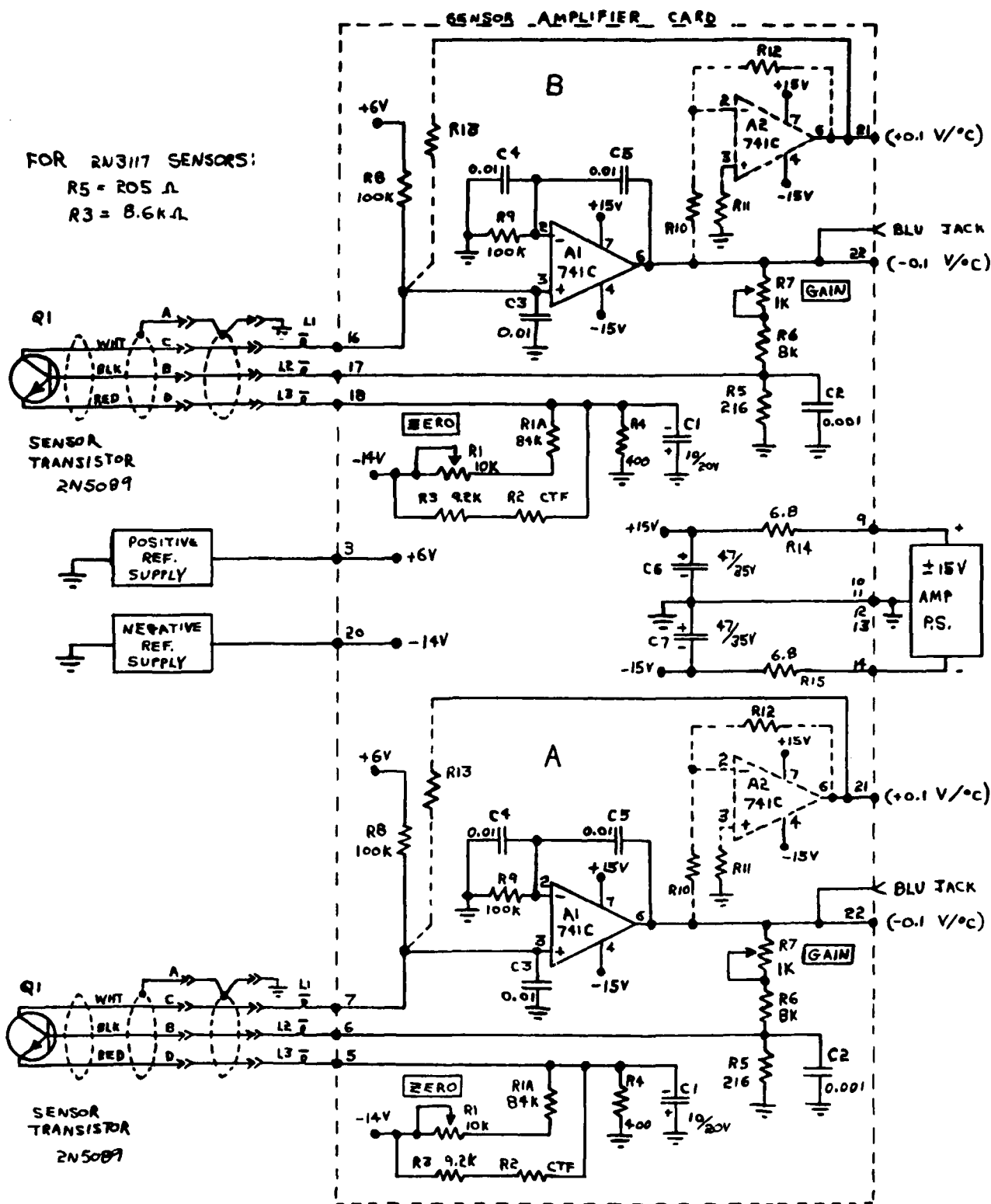


FIGURE 1

8/2/75 JWB



ALL RESISTANCE VALUES
ARE IN OHMS

ALL CAPACITANCE VALUES
ARE IN MICRO FARADS

R_2 SHOULD BE 0 Ω
PRIOR TO CALIBRATION

DUAL TRANSISTOR THERMOMETER
SCHEMATIC DIAGRAM
CLOUD PHYSICS RESEARCH

FNB 10/20/75

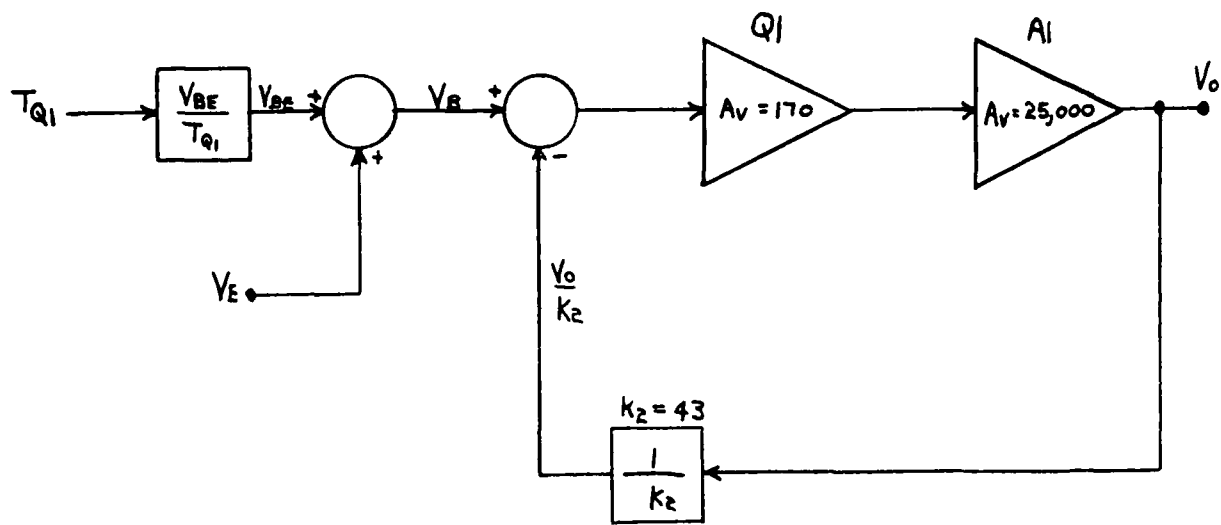
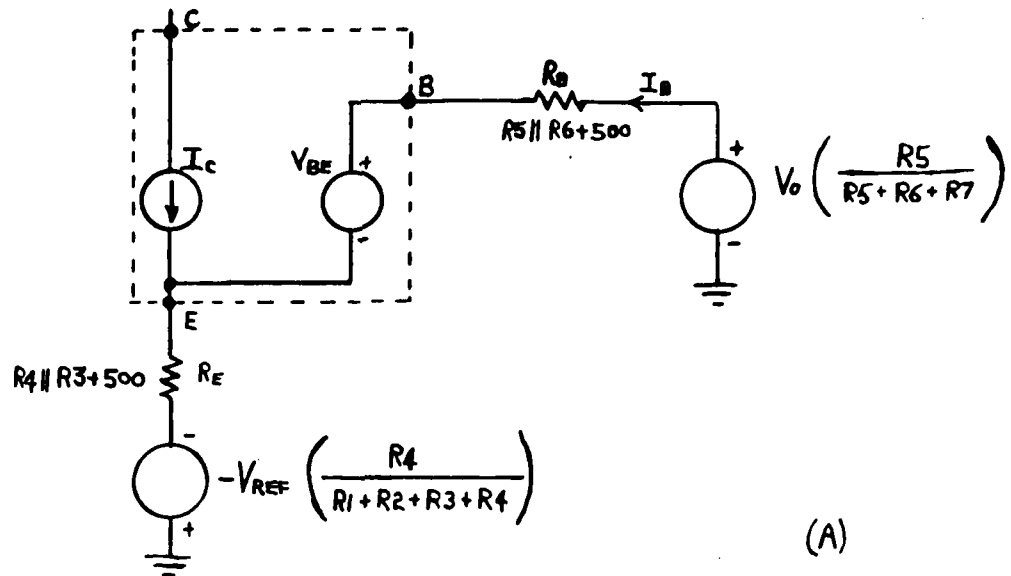
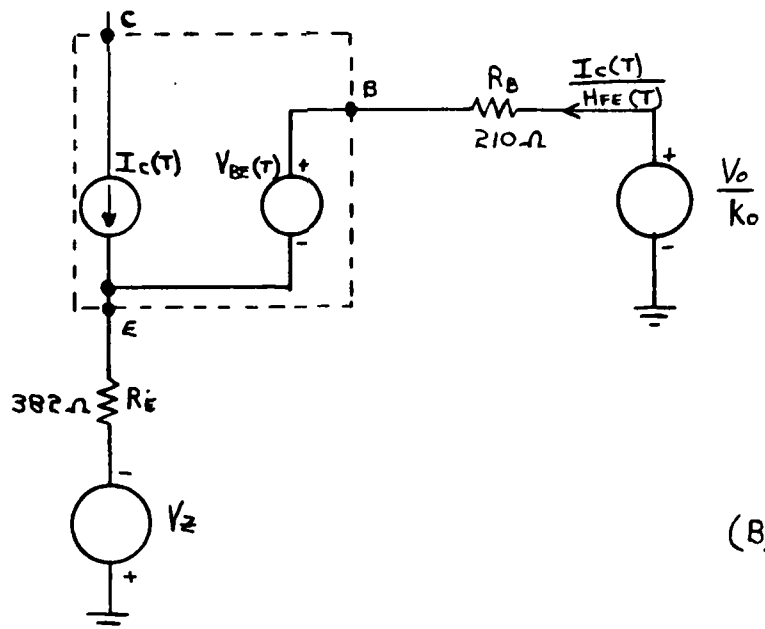


FIGURE 3

TRANSISTOR THERMOMETER
STEADY STATE FEEDBACK MODEL
CLOUD PHYSICS RESEARCH 8/10/75



(A)



(B)

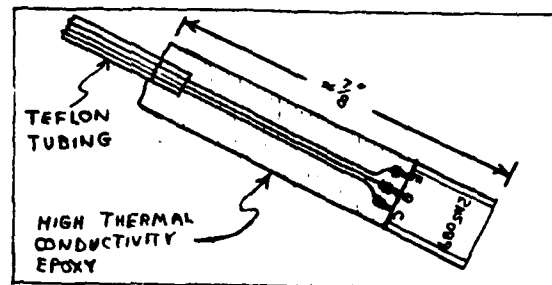
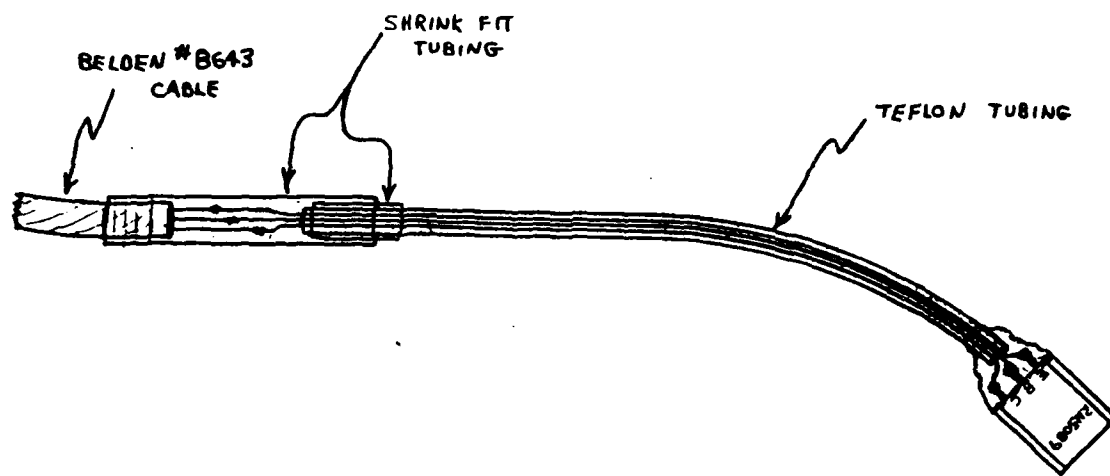
FIGURE 4

TRANSISTOR THERMOMETER
STEADY STATE OPERATIONAL MODELS
CLOUD PHYSICS RESEARCH 8/10/75

APPROX. TEMP.	EXPERIMENTAL DEVIATION		MODEL DEVIATION TEMP OUT - T	CONDITIONS
	TEMP OUT - QUARTZ °C	°C		
0	+ 0.000		+ 0.000	SENSOR = RN5089
5	- 0.017		- 0.010	$I_c = 60 \mu A.$
10	- 0.027		- 0.015	
15	- 0.027		- 0.014	
20	- 0.017		- 0.010	
25	+ 0.000		+ 0.000	
30	+ 0.031		+ 0.017	
40	+ 0.109		+ 0.055	
<hr/>				
0	+ 0.000		+ 0.000	SENSOR = RN5089
5	- 0.012		- 0.004	$I_c = \left(\frac{I_{c0}}{T_0} \right) T : T \text{ in } ^\circ K$
10	- 0.018		- 0.005	$= \left(\frac{60 \mu A}{273} \right) T : T \text{ in } ^\circ K$
15	- 0.016		- 0.005	$= 60 \mu A + 0.22 T \mu A : T \text{ in } ^\circ C$
20	- 0.011		- 0.003	
25	+ 0.000		+ 0.000	COMPONENT VALUES:
30	+ 0.019		+ 0.006	$R_{10} = R_{12} = 10 k\Omega$
40	+ 0.067		+ 0.022	$R_{11} = 5 k\Omega$
				$R_{13} = 450 k\Omega$

FIGURE 5

TRANSISTOR THERMOMETER
SUMMARY OF LINEARITY ERRORS
CLOUD PHYSICS RESEARCH 8/29/75

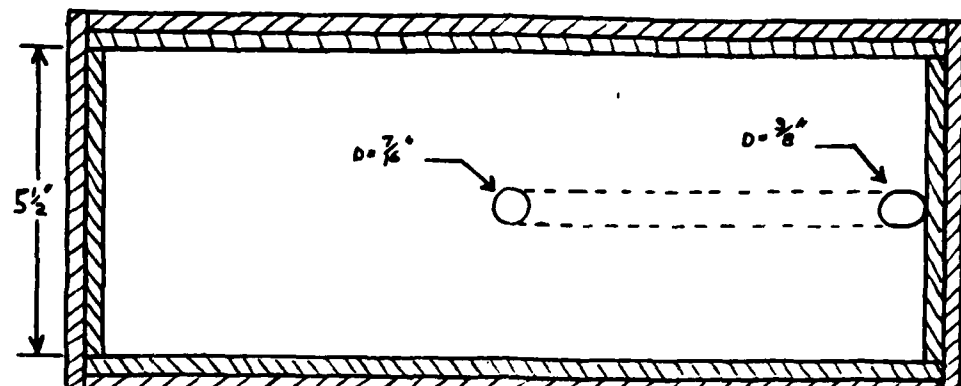
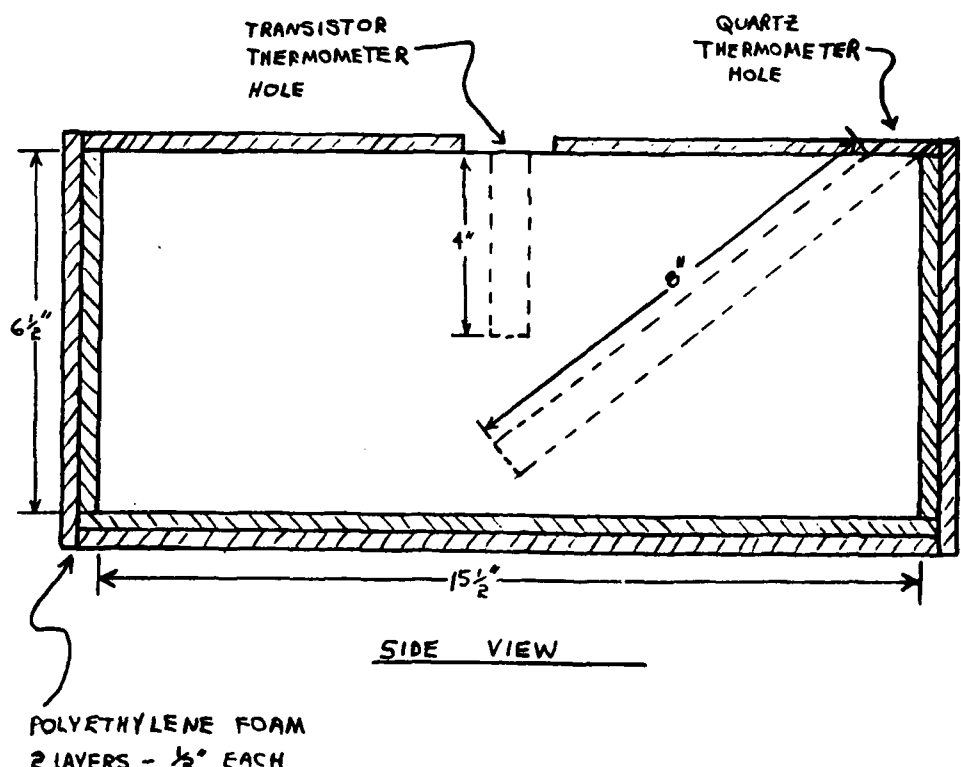


ALTERNATE PROBE TIP

NOT TO SCALE

FIGURE 6

TRANSISTOR THERMOMETER
PROBE CONSTRUCTION SKETCH
CLOUD PHYSICS RESEARCH 8/29/75

TOP VIEWSIDE VIEWFIGURE 7

TRANSISTOR THERMOMETER
GAIN CALIBRATION BLOCK SKETCH
CLOUD PHYSICS RESEARCH 9/2/75

ALL UNITS ARE °C

APPROX. TEMP.	CORRECTION
20	-0.017
21	-0.014
22	-0.011
23	-0.008
24	-0.004
25	0.000
26	+0.006
27	+0.012

THE CORRECTION IS TO BE ADDED TO THE QUARTZ THERMOMETER
READING TO DETERMINE THE DESIRED TRANSISTOR THERMOMETER
INDICATED TEMPERATURE.

THUS, IF THE QUARTZ THERMOMETER READS 25.000 °C,
THE TRANSISTOR THERMOMETER SHOULD READ 25.000 °C.

IF THE QUARTZ THERMOMETER READS 20.089 °C,
THE TRANSISTOR THERMOMETER SHOULD READ 20.072 °C.

FIGURE 8

TRANSISTOR THERMOMETER GAIN CALIBRATION CORRECTION CHART CLOUD PHYSICS RESEARCH 9/2/75
--

REFERENCES

1. Pease, Robert A., "Using Semiconductor Sensors for Linear Thermometers", Instruments and Control Systems, June, 1972, 80-81.
2. Ruehle, Robert A., "Solid-state Temperature Sensor Outperforms Previous Transducers", Electronics, March 20, 1975, 127-130.
3. Dobkin, Robert C., "1.2 Volt Reference", National Semiconductor Linear Applications, AN-56, December, 1971, AN56-1,2.
4. Brugler, Joseph S., "Silicon Transistor Biasing for Linear Collector Current Dependence", IEEE Journal of Solid State Circuits, June, 1967, 57-58.
5. Hewlett-Packard, Model 2801A Quartz Thermometer Operating and Service Manual, January, 1969, 3-6.

APPENDIX A

A Mathematical Model of the Transistor Thermometer

Figure 4 is a thermometer model based on the premise that the circuit loop gain is high enough to cause the output voltage to become whatever value is necessary to cause V_C to be zero and I_C to thus assume a value determined by the +REF, R8, and possibly R13.

The transistor is modeled according to the relationship between V_{BE} , I_C , and T as shown in equation 1. The resistors and voltage sources shown in figure 4a are Thevenin equivalents of the actual circuit configuration. The value for R_E was found by assuming nominal values for R_1 and R_2 and R_B was found by assuming $R_7=500\Omega$. These resistances are adjusted slightly during calibration but the effects on the model are negligible.

Figure 4b is the final version of the model. The value of V_Z is set during calibration when the thermometer is zeroed and K_0 is set when the gain is adjusted. The mathematical development follows from figure 4b.

$$\begin{aligned}\frac{V_0(T)}{K_0} &= \left[\frac{I_C(T)}{H_{FE}(T)} \right] R_B + V_{BE}(T) + \left[I_C(T) + \frac{I_C(T)}{H_{FE}(T)} R_E \right] - V_Z \\ &= \left[\frac{I_C(T)}{H_{FE}(T)} \right] 210 + V_{BE}(T) + \left[\frac{I_C(T) H_{FE}(T) + I_C(T)}{H_{FE}(T)} \right] 382 - V_Z\end{aligned}$$

and since the thermometer described here has a gain of -10°C per volt,

$$V_0(T) = \frac{\text{TEMP OUT}}{-10} .$$

Therefore

$$\text{TEMP OUT} = -10K_0 \left[\left(\frac{I_C(T)}{H_{FE}(T)} \right) 210 + V_{BE}(T) + \left(\frac{I_C(T)H_{FE}(T) + I_C(T)}{H_{FE}(T)} \right) 382 - V_Z \right]$$

$$\text{TEMP OUT} = 10K_0 [V_Z - 210 \left(\frac{I_C(T)}{H_{FE}(T)} \right) - 382 \left(\frac{I_C(T)H_{FE}(T) + I_C(T)}{H_{FE}(T)} \right) - V_{BE}(T)].$$

As stated earlier,

$$V_{BE}(T) = V_{g0} - T \left[\frac{V_{g0}}{T_0} - \frac{V_{BE0}}{T_0} + \frac{mk}{q} \ln \left(\frac{T}{T_0} \right) - \frac{k}{q} \ln \left(\frac{I_C(T)}{I_{C0}} \right) \right]$$

so

$$\begin{aligned} \text{TEMP OUT} &= 10K_0 [V_Z - 210 \left(\frac{I_C(T)}{H_{FE}(T)} \right) - 382 \left(\frac{I_C(T)H_{FE}(T) + I_C(T)}{H_{FE}(T)} \right) - V_{g0} \\ &\quad + T \left[\frac{V_{g0}}{T_0} - \frac{V_{BE0}}{T_0} + \frac{mk}{q} \ln \left(\frac{T}{T_0} \right) - \frac{k}{q} \ln \left(\frac{I_C(T)}{I_{C0}} \right) \right]] \end{aligned} \quad (3)$$

Equation 3 is the complete characterization of the model in figure 4b. To use the equation, V_Z must be determined so that TEMP OUT = 0°C when $T = T_0 = 273^\circ\text{K}$ (For this work assume $0^\circ\text{C} = 273^\circ\text{K}$).

$$V_Z = 210 \left(\frac{I_C(T_0)}{H_{FE}(T_0)} \right) + 382 \left(\frac{I_C(T_0)H_{FE}(T_0) + I_C(T_0)}{H_{FE}(T_0)} \right) + V_{BE0} \quad (4)$$

Then K_0 must be determined. It is adjusted during thermometer calibration to make TEMP OUT = $(T_1 - 273)^\circ\text{C}$ where $T_1 = 298^\circ\text{K}$ typically.

$$\begin{aligned} K_0 &= (T_1 - 273)/10 [V_Z - 210 \left(\frac{I_C(T_1)}{H_{FE}(T_1)} \right) - 382 \left(\frac{I_C(T_1)H_{FE}(T_1) + I_C(T_1)}{H_{FE}(T_1)} \right) \\ &\quad - V_{g0} + T_1 \left[\frac{V_{g0}}{T_0} + \frac{V_{BE0}}{T_0} + \frac{mk}{q} \ln \left(\frac{T_1}{T_0} \right) - \frac{k}{q} \ln \left(\frac{I_C(T_1)}{I_{C0}} \right) \right]] \end{aligned} \quad (5)$$

Now that K_0 is defined, equation 3 is complete.

The next step in preparing to run a model simulation is to insert some parameter values into the equations. For all simulations run to date T_0 was assumed to be 0°C . V_{BE} at 0°C (V_{BE0}) has been observed to be about 0.635 volts for typical sensors, although it may vary as much as ± 50 mv among transistors of the same type. I_{C0} is fixed at 60 microamps by the circuit configuration. Inserting these and other previously defined constants into equation 3 yields

$$\begin{aligned} \text{TEMP OUT} = & 10K_0 [V_Z - 210(\frac{I_C(T)}{H_{FE}(T)}) - 382(\frac{I_C(T)H_{FE}(T) + I_C(T)}{H_{FE}(T)}) - 1.205 \\ & + T[2.09 \times 10^{-3} + 1.3 \times 10^{-4} \ln(\frac{T}{273}) - 8.6 \times 10^{-5} \ln(\frac{I_C(T)}{6 \times 10^{-5}})]] \quad (6) \end{aligned}$$

$H_{FE}(T)$ is a quadratic function of T which fits empirical data points taken from a typical sensor. $I_C(T)$ may be a constant 60 microamps, or a linear function of temperature if the linearizer circuit is used.

APPENDIX B

Thermometer Component Parts Descriptions

PART #	DESCRIPTION	MANUFACTURER	-	NUMBER
R1	POTENTIOMETER - 10KΩ	CLAROSTAT		62JA-10K
R1A	RESISTOR - 84KΩ	KRL		560-84KF
*R2	RESISTOR - CTF	--		--
**R3	RESISTOR - 9.2KΩ	KRL		560-9200F
**R4	RESISTOR - 400Ω	KRL		560-400F
R5	RESISTOR - 216Ω	KRL		560-216F
R6	RESISTOR - 8KΩ	KRL		560-8000F
R7	POTENTIOMETER - 1KΩ	CLAROSTAT		62JA-1K
**R8-R9	RESISTOR - 100KΩ	IRC		CEA-100K <u>+1%</u> ,T2
R10-R13	RESISTORS - OPTIONAL SEL	--		--
R14-R15	RESISTORS - 6.8Ω	IRC		RC20-6.8 <u>+10%</u>
C1	CAPACITOR - 10mf./20V.	SPRAGUE		CS13BF106K
C2	CAPACITOR - 0.001 mf.	SPRAGUE		5GA-D10
C3-C5	CAPACITOR - 0.01 mf.	CENTRALAB		UK25-103
C6-C7	CAPACITOR - 47 mf./35V.	SPRAGUE		CS13BF476K
A1	INTEGRATED CIRCUIT	NATIONAL		LM741CN
A2	INTEGRATED CIRCUIT - OPT	--		--
L1-L3	FERRITE BEAD	ARNOLD		40601-TC
Q1	TRANSISTOR	MOTOROLA		2N5089
	AMPLIFIER POWER SUPPLY	CALEX		22-100
	REFERENCE POWER SUPPLIES	CLOUD PHYSICS		
	SENSOR CONNECTOR	AMPHENOL		126 SERIES
	SENSOR CABLE	BELDEN		8643

*R2 should have a low temperature coefficient for high stability thermometers.

**For thermometers with higher stability (see specifications): R3 and R4 should be more stable models, such as those made by VISHAY R8 should be a more stable resistor with a tempco of +15 ppm/°C.

APPENDIX C

Specifications of the Revision 2 Transistor Thermometers

Range: -40°C to $+60^{\circ}\text{C}$ (limited by sensor)

Resolution: 0.001°C

Gain: $-0.1 \text{ volt}/^{\circ}\text{C}$

*Temperature Coefficient, output to ambient at a constant

sensor temperature: $\pm 0.002^{\circ}\text{C}/^{\circ}\text{C}$ ($\pm 0.001^{\circ}\text{C}/^{\circ}\text{C}$) max

Drift, long term with a dry sensor: $\pm 0.001^{\circ}\text{C}/\text{month}$

Noise, 0.1 hz. to 10 hz.: $<0.0003^{\circ}\text{C}$

Linearity: Over a 0°C to 40°C range, the deviation is less than
 $\pm 0.04^{\circ}\text{C}$ from the best straight line.

Tracking error: When calibrated at 0°C and 25°C , the maximum
thermometer to thermometer difference over a 0°C to 40°C
range is 0.002°C

Hysteresis: $<0.0005^{\circ}\text{C}$

The absolute thermometer accuracy is dependent upon the
accuracy of the standard against which it is calibrated. Errors
in the temperature readout are neglected in these specifications.

*Thermometers with the $\pm 0.001^{\circ}\text{C}/^{\circ}\text{C}$ temperature coefficient
require special components, as noted in the component parts list.

APPENDIX B

ADAPTIVE CONTROL OF A CLOUD SIMULATION
CHAMBER EXPANSION SYSTEM

BY

KATIYA GREIGARN, 1952-

A DISSERTATION

Presented to the Faculty of the Graduate School of the
UNIVERSITY OF MISSOURI-ROLLA

In Partial Fulfillment of the Requirements for the Degree

DOCTOR OF PHILOSOPHY

in

ELECTRICAL ENGINEERING

1978

S. R. Davis
Advisor

Frank J. Kew
Bruel D. Stigall

James L. Hansen, Jr.
S. Bagam
Earl Roberts

ABSTRACT

This dissertation describes the design and construction of a closed-loop computer controlled expansion system for a cloud simulation chamber. The chamber is used to simulate atmospheric phenomena for the study of microphysical processes. In order to accomplish this, the sample gas inside the chamber must be expanded adiabatically. This means the wall temperature and the gas temperature must be made to agree as closely as possible. The wall is cooled by thermoelectric modules, and the temperature is controlled by analog controllers. The gas is cooled by the adiabatic expansion, and the corresponding pressure is controlled by a laboratory minicomputer, a NOVA 840. The range of operation of the expansion system is specified to be 20.7 kPa (3 psi) change in pressure. The accuracy and the rms error must be better than ± 0.0207 kPa (± 0.003 psi) and 0.0414 kPa (0.006 psi), respectively. This range of operation is large enough that an analog controller can not obtain an adequate result. The error arises due to the fact that the input function is a ramp and the expansion system has multiple non-linearities.

In order to obtain zero steady state error, the time-optimal control is implemented by the minicomputer. Table look-up and on-line identification schemes for the system parameters have been investigated. An adaptive control algorithm using on-line identification outperforms the table look-up method due the flexibility of the identification

scheme. Special efforts are made to adjust the identification scheme so that the model parameters converge close to the system parameters within one step. The results indicate that the closed-loop computer controlled expansion system yields the desired specification.

ACKNOWLEDGEMENT

The research described herein was conceived by Dr. James L. Kassner, Jr. for use with the Cloud Simulation System. Due to the size of the problems, many people and ideas were involved. The author would like to thank Dr. Daniel R. White, David C. Hollocher and Alfred R. Hopkins for their technical support during the installation of the system design.

The author also appreciates the assistance given by Dr. Donald E. Hagen and Dr. Kui C. Lam for their computer programming discussion. The author gratefully acknowledges Dr. K. R. Dunipace and his advisor, Dr. D. R. Fannin, for having suggested the dissertation topic and for valuable guidance throughout the course of this work. Acknowledgments are also extended to Dr. Frank J. Kern, Professor Sylvester J. Pagano, Dr. Paul D. Stigall, Dr. James L. Kassner, Jr. and Dr. Earl F. Richards for serving on the committee.

The author wishes to thank his parents, his aunt, Dr. Sumana Greigarn, and his fiancee, Poonsamon Sritalapat for their continued encouragement during his studies. And thanks go to Leah Pagel for typing this dissertation.

All the work was supported by the Cloud Physics Research Center and NASA, Grant Number NAS8-31849.

TABLE OF CONTENTS

	Page
ABSTRACT	ii
ACKNOWLEDGEMENT	iv
LIST OF ILLUSTRATIONS	vii
LIST OF TABLES	x
I. INTRODUCTION	1
II. REVIEW OF THE LITERATURE ON CLOUD SIMULATION CHAMBERS	9
III. DIRECT DIGITAL CONTROL SYSTEM DESIGN	13
A. DESIGN SPECIFICATION	13
B. EXPANSION CONTROL SYSTEM HARDWARE	14
1. The Cloud Simulation Chamber.	14
2. The Positive Displacement Uni-Directional Pump.	14
3. The Regulator Tank.	15
4. The Storage Tank.	15
5. The 3-Way Infinite Position Rotary Valve.	15
6. The Solenoid and Manual Valves.	16
7. The Pressure Gauge.	16
8. The Pressure Relief Valve	16
9. The Stepping Motor and Stepping Motor Interface.	17
10. The Transducers	19
11. The Computer System	23

TABLE OF CONTENTS (cont.)

	Page
C. MODEL OF THE EXPANSION SYSTEM	23
D. SYSTEM SOFTWARE	28
1. The Implementation of the Time-Optimal Control.	28
2. The Implementation of the Adaptive Control Algorithm.	34
3. System Programming	41
IV. EXPERIMENTAL RESULTS	48
V. CONCLUSION.	70
BIBLIOGRAPHY	73
VITA	78

LIST OF ILLUSTRATIONS

Figure	Page
1.1. The layout of the expansion system.	6
1.2. The block diagram of the computer controlled expansion system	8
3.1. The number format of the stepping motor interface	18
3.2. The flow chart of the stepping motor interface output routine.	20
3.3. The NOVA 840 computer system.	22
3.4. The electrical analogy of the expansion system.	25
3.5. Block diagram of the closed-loop digital control of the expansion system.	30
3.6. The implementation of the time-optimal control algorithm	32
3.7. The sequential regression identification subroutine.	37
3.8. The behavior of the coefficient A as a function of time. The rate of expansion is $-4^{\circ}\text{C}/\text{min}$	39
3.9. The behavior of the coefficient B as a function of time. The rate of expansion is $-4^{\circ}\text{C}/\text{min}$	40
3.10. The block diagram of overall identification scheme	42
3.11. The flow chart of the subroutine PREPAR . . .	45
3.12. The flow chart of PRESC	46
4.1. The coefficient A when A and B are initially set at 0.5 and 0.03, respectively .	49
4.2. The coefficient B when A and B are initially set at 0.5 and 0.03, respectively.	50

LIST OF ILLUSTRATIONS (cont.)

Figure	Page
4.3. The error of the pressure response when A and B are initially set at 0.5 and 0.03, respectively	51
4.4. The pressure response when being recorded every 2 seconds	53
4.5. The pressure error when being recorded every 2 seconds.	54
4.6. The pressure response at the rate of expansion of -0.1242 kPa/s or -6°C/min. . . .	55
4.7. The pressure error at the rate of expansion of -0.1242 kPa/s or -6°C/min. . . .	56
4.8. The coefficient A at the expansion rate of -0.1242 kPa/s or -6°C/min.	57
4.9. The coefficient B at the expansion rate of -0.1242 kPa/s or -6°C/min.	58
4.10. The pressure response at the expansion rate of -0.0828 kPa/s or -4°C/min.	59
4.11. The pressure error at the expansion rate of -0.0828 kPa/s or -4°C/min.	60
4.12. The coefficient A at the expansion rate of -0.0828 kPa/s or -4°C/min.	61
4.13. The coefficient B at the expansion rate of -0.0828 kPa/s or -4°C/min.	62
4.14. The pressure response at the expansion rate of -0.0414 kPa/s or -2°C/min.	63
4.15. The pressure error at the expansion rate of -0.0414 kPa/s or -2°C/min.	64
4.16. The coefficient A at the expansion rate of -0.0414 kPa/s or -2°C/min.	65
4.17. The coefficient B at the expansion rate of -0.0414 kPa/s or -2°C/min.	66

LIST OF ILLUSTRATIONS (cont.)

Figure	Page
4.18. The pressure response including the holding modes	67
4.19. The pressure error including the holding modes	68

LIST OF TABLES

Table		Page
I	Typical Table Look-up Model of the Expansion System	33
II	Experimental Values of AFILTER and BFILTER . .	43

I. INTRODUCTION

For centuries, man has observed and studied the weather phenomena of the atmosphere. It has been demonstrated that delicate microphysical processes occurring in the atmosphere have a large influence on the amount and character of precipitation. As technology has become more advanced, man has tried to develop a tool to control his environment in order to protect himself from inadequate precipitation and from polluted atmosphere. An invariably successful process for producing rain and snow would have tremendous significance for virtually everyone. Hence, recent experiments in the production of man-made precipitation have aroused wide interest [1-4].

At present, it is commonly known that the atmosphere contains a large quantity of solid and liquid particles. The majority of these particles are concentration nuclei, which appear at different supersaturations. The total concentration of atmospheric condensation nuclei (Aitken nuclei) is determined by counters in which moist air is cooled during adiabatic expansion [5-6]. The condensation nuclei play an important part in cloud formation. For example, if moist air is admitted into a chamber and expanded, cloud or fog will form in the chamber as a result of the cooling caused by the adiabatic expansion. The same air produces successively decreasing amounts of fog with successive expansions. If the air is made to pass

through a filter of packed cotton before entering the chamber, it is found that no cloud or fog forms. The decreasing amounts of cloud or fog formed during each repeated expansion suggest that the air becomes "exhausted" of nuclei. The lack of condensation when filtered air is expanded indicates that the nuclei operative in this case may be removed by means of a mechanical filter. The filtered air becomes again capable of producing cloud or fog if smoke is introduced into the chamber.

These microphysical processes may be carefully controlled and studied in the laboratory. In order to simulate real atmospheric conditions, a sample gas in the chamber must be expanded by an adiabatic process. Careful consideration must be given to the effects of heat flow from the wall of the chamber. This is due to the very large heat capacity of the wall in comparison to the heat capacity of the gas inside the chamber. In a laboratory environment, heat flow occurs between the chamber wall and the gas because the gas is cooler than the wall after the expansion begins. To eliminate the temperature gradient between the wall and the gas, they must be maintained at the same temperature at all times during the expansion. This may be accomplished by cooling the chamber walls and controlling the gas pressure and the wall temperature very precisely. Such a cloud simulation chamber and its supporting subsystems have been developed at the University of Missouri-Rolla. The chamber is made of aluminum. It is

a ten-sided right prism, 61 centimeters high and 48 centimeters in diameter. It has a volume of 0.11 cubic meters and 1.3 square meters inner wall surface. Subsystems are required to clean and humidify the sample gas and prepare an aerosol to provide nucleation sites of the cloud. For the wall cooling system, there are 836 thermoelectric modules sandwiched between the inner wall and the heat sink of the chamber. The thermoelectric module has the property that when electric current is passed through it the module can extract heat from the wall and pump it into the heat sink. The temperature of the heat sink is regulated by means of a circulating constant temperature bath. The inner wall temperature is monitored by transistor thermometers mounted in holes drilled through the back of the inner wall and extending to within 0.2 mm of the inside surface. These transistor thermometers are accurate to within a few millidegrees Celsius. The inner wall temperature is controlled by twenty-eight closed-loop analog controllers with a compensator in each loop and another compensator at the input [7]. The wall temperature has a small steady state offset, less than 10°C per degree per minute of input ramp slope. The settling time is about one minute. The maximum cooling rate which can be closely controlled is $7^{\circ}\text{C}/\text{min}$. The absolute maximum cooling rate (power limited) is $10^{\circ}\text{C}/\text{min}$.

The gas temperature must also be controlled to follow the wall temperature, or, in other words, both the gas

temperature and the wall temperature must follow each other as closely as possible. Unfortunately, the temperature of the gas in a supersaturated system cannot be measured directly with fine wire thermocouples because the latent heat of condensation is liberated on the element, thus causing a displacement of the observed temperature. In addition, the surface condition of the measuring element affects the onset of condensation. However, the pressure of the gas can be directly measured. In conjunction with the initial pressure P_0 and the initial equilibrium temperature T_0 of the gas in the chamber, the gas temperature at any time during the simulation can be computed by the adiabatic gas law

$$\frac{T_1}{T_0} = \left(\frac{P_1}{P_0} \right)^{\frac{\gamma-1}{\gamma}} \quad (1.1)$$

where γ is the ratio of specific heat at constant pressure to the specific heat at constant volume for the same gas. The gas temperature at any time T_1 can be calculated from the measured value of pressure P_1 at that time. This equation can be applied only for a dry adiabatic expansion. The increase in gas temperature due to latent heat of vaporization given off by droplet condensation is neglected. In the cloud simulation experiment the effects of the latent heat can be corrected for if the liquid water content of the sample gas is known. Experimental techniques for measuring the liquid water content have been

developed. They are now being implemented [8]. Since corrections can be made for the effects of the latent heat, it is sufficient to test the performance of the wall temperature and pressure control systems under the conditions of a dry adiabatic expansion.

Due to the lack of a method for measuring the gas temperature directly, the expansion system uses the gas pressure as a variable for control purposes. The layout of the expansion system is shown in Figure 1.1. The cloud simulation chamber is considered as a closed container. The pressure inside the chamber can be governed by adjusting the orifice of the 3-way rotary valve, whose position is controlled by the step motor. The pressure is measured by a strain gauge type pressure transducer.

In analyzing the expansion control system, great care must be taken in assessing the importance of thermodynamic effects because they can introduce strong non-linearities into the system. The orifice is a series resistance which usually has a quadratic constitutive equation. For small perturbations in the flow, a linearized approximation can be used in the control design. For the expansion system, the linearized range of operation is relatively small in comparison to the total change of pressure which is 21 kPa (3 psi). The desired performance specifications cannot be met by a fixed, linear controller. Therefore, it is necessary to employ identification techniques and some

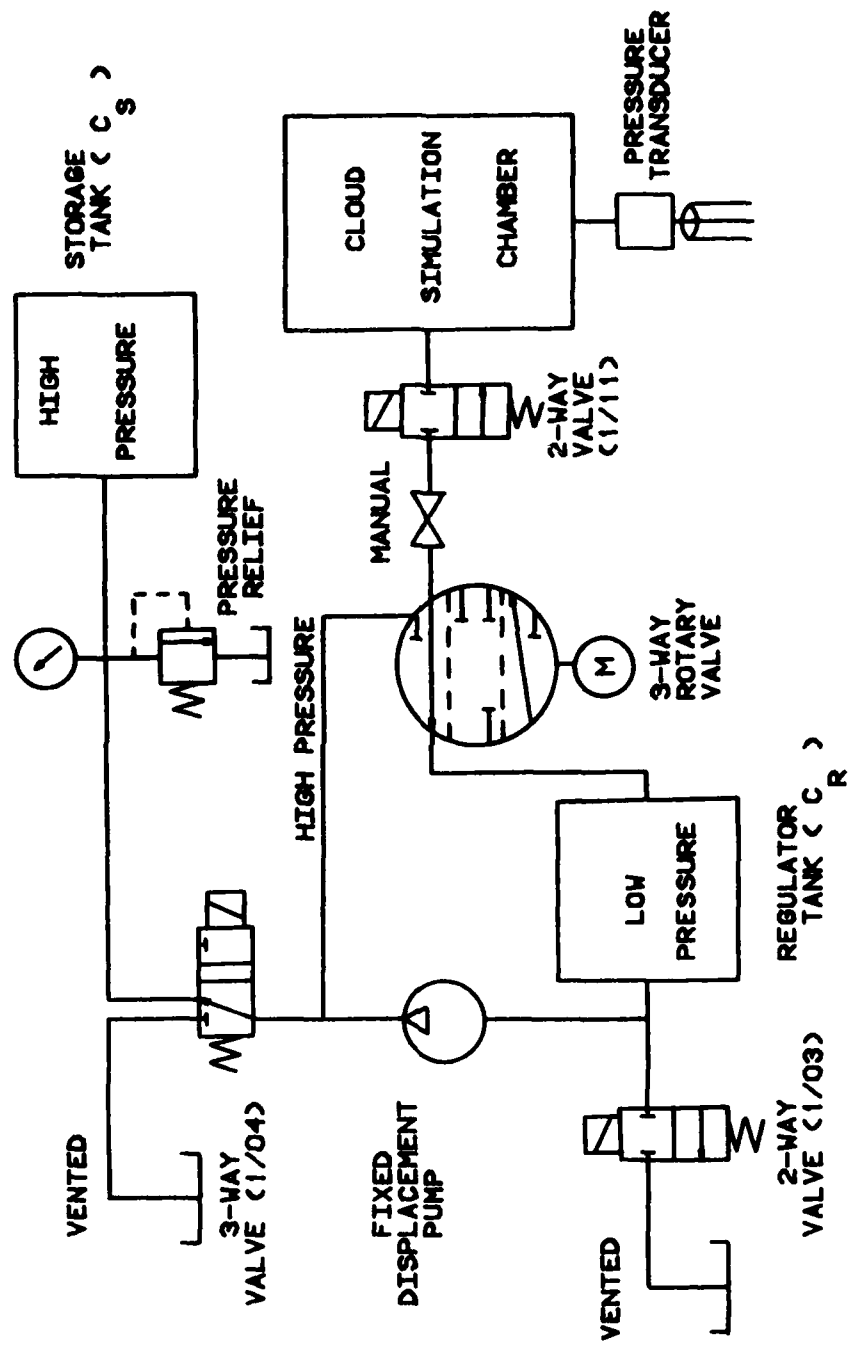


Figure 1.1. The layout of the expansion system

scheme of computing the control in real time. Such an identification and control scheme can realize the desired performance specifications. This dissertation describes the design and construction of the closed-loop, computer controlled expansion system using identification and real time computation of control. The block diagram is shown in Figure 1.2.

In a system such as that described above, the control law may be made to be optimum in some sense. Among the many different types of optimal control design problems, the time-optimal control and minimum integral square error are the most common. It can be shown that the optimal feedback gains obtained from the time-optimal control and minimum summed-square error control of the expansion system are the same [9-11]. As a consequence the time-optimal control is being used in the design because of its analytical simplicity.

AD-A102 679

MISSOURI UNIV-ROLLA GRADUATE CENTER FOR CLOUD PHYSICS--ETC F/6 4/2
MARINE FOG STUDIES - FOG SIMULATION PROGRAM, (U)

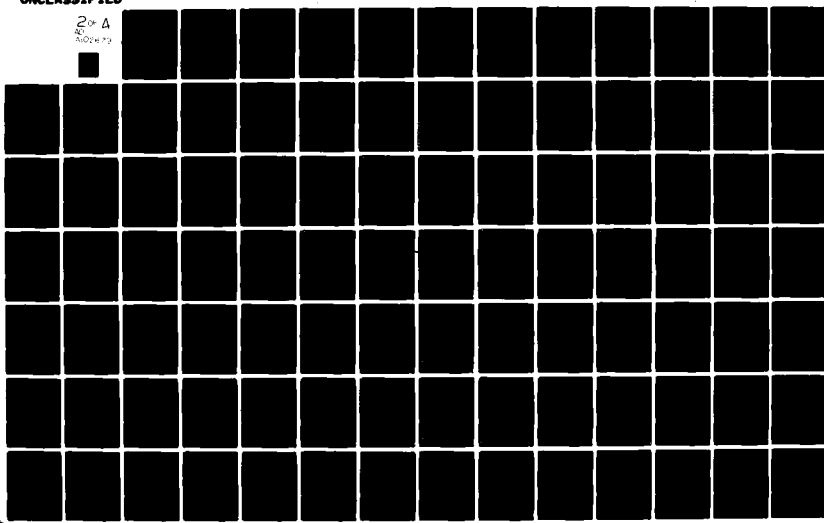
JUN 81 D R WHITE

N00014-75-C-0182

NL

UNCLASSIFIED

20th A
40
002473



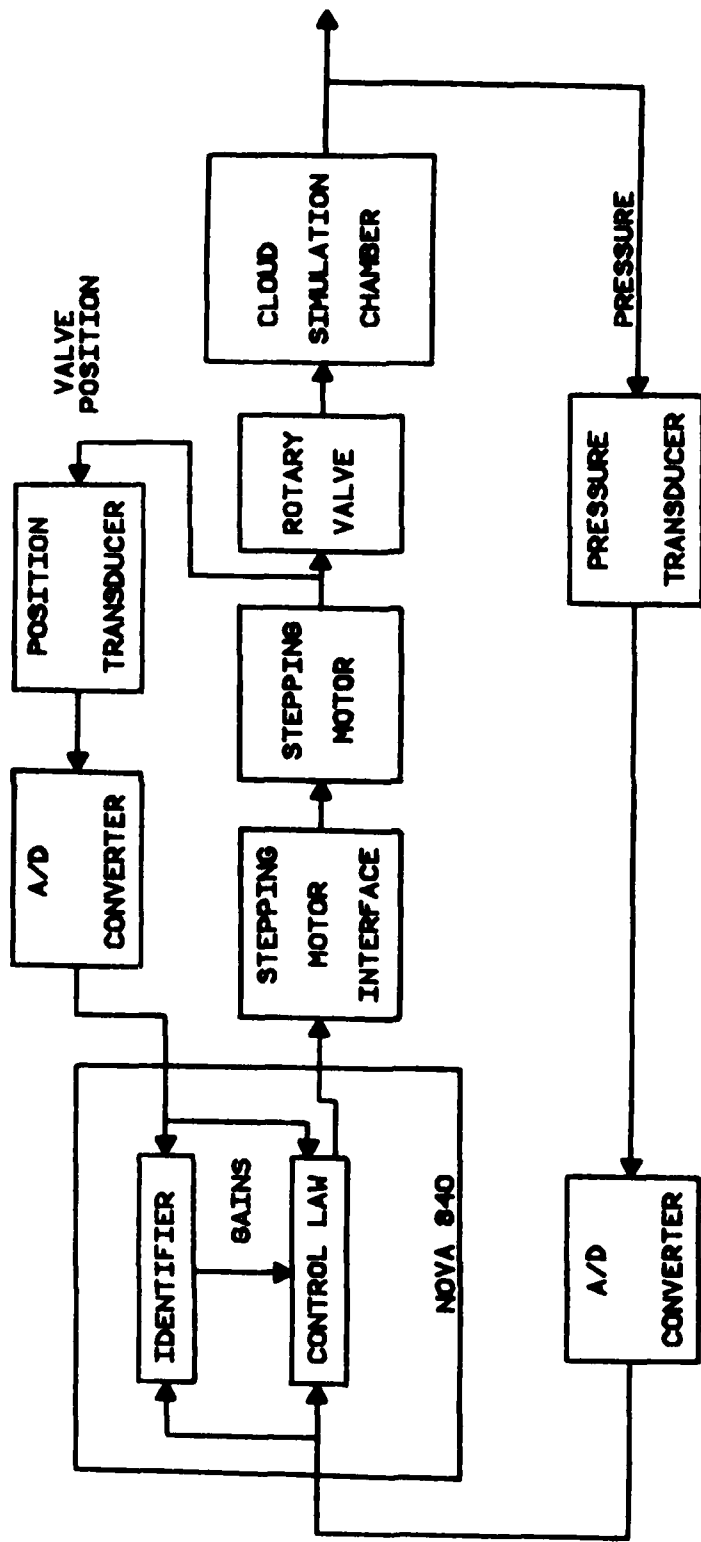


Figure 1.2. The block diagram of the computer controlled expansion system.

II. REVIEW OF THE LITERATURE ON CLOUD SIMULATION CHAMBERS

In the eighteenth century Kratzenstein resolved the question of whether cloud droplets are bubbles or liquid water spheres, using microscopic observations. This problem was later solved in a more systematic way by W. H. Dines [12] in 1880 and by R. Assmann in 1885. Simultaneously, the theory and measurement of condensation nuclei was developed. H. Beckquerel [6], in 1847, formulated with amazing clarity the existence and the physical role of condensation nuclei in atmospheric processes. M. Coulier [13] in 1875, and J. Aitken [5], in 1880, supported his ideas by observations and measurements.

Coulier enclosed air in a flask together with water and produced supersaturation by compressing a hollow india-rubber ball connected to the flask and then suddenly releasing it. In his earlier experiments, Aitken produced supersaturation by blowing steam into a large vessel containing the gas to be tested. Later he used an expansion method. Aitken also constructed apparatus for measuring the number of dust particles capable of acting as nuclei of condensation in samples of air.

Since Aitken's experiments, several cloud simulation chambers have been built. Two major approaches are evident. The first approach was characterized by very large chambers in which the designers attempted to extend the time period

of quasiadiabatic expansion of the air by making the surface to volume ratio as small as possible. Special insulating techniques are required for this type of chamber. This method was employed by Findeisen [6] in 1939 and later by R. Gunn [14] in 1952 and was also employed by J. Podzimek [15] in 1964 who operated a modified Findeisen low-pressure chamber. In spite of the improved insulation of the outer wall and of the inner volume, it was not possible to simulate the development of cumulus type clouds more than 1,500 meters above cloud base level and the artificial fog did not persist for more than 15 minutes at a temperature of approximately 0°C. R. Gunn faced similar problems. Currently, Russian scientists are attempting to solve the same kind of problems in several giant cloud chambers built during the past decade [6, 16].

The second method of simulating cloud formation is to control precisely all physical processes in relatively small chambers. Work along these lines began about three decades ago. Only a few scientists have introduced innovations leading to more efficient simulation experiments in small chambers in which the expansion rate, temperature and humidity fields were reliably controlled.

Evans [17] in 1960 was one of the first scientists who tried to eliminate the heat transfer from the wall by cooling the gas and the wall as close to the same rate as possible. This idea was later applied by R. Steele and L. Grant at Colorado State University [18] in 1967 and by

J. Kassner and R. Oetting [19] at UMR (1969) who began the development of such a chamber in 1966. The advantage gained by cooling the wall in synchronization with the cooling of the gas is that the expense of constructing exceedingly large chambers is not necessary. Moreover, the reproducibility and control obtainable in small chambers is much better.

Evans' expansion chamber was in the form of concentric copper spheres. The inner sphere had an 11.5 liter capacity and was cooled by pumping coolant through annular space. Evans used a cooling capacity of 3.5 kW (12,000 Btu/hr) at a suction temperature of -18°C . The maximum cooling rate was $1.5^{\circ}\text{C}/\text{min}$. The temperature of the gas was measured by a copper-constantan thermocouple. It was rather difficult to control the rate of cooling and the total change of temperature of the gas inside the Evans' chamber.

The dynamic cloud chamber developed at Colorado State University was designed to cool the wall at the same rate the gas was cooled by adiabatic expansion. The wall was cooled by means of a refrigeration system. The expansion was programmed by means of a function generator which produced a signal proportional to the desired time temperature curve. The chamber processes were controlled by means of chamber pressure. Expansion rates were adjustable over a range which provided rates of temperature decrease from $0.1^{\circ}\text{C}/\text{min}$ to about $7^{\circ}\text{C}/\text{min}$.

The effort at UMR has been devoted since 1966 to

meticulous design scrutiny and detailed testing of each new design concept. Tebelak [20-21], in 1973 designed and constructed an analog controller for the wall and a gas pressure control. The wall was cooled by thermoelectric modules. He approximated the adiabatic gas law, equation 1.1, by a second order Taylor series expansion and implemented the equation by using a special purpose analog computer. The rate of temperature change was low, less than $0.5^{\circ}\text{C}/\text{min}$. The total change of temperature at that time was only 1.5°C . The controller allowed $2 \text{ m}^{\circ}\text{C}$ temperature error between the wall and the gas, or 0.13% of the total temperature change.

In the ideal cloud simulation chamber it should be possible to accurately produce clouds from a saturated atmosphere containing an aerosol fully characterized by a critical activation supersaturation spectrum and the variations of the latter with time. The gas in the chamber must be expanded by an adiabatic process. To accomplish this expansion, the heat transfer between the wall and the gas must be eliminated. The wall temperature and the expansion controller should be able to support a higher rate and a larger change of temperature with reasonable accuracy.

III. DIRECT DIGITAL CONTROL SYSTEM DESIGN

A. DESIGN SPECIFICATION

The main objective of the design is to control the pressure of the gas inside the chamber such that during the cloud simulation experiment it follows a desired profile as closely as possible. The desired pressure profile is generated from the temperature profile using the adiabatic equation 1.1. The pressure profiles are normally negative slope functions with some additional holding modes during the course of the experiment.

Since the pressure transducer is calibrated against a very accurate dead weight, the accuracy of the pressure transducer becomes ± 0.0069 kPa (± 0.001 psi). The expansion control system is designed to meet the following specifications.

1. The settling time must be within 60 seconds.
2. The maximum mean error between the input profile and the output response after 60 seconds must be in the range ± 0.0207 kPa (± 0.003 psi). This error corresponds to ± 17 m°C.
3. The maximum rms error between the input profile and the output response, after 60 seconds, must be less than 0.0414 kPa (0.006 psi) corresponding to 34 m°C.
4. The maximum rate of change of pressure that can be closely controlled must be at least -0.1242 kPa/s

(-0.018 psi/s) which corresponds to $-6^{\circ}\text{C}/\text{min}$.

5. The controller must be able to handle the total pressure change of 21 kPa (3 psi) or 17°C .

An expansion system which meets the above specifications is adequate for microphysical studies. For a typical expansion the initial temperature and pressure are about room temperature and atmospheric pressure.

B. EXPANSION CONTROL SYSTEM HARDWARE

The expansion control system shown in Figures 1.1 and 1.2 consists of several subsystems. They are briefly described below.

1. The Cloud Simulation Chamber [20]. The cloud simulation chamber is made of aluminum, a ten-sided right prism, 61 centimeters high and 48 centimeters in diameter. It has a volume of 0.11 cubic meter and 1.3 square meter inner wall surface. It is a cooled-type cloud simulation chamber. The maximum rate of change of temperature that can be closely controlled is $-6^{\circ}\text{C}/\text{min}$. The chamber is considered to be a closed vessel but small leaks exist. The leaking time constant is of the order of 400 to 500 seconds. The time constant of the chamber in the expansion mode is about 50 to 60 seconds.

2. The Positive Displacement Uni-Directional Pump.

The positive displacement pump is considered as a flow generator. In theory, it is capable of providing constant flow under any pressure. In practice, due to internal leakage, it is characterized by a flow generator and an

internal leakage resistance.

3. The Regulator Tank. The regulator tank, shown in Figure 1.1, is used as a reservoir at the low pressure side of the pump. The tank helps to prevent abrupt changes of pressure across the 3-way valve due to a small change of flow. Its function is similar to that of a capacitor in a power supply.

4. The Storage Tank. The storage tank, shown in Figure 1.1, is used for storing supply gas of the same kind as the sample gas. In compression or in the holding mode of operation, the storage tank will supply gas to the cloud simulation chamber.

5. The 3-Way Infinite Position Rotary Valve. The valve, shown in Figure 1.1, is used to control the flow rate into, or out of, the cloud simulation chamber. The valve aperture is a linear function of the angular displacement [22]. The angular displacement is divided into degrees, 240 degrees in total or -120 to +120 degrees with respect to the center position. Angular position between -120 and 0 degrees are assigned to be the expansion mode. The position at zero degrees is assigned as the closed position. The position between 0 and +120 degrees are assigned to be the compression mode. The valve is driven by the stepping motor. The torque required to rotate the valve is about 0.212 N·m (30 oz-in).

From the results of the performance tests of the valve, the valve has been found to exhibit a small dead zone about

the center position and a saturation zone above ± 30 degrees. The dead zone is small and has no significant effect on the system because the valve operates in the expansion mode most of the time. The gearing inside the valve also causes a small backlash of about 0.2 degree.

6. The Solenoid and Manual Valves. There are three solenoid valves and one manual valve in the expansion system as shown in Figure 1.1. The solenoid valves are numbered 1/03, 1/04 and 1/11. The 1/03 valve is a two way, fixed position, solenoid valve. It is used only when extra air is needed to speed up pressure initialization. It must be reset (closed) during an experiment. The 1/04 valve is a three way fixed position solenoid valve. It is used to route the ventilation of the expanded gas from the chamber to the outside environment. It must be open during a simulation. The 1/11 valve is a two way fixed position solenoid valve. It is used to open or close the chamber under program control. During the cloud simulation it must be open. The manual valve can be used to reduce the flow rate for the operation of the expansion system at very low expansion rates.

7. The Pressure Gauge. The pressure gauge, shown in Figure 1.1, is used for monitoring the pressure inside the storage tank.

8. The Pressure Relief Valve. The pressure relief valve, shown in Figure 1.1, is used to automatically regulate the pressure inside the storage tank.

9. The Stepping Motor and Stepping Motor Interface.

The stepping motor used to drive the rotary valve is a Superior Electric Slo-Syn motor, model M063-FD09. The translator driving system is model STM-1800C. Since the torque required to drive the rotary valve is about 0.212 N·m. (50 oz-in), the start-stop without error curve of the stepping motor provided by the manufacturer indicates that at 0.212 N·m torque the speed must be 1050 steps/s or less. In practice, the friction torque of the valve is not constant. The torque varies non-linearly as a function of the valve position. In addition, the acceleration and deceleration effects [23] cause the stepping motor to skip or overshoot a few steps because of the unbalanced torque. It is found that at the speed of 750 steps/s or less, the stepping error is typically 0 to 4 steps. Consequently, 750 steps/s is chosen to be the base driving frequency of the stepping motor. The stepping motor has 200 steps per revolution, or one step equals 1/200 revolution.

The speed of the stepping motor is adjusted in the stepping motor interface. The purpose of the interface is to accept a digital number output from the NOVA 840 and then convert it into a string of pulses. The number of pulses is equal to the digital output number. One pulse corresponds to one step change of the angular displacement.

The output format of the digital output number must be 12-bit sign-magnitude, shown in Figure 3.1. Bits 0 through 10 give the magnitude of the number to be output. The

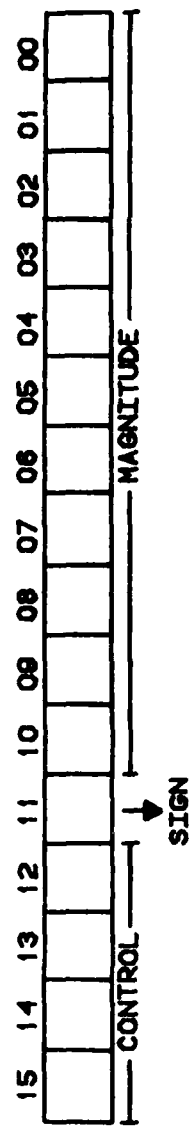


Figure 3.1. The number format of the stepping motor interface.

maximum number can be $2^{11}-1$. The 11th bit is the sign or direction control bit. Bits 12 to 15 are wired OR connected and are used as control bits. A 5 microseconds or longer pulse in any control bit will start the conversion of the stepping motor interface.

The interface is connected to digital output channel #2. Before outputting the desired number of steps to the digital output register, the format must be converted from 16-bit 2's complement binary to 12-bit sign-magnitude binary format. At the same time, a 5 microseconds pulse must be output to the control bits to start the parallel number to serial pulses conversion. The subroutine that handles the format conversion is written in NOVA Assembler called STEPM [24]. The flow chart is shown in Figure 3.2.

The base frequency of the interface determines the speed of the stepping motor. It is set at 750 Hz or 750 steps/s. Currently only 9 bits of magnitude are being implemented. This covers the range of -511 to +511 steps per one output command. It should be noted that the angular displacement of the stepping motor is relative to the previous position; it is not an absolute displacement.

10. The Transducers. The strain gauge pressure transducer is a Statham pressure transducer, model PL80TC-2-350-D, serial #2881. The transducer is a bi-directional differential type, and has a response time of less than 1 ms to step pressure changes. The pressure range is ± 13.8 kPa (± 2 psi) relative to the reference pressure.

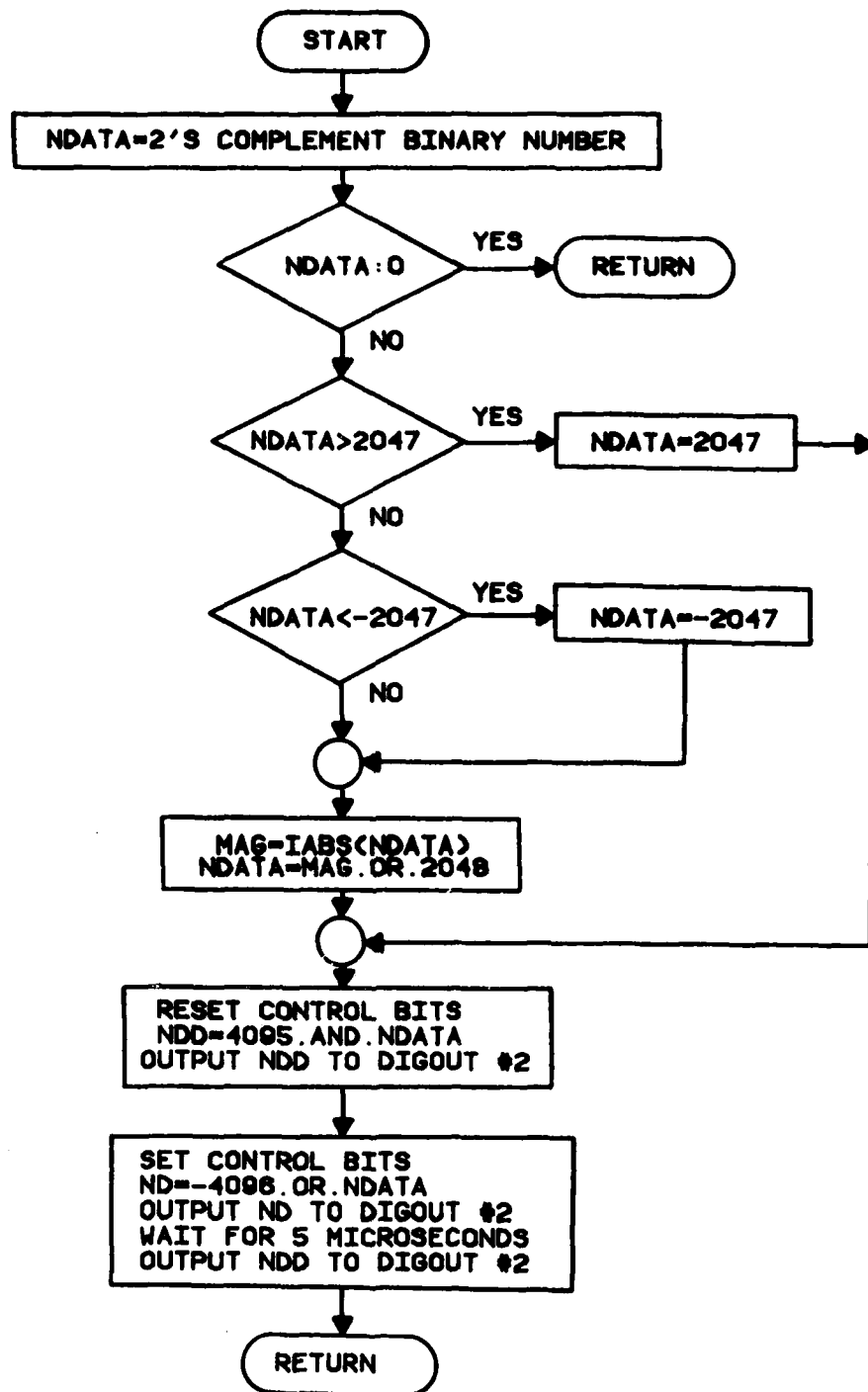


Figure 3.2. The flow chart of the stepping motor interface output routine.

The input resistance is about 350 ohms and the output resistance is about 330 ohms. The resolution is infinitesimal according to the manufacturer. The combined non-linearity and hysteresis are less than $\pm 1\%$ full scale, or ± 0.276 kPa (± 0.04 psi). To obtain better accuracy of the transducer, the transducer is recalibrated against a very accurate dead weight pressure of ± 0.00069 kPa (± 0.0001 psi) accuracy, in the decreasing pressure mode only. Thus the effect of hysteresis can be neglected. The dead weight pressure is a Ruska Instrument dead weight, model 2465-751, serial #18785.

The non-linear characteristic of the pressure transducer is fitted by a second order polynomial using a least square error fit. As a result, the accuracy of the pressure transducer is about ± 0.0069 kPa (± 0.001 psi). The sensitivity is 0.7148 volts/kPa (4.942 volts/psi). The resolution is ultimately limited to 1/2 least significant bit of 15-bit A/D converter or 0.0003125 volts which is equal to 0.000437 kPa (0.0000634 psi). The pressure transducer is connected to channel #9 of the high level A/D converter, Figure 3.3. The transducer is followed by an analog low pass filter which has a cut off frequency at 16 Hz.

The valve position transducer is a potentiometer type position transducer [22]. The valve position is measured by the voltage of a ten-turn potentiometer connected to the shaft of the valve by anti-backlash gearing. The

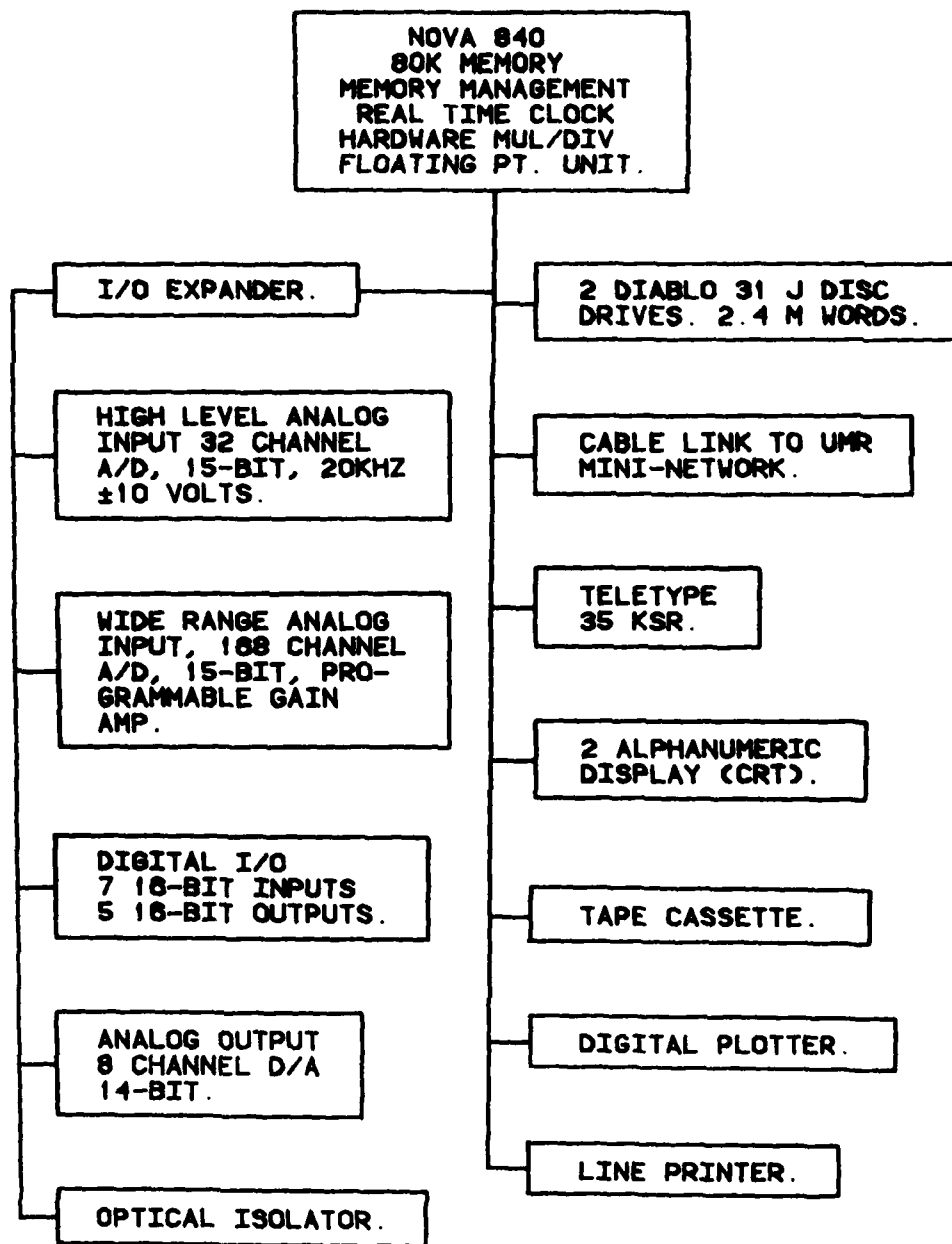


Figure 3.3. The NOVA 840 computer system.

sensitivity is 0.0225 volts/degree. The accuracy is better than ± 0.1 degree. The transducer is connected to the high level A/D converter channel #7 which has an analog low pass filter whose cut off frequency is 8 Hz.

11. The Computer System. The block diagram of the NOVA 840 system at the Cloud Physics Research Center is shown in Figure 3.3. At present, the hardware multiply/divide is being used. Typical execution times of floating point addition, subtraction, multiplication and division are 250, 275, 320 and 340 microseconds, respectively. These times will influence the time needed for identification and control.

C. MODEL OF THE EXPANSION SYSTEM

A model of the expansion system is required for designing the closed-loop control system. The model can be characterized by the thermodynamic behavior of the system [25]. The analysis indicates that the chamber constitutes a non-linear capacitance as a function of pressure. In addition, the experimental results indicate that the flow rate does not vary linearly as a function of the angular valve position of the rotary valve. Therefore, the expansion system should exhibit multiple non-linearities. These multiple non-linearities are confirmed by the experimental results. Assuming the model of the expansion is finite order, properties like capacitance and resistance of the chamber, the orifice and the valve are lumped. To represent the behavior of the system for the

whole range of operation, quasi-linear models are developed, and the values of lumped parameters can be found experimentally [26-28].

The lumped parameter circuit analogy to the expansion system is shown in Figure 3.4. Separate circuits are necessary for each mode of the 3-way infinite position rotary valve. It should be noted that the expansion system is arranged so that the pressure is referenced to room pressure and not the absolute pressure. This arrangement increases the accuracy and simplifies the model of the expansion system since pressures of interest lie fairly near room pressure.

The most important mode of operation is the expansion mode. In Figure 3.4, the R_{SC} represents the lumped leaking resistance of the chamber. The $R(P, \theta)$ represents the variable resistance of the valve as a function of the chamber pressure, P_{SC} , and the angular position of the valve, θ . R_p represents the internal resistance of the pump, and $C_{SC}(P)$ is the cloud simulation chamber lumped capacitance. The regulator tank and the pump produce a pressure source, P_S , across the 3-way infinite position rotary valve. This simplifies the model of the expansion system since it is preferable for a computer-limited application to start with a simplified model. Then the resulting controller synthesized by optimal control theory will require much less computer time than a control law based on a higher order model [29]. The expansion system

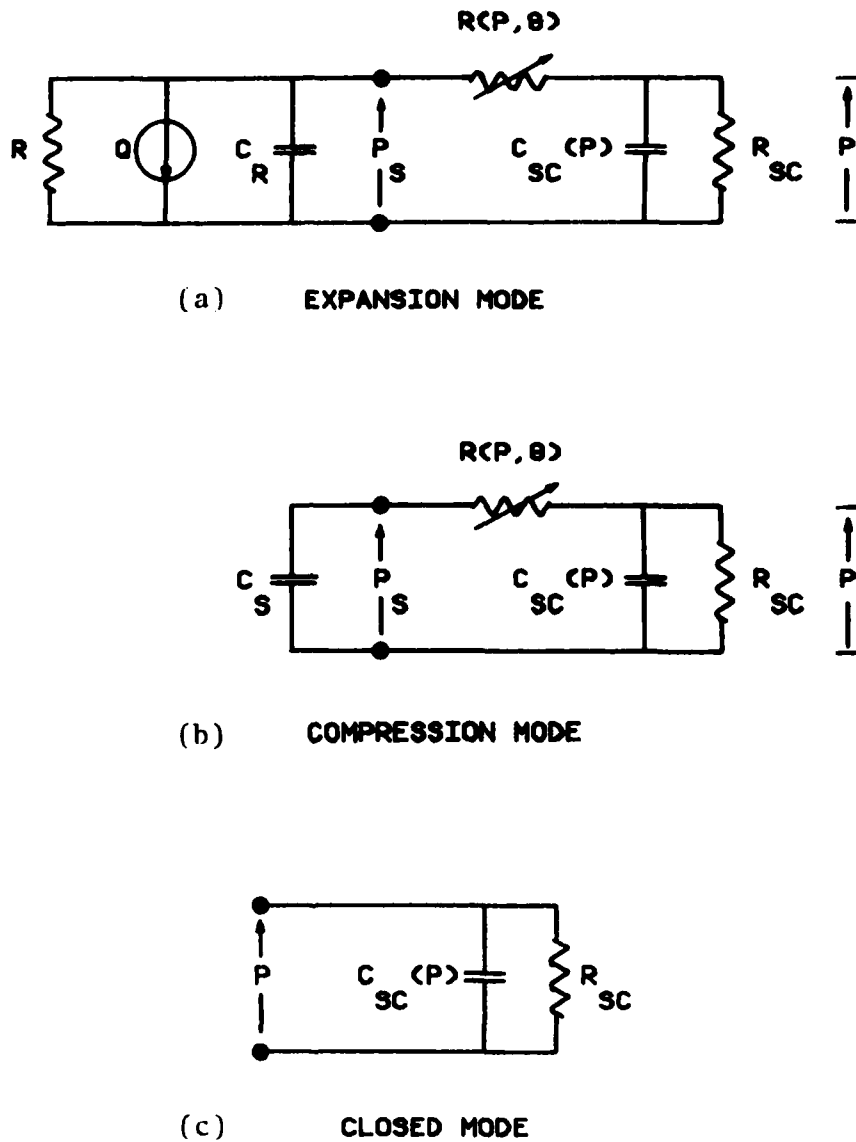


Figure 3.4. The electrical analogy of the expansion system.

model is simplified to be a first order system which consists of the pressure source, P_S , the variable resistance valve, $R(P, \theta)$, and the cloud simulation chamber $C_{SC}(P)$. The approximate model, Figure 3.4a, can be written in the form

$$\dot{x}(t) = f(x(t), \theta(t), t) \quad (3.1)$$

$$P(t) = x(t) \quad (3.2)$$

where $x(t)$ is the state variable at time t and $\theta(t)$ is the valve position at time t . This relation can be linearized in the vicinity of an operating point [25]. For a small perturbation about a particular operating point, $\theta_0(t)$ and $x_0(t)$, the linearized equation becomes

$$\dot{\delta x}(t) = a(t)\delta x(t) + b(t)\delta\theta(t) \quad (3.3)$$

where $a(t) = \frac{\partial f(x, \theta, t)}{\partial x} \Big|_{\theta=\theta_0(t), x=x_0(t)}$ and

$$b(t) = \frac{\partial f(x, \theta, t)}{\partial \theta} \Big|_{\theta=\theta_0(t), x=x_0(t)} .$$

In classical control systems analysis, either sine waves at various frequencies or step functions are usually used as excitations in order to develop a system model from experimental data. The frequency response or step function response can then be analyzed to obtain the coefficients of differential equations [26].

For the discrete control systems, the dynamic model of a system is assumed to be a difference equation. The

quasi-linear dynamic model equations of the expansion system are

$$x(k+1) = A(k)x(k) + B(k)\theta(k) \quad (3.4)$$

$$P(k) = X(k) \quad (3.5)$$

where $x(k)$ is the discrete state variable, $P(k)$ is the chamber pressure relative to equilibrium pressure (room pressure) at $\theta(k)=0$, $\theta(k)$ is the valve position, $A(k) = A(P(k), \theta(k))$, $B(k) = B(P(k), \theta(k))$ and k is the number of sampling periods. The values of $A(k)$ and $B(k)$ of the difference equation can be obtained experimentally [26]. The sampling period, T , is determined from the sampling theorem (Shannon Theorem) [9]. The sampling period must satisfy the equation

$$T \leq \frac{1}{2} \left(\frac{2\pi}{\omega_e} \right) \quad (3.6)$$

where ω_e is the highest natural frequency of the band limited signal in radians per second. For the expansion system, ω_e is about 1/50 radian per second. Then T must be less than 157 seconds or the sampling frequency must be faster than 0.00637 Hz. In the design, the sampling period has been chosen to be quite small in order to reduce the pressure error caused by the error of the control signal. Theoretically, there is no lower limit on the sampling period but the number and the period of on-line computation tasks limit the minimum sampling period to be only 4

seconds or 0.25 Hz sampling frequency.

From the experimental results, the values of $A(P(k))$, $\theta(k)$) are always less than 0.98 for $P(k)$ between 0 and -27.6 kPa (-4 psi) with respect to room pressure and $\theta(k)$ is between -120 and +120 degrees. This means that the expansion system is always stable in the range of operation [9,30]. The system is also controllable and observable. The first order quasi-linear approximation has a significant advantage in the design of the digital control system in the sense that the complexity of the optimal control analysis has been reduced, which also reduces the required computer time [29].

D. SYSTEM SOFTWARE

1. The Implementation of the Time-Optimal Control. In order to perform an interesting microphysical experiment, the high performance pressure and wall temperature controllers are required by the given specification. In the pressure control case, the pressure error between the desired profile and the pressure response must be minimized. The characteristics of the problem, the system non-linearity and the ramp input function, make it very difficult to have a zero steady state error by using ordinary classical closed-loop control laws. Theoretically, zero steady state error can be obtained from the optimal control law by selecting the right performance index and the right value of weighting parameters. Commonly, the minimum summed-square error (quadratic performance index) and the time-

optimal control yield a zero steady state error for the input ramp function, provided the weighting parameter on the control is zero [11]. The typical performance index of the minimum summed-square error [9,11] is

$$J = \sum_{k=0}^{\infty} [(P(k) - Y(k))^T (P(k) - Y(k))] \quad (3.7)$$

where $P(k)$ and $Y(k)$ are the output response and desired output at sampling instant k , respectively.

For the time-optimal control, given a linear system and an initial state at any point in state space, there exists a control to bring the system from the initial point to the origin in minimum time. If the control is unconstrained, the origin can be reached in one sampling period [9].

The closed-loop control of the expansion system is arranged as shown in Figure 3.5. Here, the linearized transfer function of the expansion system in the expansion mode is the system to be controlled. K and τ , in Figure 3.5 are the linearized gain and time constant of expansion system in the expansion mode, respectively. V_p and θ are pressure voltage and the valve position, respectively.

Since the expansion system is approximated by a first order quasi-linear model, the state feedback gains obtained from the minimum summed-square error control strategy and the time optimal control strategy are exactly the same [9-11]. The time-optimal control is chosen for the design since the analysis of the control is much simpler than the

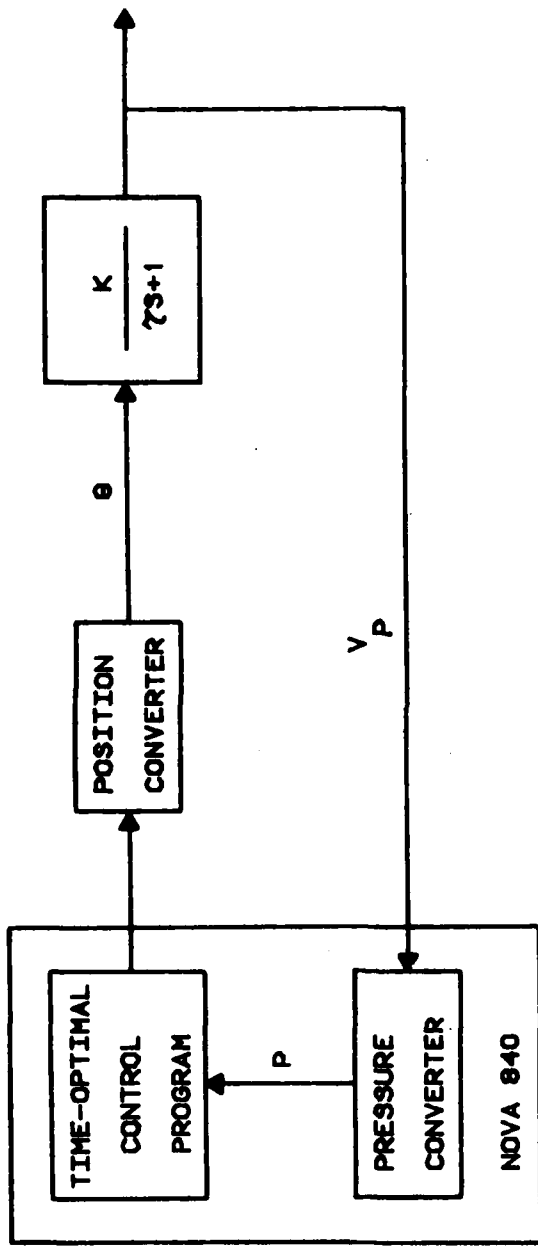


Figure 3.5. Block diagram of the closed-loop digital control of the expansion system.

minimum summed-square error.

In the implementation of the time-optimal control, a particular pressure $P(k)$ is treated as an initial point and the desired final point $PD(k+1)$ is treated as the origin. The control, $\theta(k)$, that will bring the pressure from the initial point to the origin within minimum time is shown in Figure 3.6, where $GAIN2=1.0/B(P(k),\theta(k))$ and $GAIN1=-GAIN2*A(P(k),\theta(k))$. The values of A and B are needed for the control computation, but they are not constant due to the non-linearities of the system. From the experimental results, the optimal feedback gains are valid only for small perturbations of $P(k)$ and $\theta(k)$. To extend to the full range of operation, a table look-up for the values of A and B as functions of $P(k)$ and $\theta(k)$ was developed. A typical table for the parameters is shown in Table I. At each step of control computation, two dimensional linear interpolations of A and B are obtained from this table for particular values of $P(k)$ and $\theta(k)$. It is found that the error of the pressure response using this table met the design specification only at certain rates of expansion. The validity range of a particular table is small, only ± 0.0104 kPa/s (± 0.0015 psi/s). Therefore, for all expansion rates between 0 and -0.1242 kPa/s, six tables would be needed. Since this requires a large amount of core memory and since searching for table entries requires a large amount of time, this approach has serious drawbacks. Moreover, when any part of the control

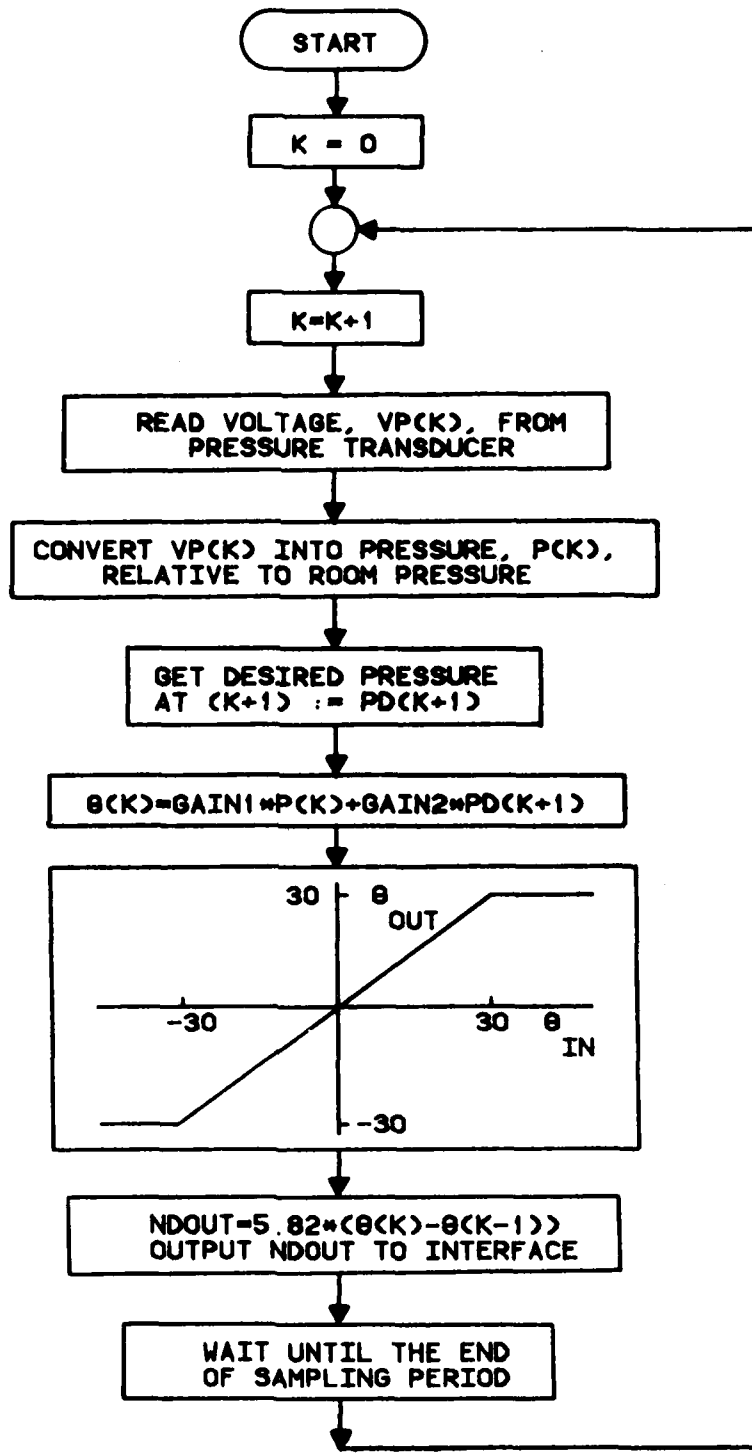


Figure 3.6. The implementation of the time-optimal control algorithm.

TABLE I
TYPICAL TABLE LOOK-UP MODEL OF THE EXPANSION SYSTEM.
 $\Delta\theta = 5$ DEGREES, $\Delta P = 9.66$ kPa (1.4 psi)

<u>P</u> (kPa)	<u>θ</u> (degree)	<u>A</u>	<u>B</u> (kPa/degree)
0	- 5	0.958	0.0126
0	- 10	0.941	0.0142
0	- 15	0.931	0.0137
0	- 20	0.920	0.0124
- 9.66	- 5	0.952	0.0237
- 9.66	- 10	0.939	0.0207
- 9.66	- 15	0.929	0.0181
- 9.66	- 20	0.916	0.0163
- 19.32	- 5	0.949	0.0270
- 19.32	- 10	0.943	0.0242
- 19.32	- 15	0.923	0.0234
- 19.32	- 20	0.912	0.0207

configuration is changed, all entries in the tables must be reidentified. For example, when the cover of the chamber is opened for service, there is no guarantee that when the cover is replaced and sealed the leakage resistance of the chamber would be the same. Unless the leakage resistance were the same, the characteristics of the chamber would be changed. Consequently, the table look-up approach is not suitable for the development of the cloud simulation pressure control system. The method of table look-up has been dropped and an adaptive control algorithm is implemented. However, the tabulated data gives some useful information in the design of the adaptive control system.

2. The Implementation of the Adaptive Control

Algorithm. A real time adaptive control system is not a new subject. In fact, it is used in systems where high quality of control is needed [31]. An adaptive control system has two principal functional elements: a plant to be controlled and a controller where the controller design is based on a nominal but inexact mathematical model of the plant and/or its environment, and a method for altering the controller structure in a dynamic manner. The functional block diagram of the adaptive control system of the expansion system is shown in Figure 1.2. First of all, the on-line (real time) identification of the system parameters is required. There are several published research results [32-36] concerning on-line identification

schemes. The response error of the adaptive control system is directly dependent on the accuracy of the identification scheme. For the time-optimal control of the expansion system, the steady state error will be within ± 0.069 kPa (± 0.01 psi) if the value of A and B of the model converge close to their exact value within one step and, assuming B is correct, A must be accurate within $\pm 1\%$, or assuming A is correct, B must be accurate within $\pm 7\%$.

The linear sequential regression perturbation identification [26] for the quasi-linear model of the expansion system is implemented for the on-line identification scheme, since it minimizes the differences between the model and the actual system responses. It also has closed form equations, so no searching techniques are required. Warner [27] pointed out that this type of identification worked very well for a linear system in the presence of measurement noise, and that the accuracy should increase as the number of data points, N, is increased. It should be noted that for a linear system the parameters converge in one step.

The system of interest in this investigation is non-linear. Consequently, some precaution must be taken when applying the identification method. A non-linear system with a ramp input can be considered as a time-variant linear system. For a first order system, there are two time varying parameters, A and B. The characteristics of the time varying parameters can be divided into

three groups. First is the group of systems in which both A and B are strictly monotone increasing/decreasing in the same direction as a function of time. The second group is the systems which have either constant A and B (linear system), or monotone increasing/decreasing A and B but in opposite directions as a function of time. The third group consists of those systems in which A and B are not monotone, but which can be broken up into time intervals such that within each interval the system falls into either group one or group two. The regression identification can not converge within one step for the systems of the first group. In fact, from the digital simulation the parameters A and B oscillate due to self-compensation of each other. For the second group of systems, the regression identification converges close to the correct values within one step. The expansion system is found to be a system of the third group. It is expected to behave like the mixture of the first two systems.

In the preliminary tests, the regression method has been used for the identification scheme. Figure 3.7 shows the corresponding flow chart of the scheme. From knowledge obtained in applying the table look-up method, the values of A and B are limited to lie between 0.99, 0.89 and 0.027, 0.007 respectively. The adaptive control using this scheme yields a small mean error, less than ± 0.0207 kPa (± 0.003 psi) for rates between $0^{\circ}\text{C}/\text{min}$ and $-6^{\circ}\text{C}/\text{min}$, but the rms error increases from 0.0552 kPa

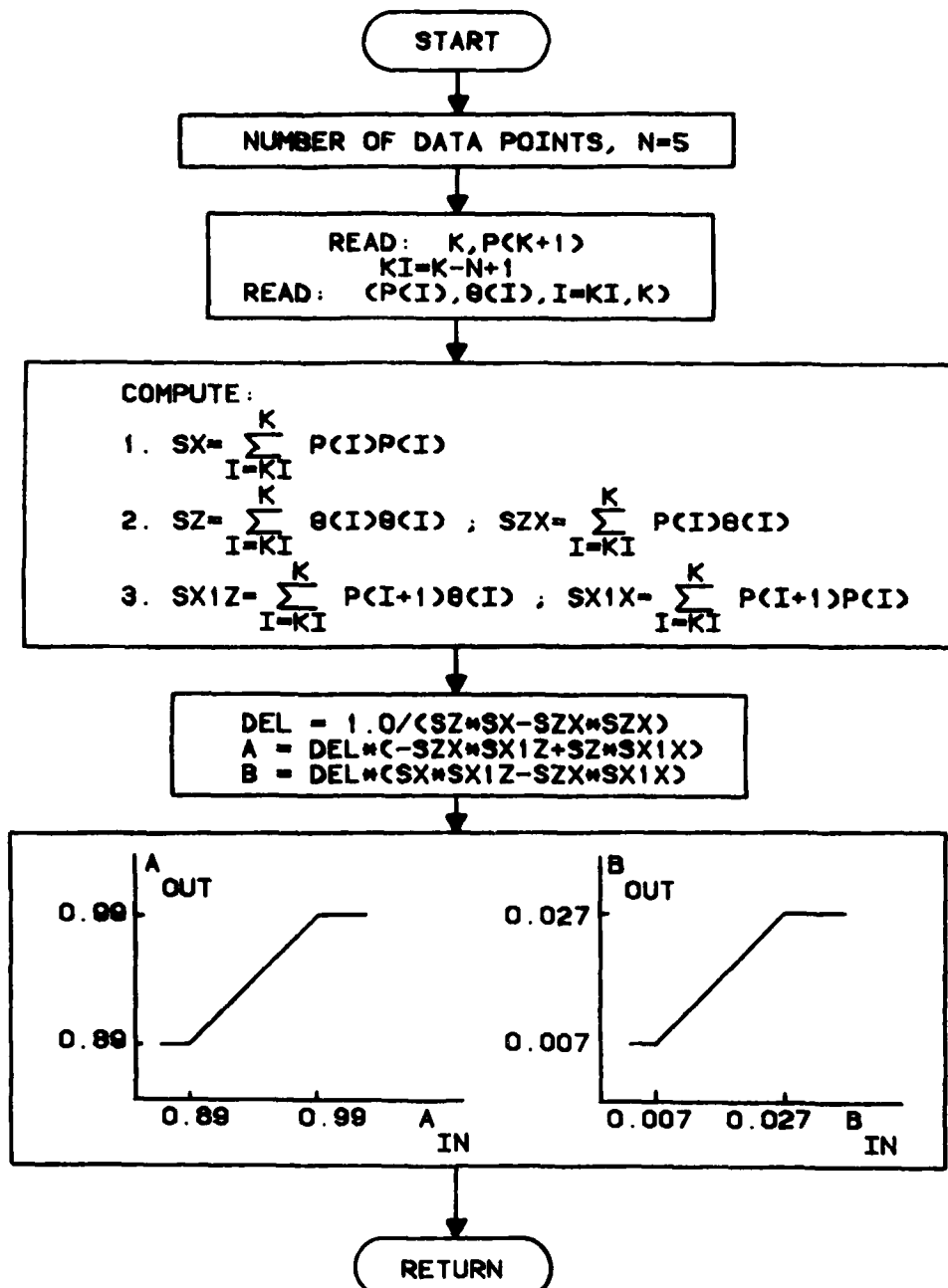


Figure 3.7. The sequential regression identification subroutine.

(0.008 psi) to 0.0828 kPa (0.012 psi) as the rate increases. This scheme can operate without tables over the desired range of operation of the system. The closed-loop pressure response shows some recurrent noise spikes approximately every 40 seconds. The values of $A(P(k), \theta(k))$ and $B(P(k), \theta(k))$ exhibits a wide variation, jumping back and forth. The behavior of $A(P(k), \theta(k))$ and $B(P(k), \theta(k))$ are shown in Figure 3.8 and 3.9, respectively. Five data points are used in the sequential regression identification scheme. It is evident that the larger the number of data points, N , the smoother the regression. But if N is too large, the past data will dominate the present data. This introduces a certain offset of the parameters and leads to increasing the offset of the pressure response. Again, from the table look-up results, it is known that the model parameters change slowly with time. It can be assumed that the real values of parameters also change slowly with time. Assuming the oscillation of A and B are due to the presence of high frequency noise introduced by an imperfect identification scheme, the high frequency oscillation can be filtered out by first order low pass digital filters. The parameters become

$$A(P(k), \theta(k)) = A(k) = AFILTER * A(k-1) + BFILTER * A_{IDENT} \quad (3.8)$$

$$B(P(k), \theta(k)) = B(k) = AFILTER * B(k-1) + BFILTER * B_{IDENT} \quad (3.9)$$

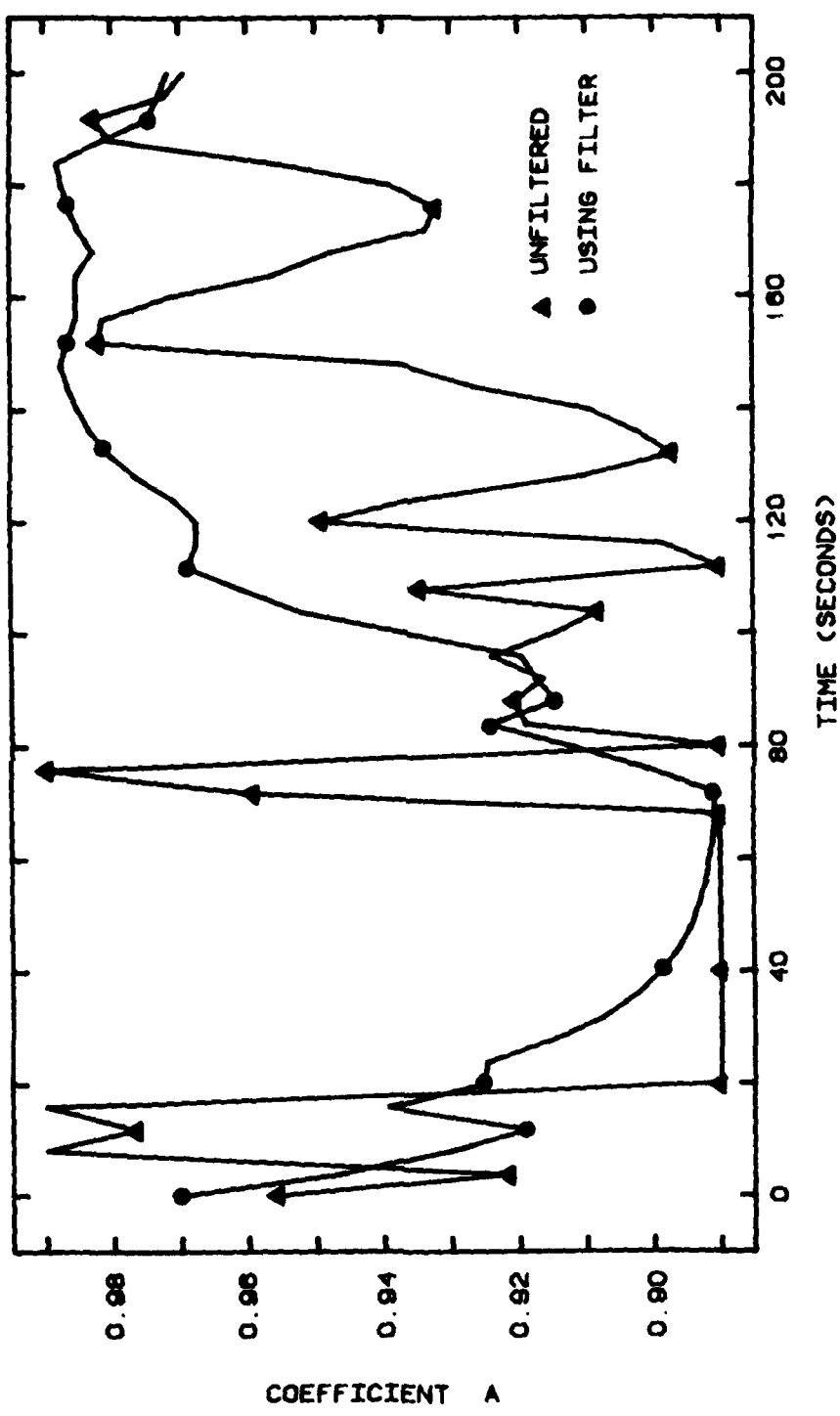


Figure 5.8. The behavior of the coefficient A as a function of time.
The rate of expansion is $-4^{\circ}\text{C}/\text{min}$.

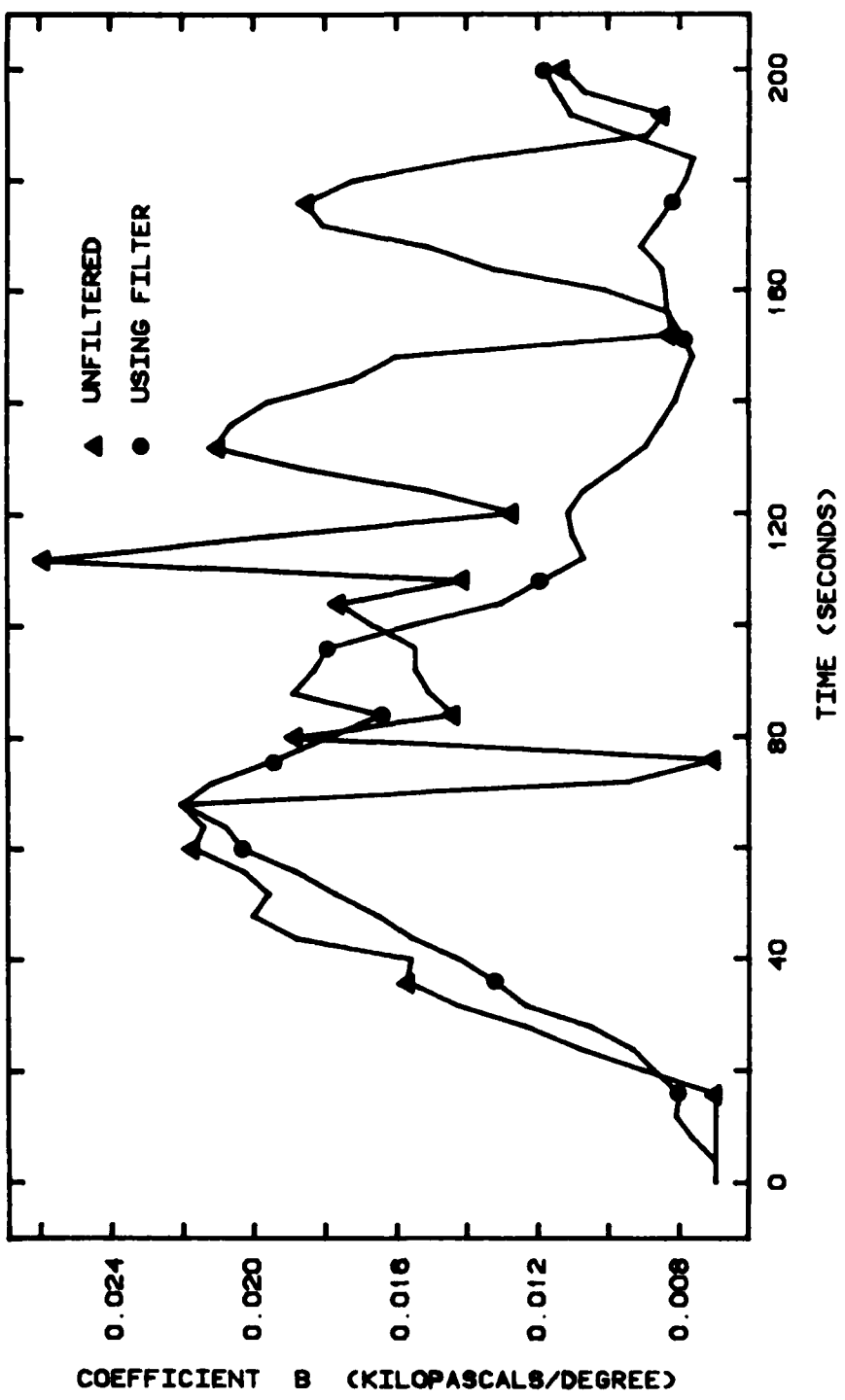


Figure 3.9. The behavior of the coefficient B as a function of time.
The rate of expansion is $-4^{\circ}\text{C}/\text{min}$.

where $B_{FILTER} = 1.0 - A_{FILTER}$ and A_{FILTER} must vary with the rate of change of pressure in kPa/s or temperature in $^{\circ}\text{C}/\text{min}$. The block diagram of the identification scheme with low pass filter is shown in Figure 3.10. The reason that the value of A_{FILTER} varies with the rate of change of pressure or temperature is that the change of $A(k)$ and $B(k)$ can be approximated by ramp functions. The low pass filter usually introduces offsets at steady state when the input is a ramp. The offset may be kept small or held constant by varying the cut off frequency of the filter. The values of A_{FILTER} are found experimentally and are shown in the Table II. The comparison between the unfiltered and the filtered curves of A and B are shown in Figure 3.8 and 3.9, respectively.

After the low pass filters are employed, the results indicate that the closed-loop control system has improved. The rms error is reduced to below 0.0414 kPa (0.006 psi) for rates from $0^{\circ}\text{C}/\text{min}$ to $-6^{\circ}\text{C}/\text{min}$.

3. System Programming. The control program and other programs required to run the cloud simulation chamber are written using multitasking concepts [37]. The programs are written in separate small programs called tasks. A task is defined as a logically complete execution path through a user program that demands use of system resources such as peripheral devices for I/O or simply CPU control work; task execution may occur independently and asynchronously with other tasks. In the multitask

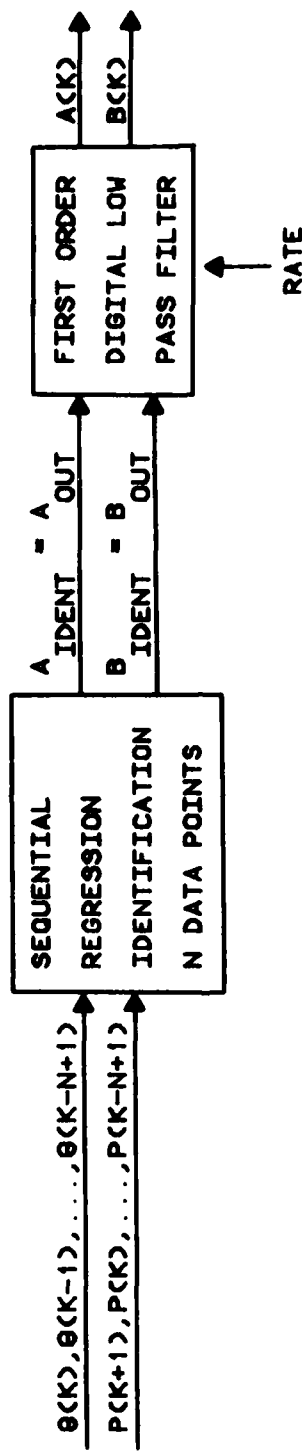


Figure 3.10. The block diagram of overall identification scheme.

TABLE II
EXPERIMENTAL VALUES OF AFILTER AND BFILTER

RATE (°C/min)	AFILTER	BFILTER
0 to -2	0.86	0.14
-2 to -4	0.71	0.29
-4 to -6	0.56	0.44

environment, each task competes simultaneously for the use of system resources. At any single moment, only one task receives CPU control and the desired resources. The allocation of tasks depends on their priority and the readiness to use the resources. A task scheduler governs the transfer of control to each task. All tasks are synchronized to the RTC (real time clock). For more detail, see Chapter 4, Part II, of reference [37].

When a task is activated, by FTASK or ITASK statements, it enters the ready state and competes with other ready tasks for control of the processor based on assigned priorities. The wall temperature output task, called TWALL [24], has the highest priority among other tasks since it is the most important task and the execution time is very short. The pressure control task, called PRESC [24], has the second highest priority. The priority for the rest of the tasks are assigned according to their functional importance.

The main cloud simulation program called SCPROG3 [24] consists of statements activating all the tasks. For the pressure control task a subroutine PREPAR [24] is called to initialize the variables, read in parameters and open a data file to store the experimental results. The flowchart of PREPAR is shown in Figure 3.11. Next the task PRESC, the expansion control task, is activated by the main program. The flowchart of PRESC is shown in Figure 3.12. The sampling period (cycle event) of task PRESC is 4

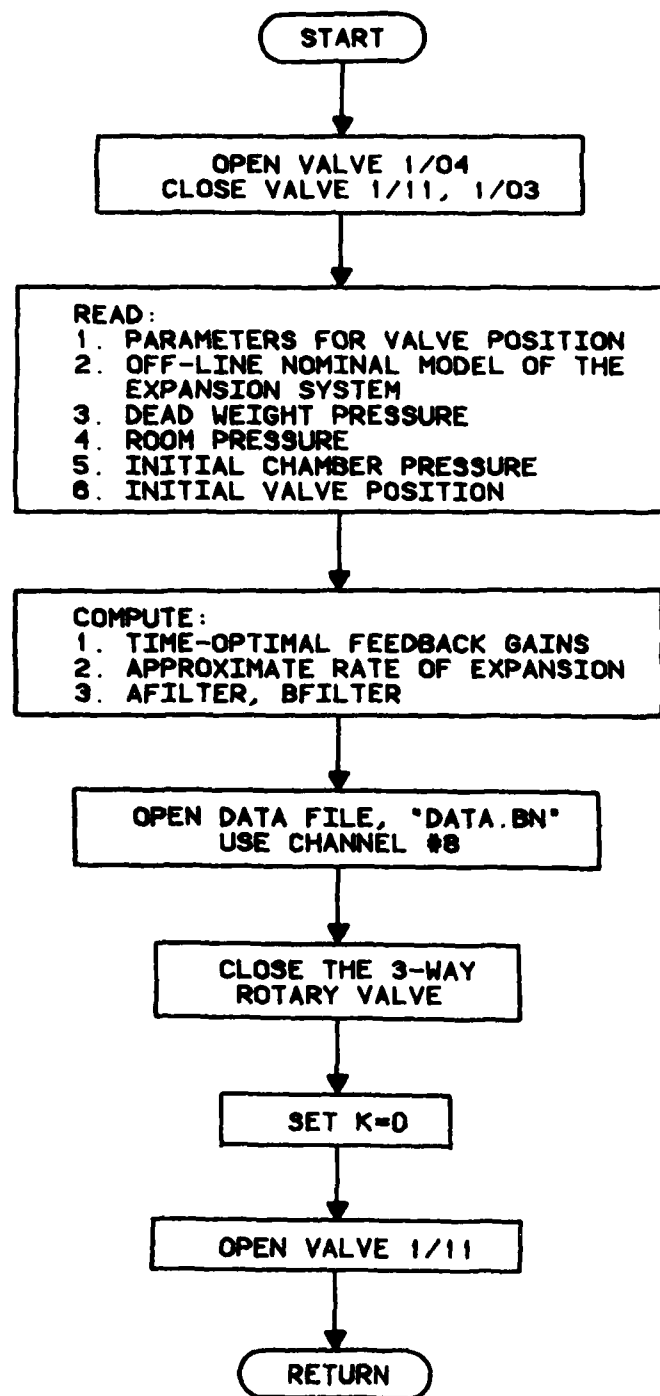


Figure 3.11. The flow chart of the subroutine PREPAR

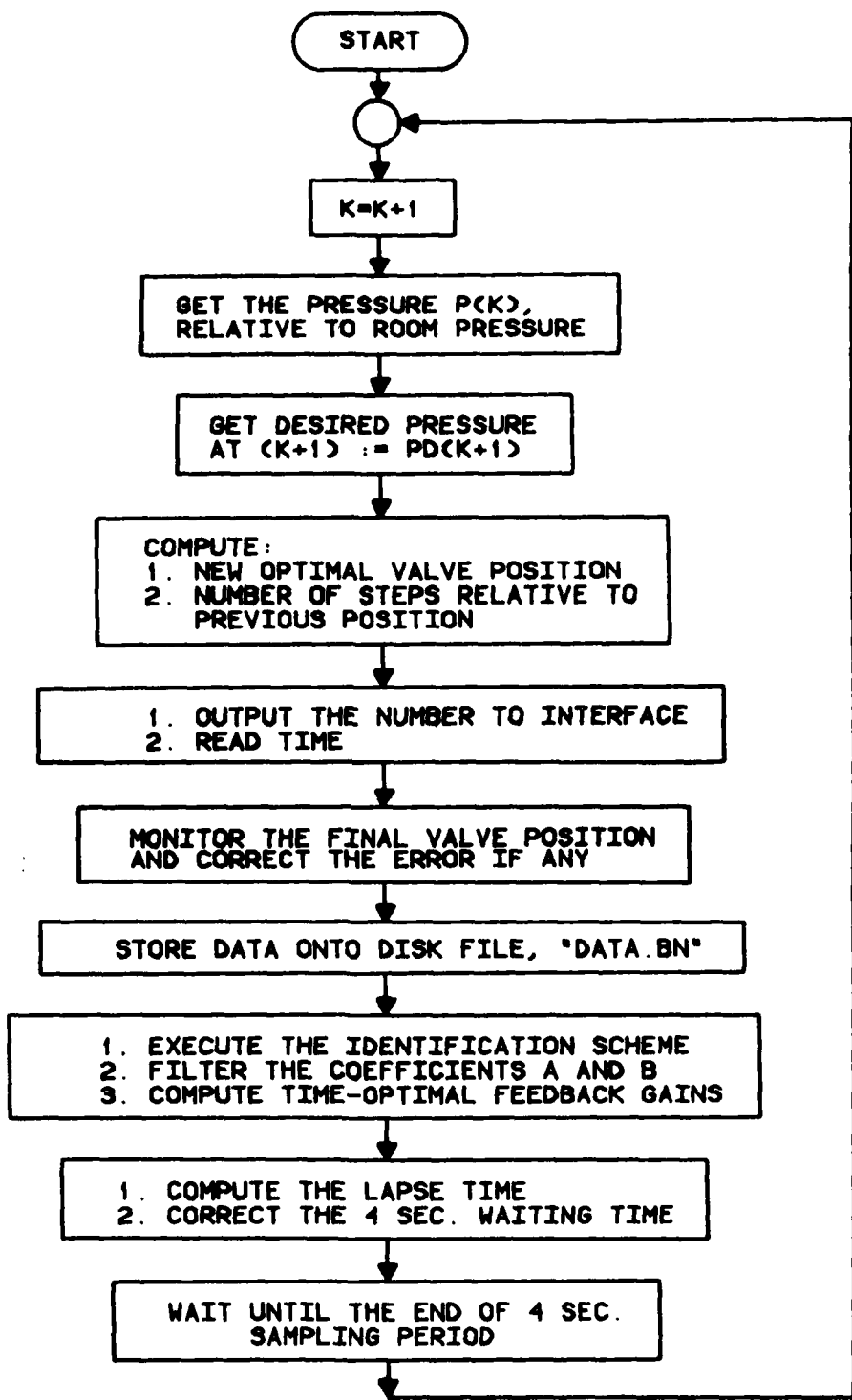


Figure 3.12. The flow chart of PRESC

seconds. The execution time of the time-optimal control computation is about 20 ms. The new valve position is updated via the stepping motor interface. Then the computer waits until the completion of the stepping motor movement and corrects the valve position error if there is any. It takes about 250 ms for this execution. The identification and filtering take place after the completion of the correction of the valve position and require less than 50 ms computation time. The total time occupied by PRESC is about 320 ms, which is about 8% of total available time. The rest of the available time can be used for the execution of other tasks, primarily taking and storing data relating to the aspects of the experiment. The control tasks are given highest priority for the simple reason that other data is useless unless good control of the experiment is achieved.

IV. EXPERIMENTAL RESULTS

Performance tests of the expansion control system are accomplished by a dry adiabatic expansion in which the wall and the gas are cooled at the same rate by using the adiabatic equation, equation 1.1. The program SCPROG [24] is used to prepare the chamber; the program SCPROG2 [24] proceeds after the completion of SCPROG. SCPROG2 holds the pressure and the wall temperature at their equilibrium states before proceeding to SCPROG3 [24], which computes the control and performs other tasks. The input to the wall temperature controller is output via the D/A converter channel #7. At the same time the computer monitors and controls the chamber pressure. The desired and output pressure responses are recorded onto a disk file named "DATA.BN".

To test the convergence of the sequential regression identification scheme, the initial values of A and B are set to be 0.5 and 0.03, respectively. These values are about 50% and 100% off the nominal values. The rate of expansion is set at -0.0828 kPa/s (-0.012 psi/s) or $-4^{\circ}\text{C}/\text{min}$. Figures 4.1, 4.2 and 4.3 show the results of the coefficients A and B and the pressure error, respectively. Evidently, from the error curve, the identification scheme converges within 60 seconds. It should be noted that the response between two discrete data points is approximated by a straight line connecting

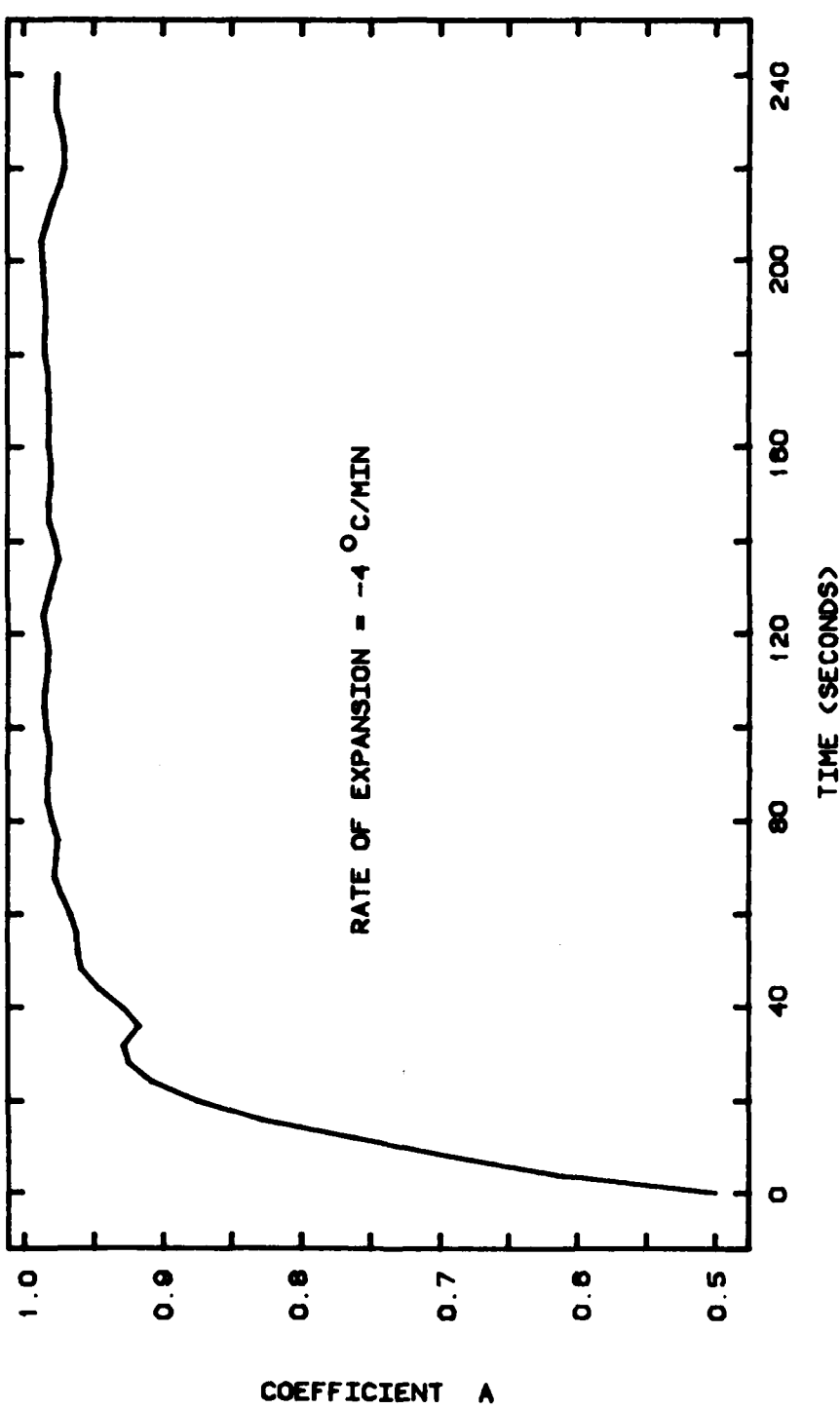


Figure 4.1. The coefficient A when A and B are initially set at 0.5 and 0.03, respectively.

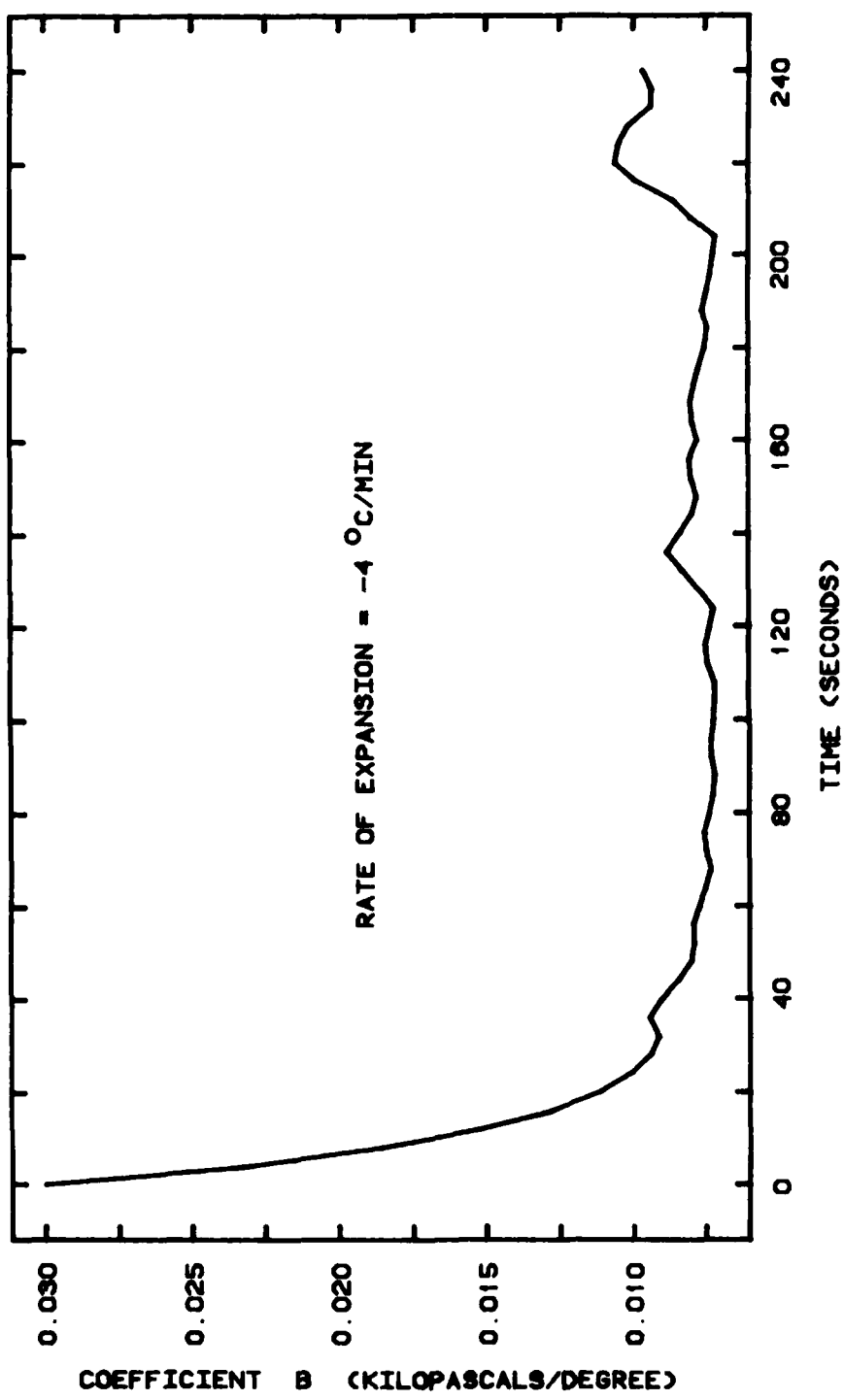


Figure 4.2. The coefficient B when A and B are initially set at 0.5 and 0.03, respectively.

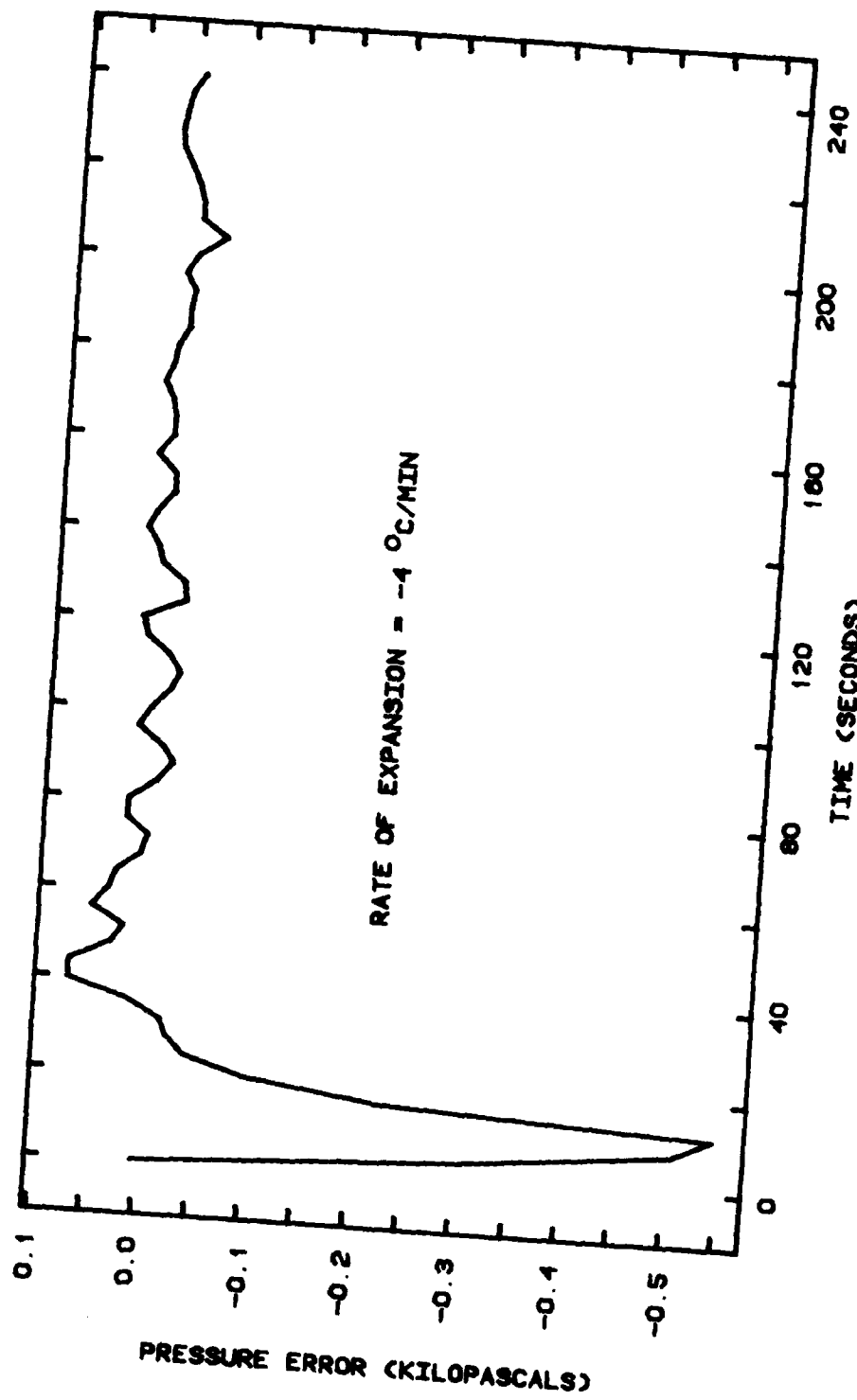


Figure 4.5. The error of the pressure response when A and B are initially set at 0.5 and 0.03, respectively.

the two points. To guarantee that the response between the sampling period has no oscillation, the pressure is recorded every 2 seconds instead of 4 seconds. The pressure response and the pressure error, in Figure 4.4 and 4.5, indicate that there is no significant oscillation between the sampling instant. The straight line approximation between two consecutive data points is acceptable.

Figures 4.6 to 4.9 show the pressure response, the pressure error and the coefficients A and B of the expansion control system at the rate of expansion of -0.1242 kPa/s (-0.018 psi/s) or -6°C/min . Figure 4.10 to 4.13 and 4.14 to 4.17 show the same set of curves but at the rate of -0.0828 kPa/s (-0.012 psi/s) or -4°C/min and -0.0414 kPa/s (-0.006 psi/s) or -2°C/min , respectively. The results indicate that the mean and rms error of the pressure responses at steady state or after 60 seconds are well below $\pm 0.0207 \text{ kPa}$ ($\pm 0.003 \text{ psi}$) and 0.0414 kPa (0.006 psi), respectively. The total change of pressure is 20.7 kPa (3 psi) except at -0.1242 kPa/s where the total change of pressure that can be closely controlled is about 18.6 kPa (2.7 psi). This is due to the limited pumping capacity of the pump.

Figures 4.18 and 4.19 show the pressure response and the pressure error when the holding mode is incorporated into the desired pressure profile. The initial holding time is 60 seconds. The expansion proceeds at the rate of -0.0828 kPa/s (-0.012 psi/s) for 100 seconds. The final

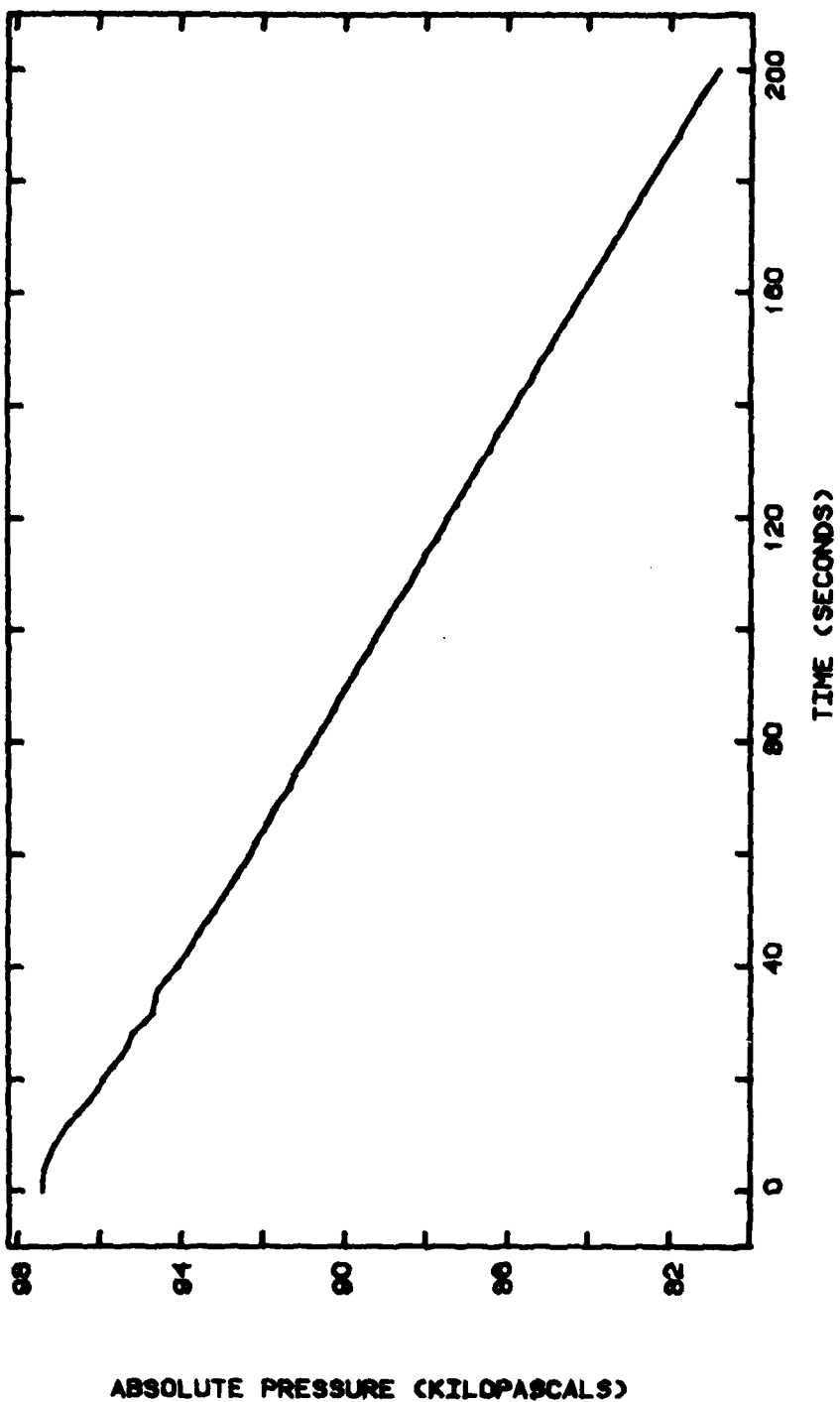


Figure 4.4. The pressure response when being recorded every 2 seconds.

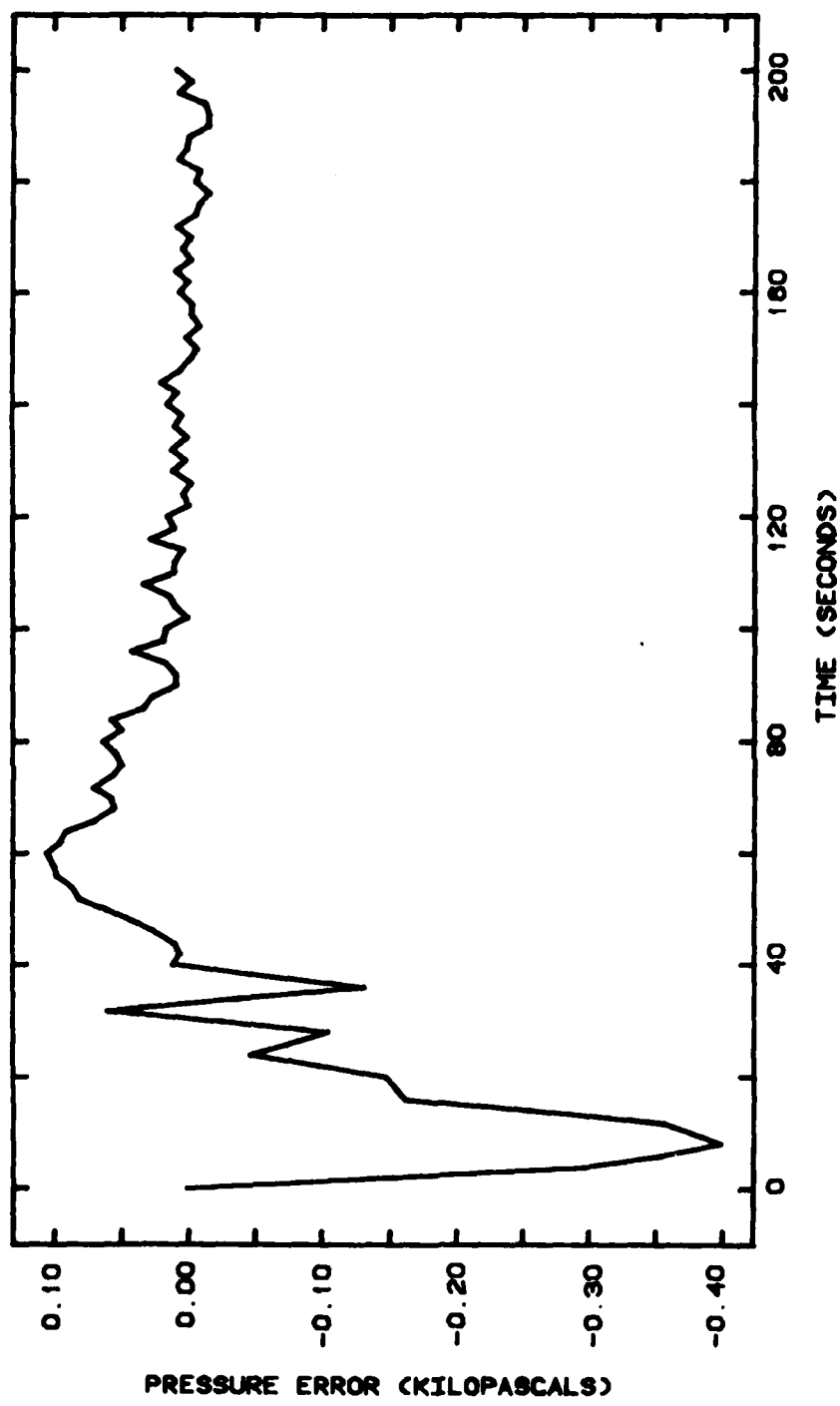


Figure 4.5. The pressure error when being recorded every 2 seconds.

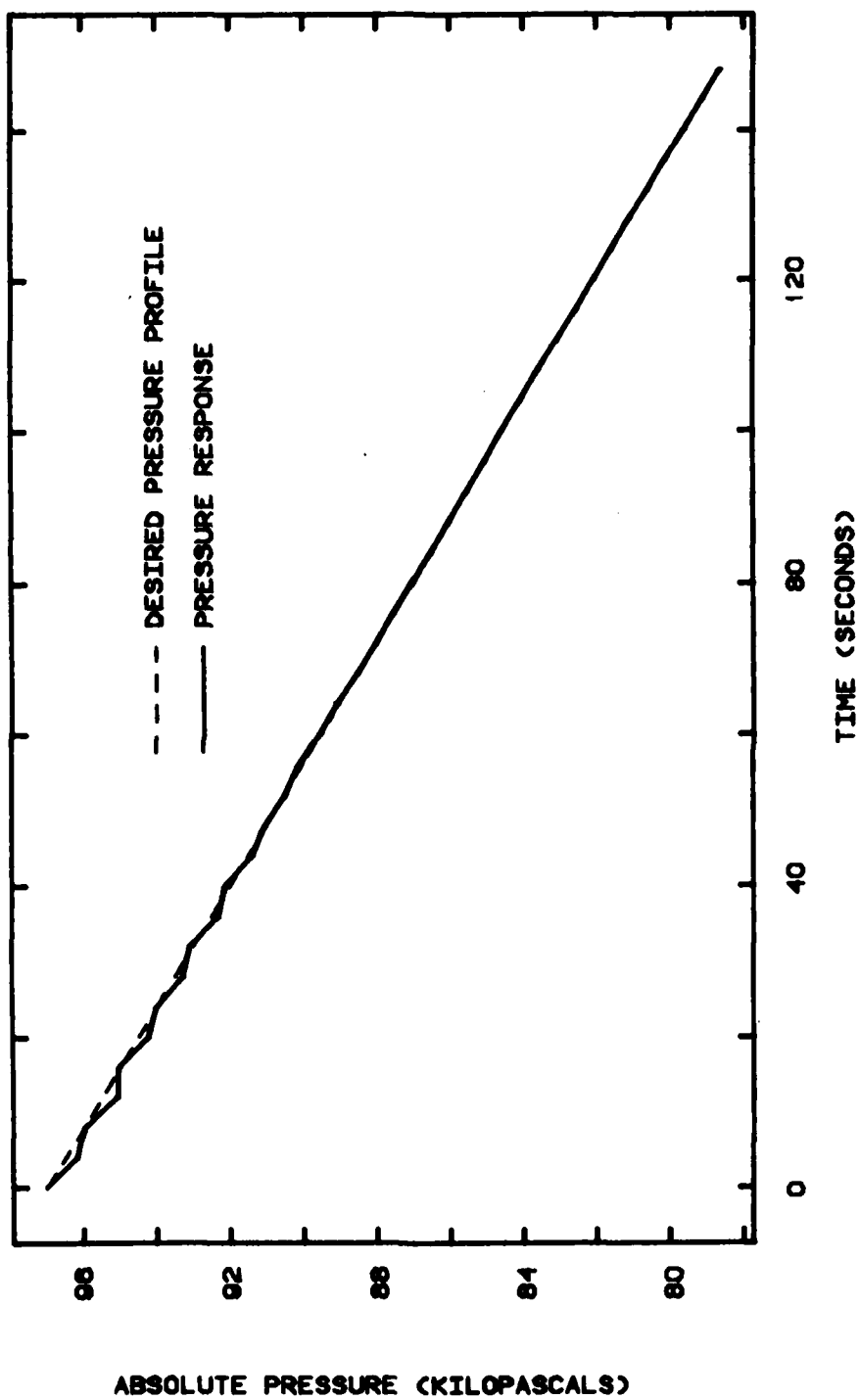


Figure 4.6. The pressure response at the rate of expansion of -0.1242 kPa/s or -6°C/min.

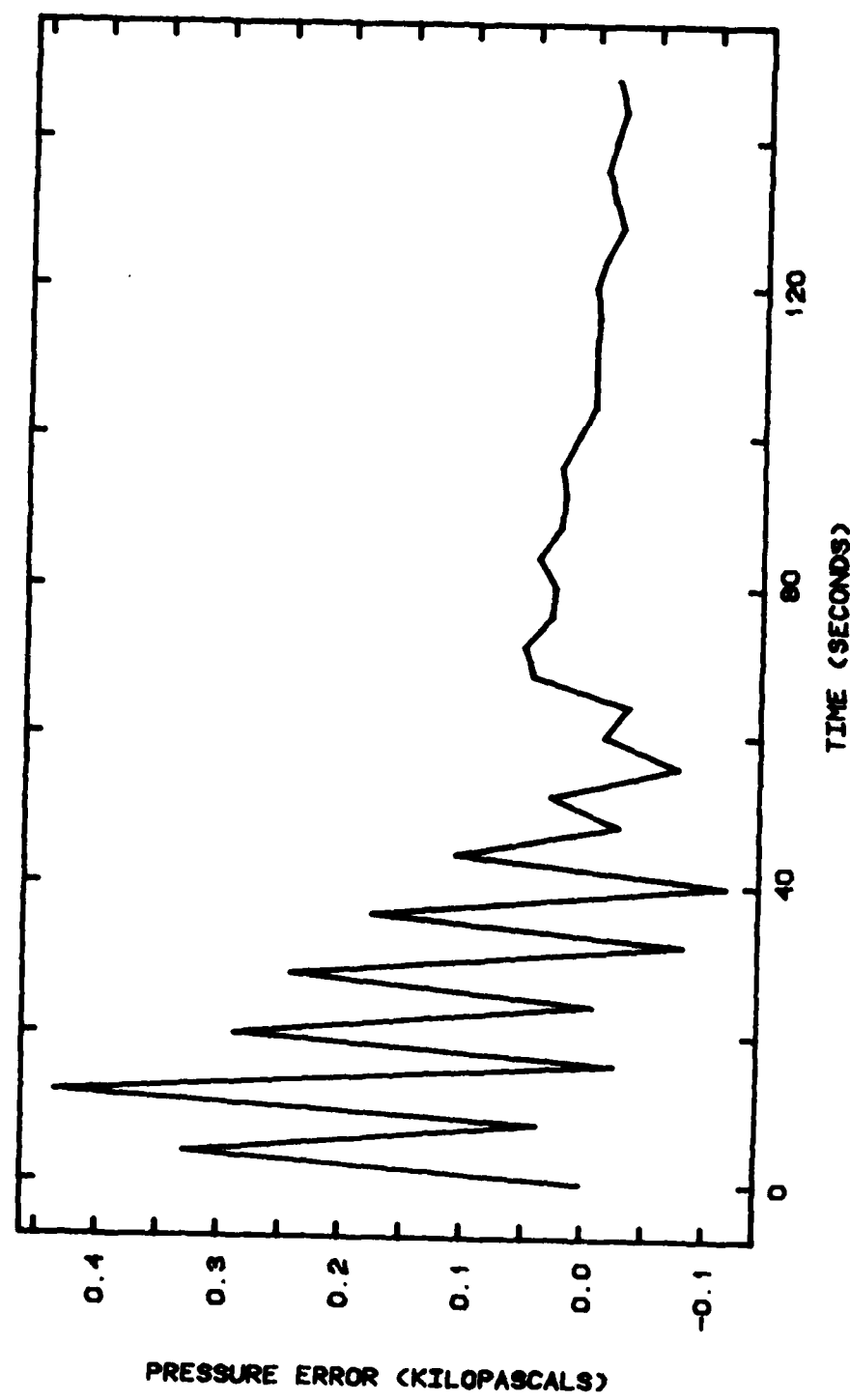


Figure 4.7. The pressure error at the rate of expansion of -0.1242 kPa/s or -6°C/min.

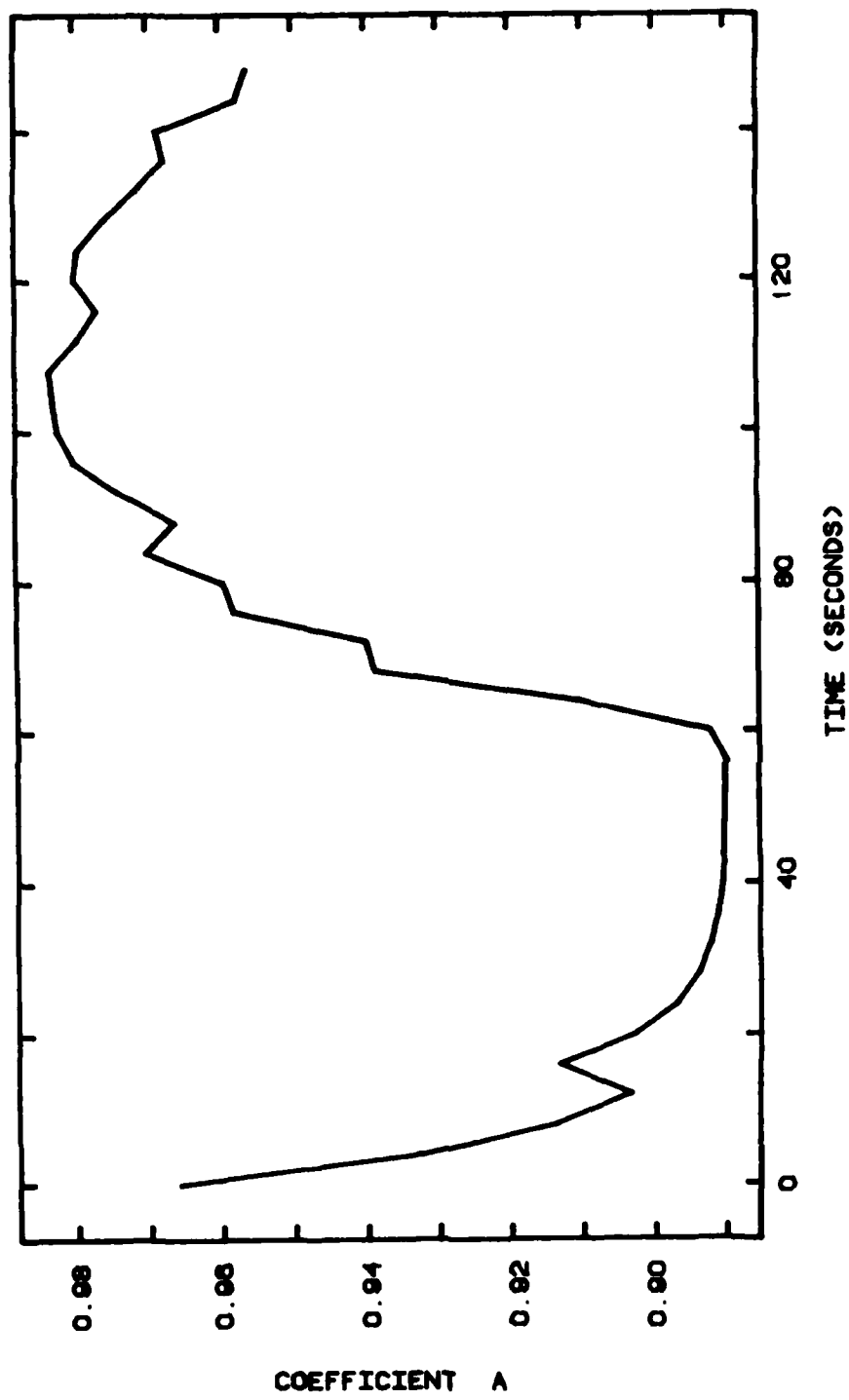


Figure 4.8. The coefficient A at the expansion rate of -0.1242 kPa/s or $-6^{\circ}\text{C}/\text{min}$.

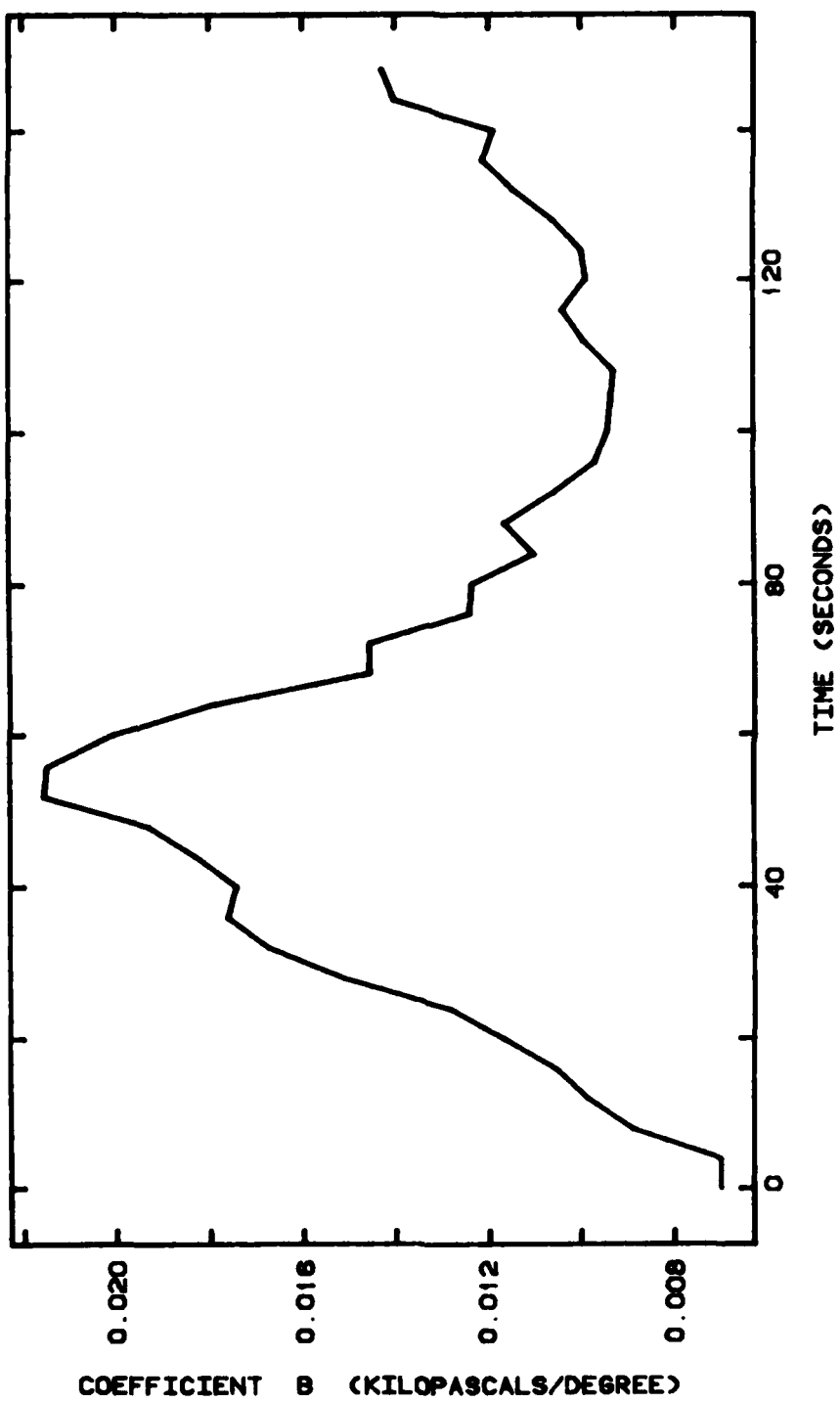


Figure 4.9. The coefficient B at the expansion rate of -0.1242 kPa/s or $-6^{\circ}\text{C}/\text{min}$.

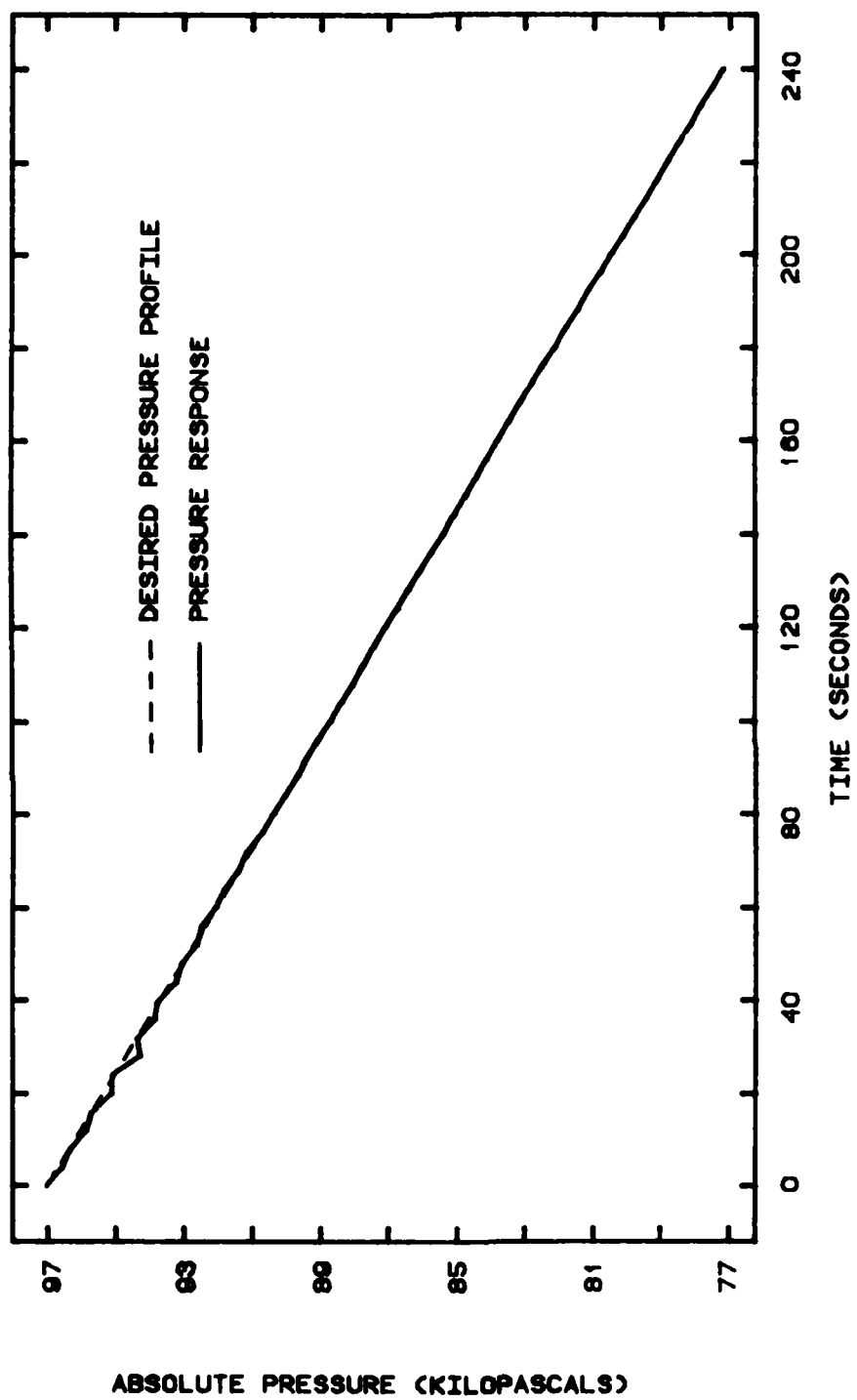


Figure 4.10. The pressure response at the expansion rate of -0.0828 kPa/s or $-4^{\circ}\text{C}/\text{min}$.

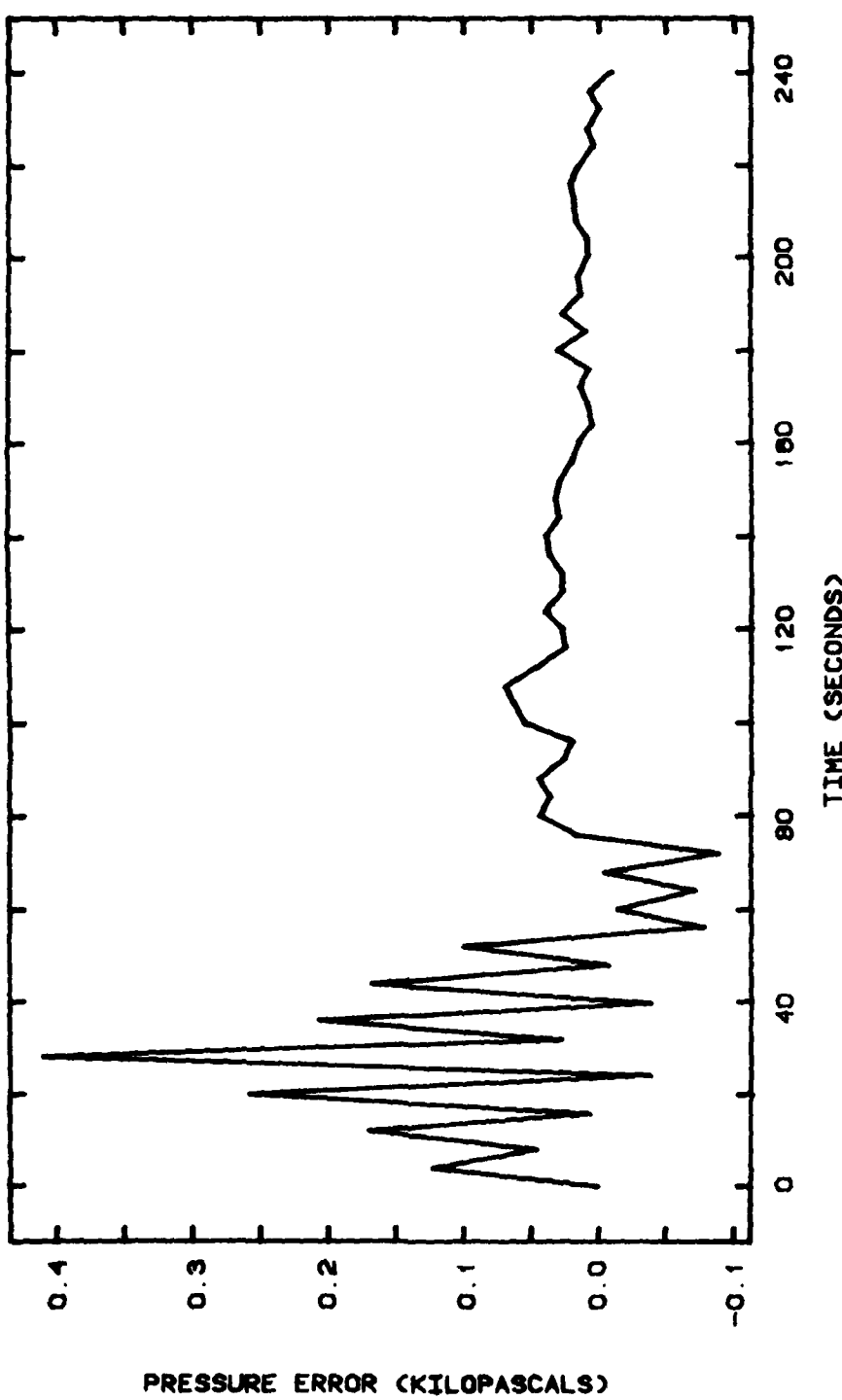


Figure 4.11. The pressure error at the expansion rate of -0.0828 kPa/s or -4°C/min.

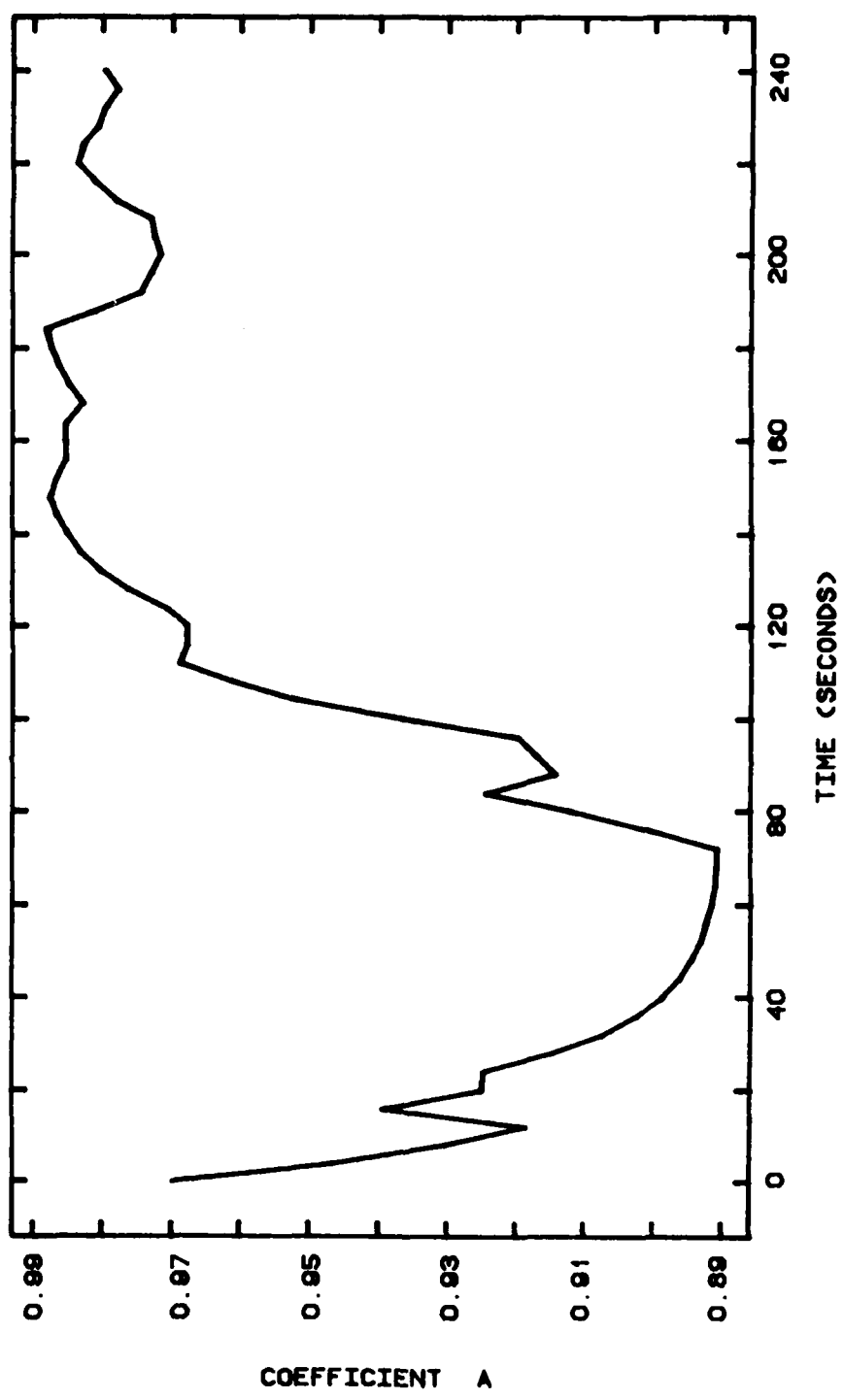


Figure 4.12. The coefficient A at the expansion rate of -0.0828 kPa/s or $-4^{\circ}\text{C}/\text{min}$.

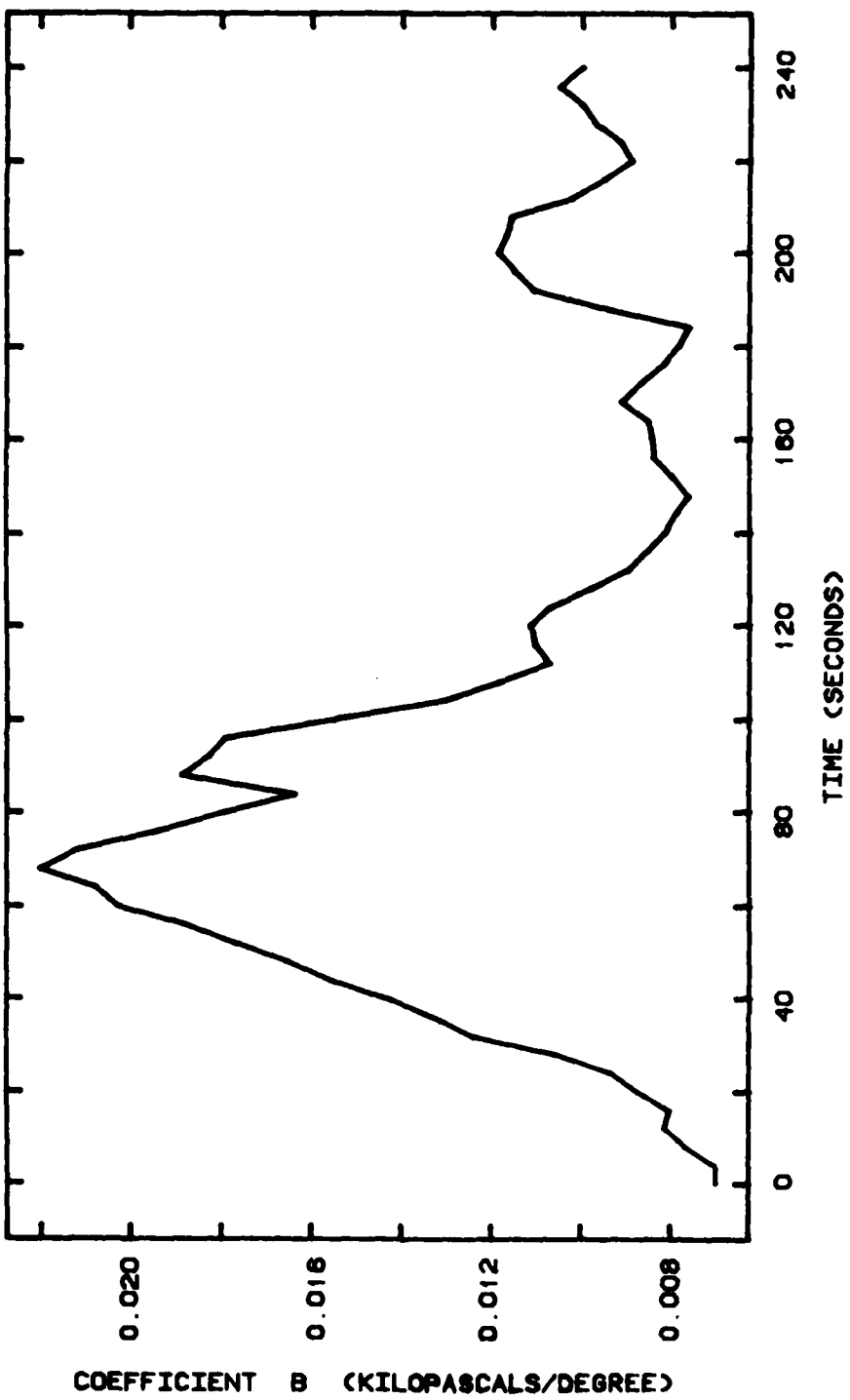


Figure 4.13. The coefficient B at the expansion rate of -0.0828 kPa/s or $-4^{\circ}\text{C}/\text{min.}$

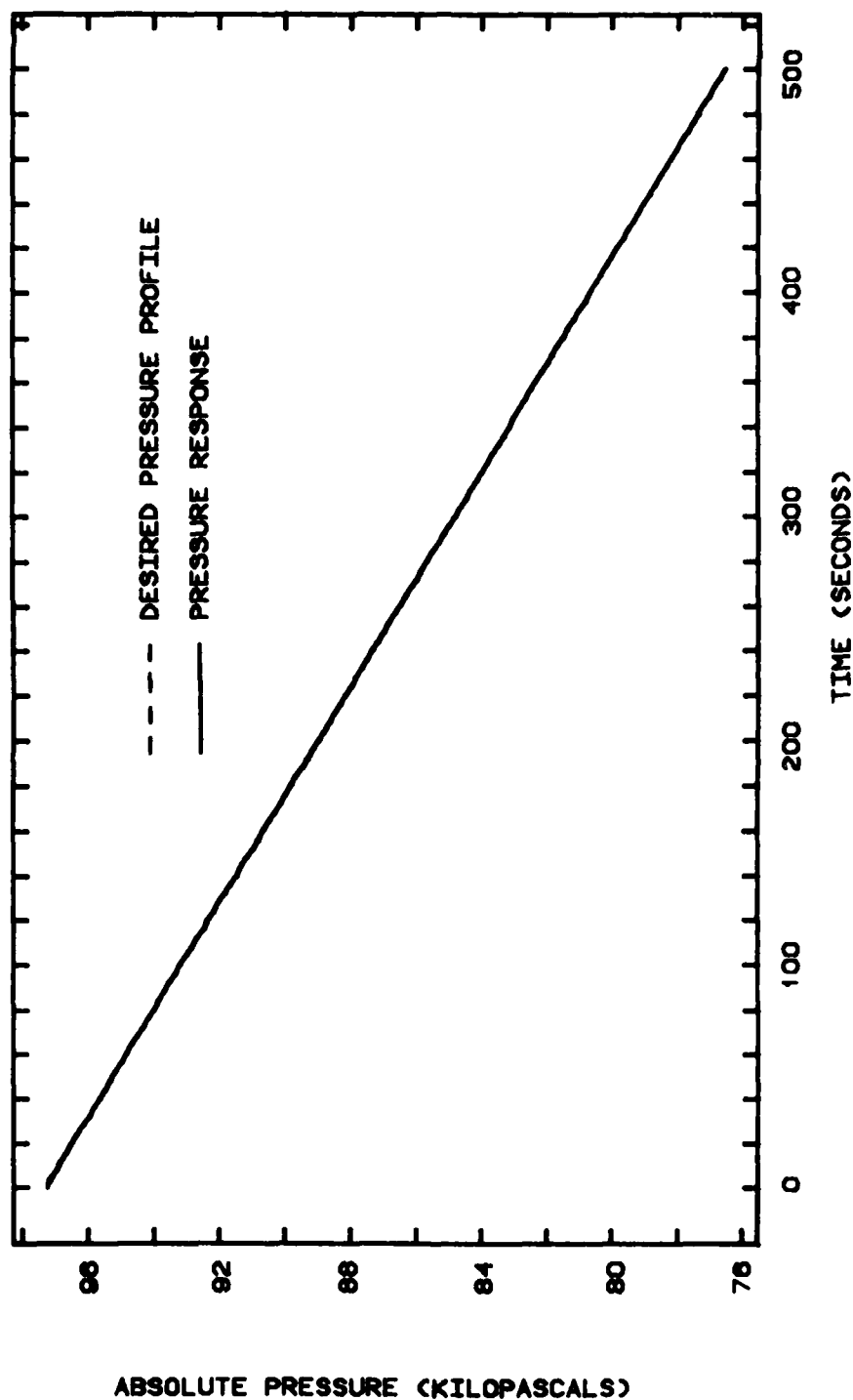


Figure 4.14. The pressure response at the expansion rate of -0.0414 kPa/s or -2°C/min.

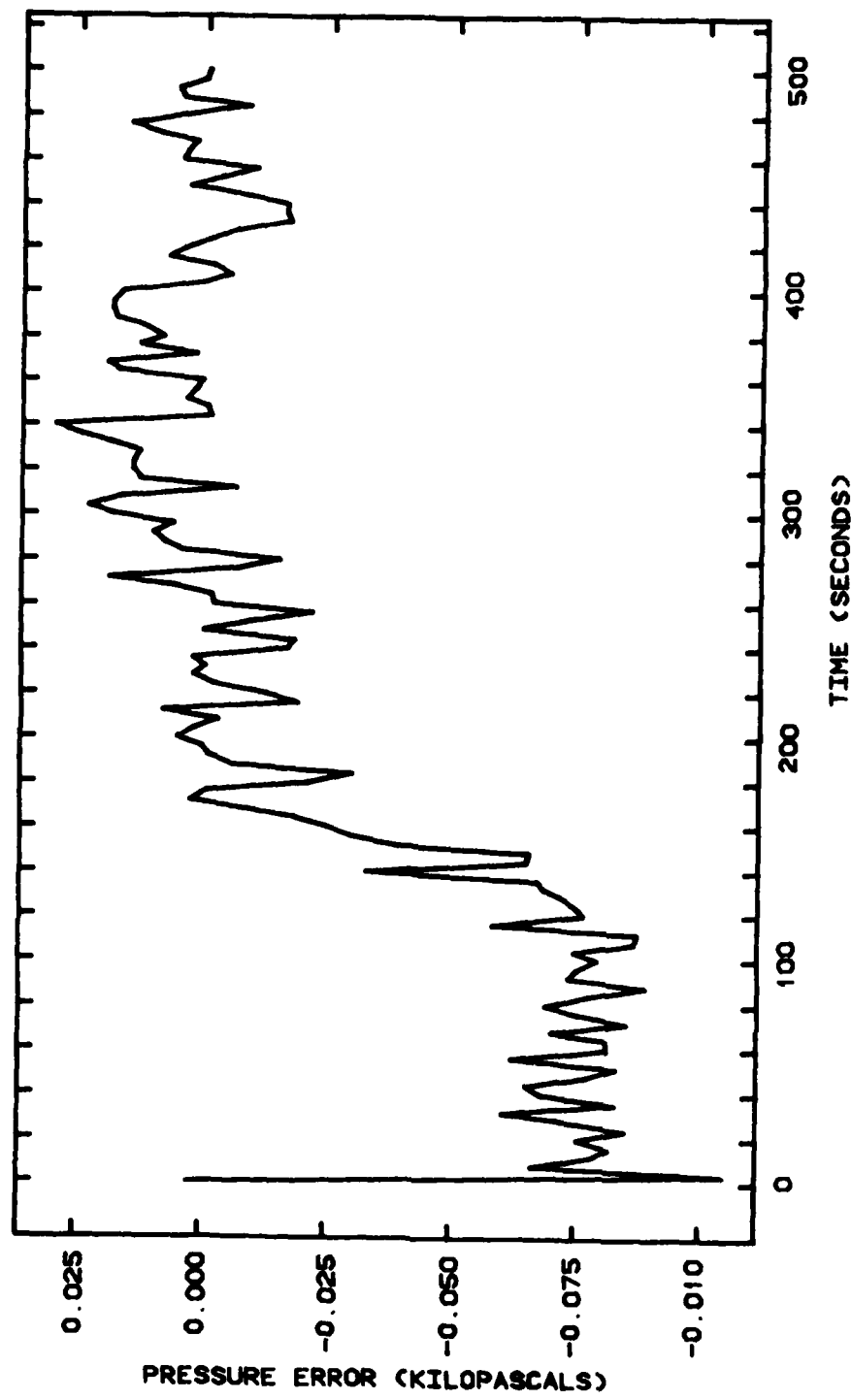


Figure 4.15. The pressure error at the expansion rate of -0.0414 kPa/s or $-20^\circ\text{C}/\text{min.}$

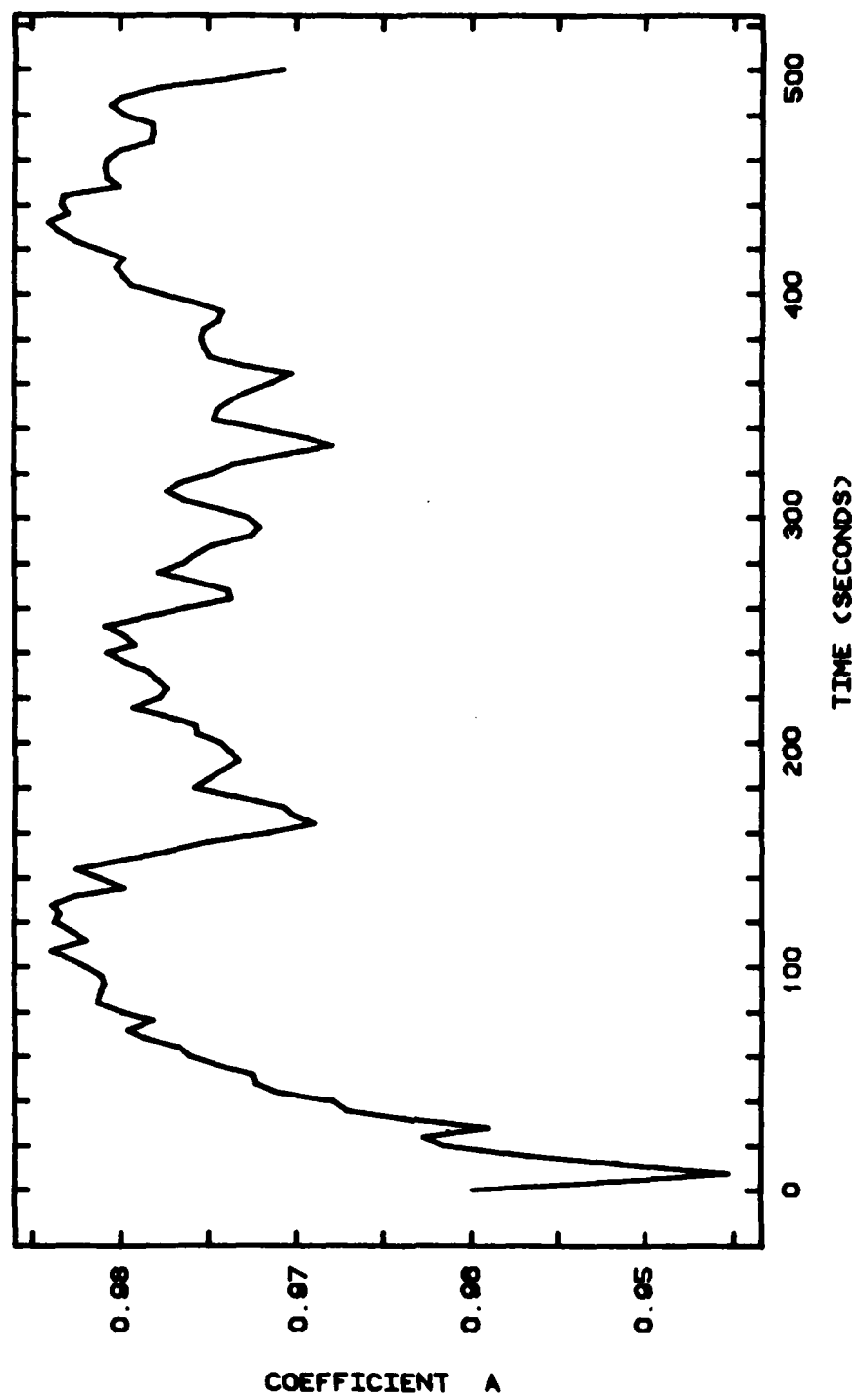


Figure 4.16. The coefficient A at the expansion rate of -0.0414 kPa/s or $-2^{\circ}\text{C}/\text{min}$.

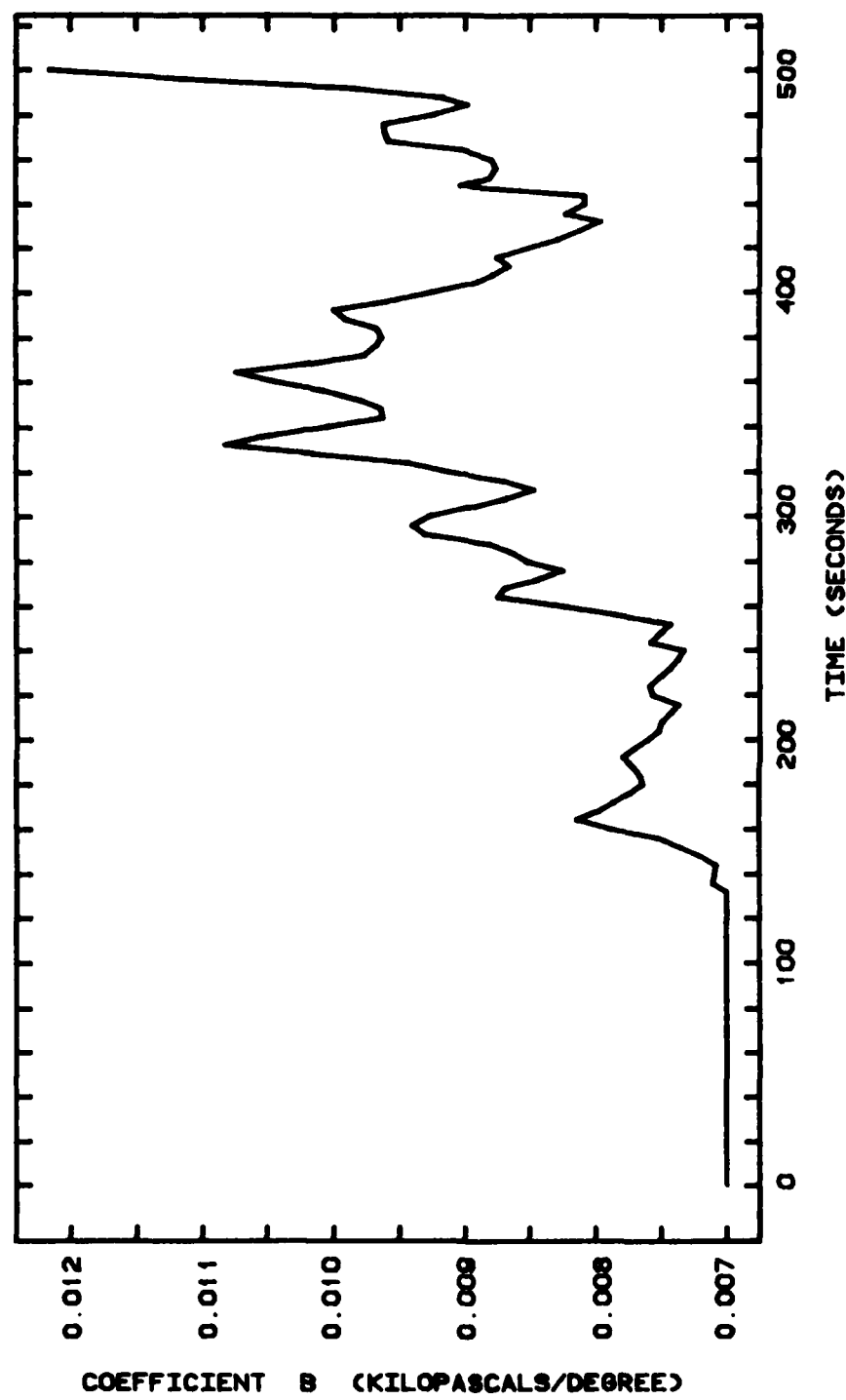


Figure 4.17. The coefficient B at the expansion rate of -0.0414 kPa/s or $-2^{\circ}\text{C}/\text{min}$.

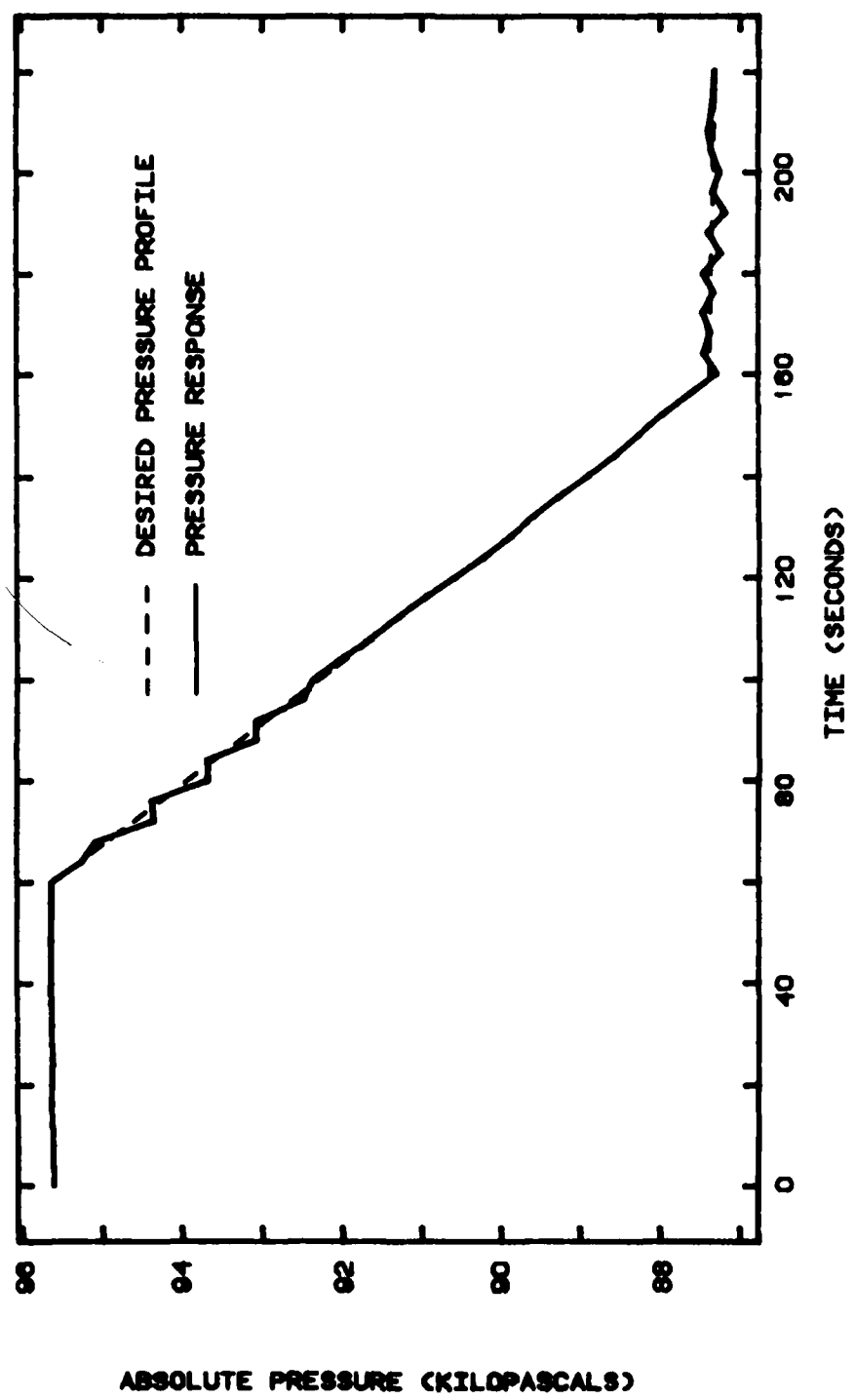


Figure 4.18. The pressure response including the holding modes.

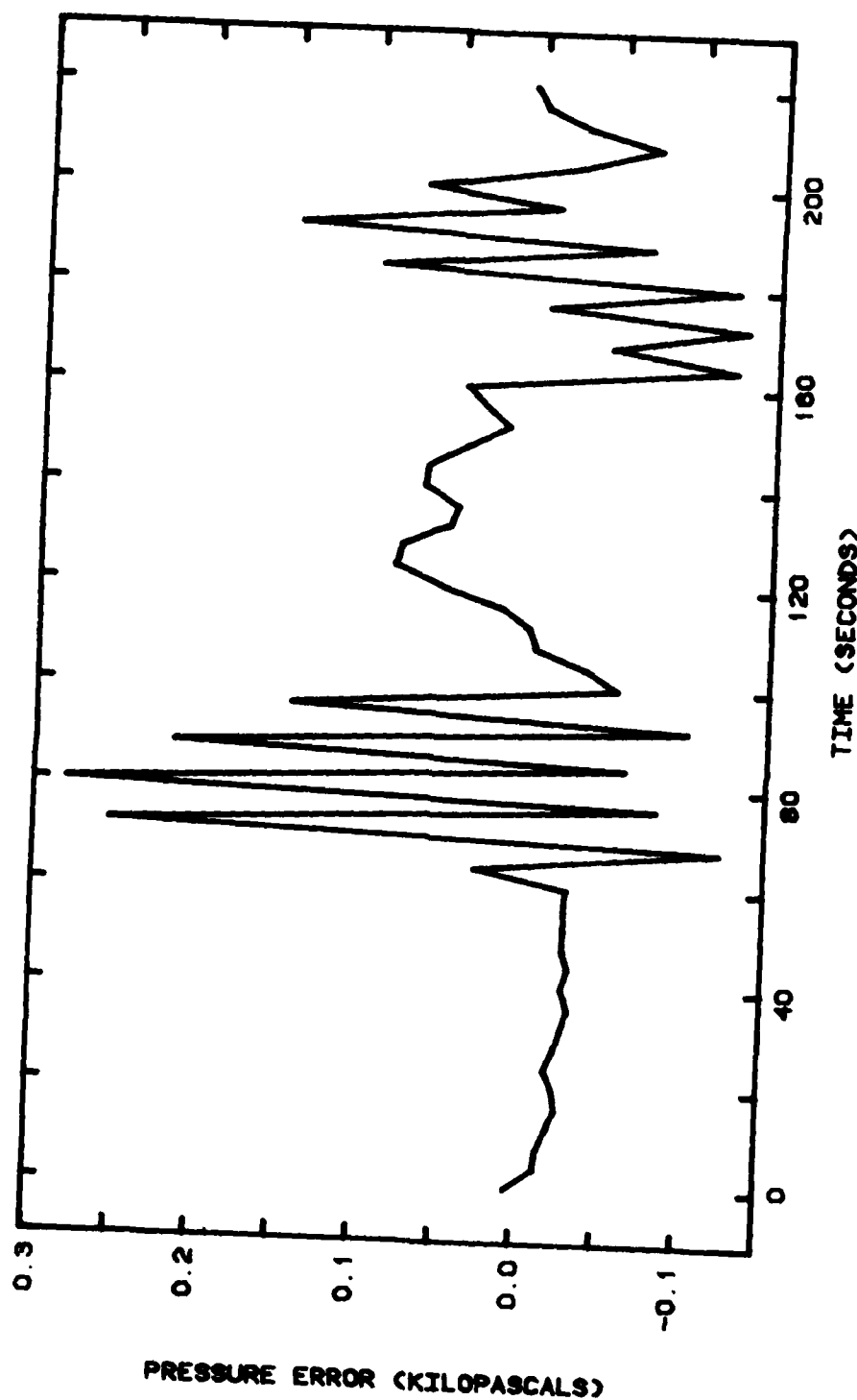


Figure 4.19. The pressure error including the holding modes.

holding time is 60 seconds. The result shows that the pressure response settles down within 60 seconds after the desired pressure profile changes slope.

V. CONCLUSION

The expansion system can be approximated by a first order quasi-linear model whose coefficients are A and B as shown in equation 3.5. A time-optimal control scheme using table look-up for the values of A and B was attempted. The attempt failed due to the fact that the range of validity of each table was very small. Thus, many tables were required and too much core memory was needed to store the tables on-line. Adaptive control using a sequential regression identification scheme eliminates the use of tables completely. But it still produces high rms error because the coefficients A and B belong to a system of the third type discussed in Section 3.D. The low pass digital filter and the constraint on the parameters ("flyability" [38]) introduced into the identification can reduce the rms error of the expansion system significantly. The closed-loop system is found to be stable and the parameters converge even though the initial values are off by 50%.

Based upon the experimental results, the following conclusions are reached:

1. The adaptive controller is capable of recovery from highly erroneous parameter estimates.
2. Control can be satisfactory even in the presence of parameter offset introduced by the low pass digital filter.

3. In view of computational requirements, the adaptive controller based upon the time-optimal control theory is implementable by the laboratory minicomputer, a NOVA 840.
4. Extension of the theories of linear systems to non-linear situations is quite successful in this case.
5. Use of a high level language, FORTRAN, again shows significant reduction of programming effort at the expense of small increases in computing time and memory.

This controller still has limitations. For example, it can control an expansion at the rate of -0.1242 kPa/s (-0.018 psi/s) or $-6^{\circ}\text{C}/\text{min}$ for only 18.6 kPa (2.7 psi) change in pressure because of limited pumping capacity. This problem can be eliminated by using a higher pumping capacity when the high rates of expansion are to be simulated.

The digital control of the expansion system described in this dissertation is presently in use with satisfactory results. Together with the wall temperature controller, the chamber is now operational over a much larger range of temperature and pressure change than before. Currently, about 15°C change in temperature and 20.7 kPa (3psi) change in pressure can be controlled. This is about 10 times the range of operation of the analog controller

built by Tebelak [21]. The relative accuracy of the expansion controller, which is about 0.1% with respect to the total change of pressure, is slightly better than the relative accuracy, 0.13%, obtained from Tebelak's controller. The maximum rate of expansion is also increased to -0.1242 kPa/s (-0.018 psi/s) compared to -0.0104 kPa/s (-0.0015 psi/s) for Tebelak's controller.

It is also true that the adaptive controller exhibits an advantage over other control systems due to the fact that whenever a piece of hardware of the expansion system is updated, there will be either no change or a minor change in the software that controls that piece of hardware. In addition, the computer time required is only 8% of the total available time. This is a significant benefit, because the computation for the control does not load the computer. The computer time can be reduced to about 2% of time available by eliminating the minor loop for position control of the valve. This could be accomplished if a digital valve were used in place of the 3-way rotary valve.

The significant improvements in the quality of control mentioned above can not be accomplished without the implementation of the optimal control law and the use of the computer as an intelligent controller. It is hoped that this dissertation will serve as a reference for further development of the control systems of the cloud simulation chamber.

BIBLIOGRAPHY

1. Batten, Louis J., Cloud Physics and Cloud Seeding, 1st Ed., Anchor Books, New York, 1962.
2. Volkovitskii, O. A., Cloud Physics Experimental Investigations, Keter Publishing House Jerusalem Ltd., Jerusalem, 1974.
3. Perrie, D. W., Cloud Physics, John Wiley & Son, New York, 1950.
4. Kassner, J. L., Jr., J. C. Carstens, M. A. Victti, A. H. Bierman, Paul C. P. Yue, L. B. Allen, M. R. Eastburn, D. D. Hoffman, H. A. Noble, and D. L. Packwood, "Expansion Cloud Chamber Technique for Absolute Aitken Nuclei Counting", Rolla: The University Press, 1967.
5. Aitken, J., Collected Scientific Papers of John Aitken, Cambridge Univ. Press, 1923
6. Report to McDonnell Douglas Astronautics Co., "Cloud Simulation Program", Graduate Center for Cloud Physics Research, University of Missouri-Rolla, Missouri, July, 1974.
7. White, D. R., D. E. Hagen, J. L. Kassner, Jr., D. R. Fannin, Paul Kriegshauser, and Alfred R. Hopkins, "A Thermoelectric Cooled Expansion Cloud Chamber", 2nd International Conference on Thermoelectric Energy Conversion, Arlington, Texas, March 22-24, 1978.

8. Hagen, Donald E., George M. Hale, and James M. Carter, "Laser Doppler Method for Cloud Droplet Size Spectrum" Graduate Center for Cloud Physics Research, Univ. of Missouri-Rolla, Missouri.
9. Kuo, B. C., Discrete-Data Control System, Science Tech, Champaign, Illinois, 1974.
10. Anderson, Brian D. O., and John B. Moore, Linear Optimal Control, 1st Edition, Prentice-Hall, N.J., 1971.
11. Report NAS8-31849-0003, Cloud Physics Laboratory Science Simulator, Third Quarterly Progress Report, Oct. 30, 1976 to Jan. 29, 1977, University of Missouri-Rolla, Missouri.
12. Podzimek, J., Fysike Oblaku (Cloud Physics), NCSAV, Praha, 1959, pp. 248.
13. Wilson, J. G., The Principles of Cloud-Chamber Techniques, Cambridge University Press, 1951.
14. Gunn, R., "The Electrification of Clouds and Rain-drops", Atmosphere Explorations, H. G. Houghton, Editor (The Technology Press of M.I.T. and John Wiley, New York, 1958).
15. Podzimek, J., "A Study of the Formation of Ice Crystals in Low Pressure Chamber", Trans. Inst., Geophysics Techn. Acad. Sci, No. 213, Geofysikalni Sbornik, 1964.

16. Volkovitskii, O. A., "A Complex of Experimental Installations for Geophysical Investigations", Meteorologiya i gidrologiya, No. 6 (in Russian), 1955.
17. Edwards, G. R. and L. F. Evans, "Ice Nucleation by Silver Iodide: II Collision Efficiency in Natural Clouds", J. Metcor., Dec, 1961.
18. Steele, R. L. and F. W. Smith, "Experimental Facility for Simulation of Adiabatic Cloud Processes", Proceedings, First National Conference on Weather Modification, Albany, New York, April 28 - May 1, 1968.
19. Oetting, R. B., J. L. Kassner, Jr., and T. L. Holeman, "Design and Development of a New Type Cloud Simulation Chamber", Paper presented at Meeting of American Geophysical Union, San Francisco, California, Dec 15-18, 1969.
20. Tebelak, A. C., "Design of an Analog-Temperature Control System for an Expansion Cloud Chamber", M.S. Thesis, University of Missouri-Rolla, Missouri 1973.
21. Hagen, D. E., A. C. Tebelak, and J. L. Kassner, Jr., "A Cloud Chamber Control System", Rev. Sci. Instrum., Vol. 45, No. 2, February 1974.
22. The Expansion Control System User's Manual, Graduate Center for Cloud Physics Research, University of Missouri-Rolla, Missouri, 1978.
23. Cutler, H., "Linear Velocity Ramp Speeds Stepper and Servo Positioning", Control Engineering, May, 1978.

24. The Expansion Control System Software Manual,
Graduate Center for Cloud Physics Research, University
of Missouri-Rolla, Missouri, 1978.
25. Takahashi, Yasundo, Michael J. Rabins, and
David M. Auslander, Control and Dynamic Systems, 2nd
E., Addison-Wesley Publishing Company, 1972.
26. Lee, T. H., G. E. Adams, and W. M. Gaines, Computer
Process Control Modeling and Optimization, John Wiley
& Son, New York, 1968.
27. Warner, D. E. and E. Dawson Ward, "Filter Sequential
Regression Parameter Identification Applied to a Gas
Turbine Engine Model", Journal of Dynamic Systems,
Measurement and Control, Trans. ASME, Series G,
Vol. 99, No. 4, December, 1977.
28. Salahi, Javad, "System Transfer Function Identifica-
tion by Gradient Techniques", M.S. Thesis, University
of Missouri-Rolla, Missouri, 1976.
29. Widnall, William S., "Applications of Optimal Control
Theory to Computer Controller Design", Research Mono-
graph No. 48, The M.I.T. Press, Cambridge,
Massachusetts, 1968.
30. Athens, Michael, Michael L. Dertouzos, Richard N.
Spann, and Samuel J. Mason, Systems, Networks, and
Computation: Multivariable Methods, McGraw-Hill, 1974.
31. Mini-issue on NASA's Advanced Control Law Program for
the F-8 DFBW Aircraft, IEEE Trans. Auto. Control,
Vol. AC-22, No. 5, October, 1977.

32. Rault, A., J. Richalet, A. Barbot, and J. P. Sergenton, "Identification and Modelling of a Jet Engine", IFAC Symposium on Digital Simulation of Continuous Processes, Györ, Hungary, 1971
33. Kohr, R. H., "On the Identification of Linear and Non-Linear Systems", Simulation, March, 1967.
34. Ward, E. D., "Identification of Parameters in Non-linear Boundary Conditions of Distributed Systems with Linear Fields", Journal of Dynamic Systems, Measurement and Control, Trans. ASME, Series G, Vol. 95, No. 4, December 1973.
35. Ward, E. D., and R. G. Leonard, "Automatic Parameter Identification Applied to Railroad Car Dynamic Draft Gear Model", Journal of Dynamic Systems, Measurement and Control, Trans. ASME, Series G, Vol. 96, No. 4, December, 1974.
36. Weinberg, M. S., and G. R. Adama, "Low Order Linearized Model of Turbine Engines", Report Number ASK-TR-75-24, Air Force Systems Command-Aeronautical Systems Division, Wright-Patterson Air Force Base, Ohio, July, 1975.
37. System Reference Manual, "Fortran IV User's Manual, 093-000053-06", Sixth Revision, Data General Corporation, 1973.
38. Cicolani, L. S., and George Meyer, "Digital Simulation of V/STOL Aircraft for Autopilot Research", Large Scale Dynamic Systems, NASA SP-371, 1975.

VITA

Katiya Greigarn was born on June 10, 1952, in Samutprakan, Thailand. He received his elementary education at various schools in Bangkok, and was graduated from Tram Udom Suksa High School in Bangkok, Thailand in March, 1969. He received his college education from Chulalongkorn University, Bangkok, where he received his Bachelor of Electrical Engineering degree in June, 1973. He enrolled in the Graduate School of the University of Missouri-Rolla in January 1974. He has worked as a graduate research assistant in the Cloud Physics Research Center since August 1975. He received his Master of Science Degree in Electrical Engineering at the University of Missouri-Rolla in July 1976.

He is a member of the Engineering Association of Thailand and the Institute of Electrical and Electronics Engineers in the United States. Currently, he is the president of the Thai Student Association of the University of Missouri-Rolla.

APPENDIX C
HUMIDIFIER CALCULATION
C. L. Lin

INTRODUCTION

Phase change processes generally lead to a mutual dependence of the rate of heat and mass transfer. For a parallel plate channel with wet plates, both of the plates will exchange heat and mass while the gas flows through the duct. Their mutual dependence must be given special consideration. The latent heat required by the evaporating vapor must be transferred to the plates by the surroundings either by gas stream or by other method. It is apparent that the rates of heat and mass transfer are mutually dependent and are influenced by the gas stream.

If the plate temperature can be kept uniform and constant by a method other than the heat transfer from the gas stream, the mutual dependence of heat and mass transfer diminishes. The gas will then become enriched with the evaporating vapor. The variation of the vapor content however is not known in advance, but rather is determined by the mass transfer analysis. At a sufficiently large downstream distance, a fully developed state will be attained where the vapor content will be uniform across the section.

The analysis of our present humidifier design will be based on the type of a parallel plate channel and on the concept of the mutual dependence of gas velocity and mass transfer, rather than heat and mass transfer.

The flow developing region of the gas stream in the entrance region of the duct usually carries away more evaporating vapor from the plate than that of the fully developed region of the gas stream. We may, therefore, be sure that the analysis of the humidifier design will be practical for a fully developed flow region in order to much simplify its analysis without any loss of accuracy.

Theoretical Analysis

The governing equation of the species conservation for the vapor may be written as follows:

$$u \frac{\partial c}{\partial x} = D \frac{\partial^2 c}{\partial y^2} \quad (1)$$

$$u = 1.5 \bar{u} \left(1 - \frac{y^2}{h^2}\right) \quad (2)$$

where c is the concentration of the vapor, D is the diffusivity of the mixture, \bar{u} is the average velocity of the air, and h is the haft distance of the separation of the channel.

The coordinates are selected so that x measures the axial distance along the duct from the entrance section, while y specifies the position in the cross section. The duct centerline coincides with $y = 0$, so that $-h \leq y \leq h$.

Before going into further analysis, assumptions are made: the variations of the mixture density, the mixture velocity, and the mixture diffusivity are extremely small between the duct inlet and exit.

Using the length, h , as the characteristic length, the non-dimensionalized variables of y , x , and c become:

$$\eta = \frac{y}{h} \quad (3a)$$

$$x^* = \frac{x/h}{R_e \cdot S_c} \quad (3b)$$

$$c^* = \frac{c - c_w}{c_{IN} - c_w} \quad (3c)$$

where c_{IN} is the initial concentration of the vapor in the entrance of the duct, c_w is the saturated vapor on the wall, $R_e = 1.5 \bar{u}h/\nu$, $S_c = \nu/D$, and ν is the kinematic viscosity of the air.

Introducing equation (e) into (1), the nondimensionized governing equation then becomes:

$$(1 - v^2) \frac{\partial c^*}{\partial x^*} = \frac{\partial^2 c^*}{\partial \eta^2} \quad (4)$$

with the following boundary conditions:

$$\frac{\partial c^*}{\partial \eta} = 0 \text{ at } \eta=0 \quad (5a)$$

$$c^* = 0 \text{ at } \eta=1 \quad (5b)$$

$$c^* = 1 \text{ at } X^*=0 \quad (5c)$$

The Poiseuille parabolic velocity profile (equation (2) has been used in equation (4).

Solution of the Governing Equation

Equation (4) can be solved analytically or numerically in our present report. Less effort has been needed in solving equation (4) analytically. We therefore try separable solution in the form:

$$c^*(X^*, \eta) = A e^{-\beta^2 X^*} \psi(\eta) \quad (6)$$

where

$$\psi'' + \beta^2(1-\eta^2)\psi = 0 \quad (7)$$

The boundary conditions of equation (7) require that

$$\psi' = 0 \text{ at } \eta=0 \quad (8a)$$

$$\psi = 0 \text{ at } \eta=1 \quad (8b)$$

It is clear that β in equation (7) plays the role of an eigenvalue. The successive eigenvalues, β , which satisfy the boundary conditions of equation (7) can be found by numerical integration of equation (7). The process of determining each β is one of systemized trial and error. For each trial value of β , equation (7) is integrated from $\eta=0$ to $\eta=1$ whereupon the (8b) is evaluated and compared with zero. The trial value of β is accepted as an eigenvalue when equation (8b) is satisfied to within a pre-assigned tolerance. The numerical integration was carried out by the Runge-Kutta method with a step size of $\Delta\eta=0.01$.

Assuming that the eigenvalues have been attained, the

solution for the nondimensionalized concentration, c^* , can be written as:

$$c^* = \sum_{n=1}^{\infty} A_n e^{-\beta_n^2 x^*} \psi_n(\eta) \quad (9)$$

with the constant, A_n , undetermined. The A_n can be obtained by imposing the entrance condition (5c) on equation (9):

$$1 = \sum_{n=1}^{\infty} A_n \psi_n(\eta) \quad (10)$$

A standard Sturm-Liouville type orthogonality will suffice to obtain the A_n as follows:

$$A_n = \frac{\int_0^1 (1-\eta^2) \psi_n(\eta) d\eta}{\int_0^1 (1-\eta^2) \psi_n^2(\eta) d\eta} \quad (11)$$

The integration in the righthand side of equation (11) may be performed by Simpson's rule.

Derivation of Bulk Concentration

Numerical values of the vapor concentration at any point in the flow can be found directly from equation (9). The bulk concentration, d_b , may be derived as follows:

$$c_b = \frac{\int_0^h u c dy}{\int_0^h u dy} = \int_0^1 \frac{u}{\bar{u}} dc \eta \quad (12)$$

from which it follows:

$$c_b^* = \frac{c_b - c_{IN}}{c_w - c_{IN}} = 1 + 1.5 \sum_{n=1}^{\infty} \frac{A_n \psi_n'(1)}{\beta_n^2} e^{-\beta_n^2 x^*} \quad (13)$$

Any entrance length can be evaluated according to the criterion set by equation (13) if the required factors are known.

Results and Discussion

The bulk concentration of the vapor is the most important factor in designing a humidifier. Results for the axial variations of the bulk concentration are plotted in Figure 1. The

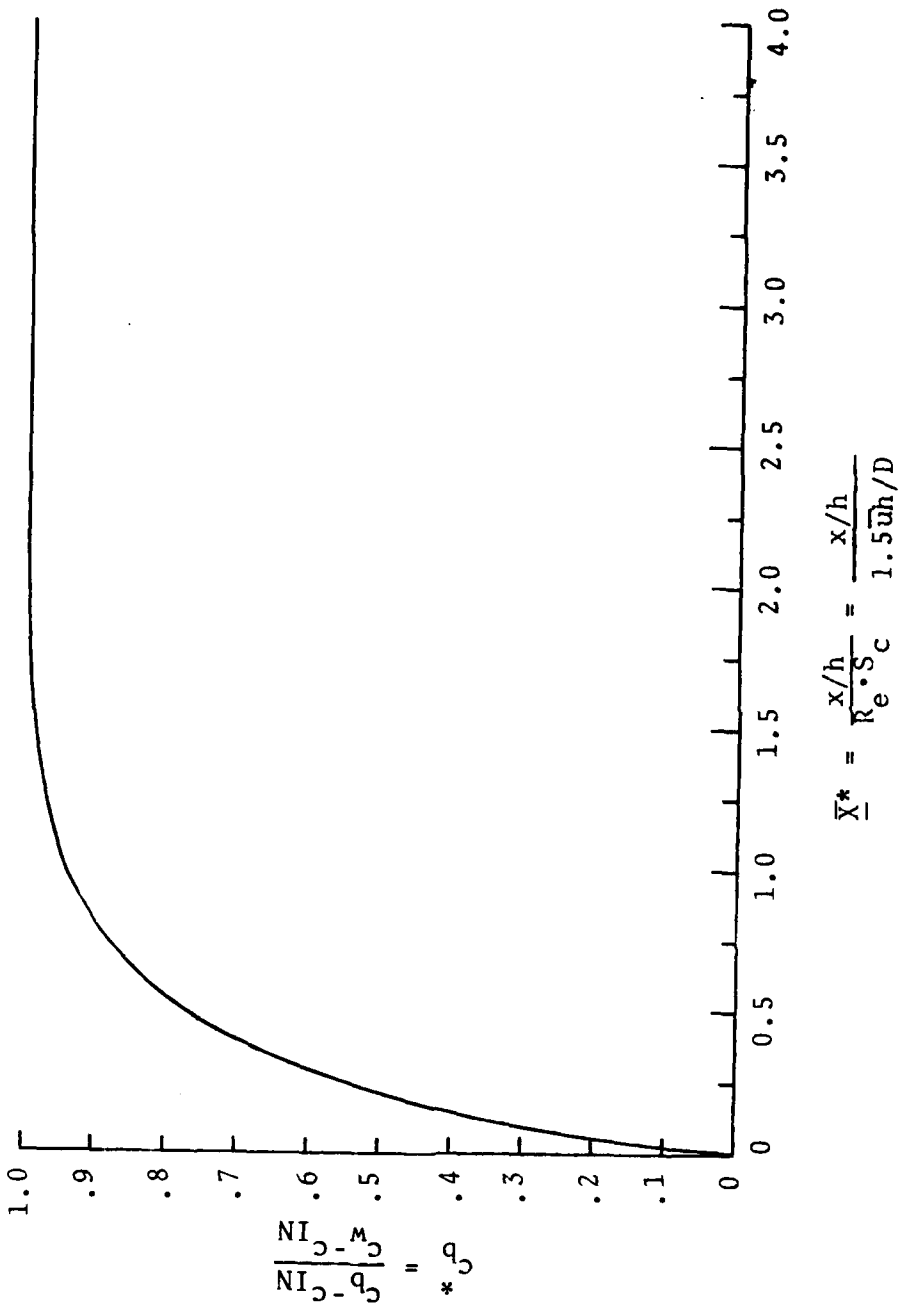
abscissa variable represents the nondimensionalized axial distance from the channel inlet while the nondimensionalized variable, c_b^* , on the ordinate. The curve increases rather rapidly at small values of x , but the rate of increase becomes slower at greater x .

In order to have a clear picture of calculation of c_b^* , we list A_n , β_n , and $\psi_n(1)$ on Table 1 such that desirable entrance length can be directly calculated with equation (13) to any criterion required. Or equation (13) can be rewritten as:

$$\begin{aligned} c_b^* = & 1 - 1.5 [0.6068862849 \exp(-2.82778696X^*) + 0.035427474 \exp \\ & (-32.14731129X^*) + 0.0101856657 \exp(-93.47496718X^*) + \\ & 0.0045391765 \exp(-186.8052306X^*) + 0.0024930768 \exp \\ & (-312.1465986X^*) + 0.0015483635 \exp(-469.4717593X^*) \\ & + \dots] \end{aligned} \quad (14)$$

Table 2 lists the relation between X^* and c_b^* for references.

If we assume that our configuration can be approximated by a set of parallel plate with a length of 72 inches and an interplate spacing of 0.375 inch, then a flow of 2 ℓ/p has an average velocity of 0.3 ft/s. The vapor diffusion constant is 2.376×10^{-4} ft²/sec. These values yield $x^* = 3.24$ for which $c_b^* = 0.9999$ or less than .05% from saturation.



6C

Figure 1

Table 1

	A_n	β_n	$\psi_n(1)$
n= 1	1.2008324	1.6816025	- 1.4291296
n= 2	- 0.29915899	5.6698599	3.8069992
n= 3	0.16082501	9.6682453	- 5.9201288
n= 4	- 0.10743695	13.667671	7.8924608
n= 5	0.079646051	17.667404	- 9.7707977
n= 6	- 0.062775254	21.667297	11.579610
n= 7	0.05151971	25.667297	- 13.333608
n= 8	- 0.043510258	29.667465	15.042241
n= 9	0.037543193	33.667801	- 16.712799
n=10	- 0.032933667	37.668381	18.349487

Table 2

x^*	c_b^*
0.01	0.0692812136
0.05	0.1989028385
0.1	0.3117611336
0.2	0.482807611
0.3	0.6112602185
0.4	0.7062609588
0.5	0.7786128316
0.7	0.8742424722
1.0	0.9461598441
1.5	0.9369065668
2.0	0.9968156996
3.0	0.9998116691
4.0	0.9999888615

APPENDIX D

VISIBLE TRANSMISSION SYSTEM - CLOUD SIMULATION CHAMBER

John L. Schmitt

December 2, 1976

The following describes the visible transmission system designed for and presently in the final stages of installation on the Graduate Center for Cloud Physics cloud simulation chamber. The initial design specifications were as follows: The system should give very accurate (up to 0.01% if possible) measurements of the transmission as a function of time in the optical path from one side of the simulation chamber to the other during the operation of the system. Attenuation is expected to be in the range 0 to 10%, therefore the system should perform best in this region. Also the system should be in addition to and not in place of the argon ion laser system now on the chamber (the laser system measures Mie scattering and doppler velocities of the drops in the chamber).

Initial experiments with the system yielded the following results: The argon ion laser could not be used as a light source because its light output is not constant to 0.01% with time. In particular, abrupt jumps in the intensity level of about 0.5% were seen in the output. It thus becomes necessary to introduce an extra beam into the chamber on top of the laser beam. This beam is used to measure the attenuation.

A search was begun for a suitable light source and suitable detector. We decided that a moderately intense red light emitting diode (LED) might be a very good choice. It is compact, has a long life, can be pulsed, and the actual light emitting area of the diode appeared to be a good approximation to a point source. A red diode was selected so that the system could be adjusted visually (as compared to an infrared LED). Also the red diode finally selected has a spectral output that avoids the many water vapor spectrum lines that are in the near infrared.

We decided upon silicon photodiodes as detectors. They are

small, linear, have the red sensitivity required to detect the red LED and can be obtained with an amplifier in the same package. Size of components is a consideration in the selection because the transmission system fits into an existing installation.

Using the selected components, a prototype system was constructed. The prototype sent a beam straight through the chamber. A regulated power supply was used to power the LED. One photodiode was used to detect changes in the LED output and another across the chamber to detect the changes in transmission. The outputs from the photodiodes were put into separate A to D converters on our NOVA computer. The computer calculated the ratio of one detector to the other to give a measure of the signal. The laser system could not be used simultaneously with the prototype.

The simulation chamber was run through two data expansions with the prototype on it. The data showed that the system would perform well. It also verified our initial expectations as to the level of attenuation we would experience.

A full scale system was then designed. This is shown schematically in Fig. 1D. The LED beam enters the optical system vertically. The first beamsplitter deflects the beam into an almost horizontal path (at 2° to the laser beam). After passing through the first laser wedge (4° apex angle prism that deflects a beam 2°) the beam traverses the chamber horizontally. A similar optical configuration on the receiver side returns the beam to a vertical path and into the detector. Specific details of the equipment are covered in the following paragraphs.

The light source is a light emitting diode manufactured by Fairchild. The Fairchild FLV - 104 red LED is able to conduct a continuous current of 100 ma and a peak pulsed current of 1 amp. We modified this diode. The clear epoxy lens were machined and polished flat. One then sees that the actual emitting region is of the order of 0.3 mm in diameter. Because of its brightness and its small emitting region, this diode with a 0.0135 inch (a number 80 machine drill) pinhole in front of it makes an

excellent point source (the pinhole is used to eliminate back-scatter from the epoxy matrix of the diode). This point of light is focused into a collimated beam by an achromatic lens. The beam diameter is 5/8 inch. This size is the maximum diameter beam that can be used and is set by the existing installation.

Two dielectric coated beamsplitters direct the beam across the chamber and extract it on the other side. These serve to direct the beam and to allow the laser beam to be used simultaneously. Their construction and availability is facilitated by the use of the red LED (670 nm with a 50 nm bandwidth) as one light source and the blue argon ion laser line (488 nm) for the other measurements. This wide separation in wavelength of the two sources means that the coatings on the beamsplitters need not have very rapid changes in their transmission and reflection curves with wavelength. This reduces the complexity of the coatings and their cost. At 45° the beamsplitters reflect more than 99% of the LED beam and transmit more than 85% of the laser beam. The high reflectivity for the LED beam prevents that beam from reaching the laser detection system. We have not seen an effect on the LED detection system due to the laser but if needed a filter similar to the type designed for laser protection goggles can be used for this purpose (a filter of this type will transmit about 85% of the red LED beam and about 1 part in 10^6 to 10^{15} of the laser beam). The beamsplitters are placed in mounts that allow 5 motions for adjustment. They are made from 1/2 inch schlieren grade fused quartz and are held by the spring action of the sides of the mounts. In practice the system has been reasonably easy to adjust visually in a darkened room.

Directly adjacent to the LED light source is a photodiode which receives the light scattered in the epoxy encapsulation surrounding the diode emitting region. This photodiode provides a signal for control of the light level of the LED. Its associated circuitry will be described below.

The receiver is a silicon photodiode. The transmitted light reaches it via the optical system sketched in Fig. 2D. The achromatic lens focuses the beam on a pinhole. The pinhole

eliminates off axis stray light. The diverging beam from the pinhole enters a second lens (Fabry lens) which collimates it. The collimated beam size is the same as the detector size (5 mm^2). The function of the Fabry lens is to not only collimate the light but to image the aperture of the system onto the detector to provide uniform illumination. The electronics that generate and detect the light beam are covered in the next paragraph.

The LED light source is controlled to give a constant output. Fig. 3D is a block diagram illustrating its operation. A 1 KHz (crystal) oscillator turns the LED off and on. The current into the LED is controlled to produce the constant light output. The control network uses a Bell and Howell model 529 photodiode with an amplifier in its TO - 5 case to monitor the 1 KHz (50% duty cycle) pulsed LED output. The signal from the model 529 is put through a 1 KHz bandpass filter to eliminate noise. It is then passed through a synchronous demodulator and a low pass filter. The DC output of these stages is compared to a very stable reference diode and the difference signal is used to control the current to the LED.

The receiver across the simulation chamber is a similar model 529 photodiode. It receives the 1 KHz light signal and the resulting output is processed as is indicated in the block diagram in Fig. 4D. The signal out of the 529 is first put into a bandpass filter. It is then turned into a DC signal by a precision rectifier and a low pass filter further eliminates noise. The DC signal is about 6 to 8 volts; this is a suitable level for the A to D converter associated with the NOVA control computer.

The transmission and detection schemes have been designed for low noise and high accuracy. In particular, they eliminate problems with background noise and DC offset. Tests indicate that the system does not "see" stray room light (flourescent lighting) or laser light. All components such as resistors and capacitors as well as the active components have been selected for temperature and time stability.

At present (3 Dec., 1976) the system is installed on the simulation chamber. However, the electronics are still on "breadboards". Simple stability tests, e.g. will the output into a digital voltmeter remain constant over a day, indicate an accuracy of 0.05% of full scale. Most of the error appears to be from the temperature sensitivity of the components. However, once they are placed in boxes and not exposed to the ambient air, the temperatures they experience will remain fairly constant.

In summary, the visual transmission system described above has achieved several goals. It has been installed on an existing system with little effect on the equipment already working. It is compact and the component cost is relatively low. Most important, its accuracy at this stage of testing appears to approach what had been hoped for.

Calibration by Polarizing Filters

A method of calibration has been developed that may be able to test the linearity of this transmission system in the accuracy range of 0.1 to 0.01%. Malus' Law relates the angle between a polarized beam and a following polarization filter to the intensity transmitted by the following filter, i.e., $I = I_0 \cos \theta$ where I_0 is the intensity in the polarized beam, I is the intensity transmitted by the filter and θ is the angle between the plane of polarization of the beam and that of the filter. This law allows one to calculate the change intensity as the angle, θ , changes. An elementary calculation shows that a change of θ from 0° to 20° produces a change in intensity of only 10%. Since the angle can be measured quite accurately it appears that small changes in angle can be used to produce very small changes in intensity. These small changes in intensity can then be used to measure the linearity of the photodetector.

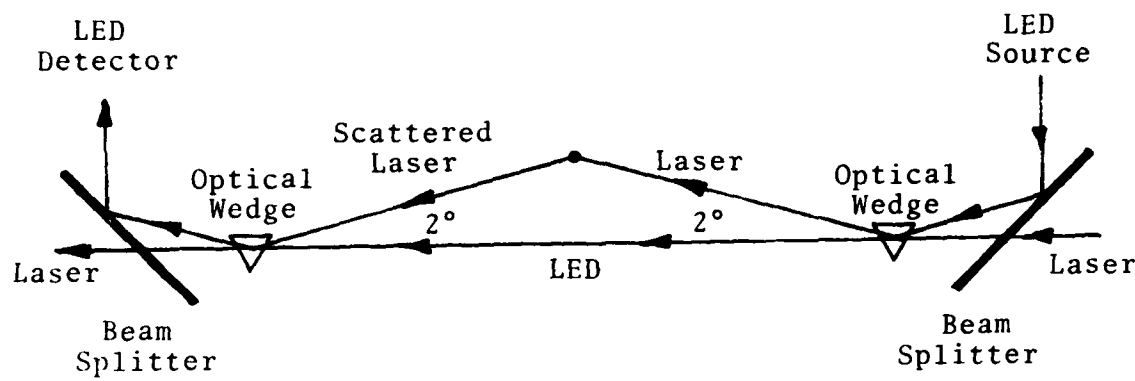


Figure 1D. Optical System

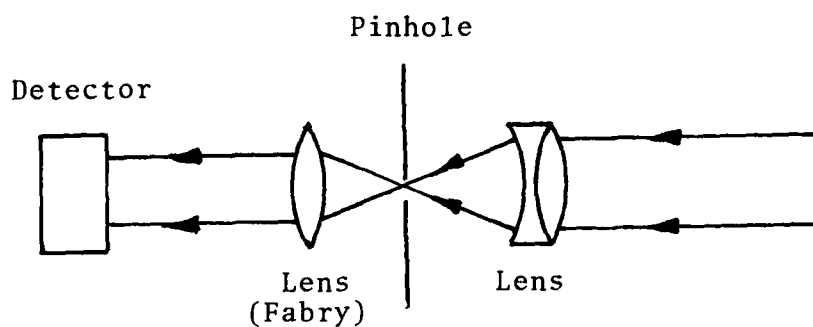


Figure 2D. Optical System Receiver

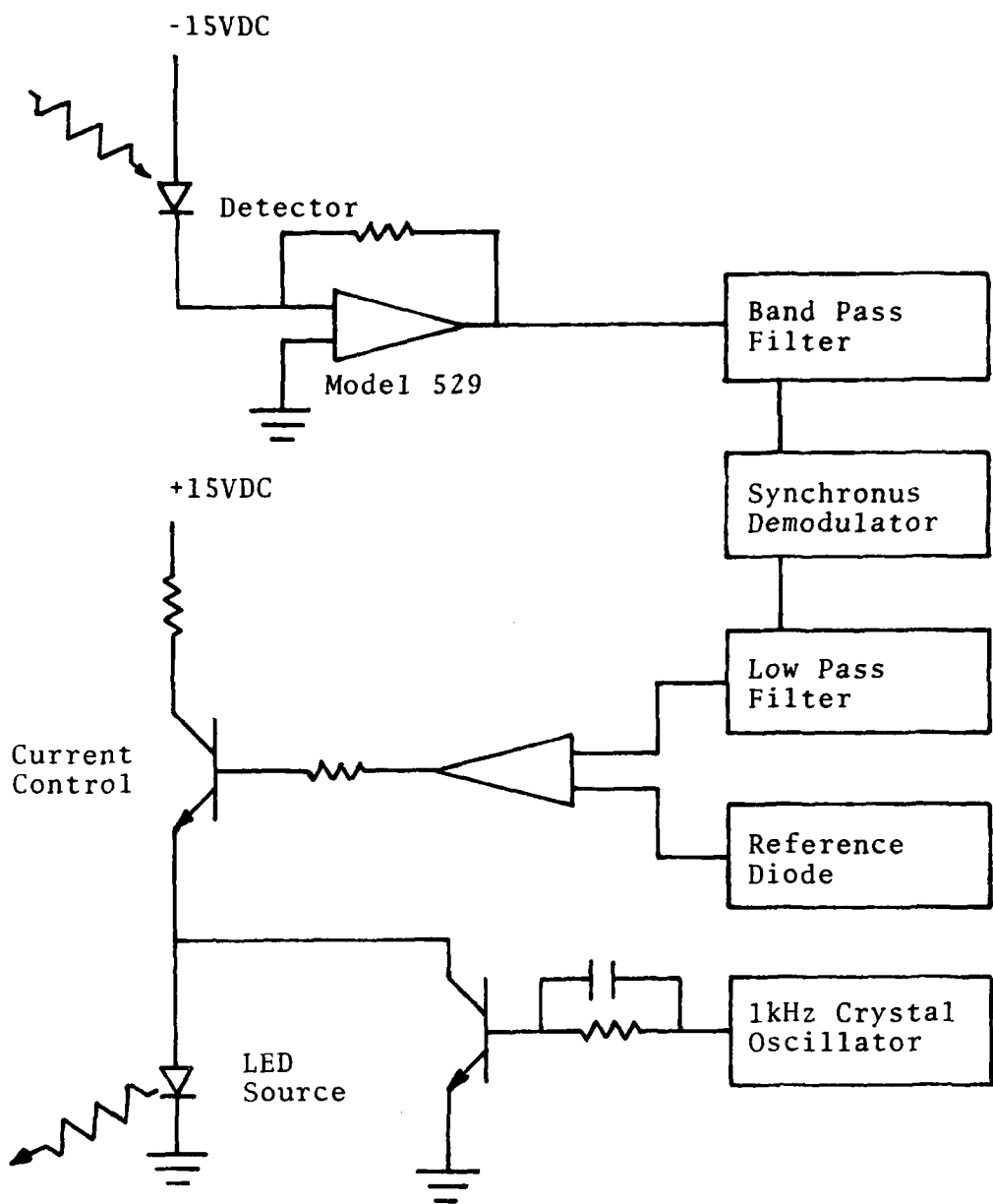


Figure 3D. Attenuation System Transmitter

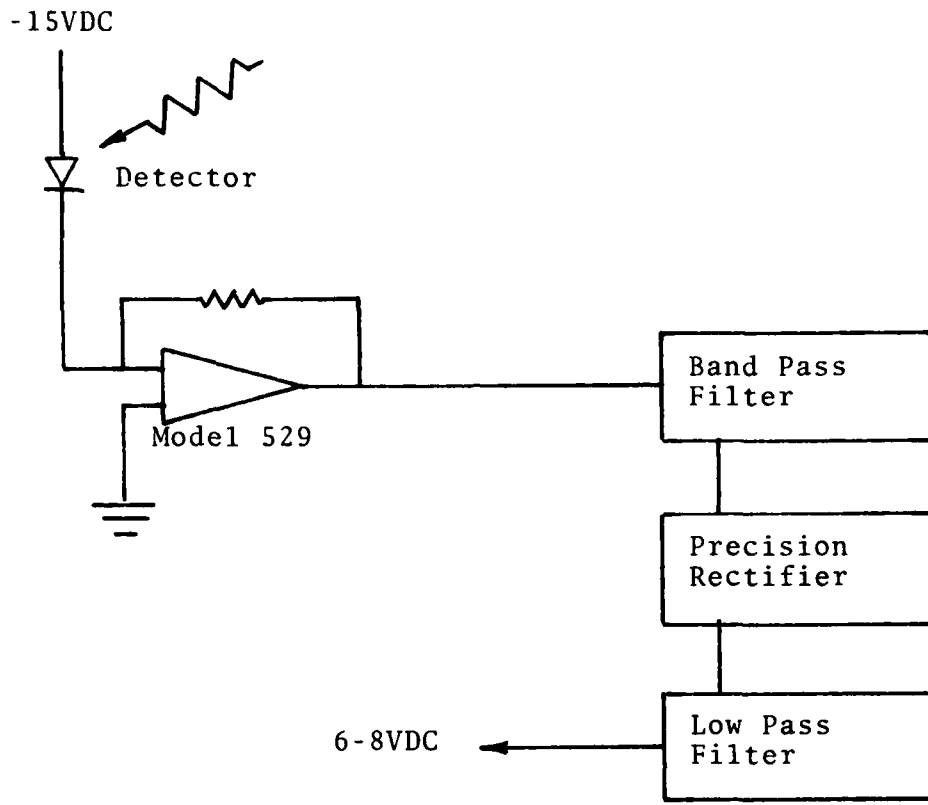


Figure 4D. Attenuation System Receiver

APPENDIX E

LASER DOPPLER METHOD FOR CLOUD DROPLET SIZE SPECTRUM

by

Donald E. Hagen, George M. Hale, and James Carter
Graduate Center for Cloud Physics Research
University of Missouri
Rolla, Missouri

I. INTRODUCTION. Cloud physics concerns itself with the characteristics of clouds and their influence on the energy balance and dynamics of the atmosphere. Man's recent progress in this field has been due in large part to his ability to bring atmospheric phenomena into the laboratory and observe them under precisely controlled conditions. One of the longest used and more important tools in the cloud physics laboratory has been the expansion cloud chamber^{1,2}. In this device a sample of moist air is cooled by expansion. The water vapor condenses to form a cloud which can then be studied.

A major limitation of expansion type cloud chambers concerns wall effects³. The expansion cools and supersaturates the gas, but the chamber walls, whose heat capacity is very high in comparison to the gas, remain at their initial temperature. Hence, a thermal gradient is created at the walls and causes the diffusion of heat into the gas. This heat soon destroys the adiabaticity of the gas and eventually leads to substantial errors in one's knowledge of the thermodynamic parameters of the gas which is necessary for a meaningful experiment.

A new cloud simulation chamber having a slow expansion capability has been constructed at the University of Missouri-Rolla. The design and construction of the cloud simulation

chamber and its supporting subsystems has been a substantial project, the scope of which is indicated in Fig. 1. Subsystems are required to clean and humidify the sample gas and prepare an aerosol to provide nucleation sites for the cloud. The control chamber allows for extensive analysis of the sample gas at its initial condition during the time the cloud is being formed in the simulation chamber. The entire system is carefully temperature controlled.

Our new cloud simulation chamber has a very unique feature which effectively moves the walls of the chamber to infinity and hence removes the above wall effects. This is accomplished by cooling the chamber walls in exactly the same manner in which the gas is cooled by the expansion. Thus the gas and the walls are maintained at the same temperature at all times during the expansion. This prevents a thermal gradient at the walls and insures an adiabatic process. The wall cooling is accomplished by thermoelectric modules placed between the chamber walls and an external heat sink. Because the chamber walls have a relatively high heat capacity and a substantial time lag to control signals, the walls are actually cooled according to a pre-determined schedule. A closed loop control system monitors the gas and wall temperatures and causes the expansion to proceed along a path such that the gas and wall temperatures are always equal. The maintenance of the cloud's adiabaticity permits a much wider class of experiments to be undertaken, particularly those involving the slower atmospheric processes.

One necessary ingredient for a successful cloud chamber experiment is a measurement of the cloud drop size spectrum, i.e., the number of drops of a given size vs. size. This is the function of the laser Doppler system. This size spectrum data is needed for two reasons. First of all, it is an experimental result. One reason for doing the experiment is to see what kind of cloud forms when a given sample of aerosol-laden moist air is subjected to a controlled set of thermodynamic conditions. Theoretical models⁴⁻⁶ for drop growth can be used to calculate theoretical size spectra which can then be compared to experimentally determined spectra to test the accuracy of the model and help lead the way to improvements in the model. This is one of the general objectives of cloud physics.

A second and equally important motive for the measurement of the cloud drop size spectra is that it is an important factor in the expansion control loop of the chamber. Again, an important feature of this chamber is that the pace of the expansion is to be adjusted to keep the gas temperature equal to the wall temperature throughout the expansion. Clearly the gas and wall temperatures must be measured precisely in order to accomplish this control. The wall temperature is relatively easy to measure. A transistor imbedded in the wall produces a voltage proportional to its temperature. Unfortunately, the gas temperature cannot be measured directly. We must measure the gas pressure and the gas mixing ratio, a function of the cloud drop size spectrum, and calculate the temperature as a function of these parameters through the first law of thermodynamics.

Since this is a part of a closed control loop it is a real time task.

II. SIZE SPECTRUM MEASUREMENT METHOD. The method used to determine the cloud drop size spectrum is based on laser Doppler velocimetry⁷. The drop's size determines its gravitational fall velocity and this determines the Doppler frequency shift of light scattered by the drop.

We first consider the case where only one drop, of radius r , is present in the light scattering volume. The drop will fall in the earth's gravitational field at a terminal velocity given by Stoke's law

$$v = 2(\rho - \rho_a)gr^2/9\eta \quad (1)$$

where ρ is the density of liquid water, ρ_a is the density of air, g is the acceleration due to gravity, and η is the coefficient of viscosity for air. Doppler shifted light scattered off the falling drop is collected by light receiving optics, mixed with unshifted light from the original laser beam (acting as a local oscillator), and finally is converted to an electrical signal by an optical detector. The a.c. component of the detector's current contains the Doppler frequency information.

Efficient use of the optical detector in the heterodyning detection scheme requires the photocurrent i_{LO} produced by the local oscillator to be much greater than that produced by the cloud. Under this condition the low-frequency power spectrum of the detector can be expressed as⁷

$$P(\omega, r) = ei_{LO}/\pi + i_{LO}^2 \delta(\omega) + i_{LO} < i_s(r) > \delta(\omega - \bar{k} \cdot \bar{v}). \quad (2)$$

δ denotes the Dirac delta function and e is the electron charge. The first term is the frequency independent shot noise. This term, being constant, poses no limitation in principle to the precision with which the signal term is measured. We assume that it has been subtracted out. The second term is the d.c. component and is normally filtered out. The last term contains the wanted signal. $\langle i_s(r) \rangle$ is the average photocurrent produced by the drop of radius r in the absence of the reference beam. In a square law detector $\langle i_s(r) \rangle$ is proportional to the energy flux scattered at a fixed angle by a drop of radius r and can be calculated except for an overall calibration constant from Mie scattering theory⁸. The total scattered intensity appears at a single frequency, Doppler shifted from the original frequency by $\bar{k} \cdot \bar{v}$. \bar{k} is given by $\bar{k} = \bar{k}_S - \bar{k}_0$, where \bar{k}_0 and \bar{k}_S are the wave vectors of the incident and scattered light respectively. For cloud drops smaller than $2\mu\text{m}$ the particle's Brownian motion is significant in comparison to its gravitational fall velocity and Eq. (2) must be modified to account for the resulting line width broadening. In this work we consider drops of radius larger than $2\mu\text{m}$ and we neglect the Brownian motion broadening.

Fig. 3 shows the light scattering geometry. For this geometry, the Doppler frequency shift becomes

$$\bar{k} \cdot \bar{v} = 2kv \sin \frac{1}{2}\theta$$

where θ is the scattering angle. Using Eq. (1) the Doppler shift can be written

$$\bar{k} \cdot \bar{v} = Cr^2$$

with $C = (4kg/9n)(\rho - \rho_a) \sin \frac{1}{2}\theta$.

Now suppose that the scattering volume contains many particles with a size distribution $N(r)$. Then the total power spectrum becomes the integral of contributions from all particle sizes

$$P(\omega) = i_{LO} \int_0^{\infty} dr < i_s(r) > \delta(\omega - Cr^2) N(r). \quad (3)$$

The delta function can be expressed as a function of r

$$\delta(\omega - Cr^2) = (2Cr)^{-1} \delta(r - r_{\omega})$$

where $r_{\omega} = (\omega/C)^{1/2}$ is the drop radius for which the corresponding Doppler shift is ω . With this, the integral in Eq. (3) can be evaluated and the power spectrum becomes

$$P(\omega) = (2C)^{-1} i_{LO} < i_s(r_{\omega}) > N(r_{\omega}) r_{\omega}^{-1}.$$

In the experiment $P(\omega)$ is the quantity measured and $N(r_{\omega})$ is the desired result so this is rewritten as

$$N(r_{\omega}) \propto r_{\omega} P(\omega) / i_{LO} < i_s(r_{\omega}) >. \quad (4)$$

The overall calibration constant is evaluated by measurements made on cloud drops resulting from an aerosol of known size and density.

Fig. 5 indicates the analog hardware used to bring the Doppler signal to the digital computer system. The computer's A/D sees the time dependent signal from the optical detector. The procedure used to generate a measurement of the drop size spectrum is as follows. The A/D samples its input signal at a known, high speed sampling rate for a certain length of time. This results in a table of data: signal amplitude as a function of time. The table of data is Fourier transformed to yield

signal power, $P(\omega)$, as a function of frequency. The transform is accomplished in real time by using a digital fast Fourier transform based on the Cooley-Tukey algorithm⁹. The response of the photo-detector to the incident light is a statistical process. In order to accomplish good statistical averaging it is necessary to take many sets of Doppler laser data, Fourier transform each one, and average the resulting power spectra. This averaging must be done for a single measurement of the drop size spectrum. The number of data sets included in the average is limited both by the rate at which the drop spectrum is changing and by the amount of computer time which can be devoted to this phase of the whole real time control loop. Once the average power spectrum, $P(\omega)$, is evaluated the drop size spectrum is calculated through Eq. (4). The mixing ratio for the cloud chamber gas can be evaluated from this information.

III. LASER OPTICAL HETERODYNE SYSTEM (LOHS). An etalon-selected 488nm (blue) line from a water-cooled argon-ion laser (Spectra Physics Model 165) passes through a spatial filter and telescope assembly to transform the beam diameter to $\sim 12.5\text{mm}$. This expanded beam follows an interferometer path represented in Fig. 4. Immediately in front of the entrance window to the cloud chamber and following its exit window are identical optical wedges W1 and W2. Light propagating along a direction perpendicular to the flat surface of the wedge is refracted through an angle of 2° . The optical path lengths in the two branches of the interferometer are not equal, but the extended coherence length of the laser

radiation renders this factor unimportant. When light in the chamber branch is Doppler frequency shifted, heterodyning occurs on recombination at BS3 and the difference frequency is observed with an electro-optical detector to which the mixed radiation is directed by mirror M4. A double pinhole arrangement (P1 and P2) defines a cone of acceptance angle viewed by the detector and the intersection of this observation cone (vertex angle 0.392°) with the laser beam inside the cloud chamber defines a scattering volume of $\sim 5\text{cm}^3$ and a scattering angle of $\sim 4^{\circ}$. Mirrors M1 and M4 were necessitated by laboratory space confinements.

With the exception of the chamber windows and wedges, which are mounted to the chamber, the optical system rests on and is enclosed by aluminum framework that is in turn attached to a support frame made of 8" iron pipe filled with sand. This frame is mounted on four vibration isolation legs (NRC Series M-4-A).

The laser is cooled by a closed circuit water circulation system. A small turbine pumps distilled water from a reservoir to the laser through a surge tank and heat exchanger network. A small part of the flow is diverted around the laser through back-to-back ion exchangers. The heat exchanger is cooled by tap water with a high mineral content that necessitated the closed circuit design.

The detector is an ITT FW130 photomultiplier tube (PMT) enclosed in an RF shielded chamber. Its preamplifier output branches into three lines (Fig. 5). One is connected to an A/D channel through which the NOVA can sample the signal and display its average d.c. level. A second line passes to a d.c. block

and thence through an amplifier to another A/D channel. This is the a.c. signal that is processed to provide Doppler shift information. For this channel, the A/D is preceded by a low-pass anti-aliasing filter to remove all frequency components higher than one-half the A/D sampling frequency. A third line is filtered to remove frequencies higher than ~ 1 hz. The remaining slow variations contain the 4^0 Mie scattering fluctuations caused by cloud droplet growth (i.e., Fig. 2). This signal is recorded on a light-beam oscilloscope but is not particularly meaningful unless the cloud droplets have a fairly uniform size.

IV. NOISE CONSIDERATIONS. For our purposes, noise is defined as any recorded voltage fluctuation having frequency less than about 4300 hz that is not due to either Doppler shifts or Mie scattering fluctuations originating in the scattering volume. There are a number of noise sources in the range of interest, but the direct causes may be narrowed to (1) the laser, (2) the interferometric nature of the optical system, (3) neutral density filters, (4) the detector, and (5) system electronics. The latter two present common problems and are not discussed below.

Laser amplitude fluctuations revealed some unexpected problems. One of these was mechanical vibration transmitted to the laser through its cooling water and by audio noise in the lab. Both factors were reduced by replacing a roller pump with a turbine pump for coolant circulation. Another problem was traced to the light-control mode switch on the laser power supply. When used at a laser output of 50 mW, the light-control mode

AD-A102 679

MISSOURI UNIV-ROLLA GRADUATE CENTER FOR CLOUD PHYSICS--ETC F/6 4/2
MARINE FOG STUDIES - FOG SIMULATION PROGRAM. (U)

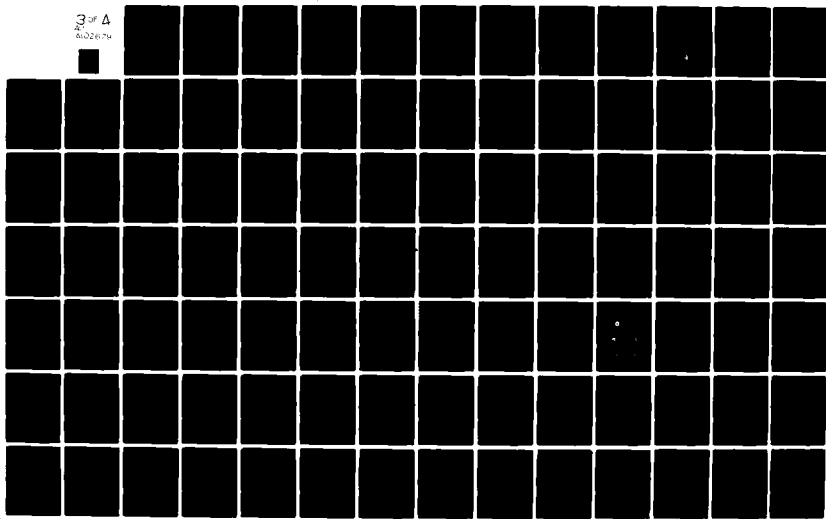
JUN 81 D R WHITE

N60014-75-C-0182

ML

UNCLASSIFIED

3 of 4
402674



introduced a 360 hz frequency peak. Increasing the laser output eliminated this peak. However, an order-of-magnitude increase to ~1 watt caused increased amplitude instability resulting in a general deterioration of the frequency spectrum.

A change in optical path length in either branch of the interferometer can cause fringes to move across pinhole P1. For example, vertical motions of the support table change its alignment with respect to the optical wedges, causing observable signal fluctuations.

A stack of Kodak Wratten neutral density filters was used to attenuate the reference beam during preliminary LOHS tests. However, exposure to continuous power densities on the order of 30 mW/cm^2 caused the transmission of these absorbent filters to fluctuate and decrease with time. The stack was replaced with a high reflectance argon-ion green line transmission filter that acted as a stable 10^{-4} attenuator for the blue line.

V. PERFORMANCE. Checks on the LOHS operation have been made utilizing a scattering disk made of mylar tracing film attached to a wire frame rotated by a 1 rpm clock motor. Light scattering sites on the rotating disk simulate falling cloud droplets. Typical Fourier transformed output is shown in Fig. 6.

The potential of the optical heterodyne technique for quantitative studies of cloud droplet size distributions was established by Gollub¹¹ using a diffusion cloud chamber. The prime irritant to satisfactory performance of the technique for obtaining droplet size distribution is thermal convection, which can overwhelm the gravitational fall velocity on which our method

relies. At the time of this writing a convection-free cloud has not been obtained in the expansion cloud simulation chamber.

REFERENCES

1. C. T. R. Wilson, "Condensation of Water Vapor in the Presence of Dust-Free Air and Other Gases," Phil. Trans. Roy. Soc. London A189, 265 (1897).
2. J. Aitken, "Collected Scientific Papers of John Aitken," Cambridge University Press, (1923).
3. J. L. Kassner, Jr., J. C. Carstens, and L. B. Allen, "Analysis of the Heat and Vapor Propagation from the Walls of the Nolan, Pollak, and Gardner Type Condensation Nucleus Counters," J. Atmos. Sci. 25, 919 (1968).
4. W. E. Howell, "The Growth of Cloud Drops in Uniformly Cooled Air," J. Meteorol. 6, 134 (1949).
5. W. Mordy, "Computations of the Growth by Condensation of a Population of Cloud Droplets," Tellus 11, 16 (1959).
6. J. C. Carstens and J. T. Zung, "Theory of Droplet Growth in Clouds," J. Colloid & Interface Sci. 33, 299 (1970).
7. H. Z. Cummins and H. L. Swinney, in Progress in Optics (American Elsevier, New York, 1970), Vol. 8.
8. M. Kerker, The Scattering of Light and Other Electromagnetic Radiation (Academic Press, New York, 1969).
9. J. W. Cooley and J. W. Tukey, "An Algorithm for the Machine Calculation of Complex Fourier Series," Mathematics of Computers 19, 297 (1965).
10. J. Gollub, "Optical Heterodyne Measurement of Cloud Droplet Size Distributions," Applied Optics 12, 2838 (1973).

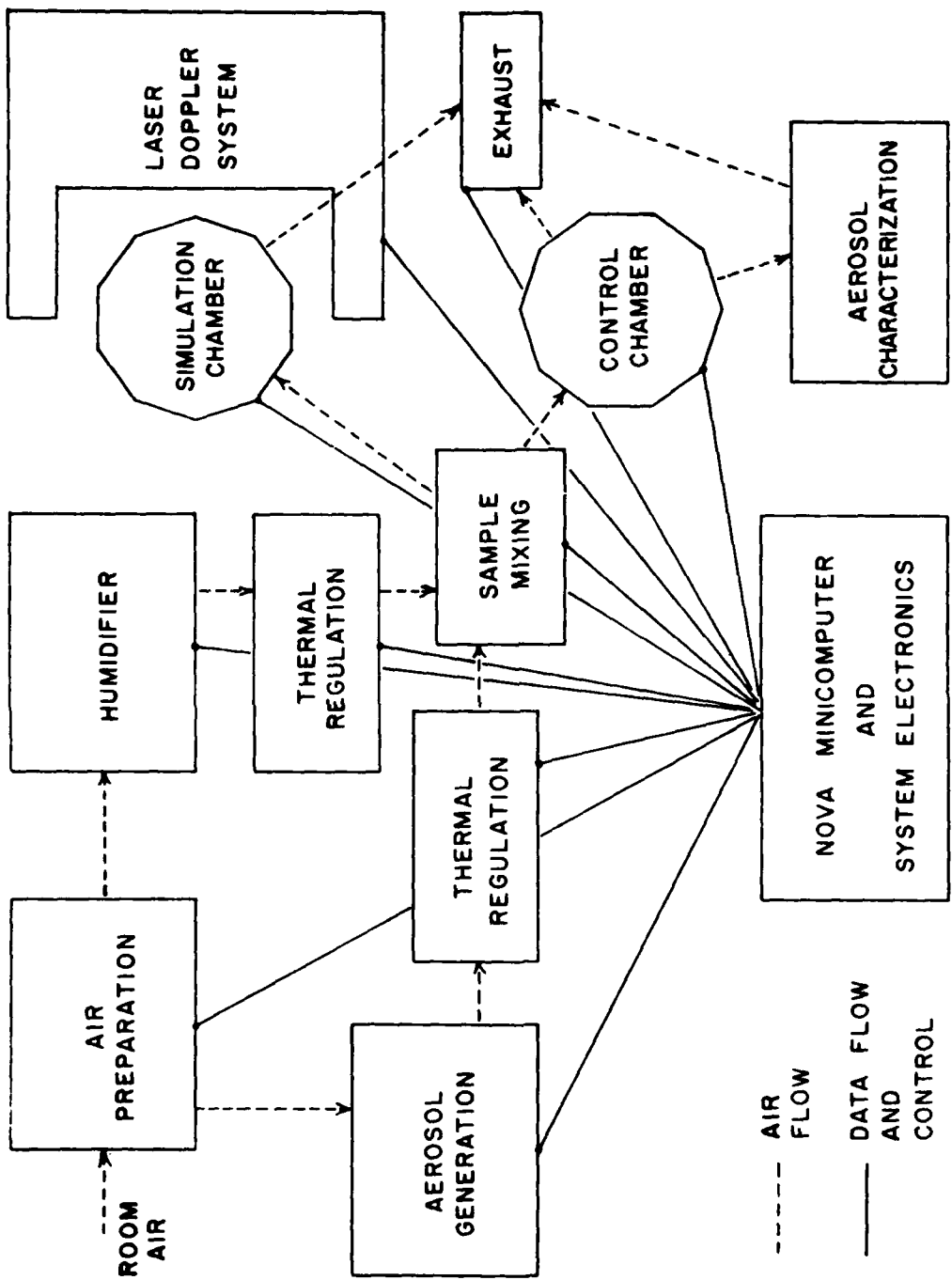
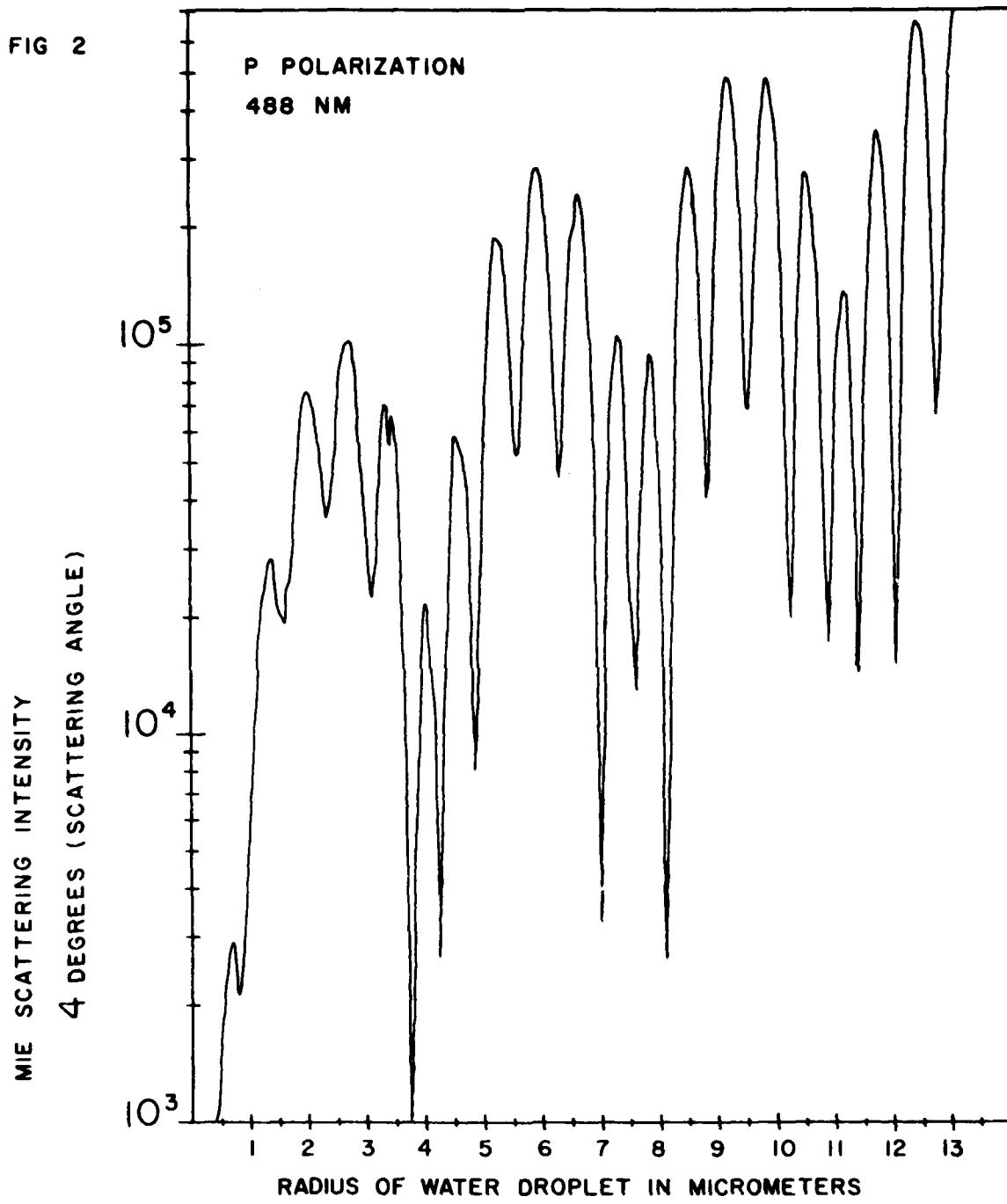


FIG. I OVERALL VIEW OF CLOUD SIMULATION CHAMBER PROJECT

FIG 2



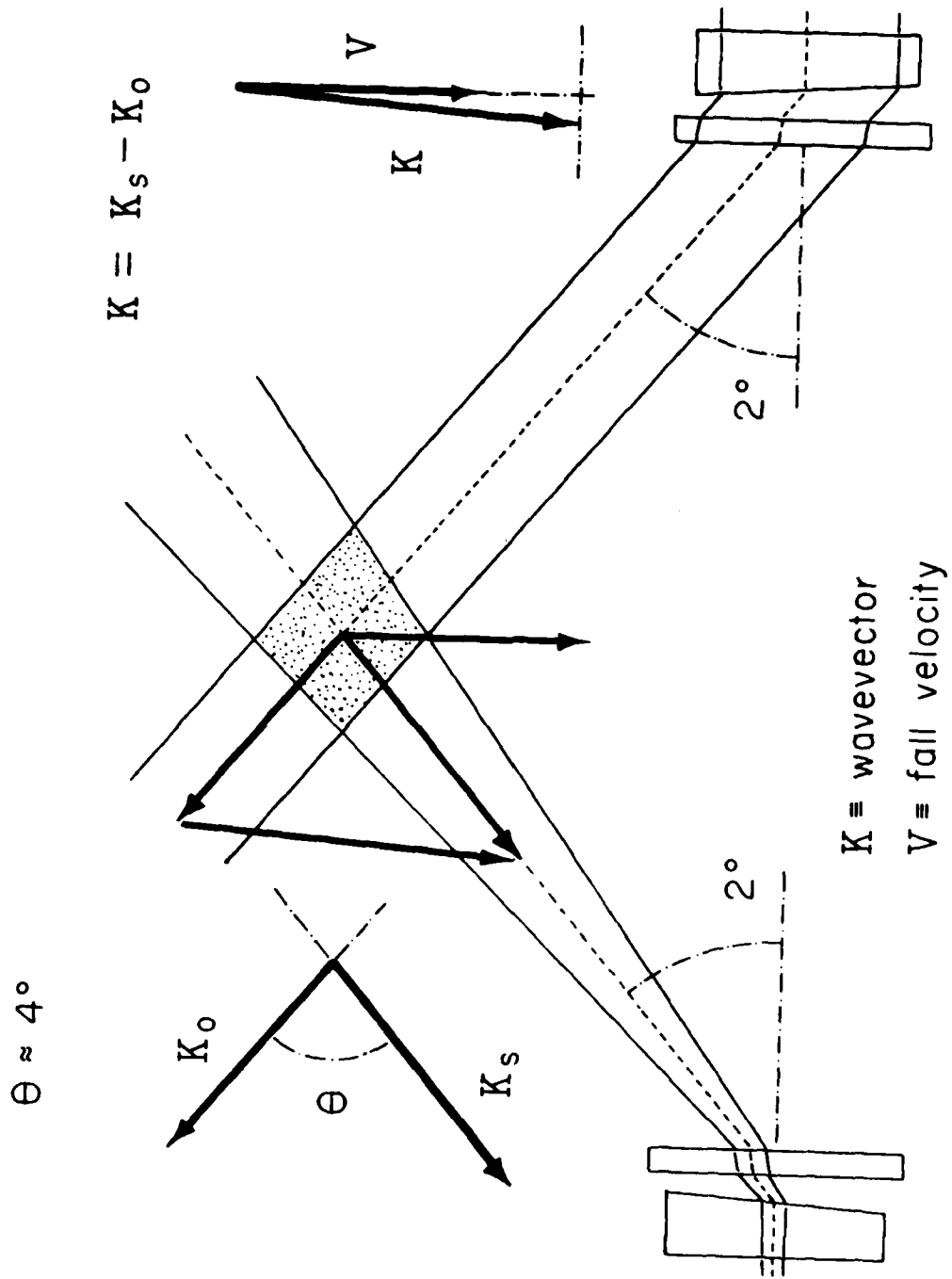


FIG. 3 LIGHT SCATTERING GEOMETRY (EXAGGERATED)

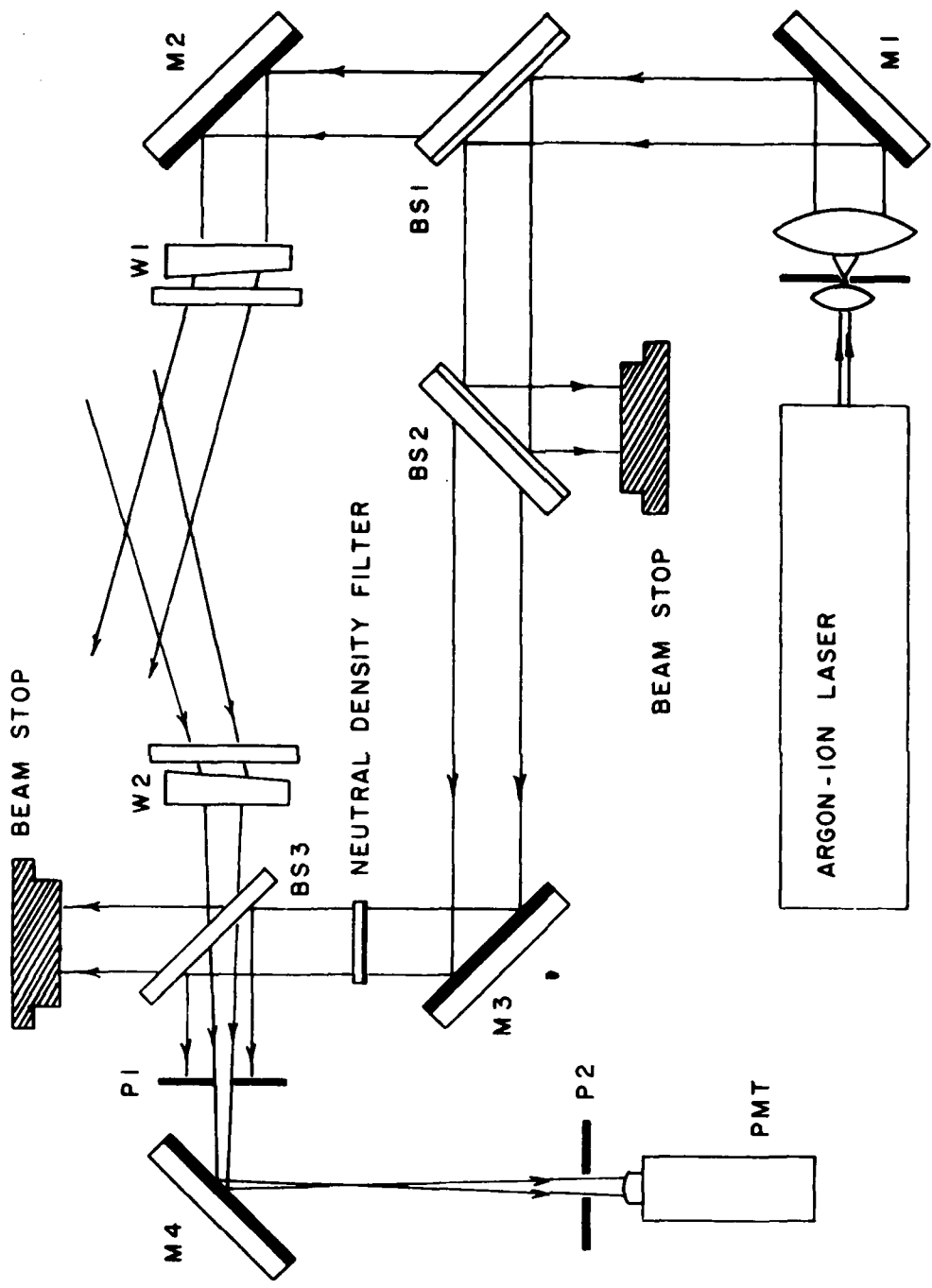


FIG. 4 LASER OPTICAL HETERODYNE SYSTEM
FOR CLOUD DROPLET SIZE DISTRIBUTION

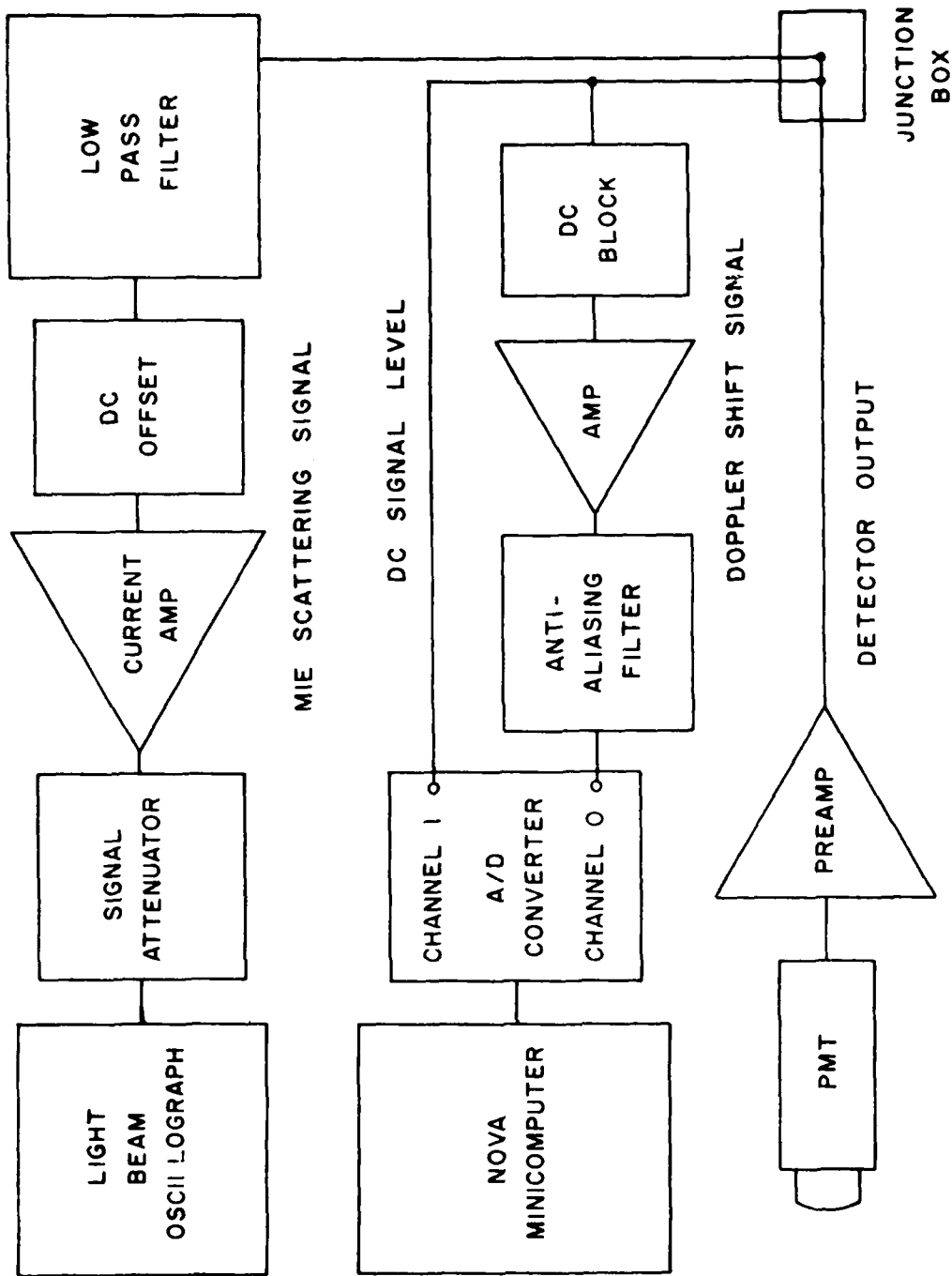


FIG. 5 SIGNAL ROUTE FOR 4 - DEGREE SCATTERING DETECTOR

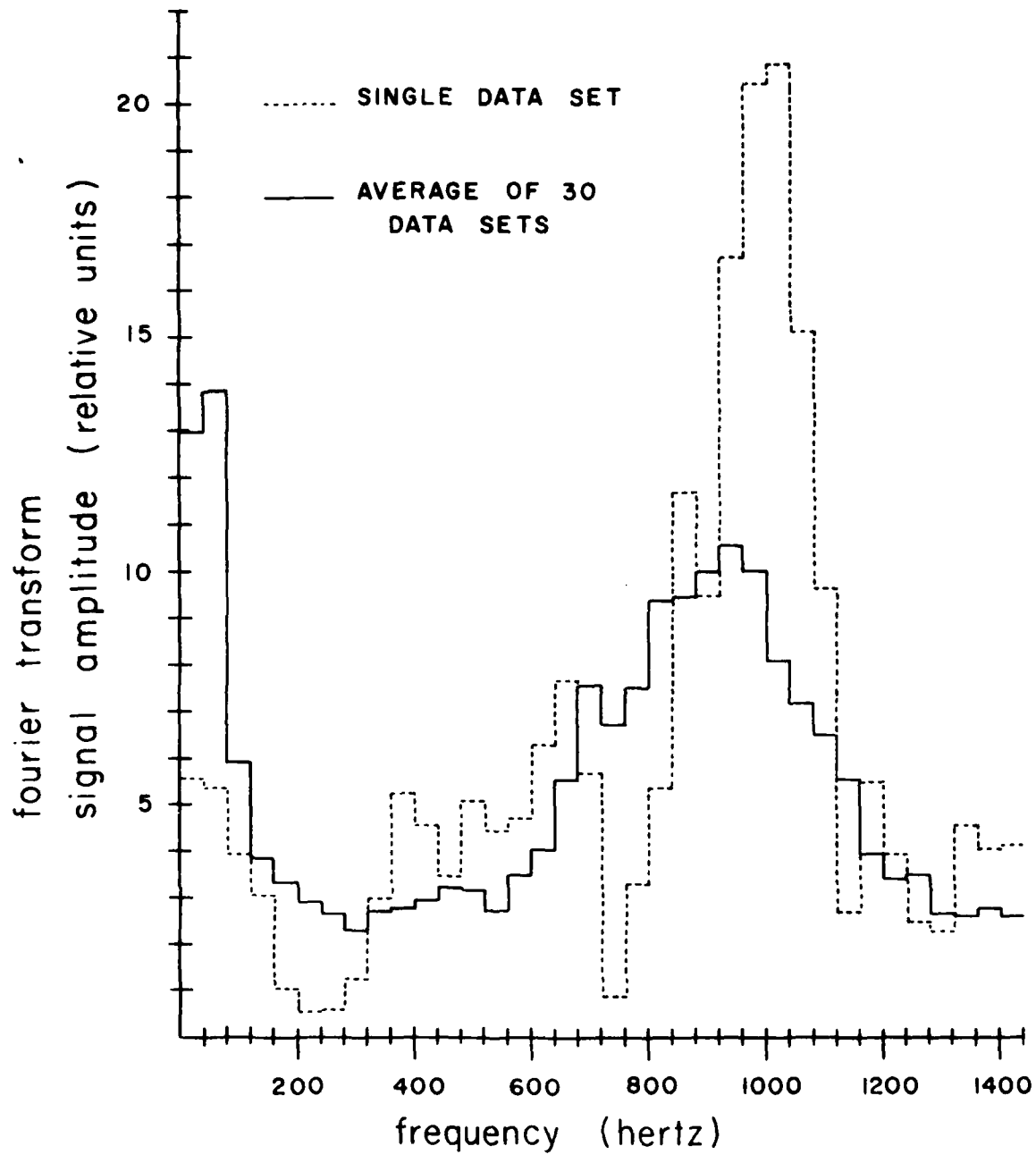


FIG. 6 SCATTERING FROM PORTION OF REVOLVING DISK

GRADUATE CENTER FOR CLOUD PHYSICS RESEARCH

SPACE SCIENCES RESEARCH CENTER
UNIVERSITY OF MISSOURI - ROLLA

PROGRESS MADE IN GENERATING A MONODISPERSE
AEROSOL OF SODIUM CHLORIDE USING TWO FURNACES

Max B. Trueblood
James M. Carter
Sung Ho Suck
Daniel R. White
James L. Kassner, Jr.

Graduate Center for Cloud Physics Research
University of Missouri-Rolla

Office of Naval Research
Contract Number N00014-75-C-0182

April 14, 1978



University of Missouri-Rolla
Rolla, Missouri 65401

ABSTRACT

Progress toward generating a monodisperse aerosol of NaCl in the range $.01\mu\text{m}$ to $.05\mu\text{m}$ using the two furnace technique is reported. All size distributions were measured with an Electrical Aerosol Analyzer (EAA) made by Thermo Systems, Inc. The effect on the size distribution caused by varying the furnace temperatures and furnace air flow rate was studied and found to be in qualitative agreement with work done by others on larger particles. A valve in the flow path was found not to affect the size distribution. Theoretical considerations related to inertial deposition and coagulation due to turbulence do not contradict this. Increasing the aerosol's path length from the furnace to the EAA was found to decrease the concentration of small particles and increase the concentration of large particles. A copper flow divider at the exit of the second oven caused the distribution to change from monotonically decreasing to having a peak in the range of the EAA ($.013\mu\text{m}$ - $1.0\mu\text{m}$). Slow cooling of the furnace air with a flow divider also yielded a peak in the range of the EAA. Immediate turbulent quenching of the furnace air and small transit times between the furnace and the EAA yielded an abundance of small particles and literally no large particles. Using air with a dew point of about -20°C caused the EAA to operate slightly outside of its specifications.

TABLE OF CONTENTS

	Page
ABSTRACT	ii
LIST OF ILLUSTRATIONS	iv
I. INTRODUCTION	1
II. EFFECT OF VARIOUS OPERATING PARAMETERS ON THE SIZE DISTRIBUTION	1
Temperature Within Oven Number 1	2
Effect of Oven Flow Rate Q_{ov} on T_1	2
Error Sources	2
Long Term Stability	7
Effect of T_1 and T_2 on the Distribution	10
Effect of Q_{ov} on Distribution	13
Effect of a Valve on Distribution	13
The Distribution's Dependence on Source of Sheath Air in EAA	18
Effect of Extra Travel of Aerosol on Distribution . . .	21
Effect of a Copper Flow Divider on the Distribution .	24
Effect of Slow Cooling and Flow Divider on the Distribution	27
Effect of Immediate Turbulent Dilution on Distribution	34
Effect of a Double Dilution and Small Transit Time .	34
III. CONCLUSION	41
REFERENCES	43

LIST OF ILLUSTRATIONS

Figure	Page
1. General View of Apparatus	3
2. Temperature T_1 vs. Distance X from End of Mullite Tube	4
3. Temperature at the Center of Oven No. 1, T_1 , vs. Oven Flow Rate, Q_{ov}	5
4. Apparatus Used to Study Long Term Stability and the Effect on Distribution from Varying T_1 , T_2 , and Q_{ov}	8
5. Long Term Stability.	9
6. Effect on Distribution from Varying T_1 with $T_2 = 822^\circ\text{C}$	11
7. Effect on Distribution from Varying T_1 with $T_2 = 870^\circ\text{C}$	12
8. Effect on Distribution from Varying Q_{ov}	14
9. Apparatus Used to Determine Effect on Distribution Produced by Inserting a Whitey Valve in the Flow Path	15
10. Effect on Distribution Produced by Inserting a Whitey Valve in the Flow Path	16
11. Two Schemes to Supply EAA's Sheath Air	19
12. Effect on Distribution from Changing EAA's Sheath Air	20
13. Apparatus Used to Determine Effect of Inserting a Variable Length L of Extra Tubing	22
14. Effect on Distribution from Inserting a Variable Length L of Extra Tubing.	23
15. Apparatus Used to Study Effect of a Flow Divider . .	25
16. Effect on Distribution Produced by a Flow Divider. .	26
17. Apparatus Used to Study Effect of a Flow Divider and and Oven Extension.	28
18. Effect on Distribution from Inserting a Flow Divider and an Oven Extension	29

Figure		V	Page
19.	Two Orientations of Mullite Tube		31
20.	Distribution with Oven No. 1 at Room Temperature . .		32
21.	Distributions with Oven No. 1 at 750°C and 200°C . .		33
22.	Apparatus Used to Study Effect of Immediate, Turbulent Dilution.		35
23.	Effect on Distribution from Immediate, Turbulent Dilution.		36
24.	Apparatus Used to Study Effect of Double Dilution and Small Transit Time.		37
25.	Effect on Distribution from Double Dilution and Small Transit Time.		38
26.	Apparatus Used to Study Effect of Single Dilution and Long Transit Time		39
27.	Effect on Distribution from Single Dilution and Long Transit Time.		40

PROGRESS MADE IN GENERATING A MONODISPERSE AEROSOL OF SODIUM CHLORIDE USING TWO FURNACES

I. INTRODUCTION.

The Simulation Chamber in the laboratory of the Graduate Center for Cloud Physics Research is designed to do the following:

1. Provide a controlled laboratory simulation of environmental conditions occurring during the formation and development of clouds and fogs.
2. Study the effects of specific pollutants on cloud and fog formation and development.
3. Study the microphysics and chemistry of the formation and development of clouds and fogs.
4. Test the validity of predictions based on numerical cloud models.

One of the aerosols found most frequently in natural air masses is NaCl. To achieve the above goals, it is necessary, therefore, to have NaCl aerosol for the Simulation Chamber. It is found that the laboratory aerosol should be such that the number of particles with diameters between $0.01\mu\text{m}$ and $0.05\mu\text{m}$ should be 500 times the number of particles with diameter greater than $0.05\mu\text{m}$. This paper reports the progress made toward this end.

II. EFFECT OF VARIOUS OPERATING PARAMETERS ON THE SIZE DISTRIBUTION.

An Aerosol Generator using three electric furnaces in series was described by Espenscheid¹ and yielded a quite monodisperse and reproducible output. He sublimated NaF in the first furnace and used this as condensation nuclei for the NaCl sublimated in the second and third furnaces. Kitani and Ouchi generated fairly monodisperse aerosol using two furnaces and having NaCl in only the first furnace².

The Aerosol Generator used at GCCPR is similar to that of Kitani and Ouchi and is shown in Figure 1. The dilution air is not shown joining the oven air since several methods to mix them were tried and these methods will be shown individually. The air used was usually room air but sometimes air from the Air Preparation System with a dew point of about -20°C was used.

Temperature Within Oven Number 1.

The temperature inside the mullite tube as a function of the distance from its left hand end is shown in Figure 2. Note the close agreement between the inside thermocouple temperature and that of the outside thermocouple. Corrosion particles are given off by thermocouples placed inside the tubes³ and so we placed the chromel-alumel thermocouples outside the mullite tube, but inside the furnace.

Effect of Oven Flow Rate Q_{ov} on T_1 .

The effect of Q_{ov} on the temperature at the center of Oven Number 1 as measured by the thermocouple inside the mullite tube is shown in Figure 3. One concludes that as long as Q_{ov} is less than $2.0\frac{1}{m}$, the boat of NaCl will be reasonably close to the temperature measured by the thermocouple outside the mullite tube.

The number density versus diameter or size distribution of aerosol particles produced was measured with an Electrical Aerosol Analyzer (EAA) made by Thermo-Systems, Inc., and first proposed by Liu, Whitby, and Pui⁴. Liu and Pui have studied the performance of the commercial version⁵.

Error Sources.

Bear in mind as you examine the data to be shown that the EAA has at least two limitations. Firstly, the manual⁶ recommends not

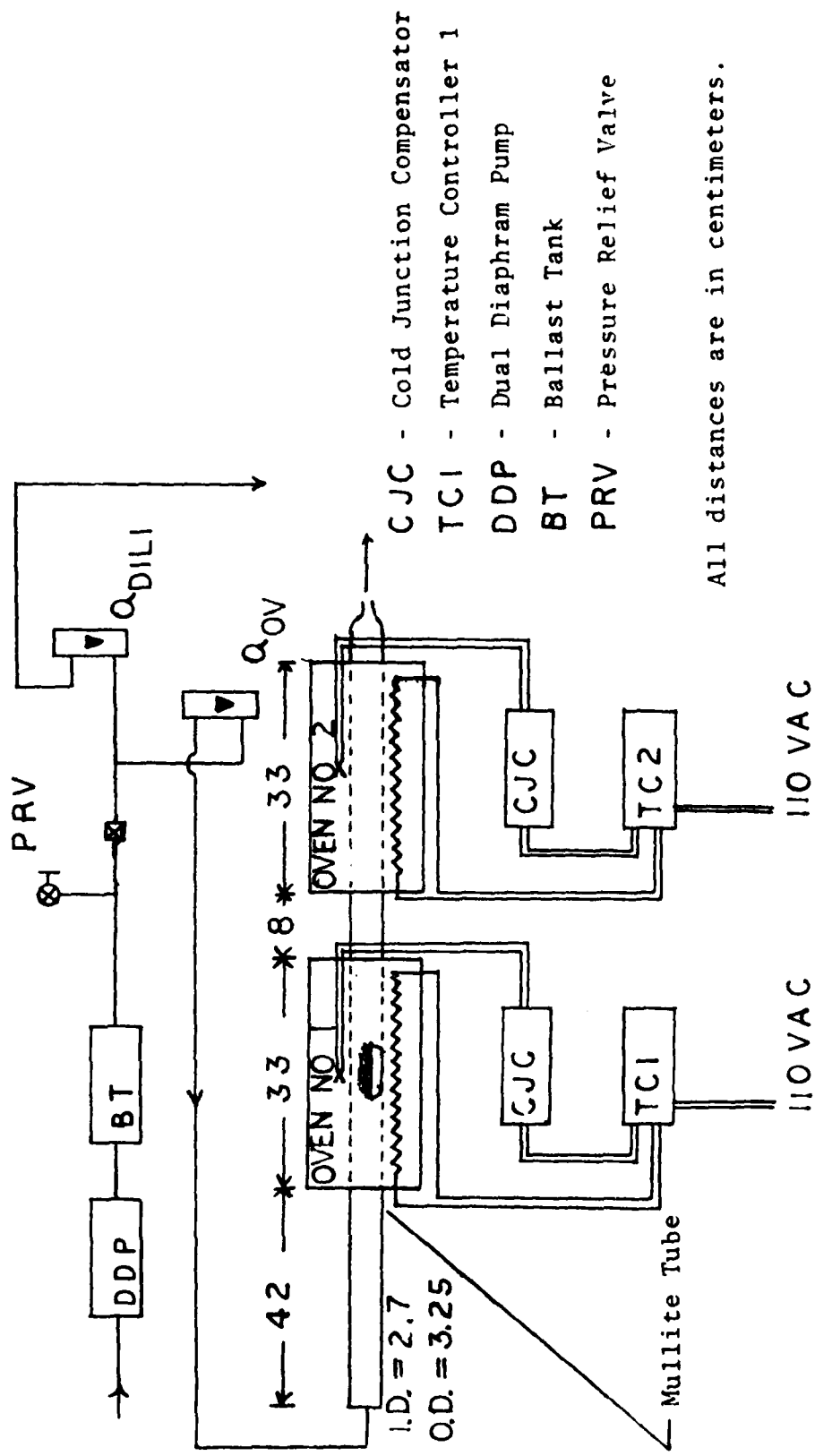


Figure 1 General View of Apparatus.

$\rightarrow T_1$ AS MEASURED BY THERMOCOUPLE OUTSIDE MULLITE TUBE

FIGURE 2

TEMPERATURE T_1 VS DISTANCE X
FROM END OF MULLITE TUBE
YR / MO / DAY = 770527

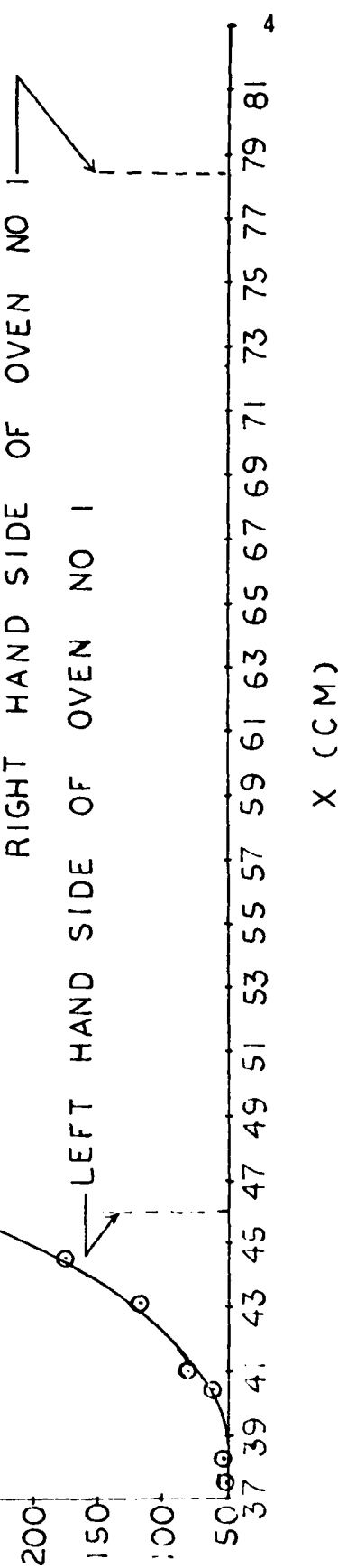
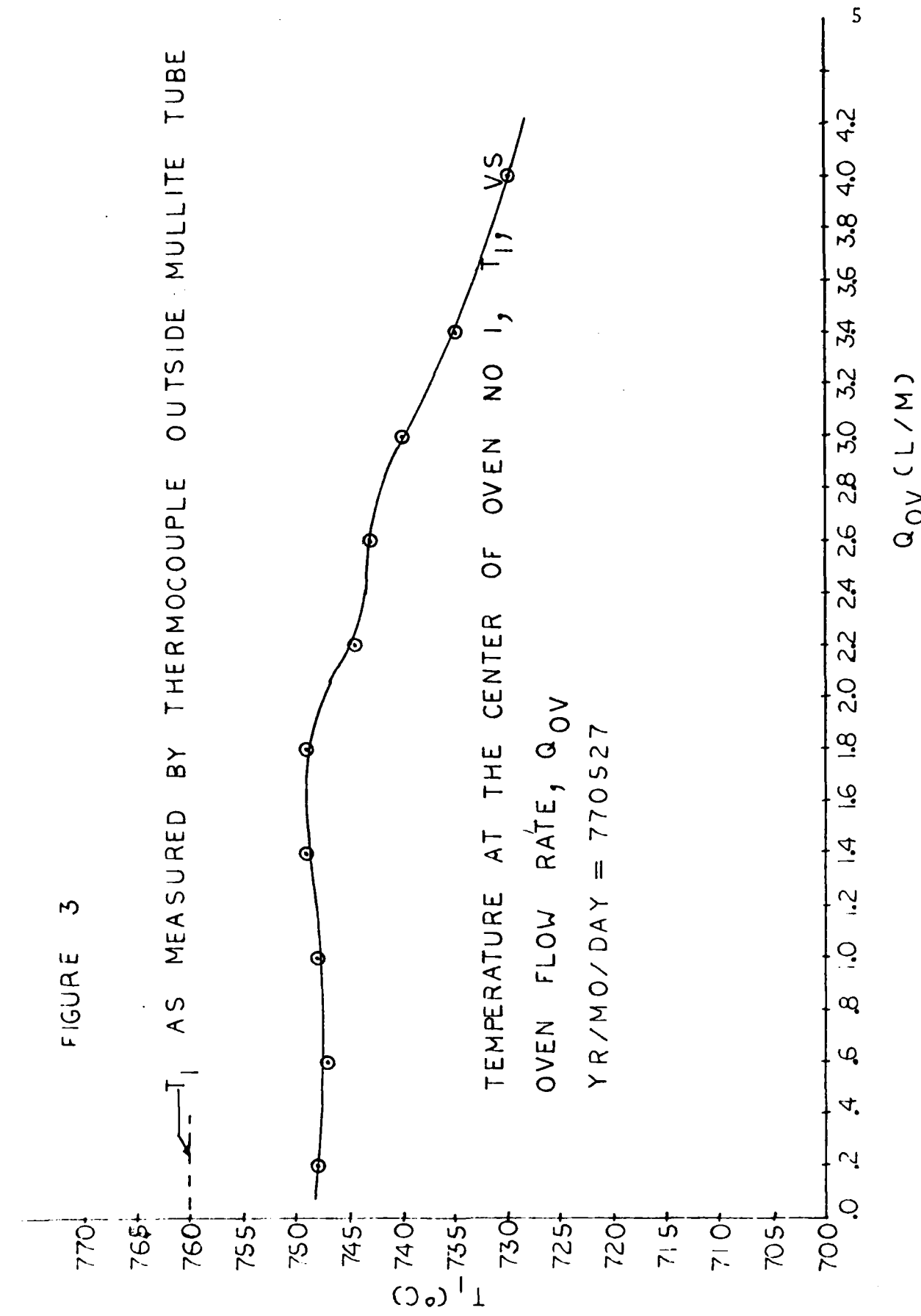


FIGURE 3



computing the concentration for diameters less than $.0133\mu\text{m}$. In some cases, however, the concentrations computed for diameters less than $.0133\mu\text{m}$ did follow the same trends as the concentrations of the larger particles. We plotted the concentrations of these small particles anyway because of this. Secondly, noise in the electrometer of the EAA is found to give rise to an uncertainty of 6 particles/cm³ at the large particle end and 20,000 particles/cm³ at the small particle end. Some of the plots fluctuate considerably at the large particle end and surely noise accounts for some of this fluctuation.

During the course of these experiments another error source was noticed. The analyzer current is the measure of the charge deposited per second on the electrometer filter by all aerosol particles larger than the cutoff size. This current varied considerably for a fixed cutoff size. The difference of two analyzer currents multiplied by the gain of the EAA at that particle size yields the concentration of particles between the two sizes. A large number of analyzer current readings is necessary to obtain a valid average value of the analyzer current. The number of analyzer current readings used to obtain the arithmetic mean of the analyzer current is written in the lower left hand corner of each graph ($N =$). Perhaps the large fluctuations at the large particle end of many of the plots is due to taking the average value of the analyzer current from an insufficient number of readings.

Another problem is that the impedance to the flow of oven air presented by the reduced end of the mullite tube changed with time. If the reduced end extended more than about one half an inch outside the oven it became cool enough to cause much condensation in its opening and therefore present a large impedance. At times it would

even clog up completely.

The seal at the joint of the reduced end of the mullite tube and the Cu tee also acted as a leak with a variable impedance. This has been solved in recent experiments by cutting off the reduced end of the mullite tube and forcing a rubber stopper fitted with a three inch piece of Cu tubing into the mullite tube. The seal between the rubber stopper and the mullite tube allows almost no leakage.

A few error bars are inserted for one of the plots in Figure 8, Figure 21, and Figure 27.

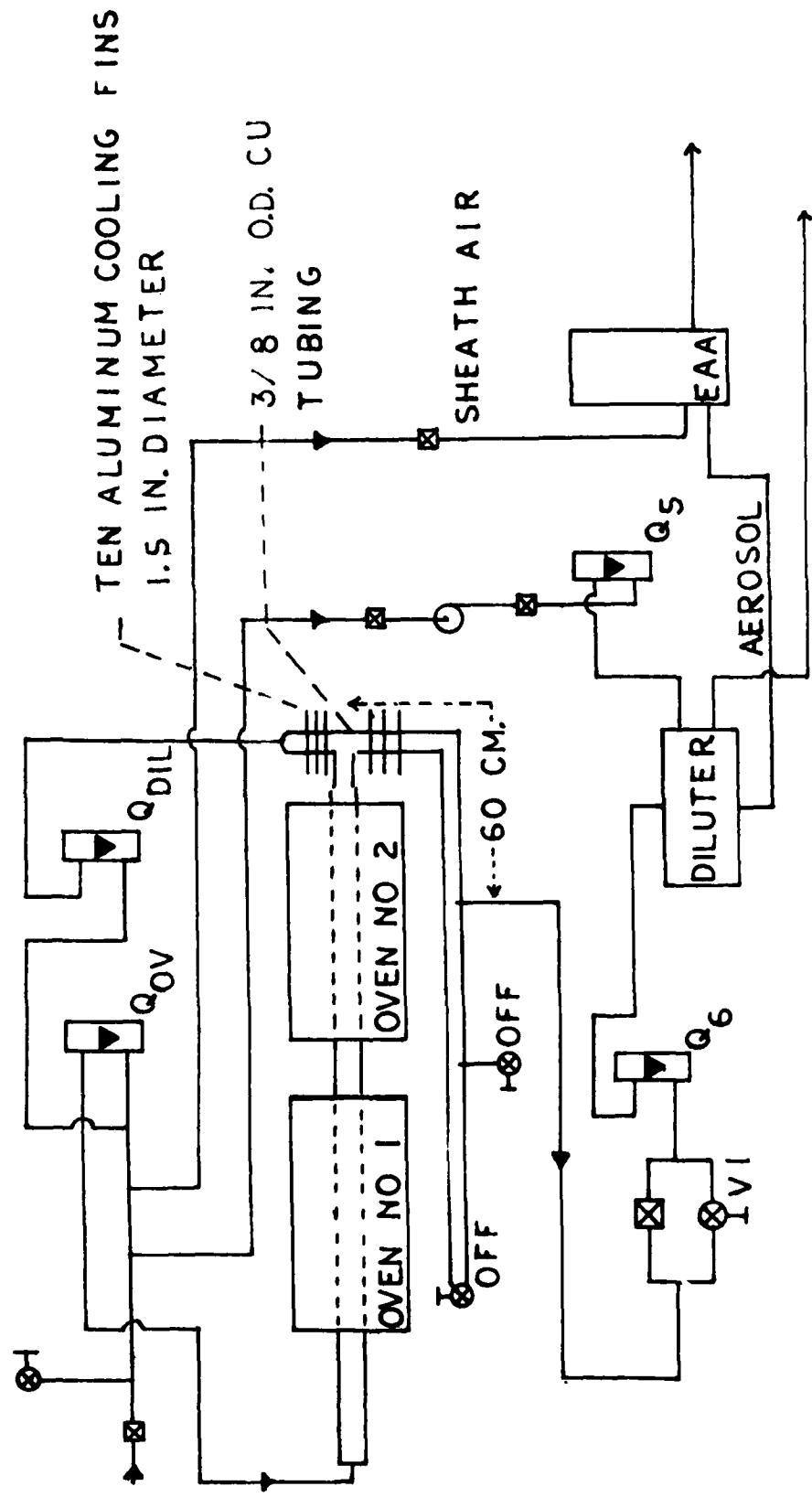
In the drawings of the various apparatuses used, one will see that some Cu tubing is used. All other tubing is 1/4 inch I.D. and 3/8 inch I.D. Tygon tubing with the majority being 1/4 inch.

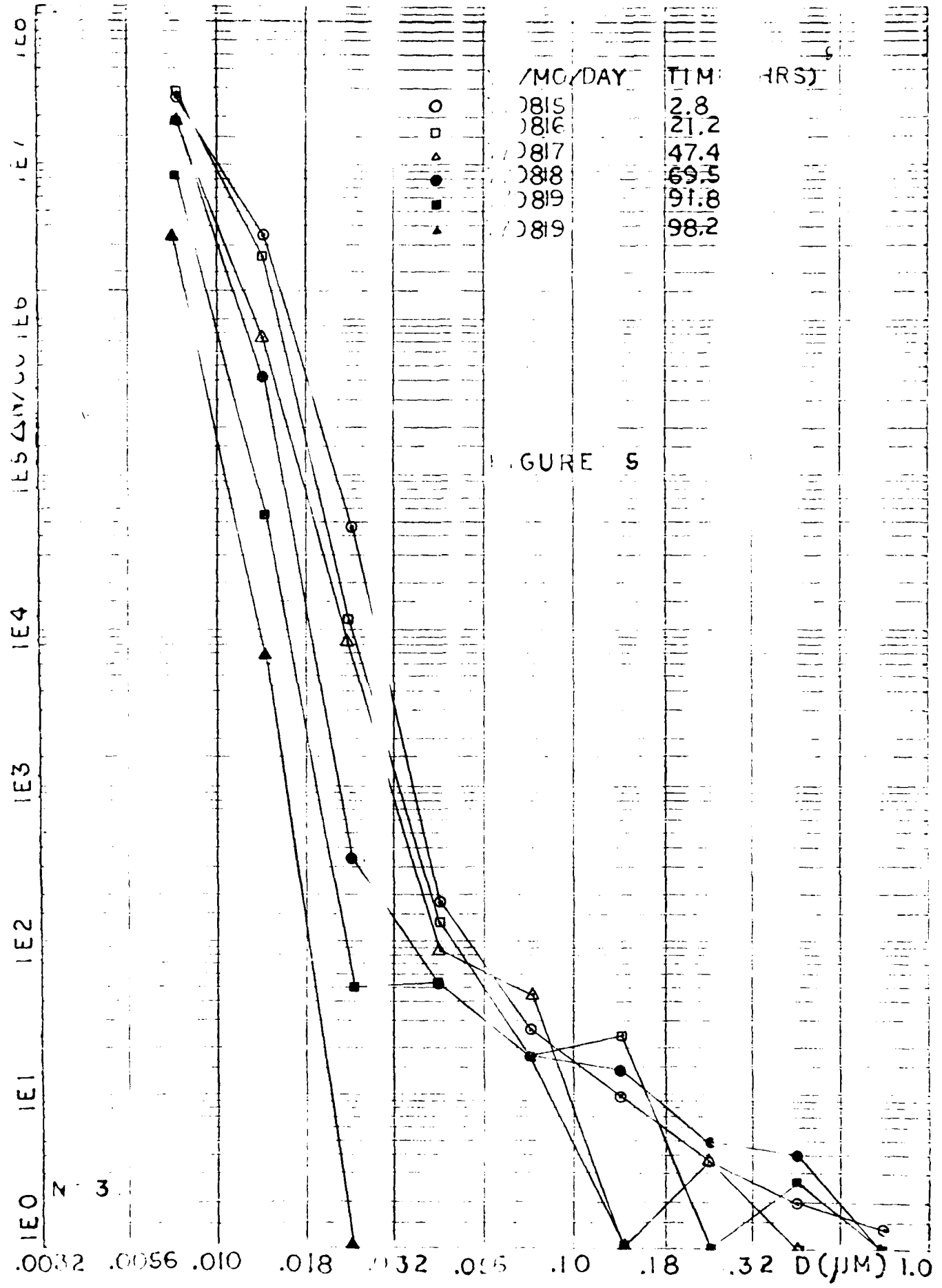
Long Term Stability.

Measuring the number density versus diameter, then changing some parameter such as oven temperature and measuring the number density again, and then bringing the system back to the original temperature and again measuring the number density would take several hours. Because of this long time involved, one needs to be sure that the output of the ovens would have remained the same over a long period of time to be able to conclude that any changes in the distribution after changing the parameter are in fact due to the change in that parameter. For this reason, long term stability measurements were taken using the apparatus of Figure 4.

Figure 5 shows the distribution as measured over a five day period. Note that the overall trend is a decay in the number density for each diameter. At least two processes are responsible for this. Firstly, it was found that the salt charge (about 5 gms) lasted about 16 days before being completely sublimated away. In a five

Figure 4 Apparatus Used to Study Long Term Stability and the Effect on Distribution from Varying T_1 , T_2 , and Q_{ov} .





day period about one third of the salt available for sublimation has been used. Secondly, it was noticed that the salt particles fused together slowly over the 16-day lifetime, thus decreasing the surface area of NaCl from which NaCl could sublime. This occurred even though Oven Number 1 was operated at 750°C, whereas the melting point of NaCl is 802°C.

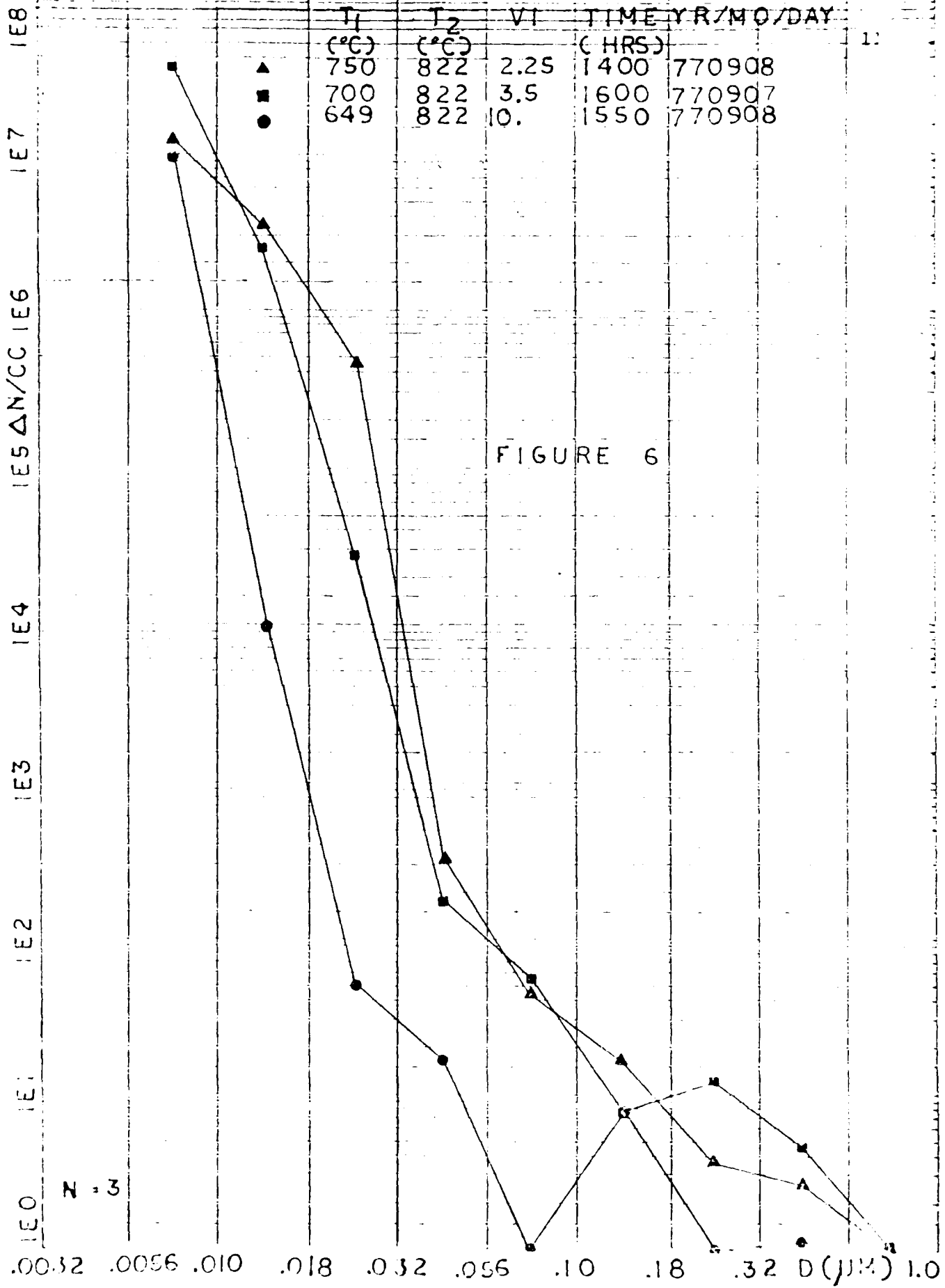
The important conclusion is that the output of the generator is fairly stable over a period of 8 hours with the main change being a decrease in the concentration by about the same fraction for all diameters. This conclusion allows one to investigate the dependence of the distribution on the operating parameters.

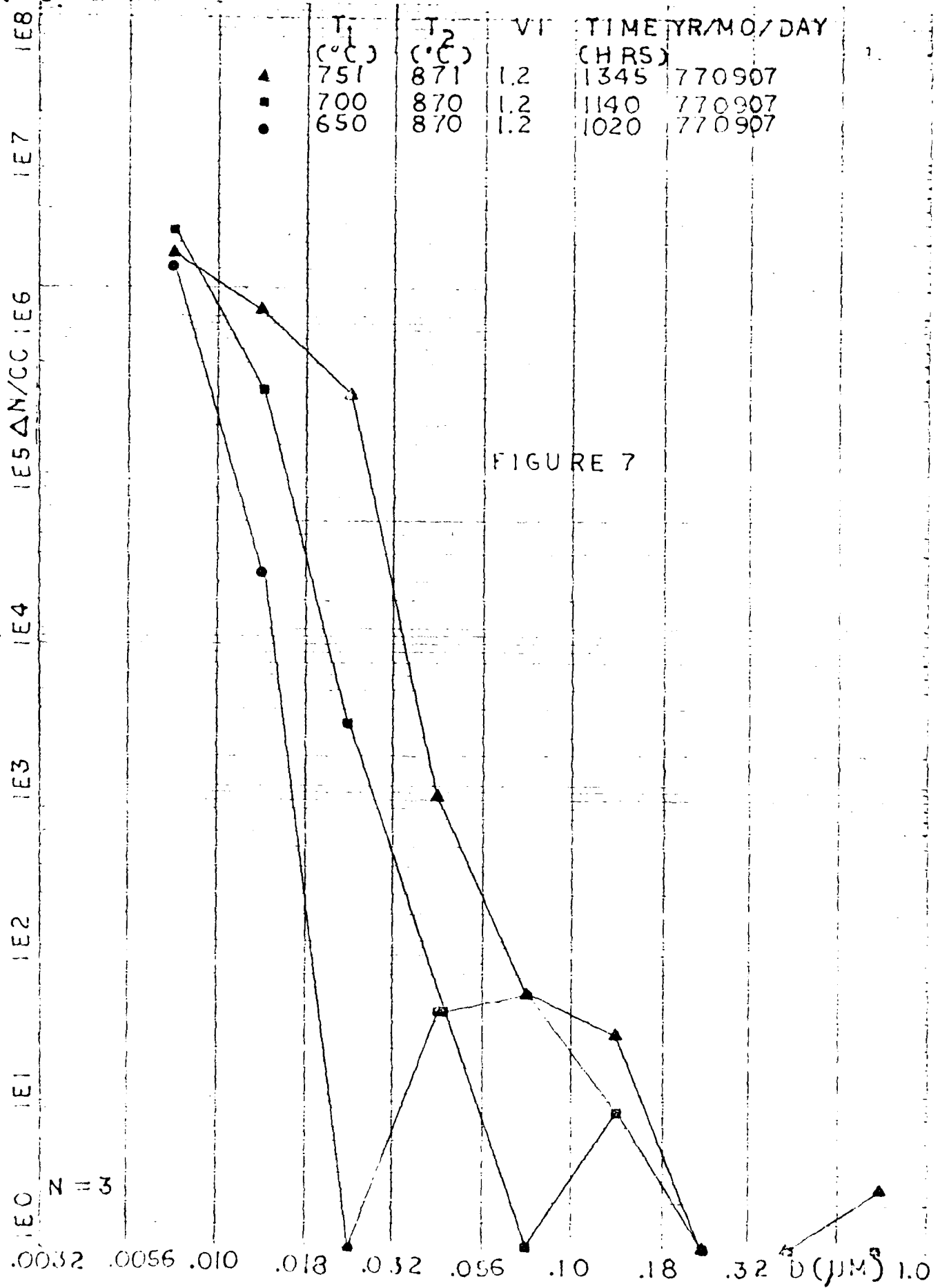
Effect of T_1 and T_2 on the Distribution.

Figure 6 shows the size distribution's dependence on T_1 with T_2 fixed at 820°C. The concentration of particles at a given diameter increases with increasing T_1 . Keep in mind as you examine this graph that valve V_1 was closed down considerably for the $T_1 = 750^\circ\text{C}$ data. This closing of V_1 amounts to a dilution since more of the flow would be forced through the absolute filter. Therefore, the concentrations for $T_1 = 700^\circ\text{C}$ and 750°C are higher than is shown by the graph.

Others have observed that the peak in the distribution occurs at larger diameters as T_1 increases^{7,8}. Since the maximums in the distributions of Figure 6 occur outside the range of the EAA, we can make no conclusions along these lines.

The distribution for $T_1 = 649^\circ\text{C}$ seems at first glance to be bimodal, the second mode centering about $D = .2\mu\text{m}$. We believe that one should actually pay little attention to this feature of the plot.





We say this because (1) $N=3$ and noise in the electrometer could almost account for the dip in concentration at $D = .07\mu\text{m}$ and (2) the concentration is so small that any real random fluctuation is a significant fraction of the average value of the concentration.

Figure 7 displays the effect of increasing T_1 with $T_2 = 870^\circ\text{C}$. Again the concentration for a given diameter increases with increasing T_1 . Note that this time valve V_1 was not changed so that the relative heights of the curves are a true indication of the relative concentrations.

The distribution for $T_1 = 650^\circ\text{C}$ again seems to have a bimodal character. It could be that it really is bimodal, but we feel that it is not for the same reasons as given for the other 650°C curve.

Effect of Q_{ov} on Distribution.

Figure 8 shows the dependence of the distribution on Q_{oven} . Kitani and Ouchi found that the modal diameter increased as Q_{ov} decreased. Since the peak in the distribution of Figure 8 occurs outside the range of the EAA, we can make no conclusions along these lines.

Effect of a Valve on Distribution.

Figure 9 shows the apparatus for investigating the effect of passing the aerosol through a Whitey valve, catalogue number 316-SS4RS4-A. The valve was opened to half the maximum number of turns. This particular valve is from our Electrostatic Classifier made by TSI. It was feared that the crooked flow path within the valve might alter the shape of the distribution. Figure 10 shows that no significant difference between the distributions with and without the valve was detected.

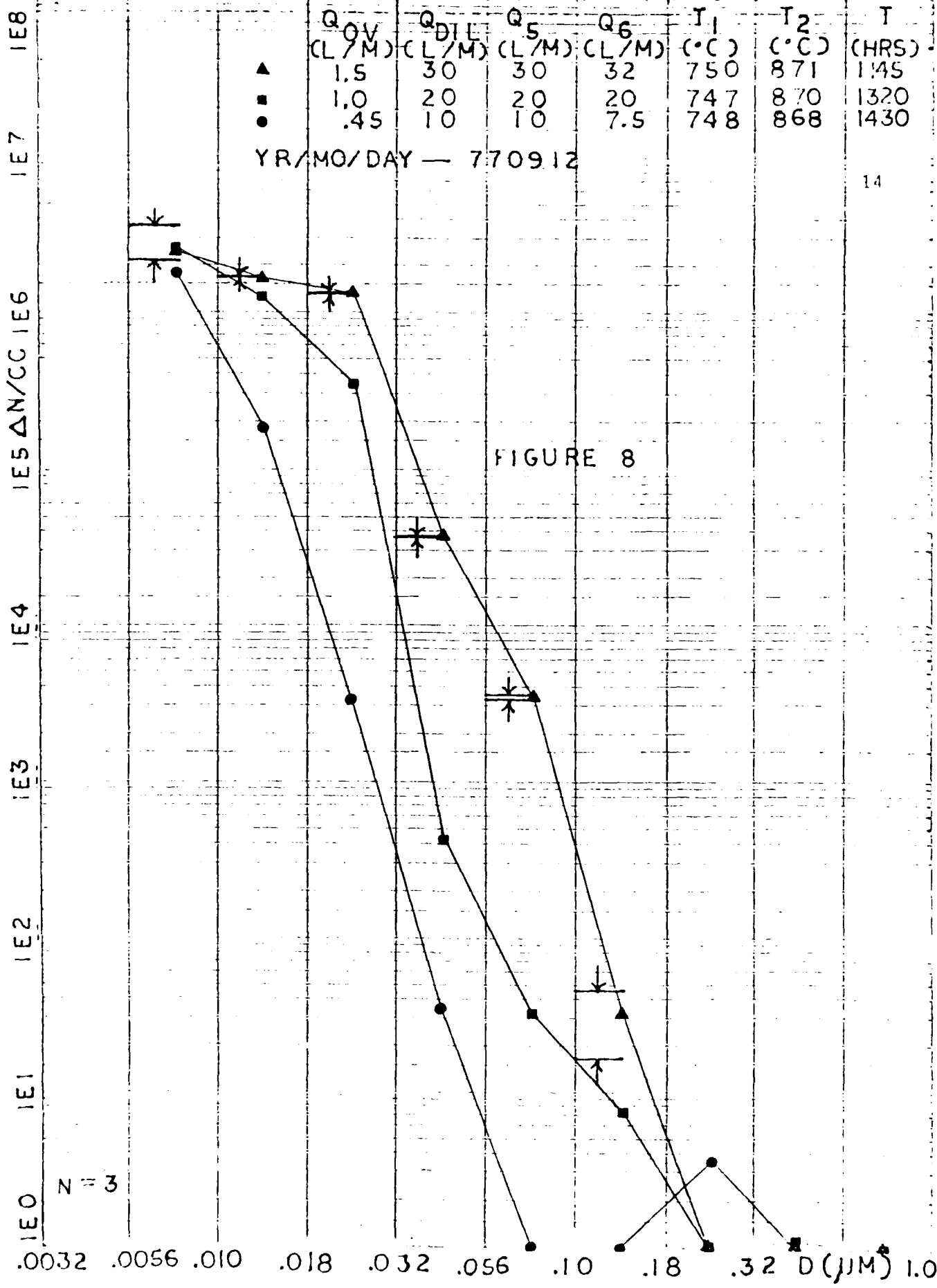


FIGURE 8

14

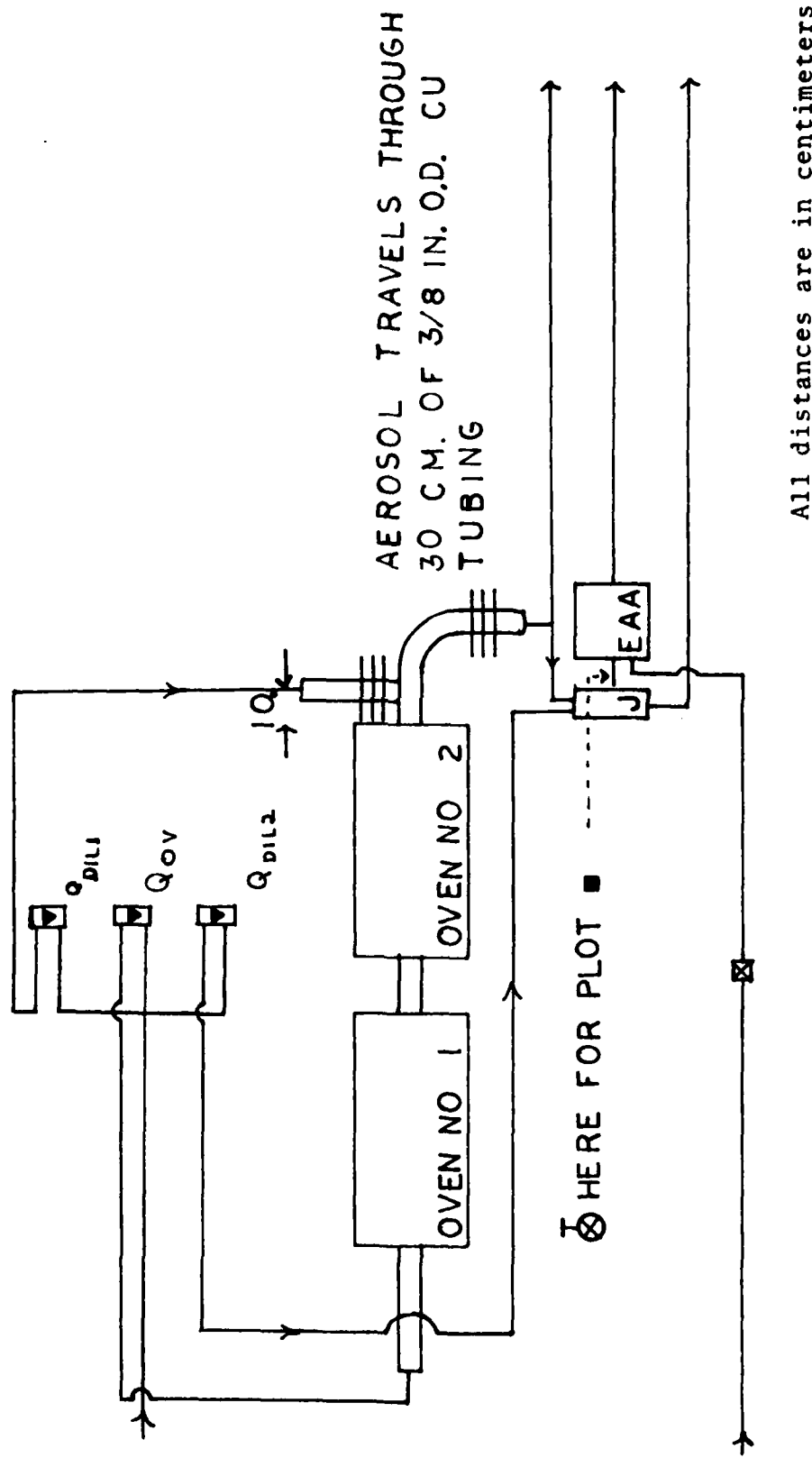
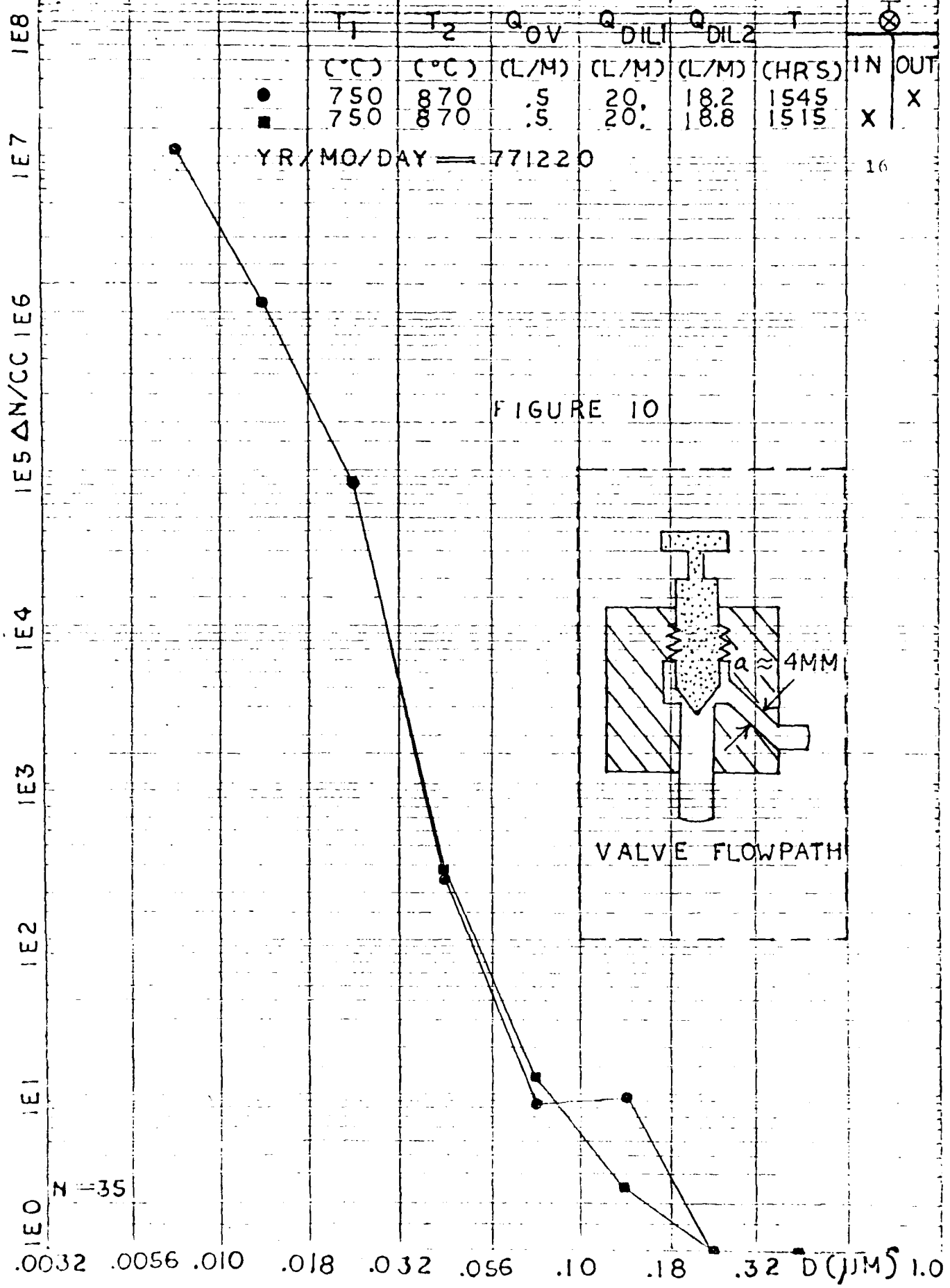


Figure 9 Apparatus Used to Determine Effect on Distribution Produced by Inserting a Whitey Valve in the Flow Path.



Let us see if we could have predicted this from theoretical considerations. The reasons why the valve might have altered the distribution are (1) inertial deposition, and (2) coagulation from turbulence due to the crooked flow path. Consider the first of these two. As an order of magnitude approximation, replace the valve by a cylinder of 2mm diameter in an otherwise unobstructed flow. Particles of $.05\mu\text{m}$ diameter will have a Stokes number St of

$$St = \frac{\rho_p D^2 \left(\frac{4 \Delta V}{\pi a^2} \right)}{18 \mu_a a} = \frac{\left(2.16 \frac{\text{kg}}{\text{cm}^3} \right) \left(5(-6) \text{cm} \right)^2 \left(\frac{4 \frac{1000 \text{ cm}^3}{\text{sec}}}{\pi (4 \text{cm})^2} \right)}{18 \cdot 1.83(-4) \frac{\text{dynes sec}}{\text{cm}^2} \cdot 4 \text{cm}} = 2.18(-5)$$

The Reynolds number of the particle, Re_p , is

$$Re_p = \frac{D \left(\frac{4 \Delta V}{\pi a^2} \right) \rho_a}{\eta_a} = \frac{5(-6) \text{cm} \left(\frac{4 \frac{1000 \text{ cm}^3}{\text{sec}}}{\pi (4 \text{cm})^2} \right) 1.29(-3) \frac{\text{gm}}{\text{cm}^3}}{1.83(-4) \frac{\text{dynes sec}}{\text{cm}^2}} = 1.87(-2)$$

The dimensionless group P is then

$$P = \frac{Re_p^2}{St} = 1.6(1)$$

Using these values and collection efficiency curves for cylinders, one obtains a collection efficiency of very, very nearly zero⁹. Although one may object to modeling the valve with a cylinder of about the same dimensions, it is emphasized that the collection efficiency was so close to zero that bringing the model closer to reality surely couldn't increase the collection efficiency appreciably. Therefore, it is not surprising that a negligible amount of impaction occurs in the valve for particles in the range $.01\mu\text{m}$ to $1.0\mu\text{m}$ with a flow rate of 4l/m through the valve.

In regard to coagulation due to turbulence, let us use as a model for the valve a straight, hollow tube of diameter 2mm. with the flow of 4 l/m passing through it. The Reynolds number for the flow is

$$Re_f = \frac{\alpha \left(\frac{4 \frac{\Delta V}{\Delta t}}{\pi \alpha^2} \right) \rho_a}{\eta_a} = \frac{(2 \text{ cm}) \left(\frac{4 \frac{4000 \text{ cm}^3}{60 \text{ sec}}}{\pi (2 \text{ cm})^2} \right) (1.29(-3) \frac{\text{ gm}}{\text{ cm}^3})}{1.83(-4) \frac{\text{ dyne-sec}}{\text{ cm}^2}} = 2.99(+3)$$

The flow in this model is turbulent. Probably the real flow in the valve was turbulent also. We might expect that coagulation due to turbulence does exist. The fact that the two distributions of Figure 10 are so similar leads one to conclude that coagulation due to turbulence was not significant.

The Distribution's Dependence on Source of Sheath Air in EAA.

Referring back to Figure 4, one sees the apparatus used to investigate the effect of the type of air used for the EAA's sheath air. Figure 11 then depicts the two methods to obtain the sheath air. In Scheme I, Air Preparation System air with a dew point of about -20°C was used. In Scheme II, a combination of filtered room air and filtered aerosol air was used. The data for Scheme II was multiplied by 10 since that aerosol had been diluted by 10 by the device in Figure 11B. The distributions shown in Figure 12 imply that the source of the EAA's sheath air does make some difference. A telephone conversation with TSI has revealed that the allowable range of values for the ratio of ionizer current to ionizer voltage in the EAA is

$$.98 \leq \frac{I}{V} \leq 1.18$$

Although the EAA's manual places specifications on I and V individually and these were fulfilled in the experiments of Figure 12,

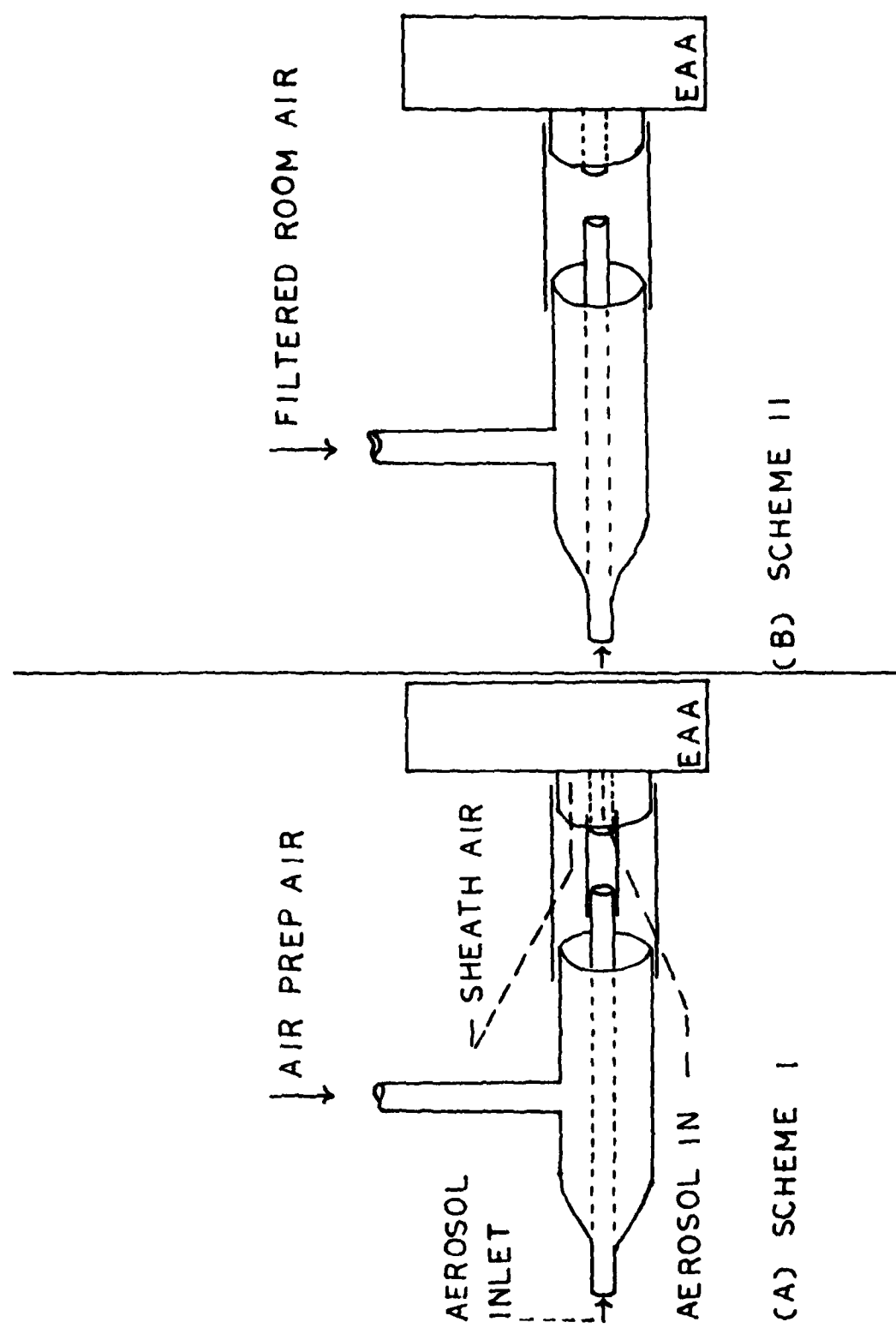


Figure 11 Two Schemes to Supply EAA's Sheath Air.

88

7
—

IE5 ΔΝ/CC | F6

三

ג

三

三

四

1

○	750	869
□	750	870
●	750	869
■	750	870
Q ₅	= 30	L/M
Q ₆	= 20.9	L/M

Q OV	Q DIL	T	I / V
(LMD)	(LMD)	(HRS)	(N.U.)
T	30	1315	121

1.	20	1313	1.2	1
1.	20	1415	1.14	11
	20	520	1.8	1

1. 20 1700 1.15 11
YR/MO/DAY = 770915

20

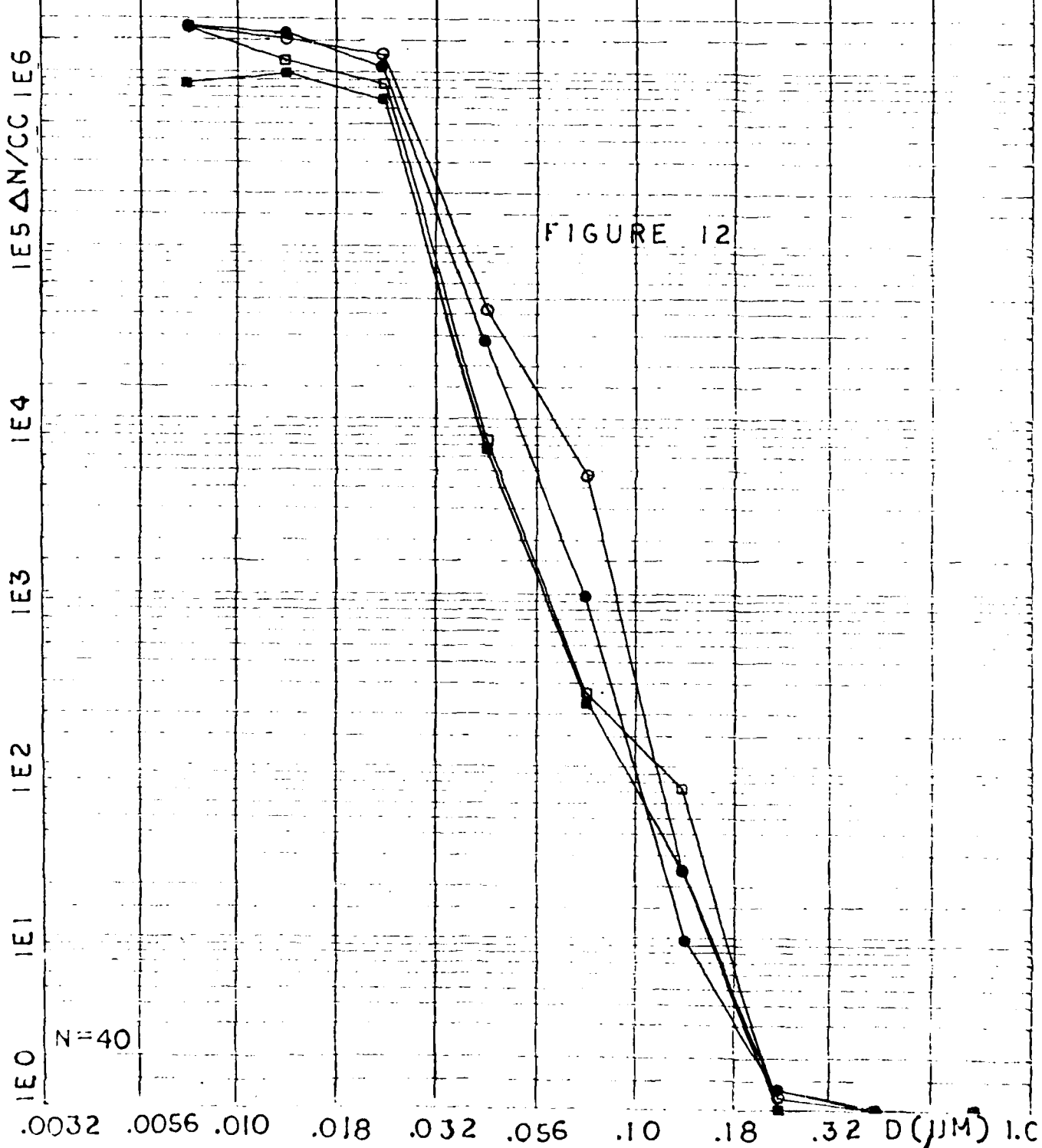


FIGURE 12

the specifications on $\frac{I}{V}$ were not fulfilled for the plot for which $T = 1315$ hours.

Effect of Extra Travel of Aerosol on Distribution.

As one tries different dilution and mixing schemes, one wonders if he is unwittingly and haphazardly changing the distribution by changing the length of tubing through which the aerosol flows. A scheme to determine the effect of tubing length is depicted in Figure 13, where a variable length L of extra tubing is inserted. The results, Figure 14, indicate that a small yet measurable change in the distribution is caused by inserting extra tubing. As L increases, the concentration of small particles decreases and the concentration of large particles increases. It is believed that coagulation accounts for this. Also tabulated on Figure 14 is the extra transit time $\Delta\tau$.

The results of this experiment also allowed us to make an important conclusion about the necessary amount of downtime between successive measurements of the distribution.

A technical oversight in the first few models of the EAA allowed charge to build up on the insulator supporting the central collecting rod of the mobility analyzer. This charge accumulation caused the analyzer current to increase with time even at fixed collector rod voltages. To achieve correct analyzer current readings, one would have to allow about one hour of down time for the accumulated charge to drain off the insulator. TSI recalled our EAA, replaced the insulator, and said that this problem had been solved. Note that only a few minutes elapsed between the taking of the data for the different plots of Figure 14. If the output of the ovens did remain constant over the time for all six runs of Figure 14, then the plots

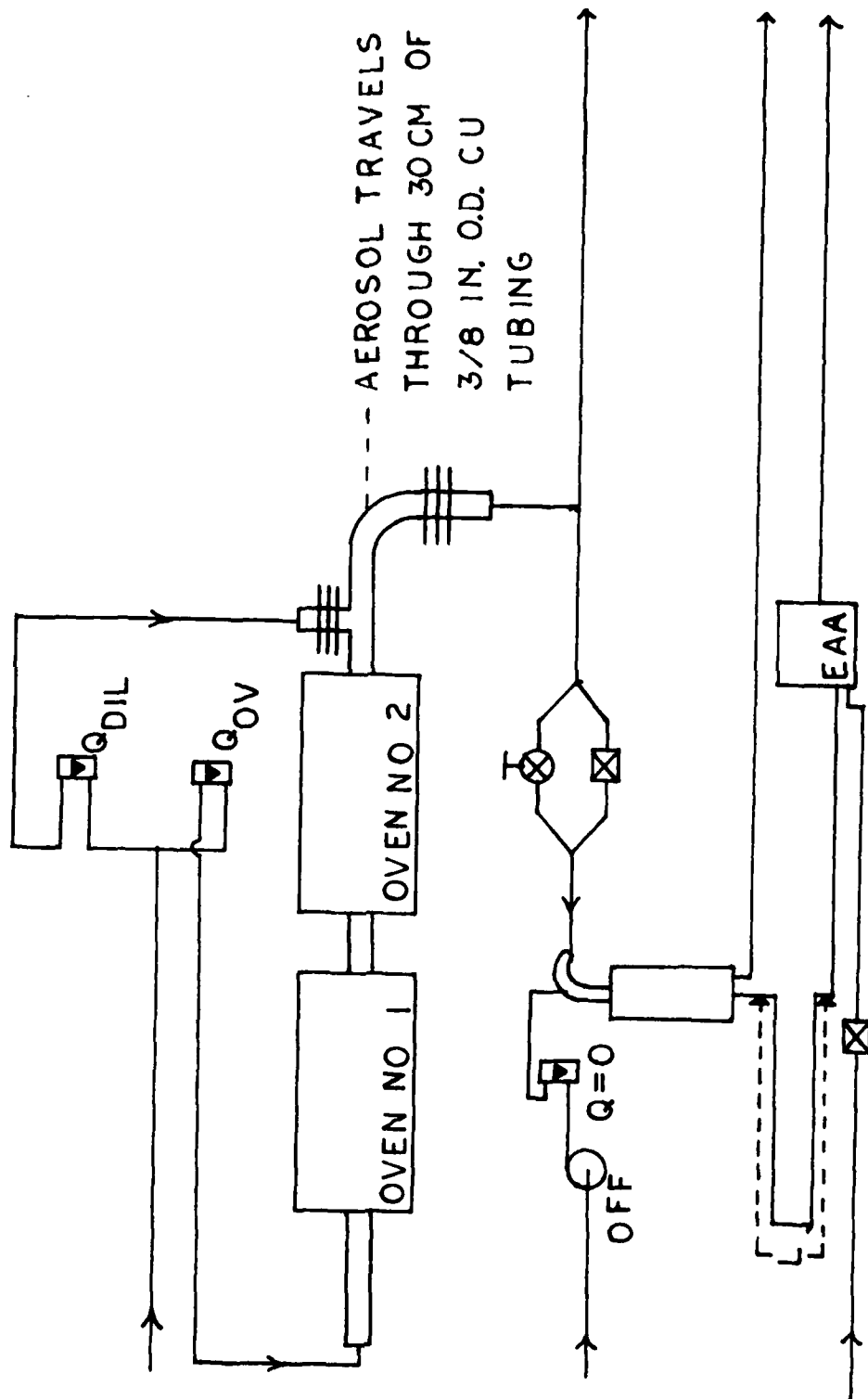
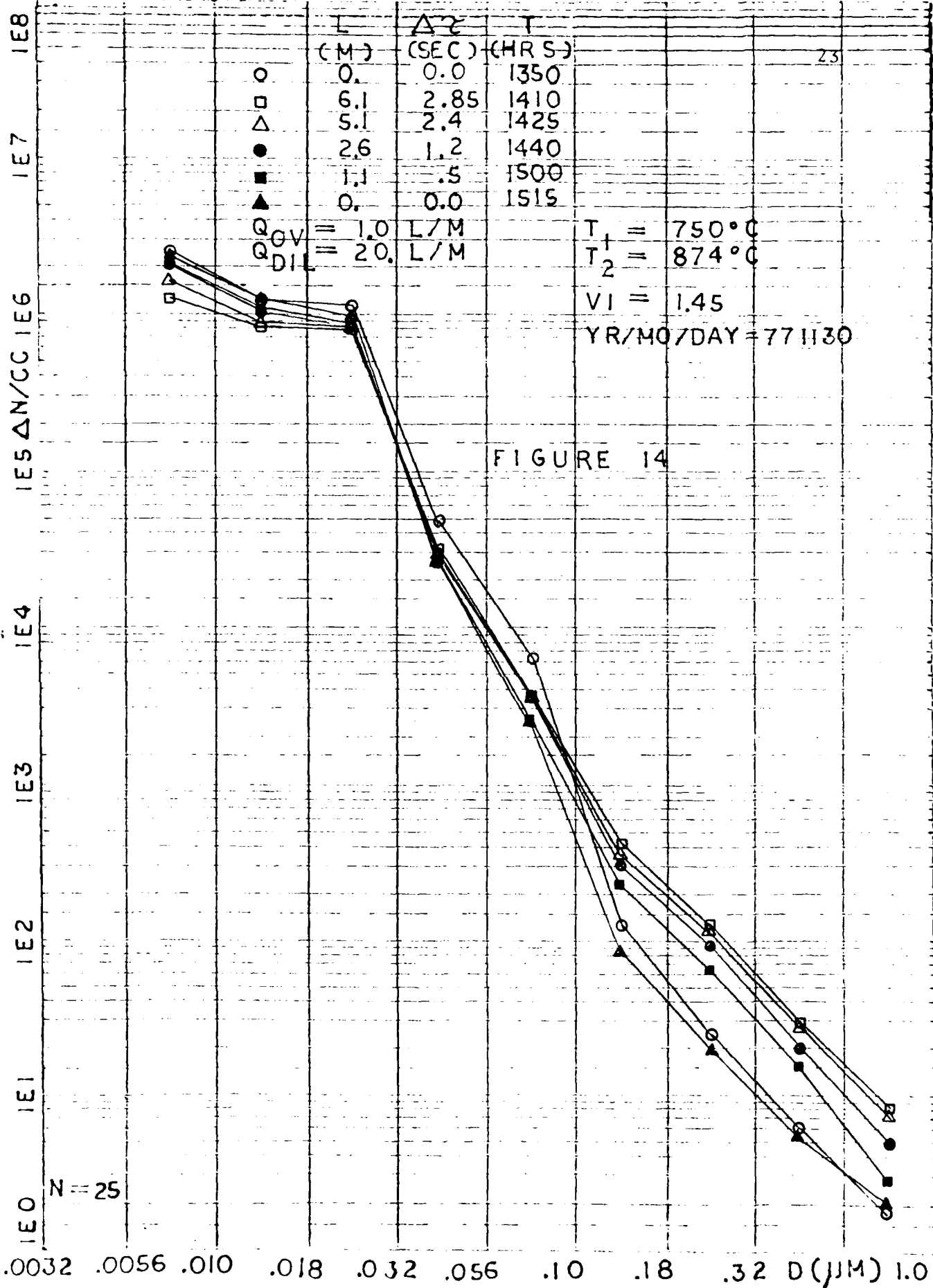


Figure 13 Apparatus Used to Determine Effect of Inserting a Variable Length L of Extra Tubing.



for $L=0$ at the beginning and end should be the same. One sees that this is the case. We can conclude that charge does not accumulate on the insulator enough to give spurious analyzer current readings and that one may take distribution measurements with small time intervals between these measurements.

Effect of a Copper Flow Divider on the Distribution.

In the formation of some aerosols, it is found that a more monodisperse distribution can be obtained by sampling from that part of the flow lying near the axis of the mullite tube as it leaves Oven Number 2. Kerker has found this helpful in the generation of dibutyl phthalate (DBP) and $\text{AgCl}^{11,12}$. The flow divider made to achieve this selective sampling is shown in the inset to Figure 15.

The resulting distribution, Figure 16, may be bimodal. Recall, however, that concentrations of particles smaller than .0133 should probably not be calculated using the EAA. On the other hand, the flow divider was made of copper and pits about 0.5mm deep were observed on the outer surface of the inner tube when the device was removed. Espenscheid observed an undesirable bimodal distribution resulting from corrosion of thermocouples placed inside the mullite tube¹³. Perhaps some of the dispersity and/or seemingly bimodal nature of Figure 16 was a result of Cu contamination.

Note also that the concentration of small particles is much less and that of large particles is much greater than in any other generating scheme tried. We hope to construct a stainless steel flow divider and determine its effect on the distribution.

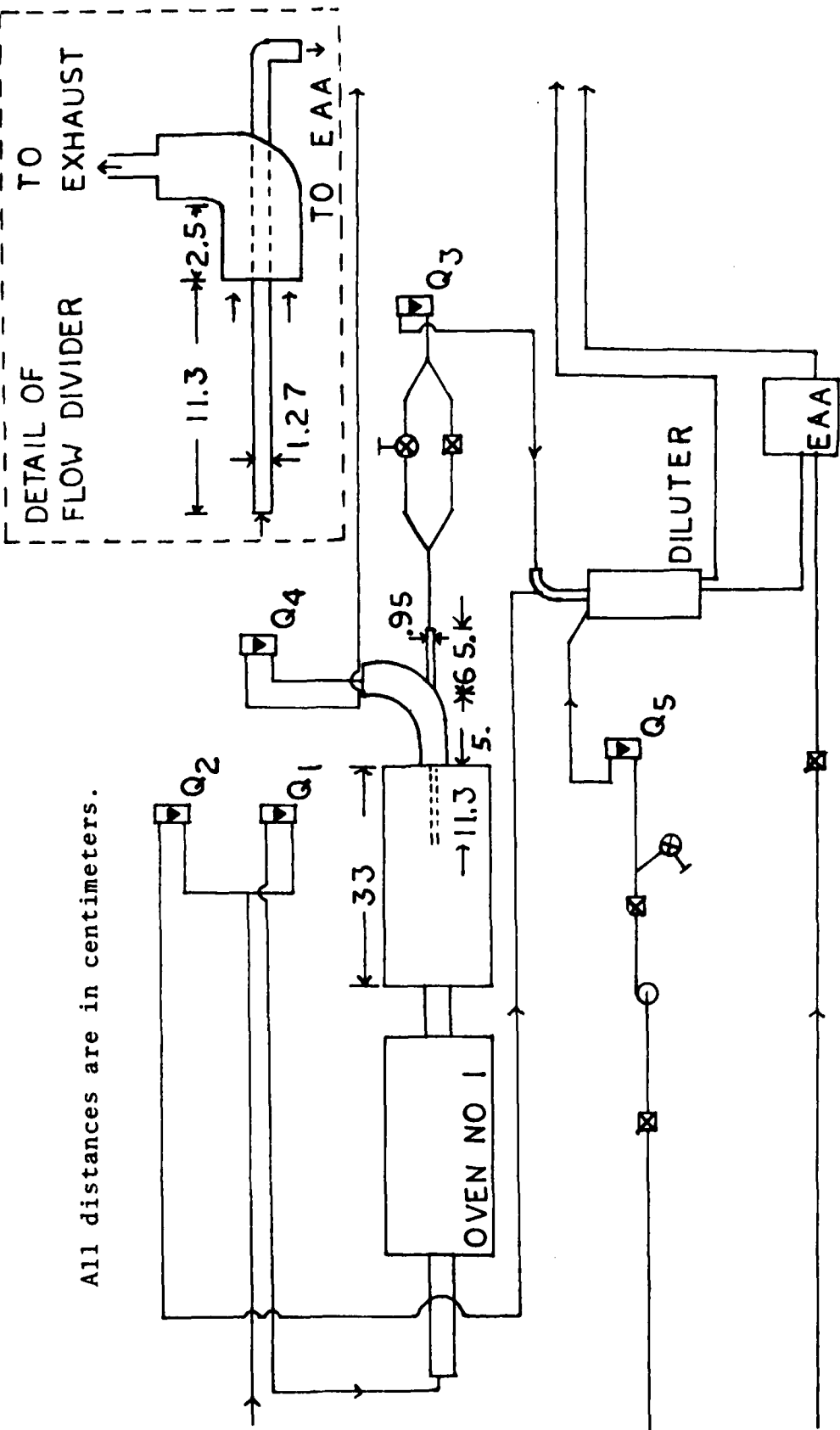


Figure 15 Apparatus Used to Study Effect of a Flow Divider.

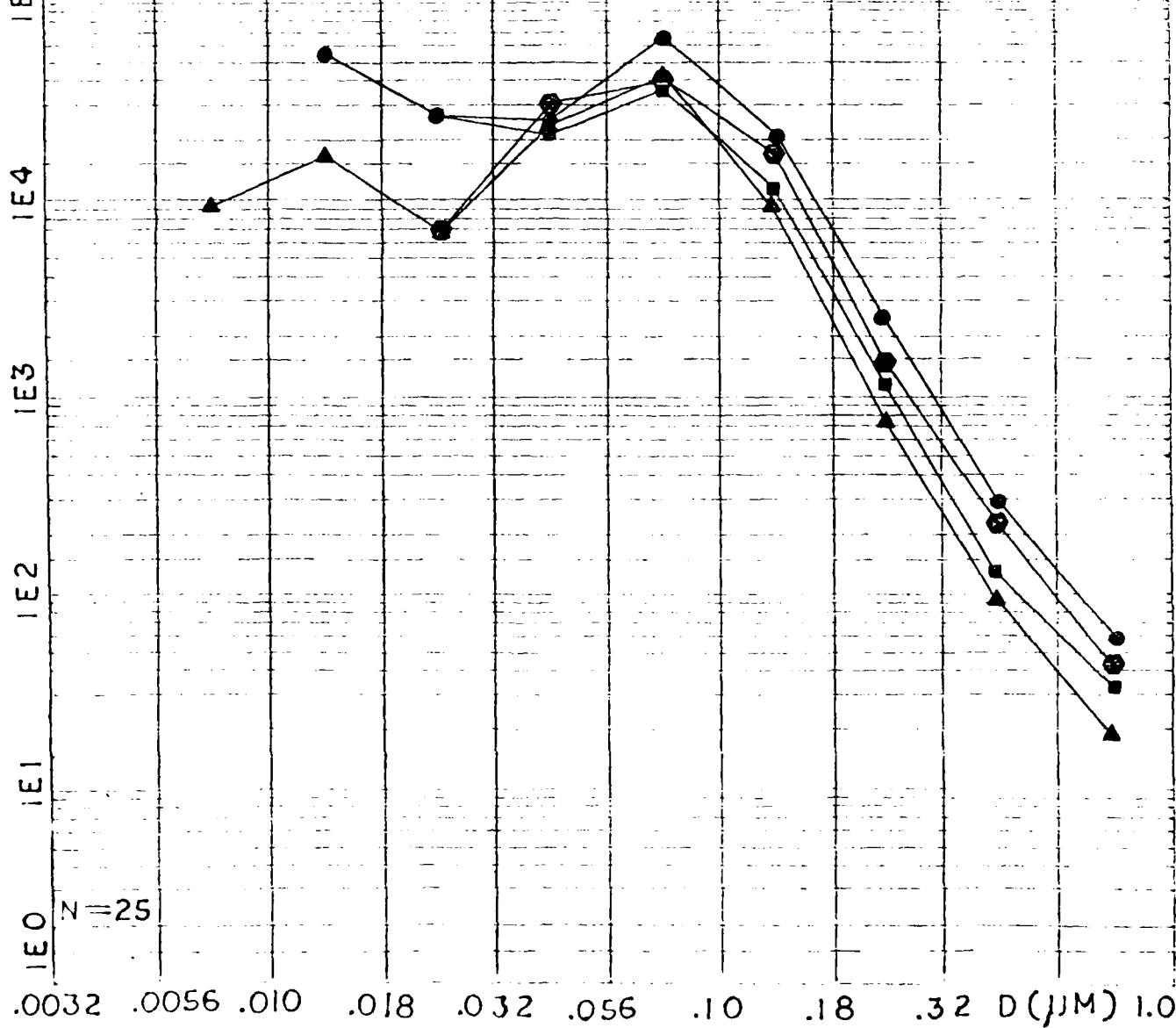
	T ₁ (°C)	T ₂ (°C)	T (HRS)	YR/ MO/DAY	Q ₁ (L/M)	Q ₂ (L/M)	Q ₅ (L/M)
●	755	870	1415	77/1003	2.	20.	30.
■	755	870	1620	77/1003	2.	20.	30.
▲	754	870	0830	77/1004	2.	20.	30.
◆	752	870	0930	77/1004	—	20.	30.

V_I = 10.

Q₃ REGULATES IN ● Q₃ SET AT A VALUE
TYPICAL OF ●, ■, ▲ (0.4 L/M).

26

FIGURE 16

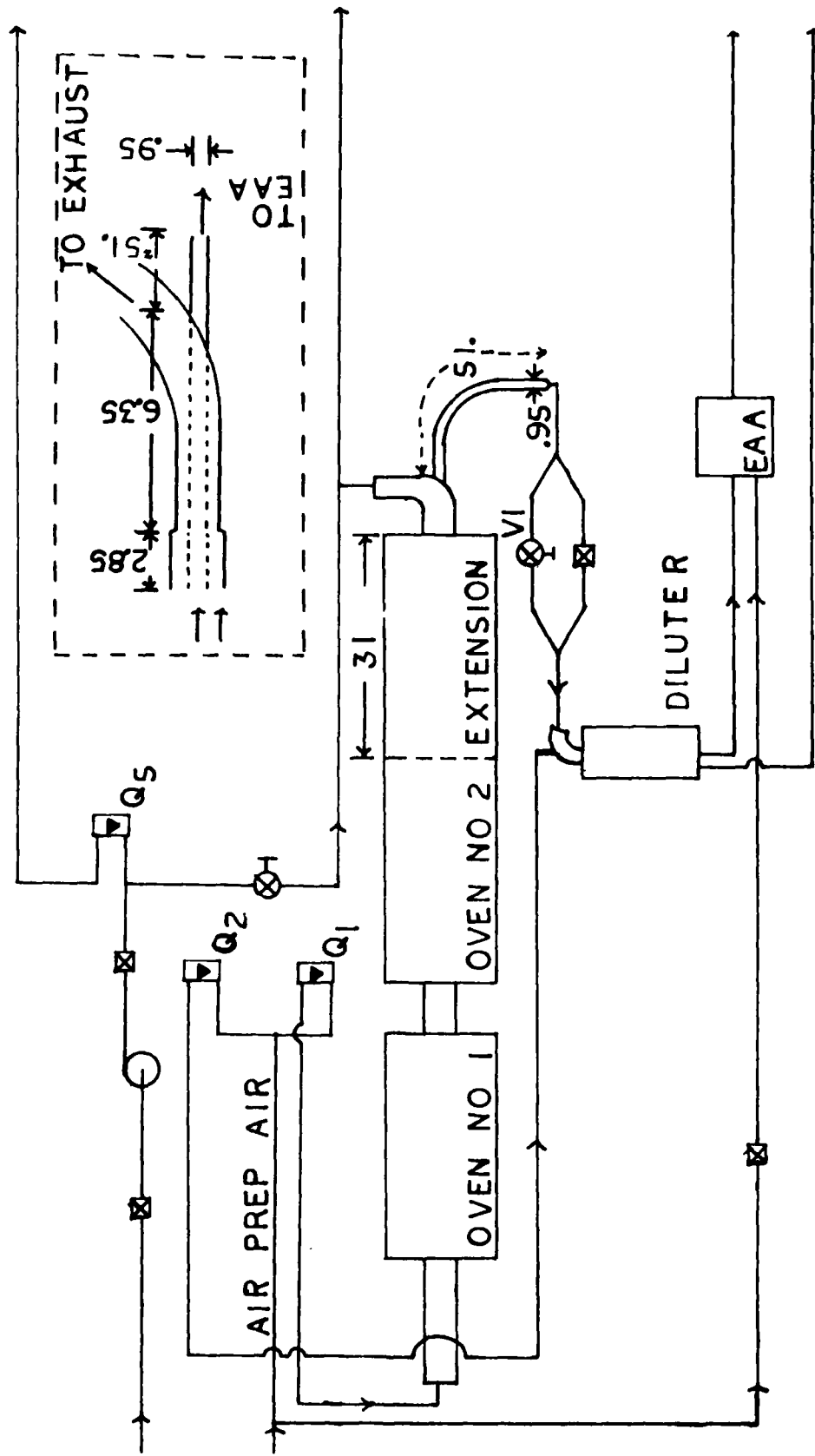


Effect of Slow Cooling and Flow Divider on the Distribution.

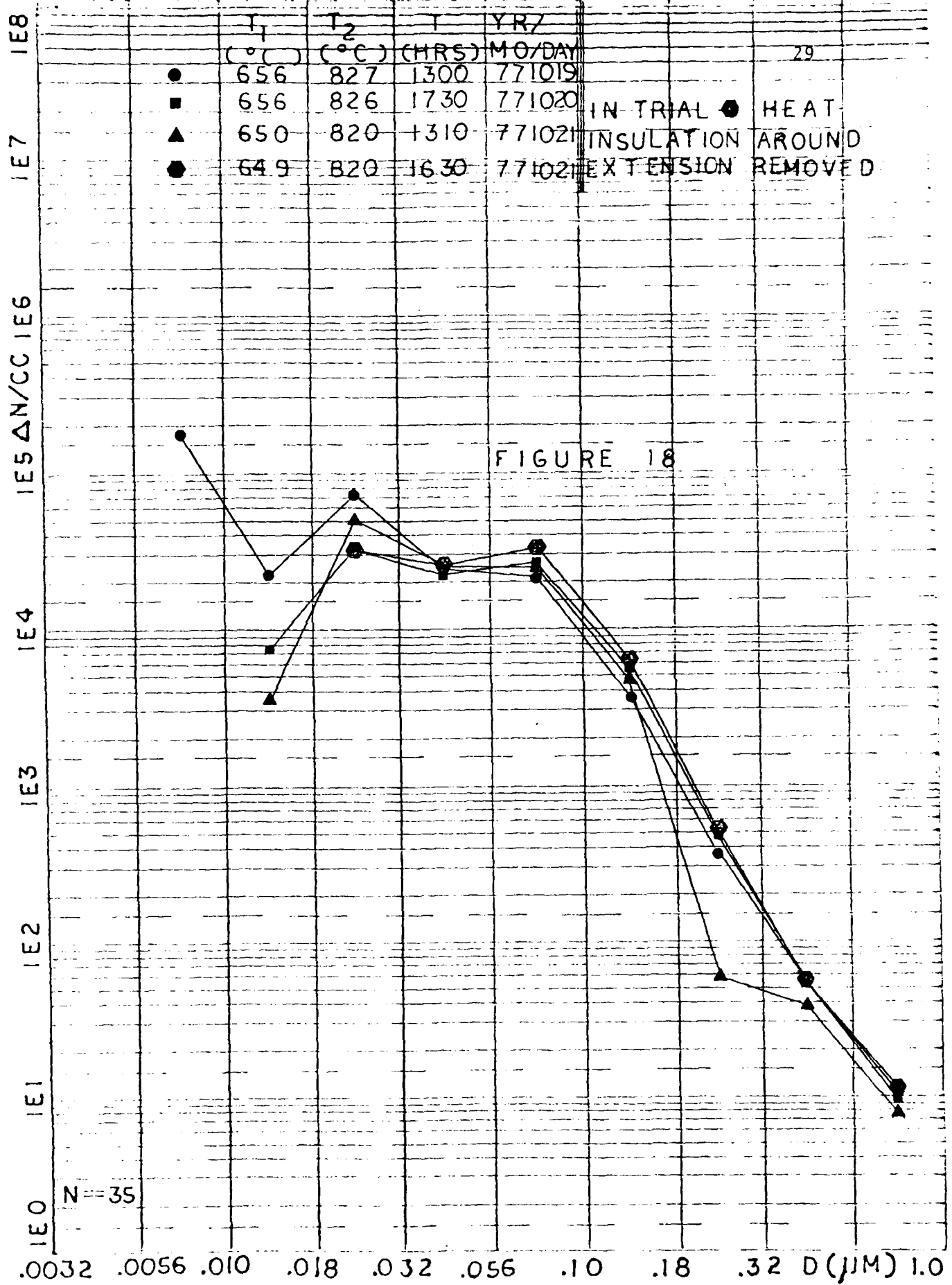
Assume that there are condensation nuclei for the NaCl vapor at the exit of Oven Number 2, and that these nuclei will activate condensation at different supersaturations depending upon their size, let's say. Further assume that nuclei of each size (activating ability) are evenly distributed across the area of the mullite tube as it leaves Oven Number 2. It seems that if the vapor of NaCl is cooled slowly, allowing only a small supersaturation, then only the largest condensation nuclei could activate condensation and these would collect all the condensing NaCl vapor. Since these are assumed to be evenly distributed across the tube, they each have an equal volume of air from which NaCl will condense onto them and hence should produce aerosol particles of equal size, i.e., a monodisperse aerosol.

The oven extension in Figure 17 allows the aerosol to condense more slowly and should provide a more monodisperse distribution. A flow divider, shown in the inset, was also used. The distribution resulting from this, Figure 18, was measured several times on three separate days. For three of the curves it was impossible to compute the concentration for small diameters since the EAA registered an increase in current when the analyzer voltage was increased and this implies a negative concentration. It could very well be that the concentration does decrease at diameters smaller than $.0178\mu\text{m}$ and that a fairly monodisperse distribution was generated.

To assemble the apparatus shown in Figure 17, the mullite tube used in all previous experiments was pulled out, turned through 180° , and pushed in so that the reduced end was only 10cm away from the left hand side of Oven Number 1. Figure 19(A) shows the mullite



All distances are in centimeters.

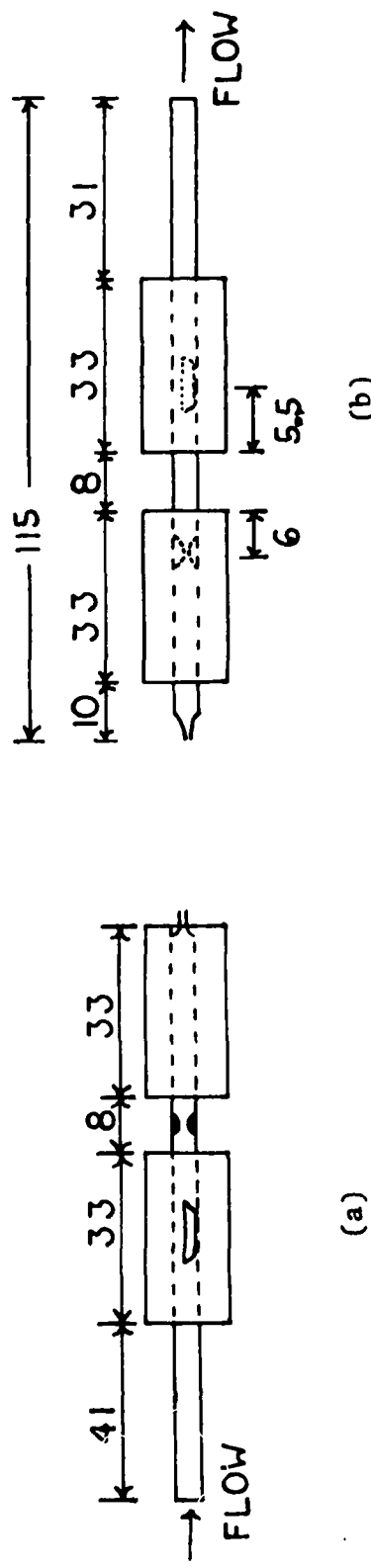


tube in its old position. Also shown are the location of the boat and the condensed NaCl layer on the inside of the tube in the cool region between the two ovens. Figure 19(B) shows the tube in its position when used in the slow cooling scheme. The old position of the boat and the condensed NaCl layer are shown in dotted lines. If NaCl had diffused into the walls of the mullite tube at these two positions, then one would have two more sources of NaCl in addition to that in the boat in Oven Number 1 of Figure 17. These two additional sources could have been responsible for some part of the distribution of Figure 18.

To test this hypothesis, data was taken with Oven Number 1 turned off. The results, shown in Figure 20, indicate that probably the NaCl had diffused into the walls of the mullite tube at the old position of the boat and was now being sublimated away providing the aerosol of Figure 20.

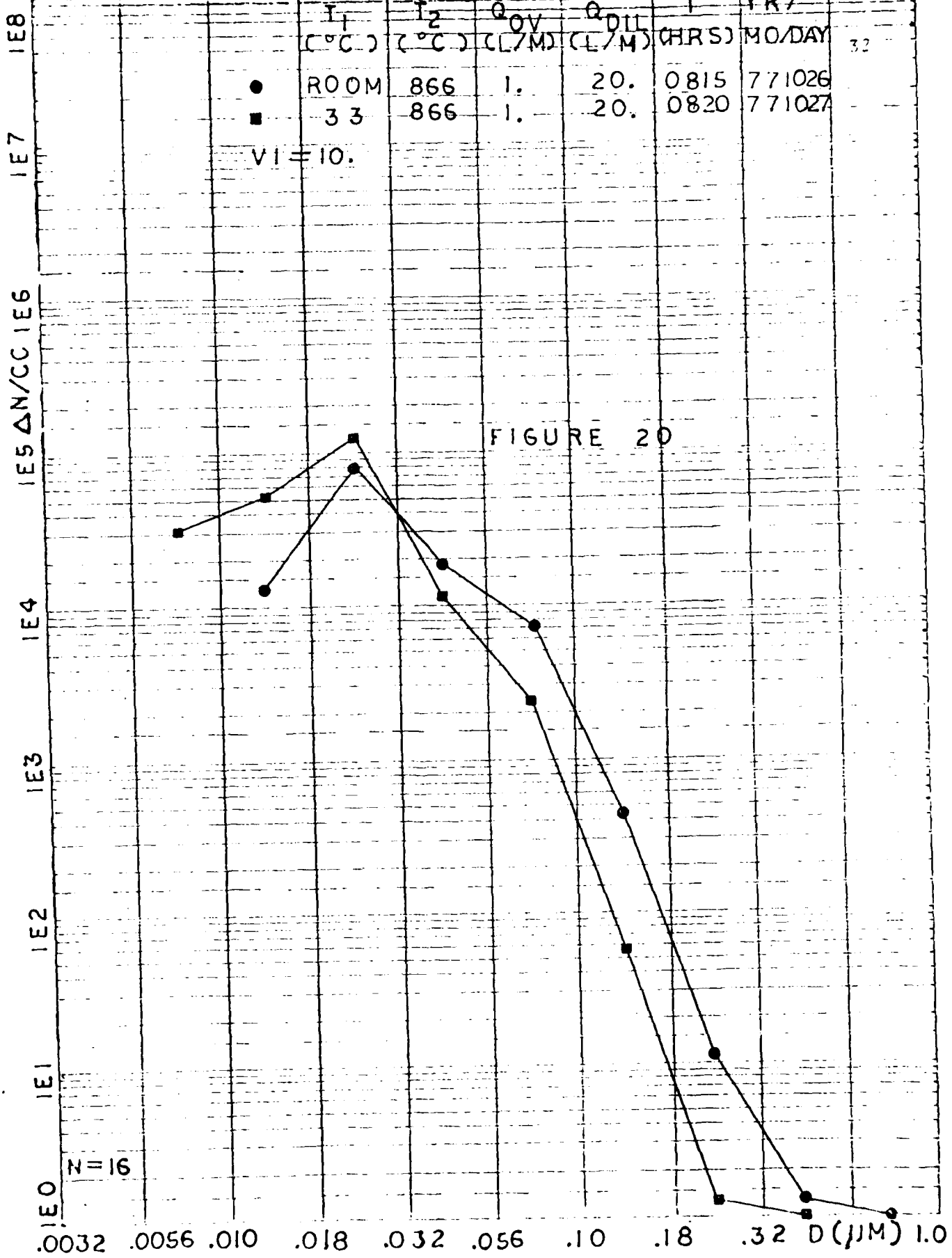
A heating element was also added to the oven extension and this region was brought to about 550°C. This also caused the concentration of the large diameter particles to increase (not shown in any graphs). After about 2 weeks, the concentration at all sizes had decreased yet was still on the order of 10^3 at $D = .03\mu\text{m}$. When the temperature in the extension was decreased to 150°C, the concentration for all diameters went to zero. Therefore, many particles must have originated in the extension to Oven Number 2.

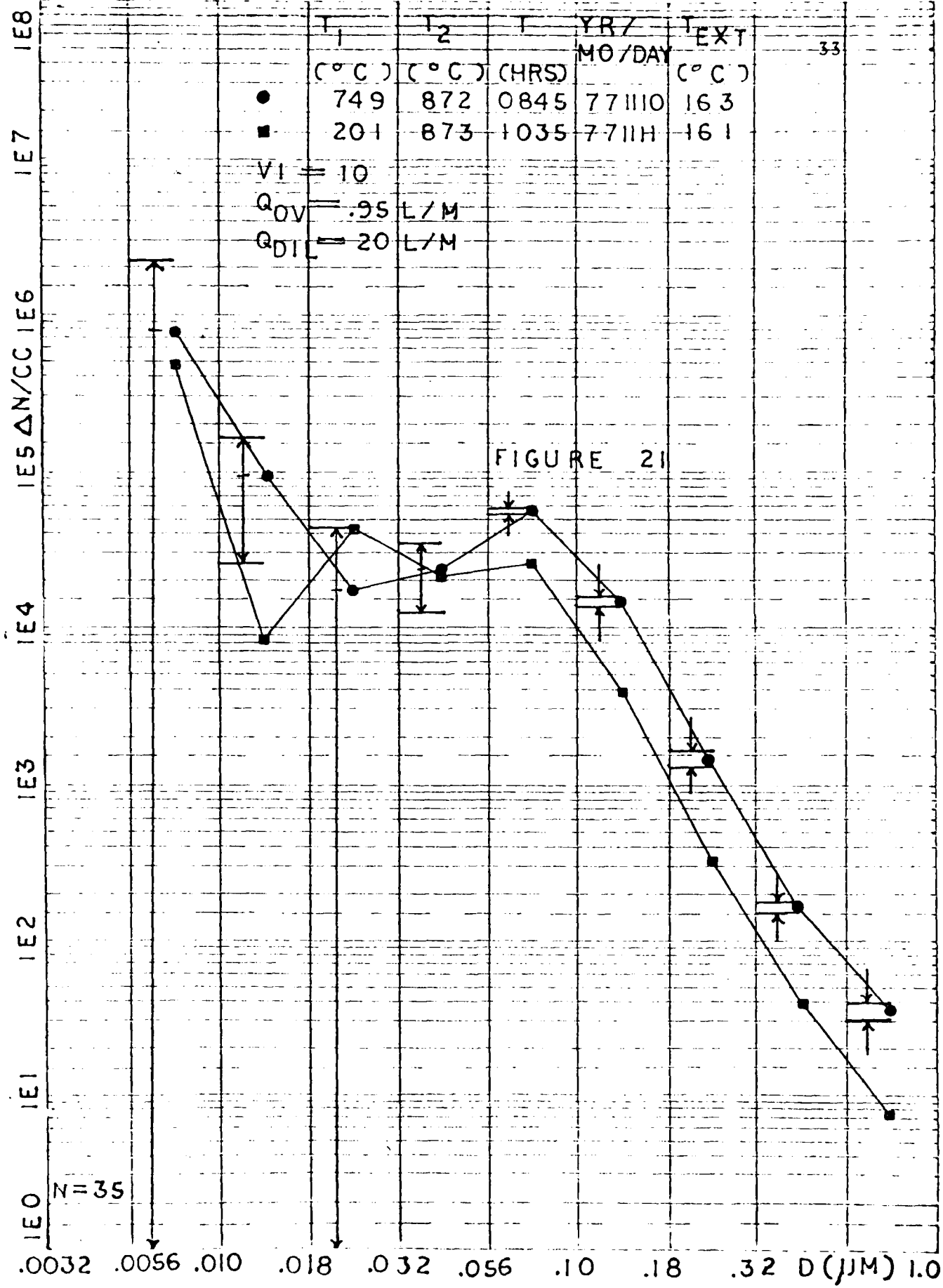
Figure 21 depicts the results of two successive experiments done after the work described above. The first is with the two ovens at their normal operating temperatures of 750°C and 870°C and seems bimodal. The second or later experiment is with Oven Number 1 at 200°C. Although one would expect a low concentration at all diameters,



All distances are in centimeters.

Figure 19 Two Orientations of Mullite Tube.





the actual distribution is almost the same with Oven Number 1 off as it is with it on! It could be that with Number 1 on, NaCl is both condensing onto and sublimating off of the wall of the extension, but that condensation is dominant. With Oven Number 1 off, there is no condensation on the wall of the tube in the extension but sublimation still exists giving rise to a considerably concentrated aerosol.

Effect of Immediate Turbulent Dilution on Distribution.

In all previous experiments when the aerosol was diluted immediately upon leaving Oven Number 2, the dilution air came through the run of the tee and the aerosol came in by the branch. The aerosol airflow, being 0.05 of the dilution airflow, was probably not mixed well until it traveled quite a ways down the tube. Some of the vapor probably cooled much more rapidly than did other parts giving rise to dispersity. Turbulence at the mixing tee would provide good mixing and a more uniform cooling for all parts of the aerosol air.

More turbulence and more uniform cooling could be achieved with the tee oriented as shown in Figure 22. The distribution resulting from this, Figure 23, has a hint of a secondary peak at $D \approx .07\mu\text{m}$. Also shown in Figure 23 is the distribution for when the tee was in its old orientation. Unfortunately, only one set of data was taken with the tee oriented in the new way and firm conclusions cannot be drawn.

Effect of a Double Dilution and Small Transit Time.

At the high concentrations and small diameters being used here, coagulation proceeds rapidly. Even if one began with a fairly mono-disperse system, coagulation would quickly provide more dispersity.

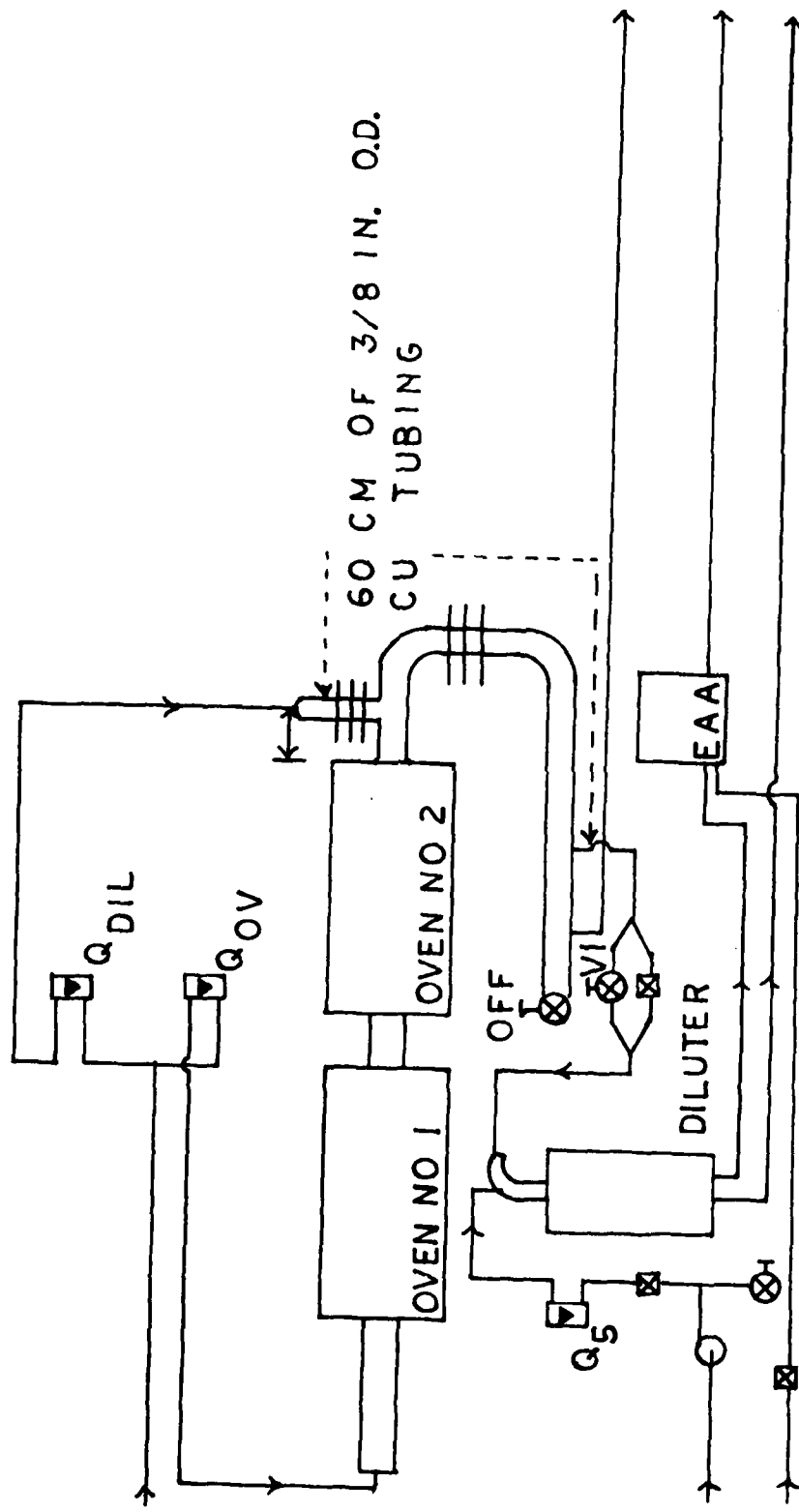
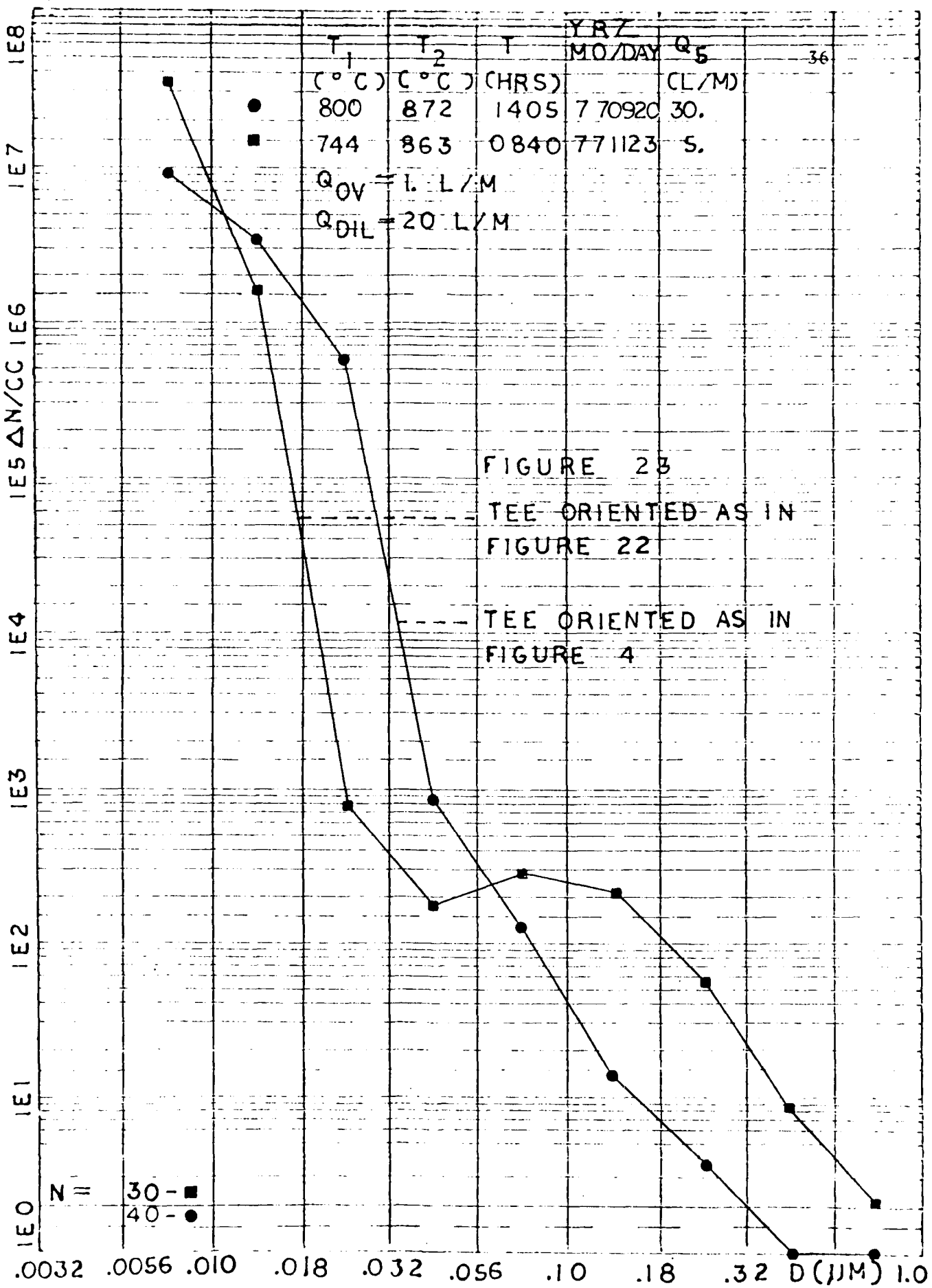


Figure 22 Apparatus Used to Study Effect of Immediate, Turbulent Dilution.



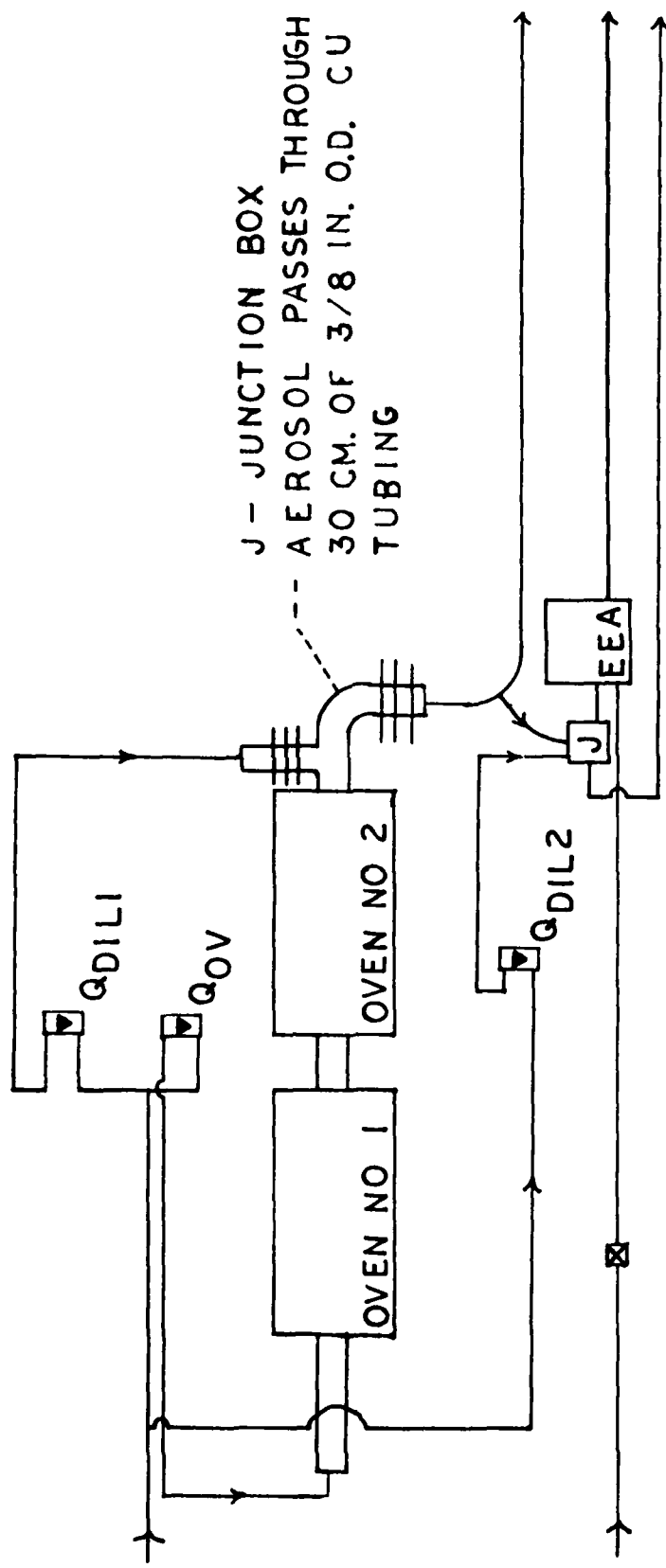
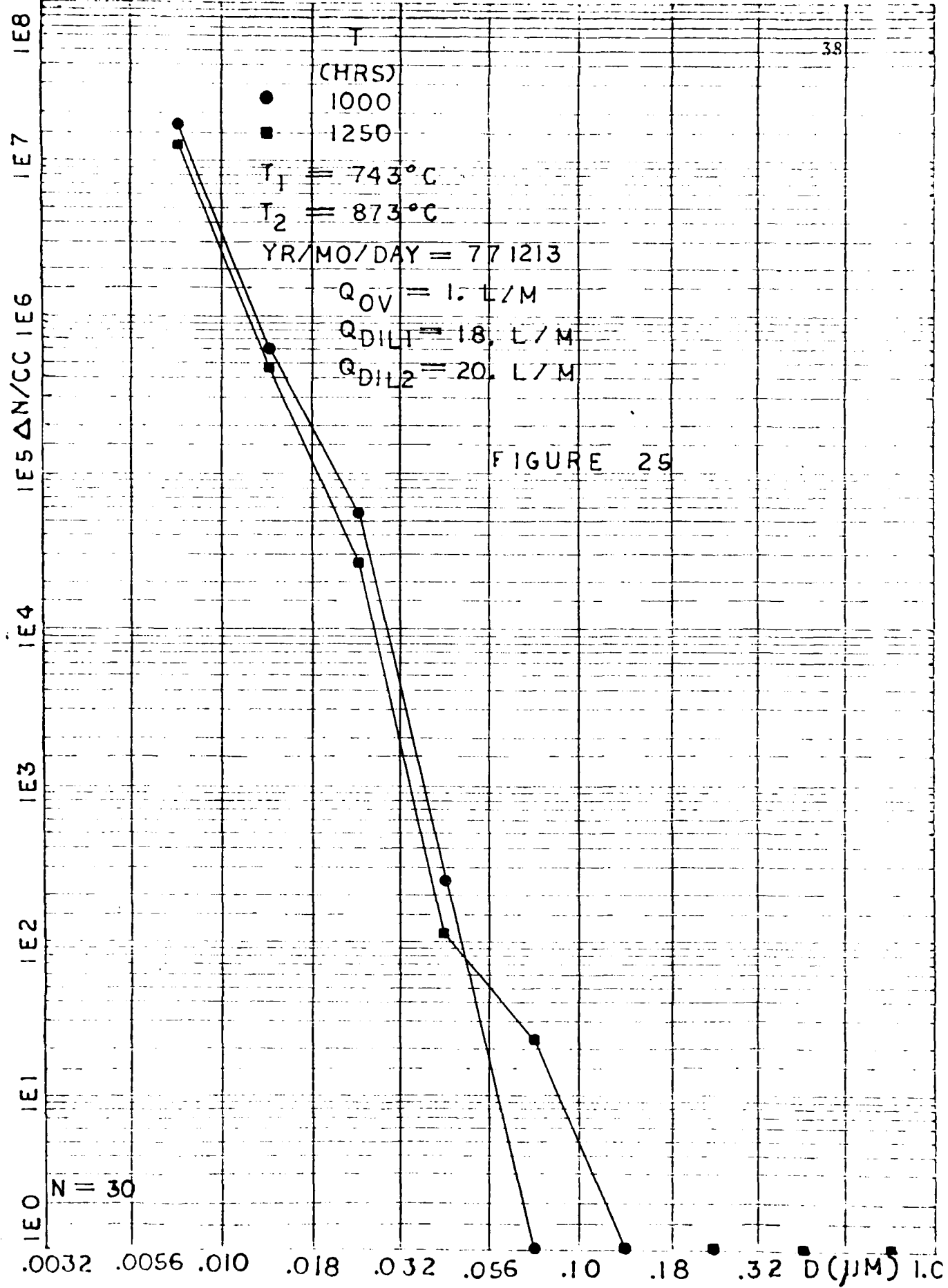
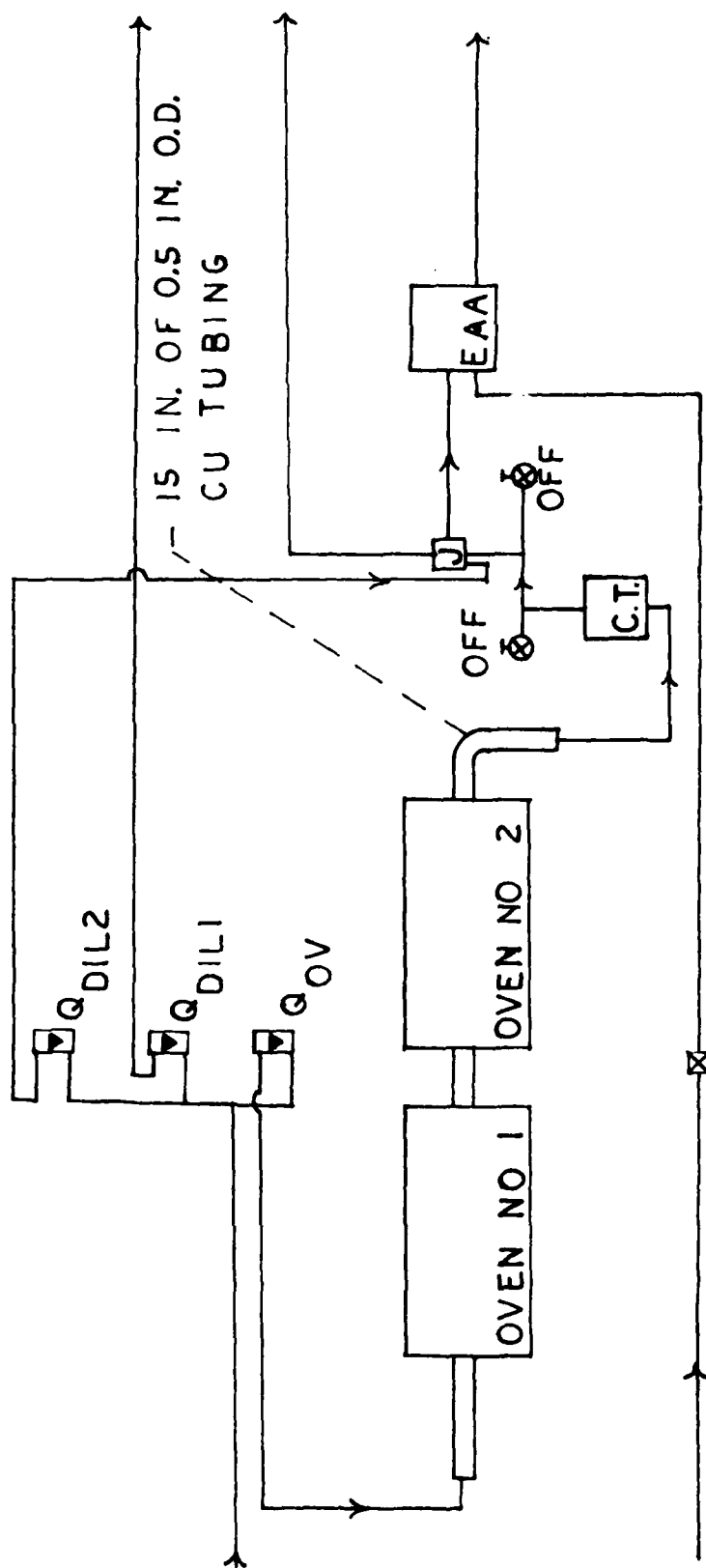


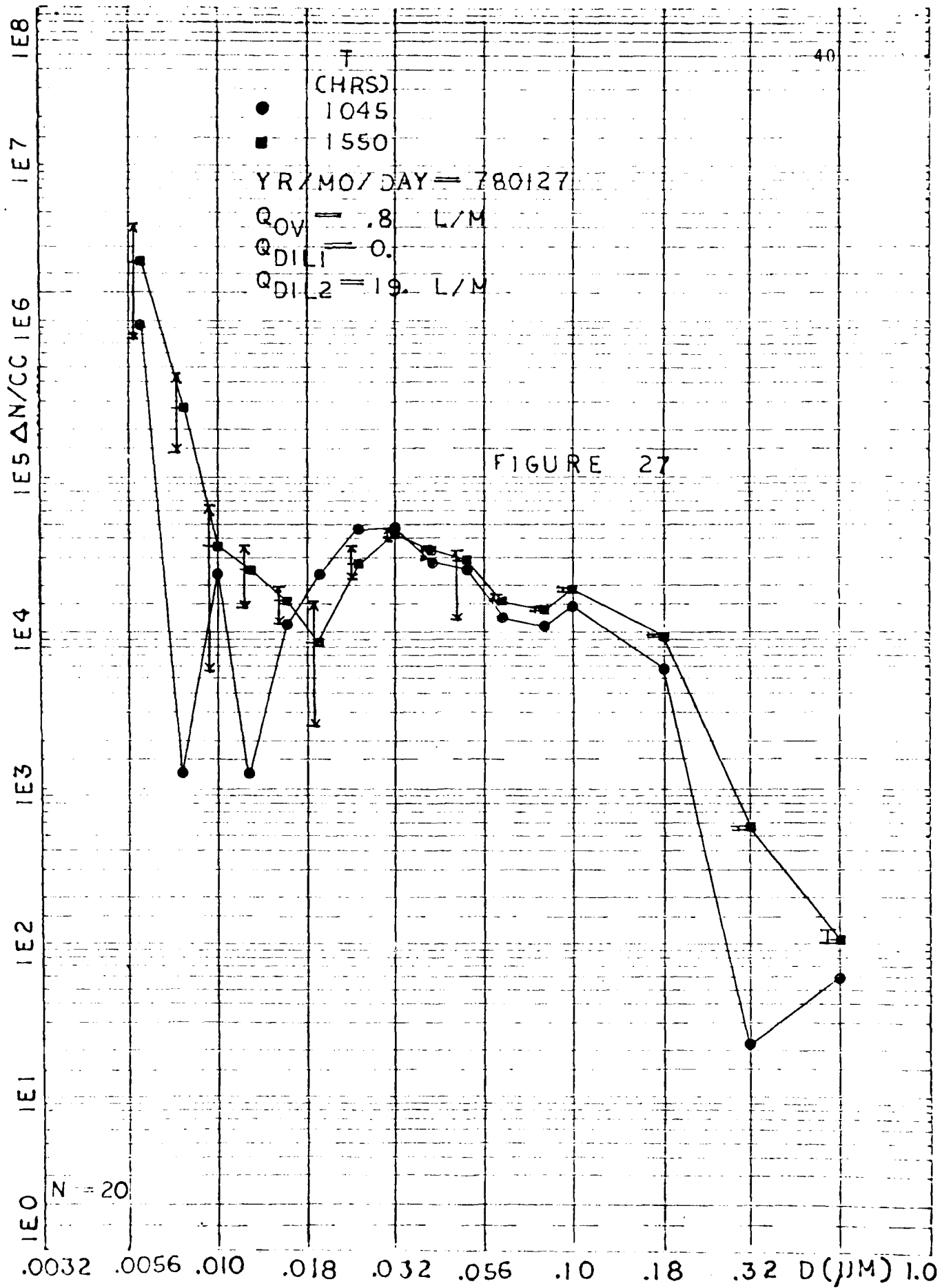
Figure 24 Apparatus Used to Study Effect of Double Dilution and Small Transit Time.





C.T. - COAGULATION TANK. VOLUME = 2.9 LITERS
 J - JUNCTION BOX. VOLUME = 0.3 LITER

Figure 26 Apparatus Used to Study Effect of Single Dilution and Long Transit Time.



For a monodisperse aerosol the concentration, n , as a function of time, t , is

$$n = \frac{n_0}{1 + n_0 k_o t}$$

where n_0 is the initial concentration, k_o is the coagulation constant, and t is time¹⁴.

The generating scheme of Figure 24 is designed to minimize coagulation. The dilution tee is oriented to give uniform cooling. The minimum amount of tubing was used to transport the aerosol to the Junction Box. A second dilution is achieved at the Junction Box and the EAA is connected directly to the Junction Box.

The distribution, illustrated in Figure 25, drops from relatively high concentrations to zero over a relatively short range of diameters with no hint of any secondary peaks.

In contrast to the above scheme, the dilution scheme in Figure 26 was assembled. Here the oven air was not diluted as it left Oven Number 2. The Q_{ov} being 0.8 l/m and the volume of the Coagulation Tank being 2.9 l means that the aerosol spent about 3.6 minutes coagulating before it was diluted. The resulting distribution, Figure 27, is in sharp contrast with that in Figure 25. One concludes that rapid dilution and small transit times yield many small particles and very few large ones.

III. CONCLUSION

From the preceding experiments, we can say the following:

1. Roughly 10^5 particles/cc in the range $.01\mu\text{m}$ to $.05\mu\text{m}$ can be generated.
2. As T_1 increases, the total number of particles generated increases.

3. The Whitey valve had no measurable effect on the distribution. Impaction considerations do not contradict this.

4. Very dry air (dew point $\approx -20^{\circ}\text{C}$) causes the EAA to operate slightly outside of its specifications.

5. A double dilution and a small transit time yield a very large number of small particles and literally no large particles.

It was stated in the introduction that the laboratory aerosol should be such that the number of particles with diameters between $0.01\mu\text{m}$ and $0.05\mu\text{m}$ should be 500 times the number of particles with diameter greater than $0.05\mu\text{m}$. One can see that the distribution of Figure 25 does satisfy this requirement. Note that the apparent number of particles with diameter less than $0.01\mu\text{m}$ is very high. It was originally hoped that we could achieve a distribution having a maximum in the range $.01\mu\text{m}$ to $.05\mu\text{m}$. Some of the distributions illustrated in this paper do, in fact, have a maximum in this range, but they are not very monodisperse. See Figure 16 for example. These generating schemes were abandoned because of their heterodispersity.

We have recently learned that the EAA's resolution is sufficiently poor that distributions such as those in Figures 16 and 18 could have been considerably more monodisperse than is shown in these figures. We are therefore intending to try some of the generating schemes again. Specifically, we hope to further investigate the effect of slow cooling and a stainless steel or ceramic flow divider.

REFERENCES

1. Espenscheid, W. F., E. Matijevic, and M. Kerker, *Aerosol Studies by Light Scattering III. Preparation and Particle Size Analysis of Sodium Chloride Aerosols of Narrow Size Distribution*, J. of Physical Chemistry, Volume 68, Number 10, pp. 2831-2842 (1964).
2. Kitani, Susumu, and Sohei Ouchi, *Preparation of Monodisperse Aerosols of Sodium Chloride*, J. of Colloid and Interface Science, Volume 23, pp. 200-202 (1967).
3. Espenscheid, Matijevic, and Kerker, *Aerosol Studies*.
4. Liu, Benjamin Y. H., Kenneth T. Whitby, and David Y. H. Pui, *A Portable Electrical Analyzer for Size Distribution Measurement of Submicron Aerosols*, J. of the Air Pollution Control Association, Volume 24, Number 11, pp. 1067-1072 (1974).
5. Liu, Benjamin Y. H. and David Y. H. Pui, *On the Performance of the Electrical Aerosol Analyzer*, J. of Aerosol Science, Volume 6, pp. 249-264 (1975).
6. *Operating and Service Manual Model 3030 Electrical Aerosol Size Analyzer*, Thermo Systems, Inc., 2500 Cleveland Avenue N., St. Paul, Minnesota, 55113, page 10.
7. Kitani and Ouchi, *Preparation of Monodisperse Aerosols*.
8. Gentry, James W., and Chung H. Ahn, *The Effect of Flow Rate and Temperature on the Particle Size Distribution of Lithium Bromide Aerosols*, Atmospheric Environment, Volume 8, pp. 765-771.
9. Friedlander, S.K., Smoke, Dust, and Haze (John Wiley & Sons, New York, 1977), p. 107.
10. Kitani and Ouchi, *Preparation of Monodisperse Aerosols*.
11. Nicolaon, G., D. D. Cooke, E. J. Davis, M. Kerker, and E. Matijevic, *A New Liquid Aerosol Generator II. The Effect of Reheating and Studies on the Condensation Tone*, J. of Colloid and Interface Science, Volume 35, Number 3, pp. 490-501 (1971).
12. Kerker, M., and V. Hampl, *Scavenging of Aerosol Particles by a Falling Water Drop and Calculation of Washout Coefficients*, J. of Atmospheric Sciences, Volume 31, pp. 1368-1376 (1974).
13. Espenscheid, Matijevic, and Kerker, *Aerosol Studies*.
14. Fuchs, N. A., The Mechanics of Aerosols, (Pergamon Press, New York, 1964), p. 290.

APPENDIX G
MONODISPERSE AEROSOL GENERATION EFFORTS

M. B. Trueblood
January, 1979

The size range of interest is from .01 μm to .05 μm . The monodisperse aerosol is supplied by a Model 3071 Electrostatic Classifier, made by Thermo Systems, Inc., which is fed somewhat polydisperse aerosol by a two furnace generator*. The Electrostatic Classifier (EC), shown in Figure D, uses a Krypton 85 bipolar charger to establish a bipolar equilibrium charge level on the particles. In the .01 μm to .05 μm range most particles remain neutral, about 10% gain a +1 or -1 charge, and 1% or so gain a +2 or -2 charge. The polydisperse aerosol then enters the annular volume of the differential mobility analyzer (DMA) and flows smoothly along the inner wall of the outer cylinder. Clean sheath air enters the annular volume through holes in the hollow top end of the central rod. The DMA takes advantage of the fact that the particles' electric mobility is a monotonically decreasing function of particle diameter. An electric field between the two cylinders forces positively charged particles inward. Small particles, having a large electric mobility, are precipitated very soon. Large particles, having a small electric mobility, are deflected only slightly and pass on through with the excess air. Holes in the hollow bottom end of the central rod allow particles of a narrow size range to pass through with a small flow of air giving rise to the monodisperse aerosol.

Since doubly charged .0731 μm particles have the same electric mobility as singly charged .05 μm particles, it is necessary to minimize the concentration of .0731 μm particles in the polydisperse aerosol input while still having about 10^5 particles/ cm^3 at .05 μm in the monodisperse output of the E. C.

*Kitani, Susumu and Sohei Onchi: "Preparation of Monodisperse Aerosols of Sodium Chloride", J. of Colloid and Interface Sci., Volume 23, pp. 200-202 (1967).

It was found in this laboratory that immediate, turbulent quenching of the furnace air yielded a size distribution that fell from 10^5 particles/cm³ for the range .010 μm to zero for the range .056 μm - .100 μm . This eliminated the .0731 μm particles but yielded too few at .05 μm . On the other hand, allowing the aerosol several minutes to coagulate before dilution* yielded 10^4 particles/cm³ in the range .0447 μm - .0562 μm but also about 10^4 particles/cm³ in the range .071 μm - .089 μm .

To strike a happy medium we constructed the system shown in Figure 1G. Notice that here the second furnace is actually composed of three furnaces with successive furnaces set at successively lower temperatures. The particles formed in the 8 cm cool region are almost completely vaporized by furnace number two, leaving only small re-evaporation nuclei. These re-evaporation nuclei serve as condensation nuclei for the vapor as it passes through furnaces three and four. If one assumes that the re-evaporation nuclei are evenly distributed across the cross sectional area of the tube, then each one has an equal volume of air around it and will collect an equal amount of NaCl vapor, and should grow to the same size.

Three size distributions with the fourth furnace temperature T_4 as parameter are shown in Figure 2G. These are the size distributions just as the aerosol leaves the last furnace. Note that for $T_4 = 764^\circ\text{C}$ the concentration of particles in the .047 μm - .053 μm range is about $10^5/\text{cm}^3$ whereas that in the the range .068 μm - .080 μm is less by an order of magnitude. It seems that we are headed in the right direction to deliver many .05 μm particles and yet very few .0731 μm ones.

Size distribution measurements on the monodisperse aerosol output of the E.C. using a continuous flow diffusion chamber (CFD)

*Trueblood, Max, J. M. Carter, S. H. Suck, D. R. White and J. L. Kassner, Jr.: "Progress Made in Generating a Monodisperse Aerosol of Sodium Chloride Using Two Furnaces", Graduate Center for Cloud Physics Research Technical Report, University of Missouri-Rolla, 14 April 1978.

developed by Alofs and co-workers* have been made in this laboratory. In the CFD the aerosol is subjected to an accurately known supersaturation, and the water drops grown on the aerosol particles are individually counted. Particles with a critical supersaturation S_c less than the applied supersaturation S produce large water drops while the inactive particles do not. The value of S_c can be related to the dry diameter D of a salt particle using a standard theory.

The results of these CFD measurements, shown in Figure 3G, plot the dry diameter D as calculated from the CFD supersaturation as the abscissa, and the corresponding cumulative concentration N of particles larger than this size as the ordinate. The median diameter was $.049 \mu\text{m}$, very close to the $.05 \mu\text{m}$ setting of the E.C. Also shown is dN/dD which should be a spike centered at $.05 \mu\text{m}$ if all systems were operating ideally. Although the aerosol is not perfectly monodisperse, the standard deviation in the diameter is $.0085 \mu\text{m}$, a result very nearly the same as the Naval Research Lab obtained** with their classifier made by Thermo-Systems, Inc.

During the first routine cleaning of the E.C. we found striations of NaCl deposited on the walls of the central rod and the outer cylinder of the differential mobility analyzer. See Figure 4G. This is caused by the fact that the sheath air enters the annular volume by exiting eight holes in the hollow top end of the central rod. A dacron screen just below these eight holes is supposed to smoothen the sheath air flow but it is insufficient. Not only does the axial velocity of the sheath air depend on θ , but there is probably a radial velocity component too which causes the aerosol laden air to be pushed in the $+\hat{\theta}$ or $-\hat{\theta}$ direction leaving an aerosol free volume. Surely this damages the monodispersity of the instrument.

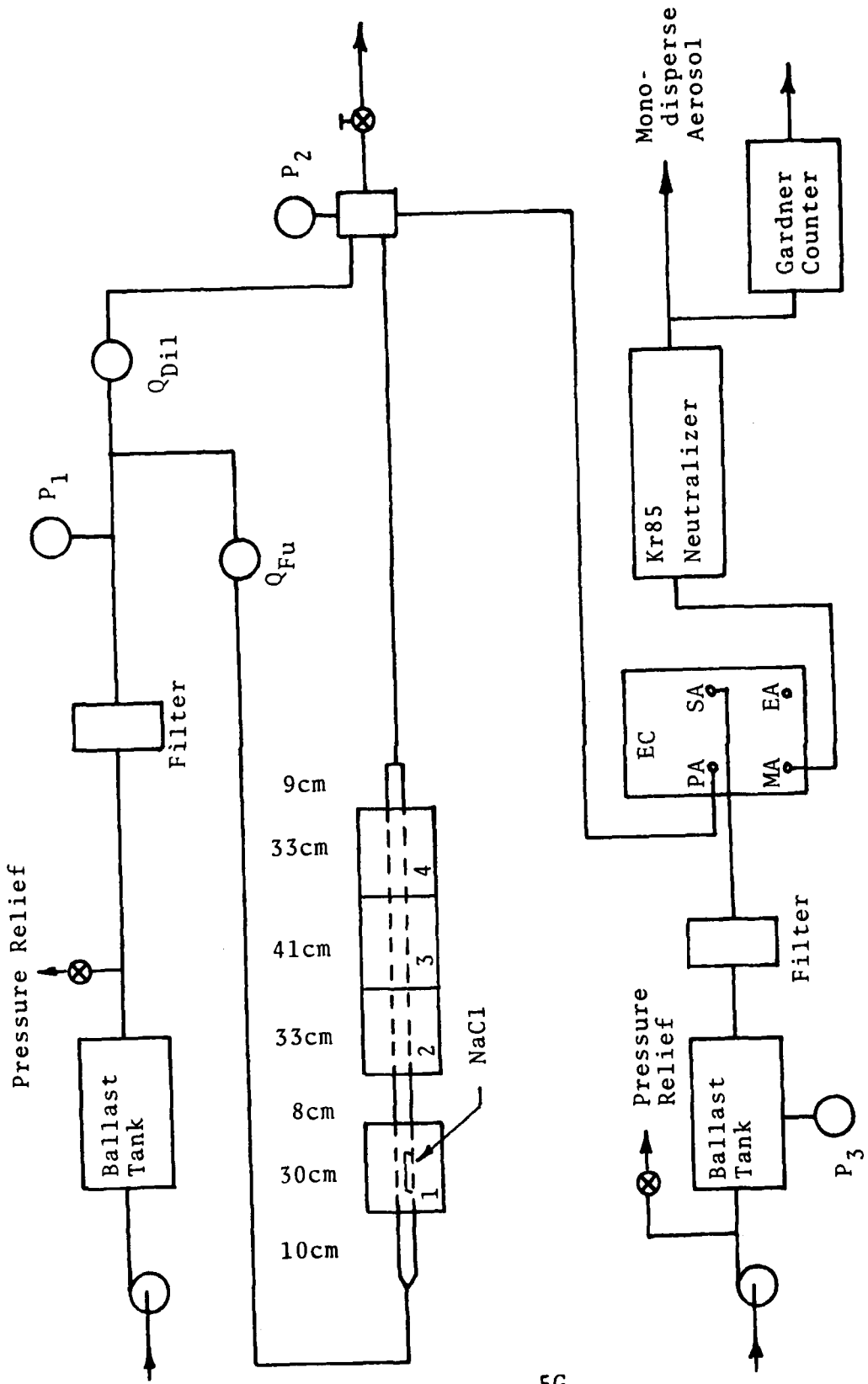
*Alofs, D. J.: "Performance of a Dual Range Cloud Nucleus Counter", *J. Appl. Meteor.*, 17, pp. 1286-1297 (1978).

**Gerber, H. E., W. A. Hoppel and T. A. Wojciechowski: "Experimental Verification of the Theoretical Relationship Between Size and Critical Supersaturation of Salt Nuclei", *J. Atmos. Sci.*, 34, pp. 1836-1841 (1977).

Another problem is that the entrance port for the polydisperse aerosol is poorly designed. The port is much too long axially which means that the electric field, which is supposed to have no Z dependence, would in fact be significantly distorted. Also the polydisperse aerosol inlet port forces this flow to negotiate several abrupt changes in direction. Although one probably need not concern himself with inertial deposition at these small sizes, some turbulence may well be caused here. Furthermore the monodisperse aerosol outlet forces this flow to negotiate several sharp corners.

Also the excess flow is θ dependent as manifested by the large accumulation of aerosol on the side of the tube above the single exit port. A brass plate with many small holes is supposed to remove the θ dependence, but it is not sufficient.

We are currently in the process of designing our own Electrostatic Classifier which will eliminate many of these problems. Our design, shown in Figure 5G, brings the sheath air in through a series of fine wire cloths and honeycomb that will remove any θ dependence from the velocity profile and minimize the radial dependence. The polydisperse aerosol enters at about 5° with the tube axis minimizing turbulence and separation from the walls. The polydisperse aerosol inlet port is small axially, minimizing the electric field distortion. The width of the port is made so that the polydisperse aerosol velocity will match that of the sheath air. The same considerations have been used in designing the monodisperse aerosol outlet port. Any θ dependence of the excess flow will be minimized by the pressure drop across the fine wire cloths at the bottom of the cylinders.



5G

Figure 1G. Apparatus used to generate monodispersed aerosols in the range 0.01 μm to 0.05 μm .

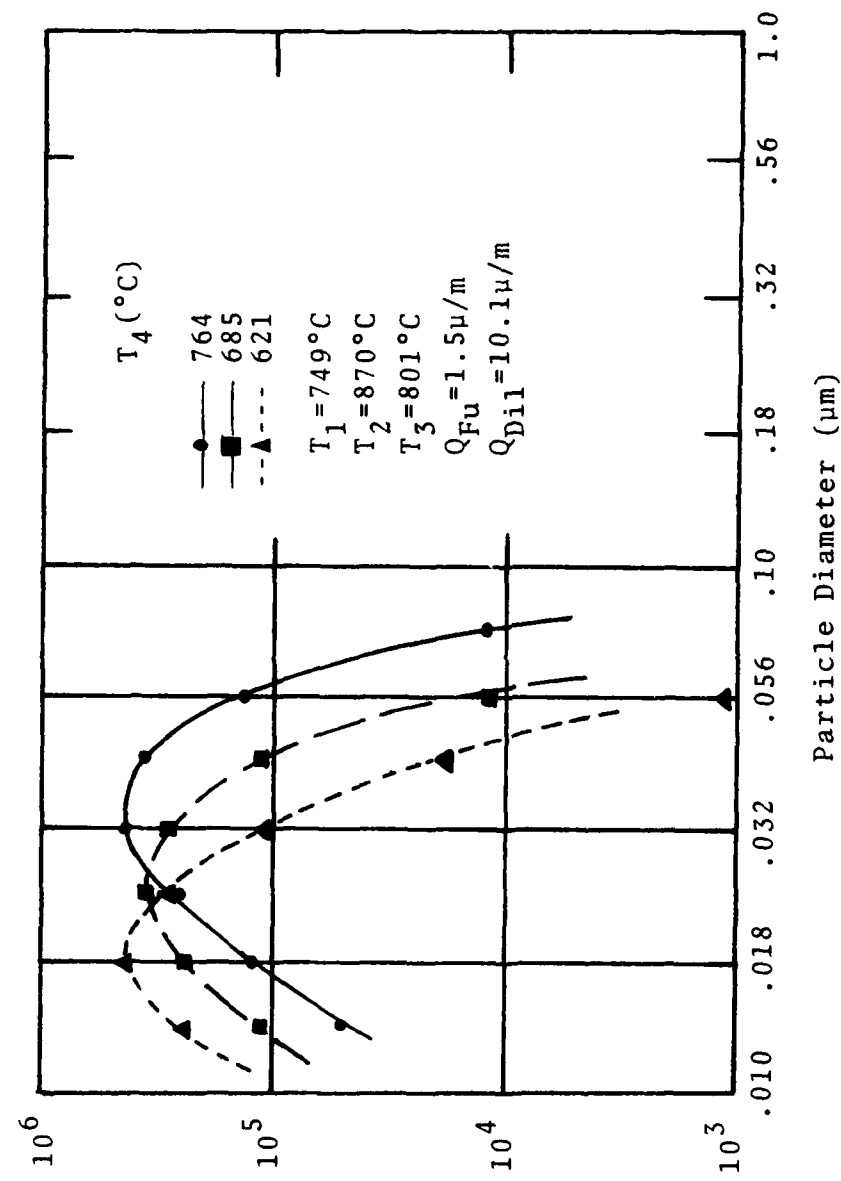


Figure 2G. The size distribution obtained for several values of the fourth furnace temperature, T_4 .

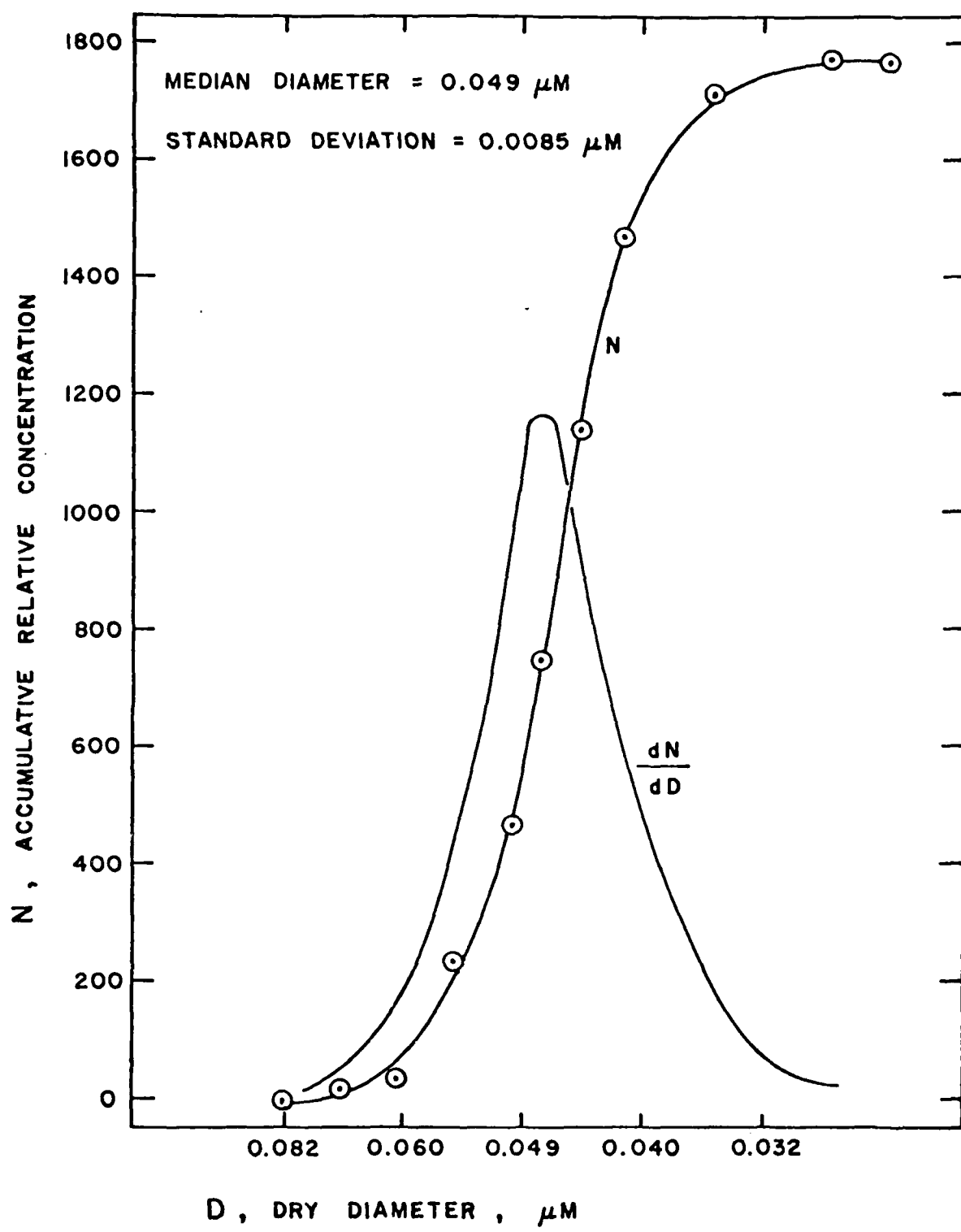


Figure 3G. CFD analysis of a NaCl aerosol generated by the vaporization method and passed through an electrostatic classifier which was set to pass 0.05 μm particles.

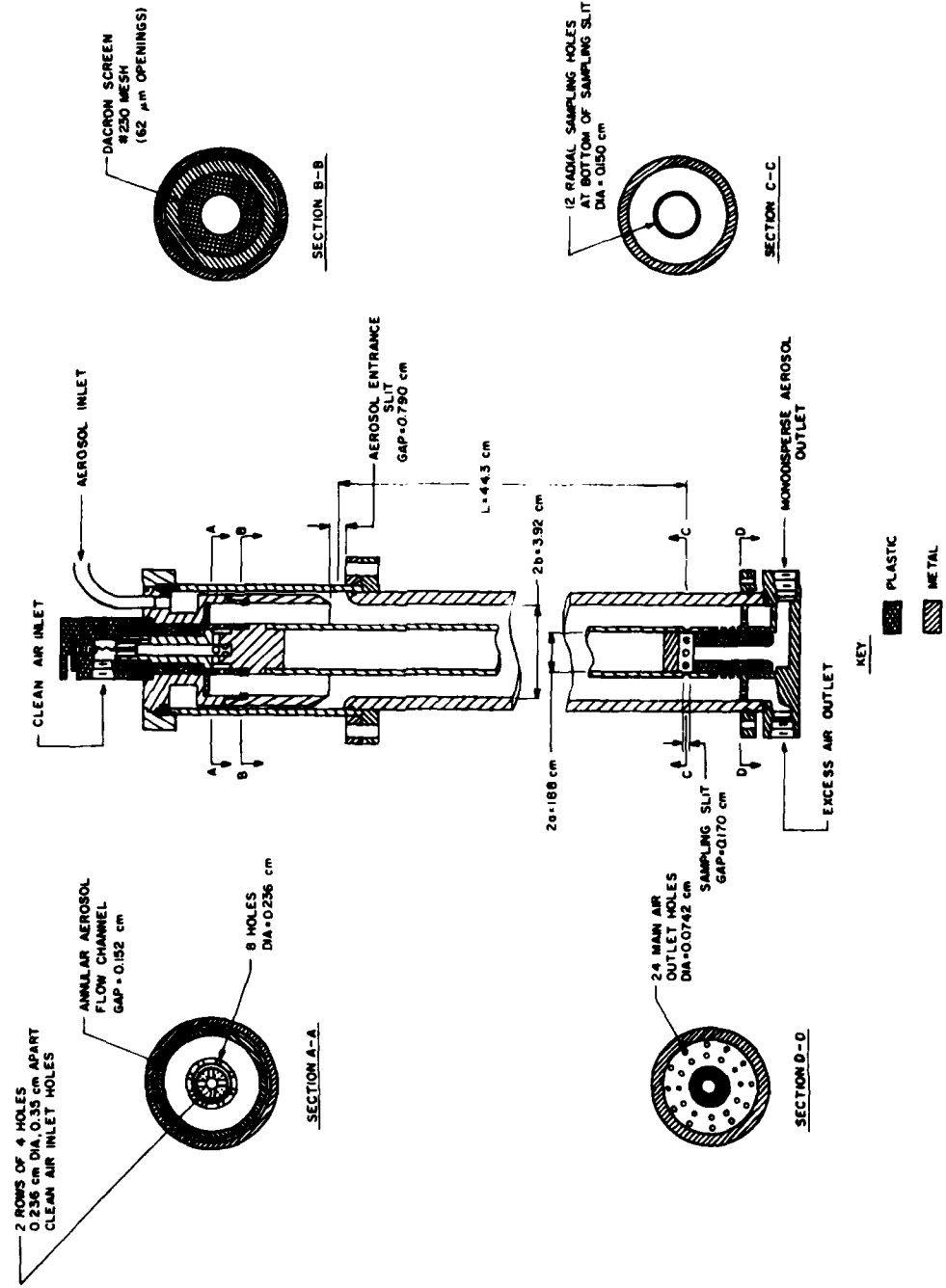


Figure 4G. Electrostatic Classifier (Cross-section).

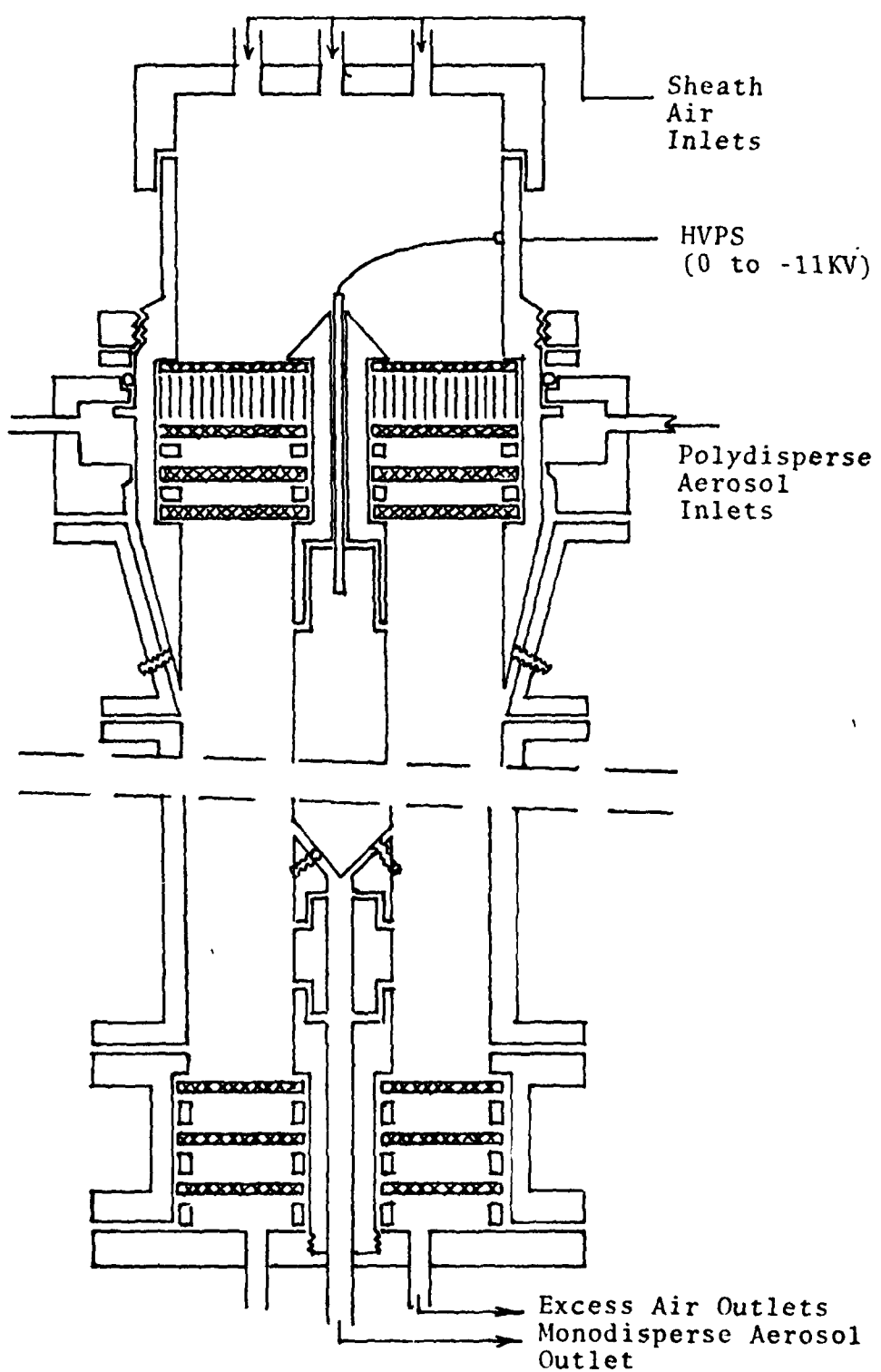


Figure 5G. Proposed design for new electrostatic classifier.

APPENDIX H

NUCLEATION EXPERIMENTS WITH
MONODISPERSE NaCl AEROSOLS

by

D. J. Alofs*, M. B. Trueblood,
D. R. White**, and V. L. Behr*

Cloud Physics Research Center
University of Missouri-Rolla
Rolla, Missouri 65401

Submitted to J. Appl. Meteor.
January, 1979

* Also Department of Mechanical Engineering
**Also Department of Engineering Mechanics

ABSTRACT

Nucleation experiments with monodisperse NaCl aerosols showed good agreement with the Köhler theory relating the critical supersaturation, S_c , to dry size. Aerosols produced by condensing NaCl showed the same S_c as those produced by evaporating aqueous NaCl solution droplets. This indicates that dry NaCl particles present no additional energy barrier for nucleation above that of NaCl particles which have retained water. These results also indicate that there is no significant contamination of the evaporated aerosol by surface active materials. The fact that the evaporation aerosol particles are cubical crystals and the condensation aerosols are amorphous spheres is shown to make no difference in the nucleation threshold.

The investigation also gives insights into the performance of the equipment used, especially the commercial electrostatic aerosol classifier and the vertical flow thermal diffusion chamber developed in this laboratory.

1. Introduction

The Graduate Center for Cloud Physics Research at the University of Missouri-Rolla is entering the final phase of development of a cooled wall expansion cloud chamber designed for simulation studies of cloud microphysics. The value of supersaturation, S , in this chamber is calculated from the initial relative humidity, and a knowledge of the thermodynamic changes that occur during the expansion, including changes resulting from the heat release and vapor depletion due to droplet growth. At the time of this writing, the performance of the simulation chamber is being experimentally investigated by using test aerosols of monodisperse NaCl particles. Since these particles all have about the same size and chemical composition, they should all have the same critical supersaturation, S_c , and in the simulation chamber they should produce a monodisperse cloud of droplets which undergo a marked increase in growth rate when the S in the chamber exceeds S_c .

This paper describes the aerosol generation facility developed for use with the simulation chamber, and describes experiments performed to verify the monodispersity and S_c of the aerosols, using the vertical flow thermal diffusion chamber developed by Alofs and co-workers (Alofs, 1978). The experimental data also provides valuable information on the resolution of this thermal diffusion chamber.

Two different aerosol generating techniques were used for these investigations. In the first, NaCl is vaporized, mixed with air in a steady flow process, and subsequently cooled so that the NaCl condenses. In the second technique, a solution of NaCl in water is

atomized and the water in the droplets subsequently evaporates to leave NaCl particles. The output from either of these generators is then made more monodisperse by passing it through a Thermo Systems Inc. Model 3071 electrostatic classifier*, developed by Liu, Whitby, and co-workers (Liu and Pui, 1974a, Knutson and Whitby, 1975).

The equipment for the evaporation technique is much simpler than for the condensation technique, but it was felt that the condensation technique might provide nuclei with a different and probably smaller amount of surface impurities. It was considered that in the evaporation technique all of the impurities in the water end up on the salt particles finally produced, whereas in the condensation technique, there are no impurities due to such water. Since impurities having surface active characteristics are known to influence droplet growth rates, (Derjaguin et al., 1971; Podzimek and Saad, 1975) it was felt important to be able to compare aerosol particles generated by two completely different means. Measurements of droplet growth rate are underway for both aerosols and will be presented in a separate report.

The experiments described in this report are quite similar to those described by Gerber et al. (1977). They used an evaporation aerosol generation technique, and then used an electrostatic classifier together with a Goetz centrifuge to achieve greater mono-dispersity. They then determined, S_c , using the Naval Research Lab static horizontal thermal diffusion chamber. The experimental values

*Thermo Systems Incorporated, 500 Cardigan Road, St. Paul, Minnesota 55165, U.S.A.

of S_c versus dry size agreed well with the Köhler equations (Pruppacher and Klett, 1978). Considering the fact that the Köhler equations are used extensively in cloud microphysics calculations, and considering that previous attempts to verify the theory had failed, their experiment was a big breakthrough. One of the contributions of this paper is that we repeat their experiment at a different laboratory, using similar but not identical equipment, and get the same good agreement with theory.

Another contribution of this paper concerns the question of whether or not there is an energy barrier in going from a dry NaCl particle to a solution droplet. C. A. Knight (1971) presented a photograph of tiny liquid water drops resting on the surface of NaCl crystals and not being absorbed. He suggested an energy barrier that is not taken into account by the Köhler equations. The transition between solution droplet and salt crystal is known to exhibit a hysteresis effect (Winkler and Junge, 1967) such that for NaCl, a dry particle does not take up water until the humidity reaches 75%, whereas a wet particle does not give up all of its measurable water until the humidity is lowered below 50%. However, perhaps in these hysteresis experiments the supposedly dry particles really contain a small amount of water too small to be measured in the experiment. Perhaps then a truly dry particle would need a humidity higher than 75% before it takes up water. Thus we feel that neither the experiments of Gerber et al. nor those by Winkler and Junge rule out the possibility of an energy barrier for a completely dry particle. Since the NaCl particles prepared by the condensation techniques are initially dry, it was felt that an energy barrier might show up in

our experiments. In this case the NaCl particles produced by condensation would give a higher S_c than those produced by evaporation.

Contamination and dryness have been discussed as being two possible differences between particles produced by condensation versus those produced by evaporation. Another difference is that evaporation produces particles which are cubical crystals, whereas condensation produces spherical particles which are amorphous (Matijevic et al., 1963). This difference also added to our curiosity about whether the two aerosols would have different nucleation thresholds.

2. Description of the condensation aerosol generator

Fig. 1 is a schematic of the condensation aerosol generator, which utilizes a series of furnaces, in accord with the investigation of Espenscheid *et al.* (1964). About 5 g. of reagent grade NaCl is placed in a ceramic boat 9 cm long by 8 mm wide by 0.6 mm deep. This boat, which is open at the top, is placed inside a ceramic mullite tube, 2.5 cm inside diameter by 223 cm long. The ceramic tube passes through four electric furnaces, which maintain the respective lengths of the ceramic tube at the desired temperatures. Each of the furnaces has a thermocouple located on the outside surface of the ceramic tube, midway along the length of each furnace. Manual control of the furnace power settings was found to be unsatisfactory, so automatic control circuits were built for each furnace. With these control circuits, the temperatures are stable to within $\pm 1^{\circ}\text{C}$.

The first furnace, denoted by T_1 in Fig. 1, contains the boat of NaCl midway along the 65 cm length of the furnace. Typically, T_1 was held at 730°C . Filtered air flows through the ceramic tube, and mixes with the NaCl vapor. This flow, denoted by Q_2 in Fig. 1, is typically 1.5 l. min.^{-1} .

The mixture of air and NaCl vapor then passes through a cooler region of the ceramic tube, which is a region 8 cm long where the tube is exposed to room air. The inside surface temperature of the tube in this cooler region was measured and found to be 300°C at the coolest spot. Within the cool region, the NaCl vapor undergoes homogeneous nucleation. The particles nucleate over an extended period

of time and produce a very high concentration aerosol which undergoes growth in particle size and reduction in concentration by coagulation. This results in a polydisperse distribution of NaCl particles.

The aerosol then enters the second furnace, denoted by T_2 , where the temperature is typically 870°C. The NaCl particles evaporate in this furnace but apparently some residue, either solid NaCl or some impurity, remains to act as a nuclei for condensation in the downstream regions of the generator.

The aerosol then flows into furnaces T_3 and T_4 , whose purpose is to give a slower cooling rate than would otherwise exist. Furnace T_3 is between 25°C and 50°C cooler than T_2 , depending upon what average particle size is desired. This same temperature drop is repeated from furnace T_3 to furnace T_4 . It was found that the rate of cooling in these regions greatly influences the average size of the particles produced, as discussed in section 5.

After leaving the last furnace, the aerosol passes through the last 10 cm length of the ceramic tube, which is exposed to room air. The aerosol is then diluted with filtered air, denoted by Q_1 in Fig. 1. This dilution flow is one of the parameters which is varied to control aerosol concentration, but typically, lies between 1.0 and 2.0 l.
min.⁻¹.

3. Description of the electrostatic classifier

The aerosol next passes through the bipolar charger, which is a Krypton 85 radioactive source that imparts a charge distribution to the aerosol particles. The charge distribution has been found to follow Boltzmann's law for particles larger than $0.01 \mu\text{m}$ diameter (Liu and Pui, 1974b). Thus the fractions of the particles having a given charge is a known function of size.

The main component of the electrostatic classifier consists of an outer cylinder at zero electrical potential, and a concentric inner rod kept at a negative potential in the range 20 to 10,000V. Two streams of air are introduced into the annulus region at the top of the classifier (Fig. 1). The smaller flow, typically 9% of the total, is the aerosol flow, Q_6 , which comes from the charger and is introduced near the outer cylinder. The other flow is filtered air (Q_3 , Fig. 1). The inlet systems are designed such that, ideally, these two air streams do not mix, but instead flow side by side down through the classifier. Near the bottom of the chamber, a small flow, Q_5 , is withdrawn through a slit in the rod. Q_5 is typically 9% of the total flow. The rest of the air, Q_4 , is withdrawn through a separate port and discarded.

The aerosol particles which have a positive charge are deflected inward toward the rod. Those possessing the same mobility arrive at the central rod at very nearly the same axial location. Those with a specific mobility arrive at the slit and become incorporated in the exit flow, Q_5 . Thus the exit flow consists of a fairly monodisperse aerosol. Limitations on the degree of monodispersity are now

discussed.

One limitation on monodispersity is the charge distribution on the particles. If the classifier is set to pass particles of size D_1 , having one positive unit charge, it will also pass particles of larger size, D_2 , carrying two positive charges. This is because the D_2 and D_1 particles have the same electrical mobility, Z_p , and experience an identical deflection path in the electric field of the classifier. By using a table of mobility values (Fuchs, 1964) one can calculate D_2 as a function of D_1 .

In the experiments of Gerber *et al.* (1977) the problem of the doubly charged particles was solved by using a centrifuge set to remove all particles larger than D_1 . In our investigations, this problem is solved by controlling the aerosol size distribution going into the classifier, such that the concentration N_1 of particles in the range $D_1 \pm \Delta D_1$ is at least four times larger than the concentration N_2 of particles in the range $D_2 \pm \Delta D_2$. Here ΔD is merely notation for the resolution of the classifier. Now let f_1 be the fraction of N_1 that carry a single positive unit charge, and let f_2 be the fraction of N_2 that carry a double positive charge. The Boltzmann equation (Liu and Pui, 1974b) is used to calculate f_1 and f_2 . Now for the classifier output aerosol, let the respective concentrations of singly and doubly charged particles be denoted by n_1 and n_2 . Then $n_1 = N_1 f_1$ and $n_2 = N_2 f_2$. The ratio $R = n_1/n_2$ is plotted in Fig. 2 as a function of D_1 assuming $N_1 = 4 N_2$. It can be seen that doubly charged particles are not much of a problem when $D_1 < 0.1 \mu\text{m}$.

Another limitation on monodispersity is the finite thickness of

the air stream which carries the aerosol particles into the classifier. Consider the case where the polydisperse aerosol inflow, Q_6 , equals the monodisperse aerosol outflow, Q_5 . The analysis of Knutson and Whitby (1975) shows that for this case, which was used throughout the present investigation, the classifier will have a triangular transfer function. The transfer function, Ω , is the ratio of the output concentration of particles with mobility Z , to the input concentration of particles with the same Z . Thus a plot of Ω versus Z is a triangle, with $\Omega = 0$ for $Z < Z_p - \Delta Z$, a linear rise in Ω from $Z_p - \Delta Z$ to Z_p , a linear decline in Ω from Z_p to $Z_p + \Delta Z$, and $\Omega = 0$ for $Z_p > Z_p + \Delta Z$. Knutson and Whitby derive the following formula

$$\frac{\Delta Z}{Z_p} = \frac{Q_6}{Q_3} \quad (1)$$

where Q_6 is the aerosol flow and Q_3 is the filtered air flow. In the present investigations $Q_6/Q_3 = 0.1$, so that the classifier would have a band width of $\pm 10\%$ in Z due to this effect alone.

A third limitation on monodispersity is due to the fact that it is impossible to prevent a finite amount of mixing between the two air streams in the classifier. Moreover, in deriving Eq. 1 it is assumed that the thickness of the aerosol stream is the same all around the circumference of the classifier. We have experimental evidence indicating that this angular uniformity is poor, because when taking apart the classifier for cleaning, we always notice that the salt deposits on the outer cylinder are substantially non-uniform. Instead the deposits show an angular pattern of 8 stripes

running the length of the tube. Thus it should be expected that ΔZ will be larger than the idealized representation given by Eq. 1.

4. Description of the evaporation aerosol generator

The set up for the evaporation generator is shown in Fig. 3, and is very similar to that used by Liu *et al.* (1975). Compressed air passes through a silica gel dryer, and then through a pressure regulator set for 25 lbf. in.⁻² gage. Part of the flow (Q_8 , 2.5 to 4 l. min.⁻¹) then goes into a standard Collison atomizer (May, 1973), the remainder (Q_7 , 9 l. min.⁻¹) serves as dilution flow. The aerosol then passes through an impactor to remove the largest drops. Part of this flow is discarded, the remainder passing through a diffusion drier. The diffusion drier consists of two concentric tubes 64 cm long. The inner tube, 2 cm diameter, is made of fine mesh screen, and the outer tube, 8 cm inside diameter, is made of Plexiglass. The annular volume between the tubes is filled with dry silica gel. Thus the air passing through the inside tube looses water vapor by diffusion to the silica gel, but the air itself does not pass through the silica gel. After passing through the diffusion drier, the air then enters the bipolar charger, and finally, the classifier.

The size distribution of the dry salt particles from this generator has been found to be log-normal (Fuchs, 1964) both by Liu and Pui (1974a) and by ourselves. Liu and Pui present a graph which relates the salt solution strength and the average size of the dry salt particles produced. This information was used by us to determine the concentration of salt, with the criterion that the aerosol going into the classifier have a geometric mean size equal to the size of the desired monodisperse aerosol. An exception to this

rule is that for producing a monodisperse aerosol larger than 0.05 μm diameter, the same salt solution as for 0.05 μm diameter was used. This had the undesirable effect of decreasing the aerosol concentration at the output of the classifier, but was necessary because it was found that more concentrated salt solutions caused frequent plugging of the jets in the Collison atomizer. Reagent grade NaCl and doubly distilled water were used to make up the salt solutions.

5. Effect of temperatures and flow on the size distribution from the condensation generator

A series of experiments were performed to determine how the various operating parameters of the condensation aerosol generator influence the aerosol size distribution. To measure the size distribution, the classifier was used. The output of the classifier was measured with a Gardner Counter* as a function of the classifier rod voltage. This procedure is referred to as a classifier voltage sweep. Hoppel (1978) has described a rigorous procedure for analyzing such data in order to extract the input size distribution. However, in this investigation Hoppel's procedure is not used because the size distributions are sufficiently narrow that a simpler analysis suffices. Recalling the notation of section 3, the Gardner counter measures the concentration $n_1 + n_2 = N_1 f_1 + N_2 f_2$. When analyzing the data from a voltage sweep, the procedure is to neglect particles with more than one charge. This simplification is justified by the large value of R as discussed in Section 3. Then N_1 can be obtained by dividing n_1 by f_1 . Recall that n_1 is the concentration of particles passed by the triangular transfer function, Ω , of the classifier. Roughly speaking, N_1 is the concentration of particles in the size range $D_1 \pm \Delta D_1$, where the value of ΔD_1 is between 10% and 20% of D_1 .

The size distributions thus measured were found to be approximately log normal (Fuchs, 1964). The relative geometric standard deviation, α , of the distributions usually had a value near 0.1.

*Gardner Associates, 3435 Carman Road, Schenectady, NY 12302.

Since aerosols with $\alpha \leq 0.2$ have been termed monodisperse (Fuchs and Sutugin, 1966), it should be recognized that the aerosol going into the classifier is already fairly monodisperse. It is also interesting to note that other investigations with condensation generators yield α near 0.1 (Kitani and Ouchi, 1967; Kerker, 1975; Espenscheid *et al.*, 1964). None of these other generators, however, produced particles as small as those produced in the present investigation.

The results of this series of experiments are not presented. Fig. 4 shows the result of varying Q_2 , the flow through the ceramic tube, while keeping the other parameters constant at the values indicated on the legend.

It can be seen from Fig. 4 that varying Q_2 does not affect α , nor does it affect the geometric mean diameter, D_g . However, Q_2 is seen to affect concentrations, higher flows giving higher concentrations. Higher concentrations would indicate more particles being formed during the first condensation process. This could be due either to a higher cooling rate or to a larger supply of vapor because of better ventilation across the boat of salt.

Fig. 5 shows the effect of varying the temperature drop in the last furnaces, i.e., varying $T_2 - T_3$ and $T_3 - T_4$. As these decrease, the cooling rate of the vapor decreases, and it is seen that larger particles are formed. Again, α is not noticeably influenced.

Fig. 6 shows the affects of varying, T_1 , the temperature of the first oven. It can be seen that α is not greatly affected,

but concentration and D_g are. Unfortunately, we do not have one unified explanation for all the behavior exhibited in Figs. 4, 5, and 6. We are surprised that α remained constant throughout and that D_g was not a function of Q_2 (Fig. 4). Therefore, these data were utilized merely as an empirical guide for setting up the generator to get the concentrations and sizes desired. For example the size was controlled chiefly by varying the cooling rate in the last ovens, in accord with the behavior seen in Fig. 5.

One other effect that should be mentioned is depletion of the salt in the boat. The furnaces and the air flow were left running 24 h per day, and it was found that about once every seven days the salt had to be replaced. As the salt was being depleted the aerosol concentration and D_g would both decrease slowly. Generally this was compensated for by increasing T_1 by about 40°C once during the middle of the seven day period.

6. Procedure for the Nucleation Experiments

The nucleation experiments consisted of determining the critical supersaturation, S_c , of the monodisperse NaCl aerosols. To do this the vertical continuous flow thermal diffusion chamber (CFD) developed by Alofs and co-workers was employed. This instrument and its performance characteristics have recently been described in detail (Alofs, 1978) and therefore only a brief description of it is given here.

The CFD consists of two vertical plates, 100 cm long in the vertical direction and 13 cm wide, with a 0.8 cm spacing between the plates. A temperature difference is generally maintained between the plates, and distilled water is supplied to filter paper on their surfaces. The temperature dependence of the equilibrium vapor pressure of water is such that a supersaturation is produced in the air-water vapor mixture contained between the plates. The supersaturation profile is nearly parabolic, with the supersaturation equal to zero at each plate, and a maximum supersaturation, S , midway between the plates.

Filtered air and the test aerosol are injected at the top of the TDC in such a way that the aerosol remains in a narrow stream centered between the plates as the aerosol passes through the chamber. Both the active nuclei, $S_c < S$, and the haze nuclei, $S_c > S$, experience growth in the CFD, however, the active nuclei produce larger water drops than the haze nuclei.

At the bottom of the chamber the water drops are drawn into a optical particle counter (OPC), where the light scattered from individual water drops is measured in order to determine the droplet size

distribution. The diameter (μm) of the largest haze drop is estimated by theory to equal $0.138 S_c^{-1}$, where S_c is in percent (Alofs, 1978). Therefore all drops larger than this are counted as coming from active nuclei. In the present investigations two CFD were employed, each with a different commercial brand of OPC. The first used a Royco* model 225 OPC, the second used a Climet** model 201 OPC.

In order to determine S_c for the monodisperse aerosols, the temperature of the colder plate was slowly changed with time, while all the other parameters were held fixed. This procedure is referred to as a temperature sweep, and required about 30 minutes to complete. Temperature sweeps were made in both directions, that is, with S both increasing and decreasing with time, and no difference in the resulting S_c was observed. This indicates that the rate of temperature change was sufficiently slow to insure that various thermal lags in the cold plate were negligible.

For the sake of completeness the values of the quantities held fixed during the temperature sweeps are now specified. The hot plate temperature was always 25°C . The aerosol flow rate into the CFD was $8.5 \text{ cc. min.}^{-1}$, and the flow into the OPC was 0.5 l. min.^{-1} . The value of the filtered air flow rate, which determines the residence time in the CFD, depended on the aerosol being tested. For aerosols with a D_1 of 0.022, 0.050, and $0.10 \mu\text{m}$, the values were 8, 5, and 3 l. min.^{-1} , respectively. The aerosol from the classifier

*Royco Instruments, 141 Jefferson Drive, Menlo Park, California 94025.

**Climet Instruments Company, 1320 W. Colton Ave., Redlands, California 92373.

was always diluted in a steady flow process to a concentration below 100 cm.^{-3} before passing it into the CFD.

The temperature sweep procedure was used for aerosols with $S_c > 0.1\%$, which includes most of the nucleation experiments performed. However, a few experiments were conducted in the range $S_c < 0.1\%$, and for these experiments the CFD was operated in the so called isothermal mode. In this mode the two plates are kept at the same temperature, 25°C , so that a relative humidity of 100% is formed between the plates. The total flow in the CFD is reduced such that the residence time of the aerosol sample increases to 200 seconds. This time is sufficient so that nuclei with $S_c > 0.016\%$ very nearly reach their equilibrium size at 100% humidity (Alofs, 1978). From this equilibrium size, the value of S_c can be determined (Alofs, 1978).

The purpose of conducting experiments in the isothermal mode is more to test the accuracy of the isothermal procedure than to verify the Köhler equations. In other words, once the Köhler equations have been verified in the range $0.1\% < S_c < 1\%$ by the temperature sweep procedure, they are used in the range $0.016\% < S_c < 1\%$ to investigate the accuracy of the isothermal procedure.

There are several reasons why the isothermal procedure needs investigation. The important question of thermostatting the OPC to avoid significant drop evaporation has been investigated by Alofs (1978). Another question is how to calibrate the OPC for particles having the same index of refraction, m , as does water ($m = 1.33$). The sensitivity to m of several commercial OPC has been investigated by theoretical calculations (Cooke and Kerker, 1975), and by

experiment (Liu et al., 1974), the former indicating a greater sensitivity than the latter. This causes a difficulty in determining S_c by the isothermal procedure, because apparently, no suitable means of generating a calibration aerosol with $m = 1.33$ has been developed. Generally, OPC are calibrated using latex spheres with $m = 1.6$.

In the isothermal experiments a Nuclear Data* model 220 multi-channel pulse height analyzer (PHA) was used to determine the most frequent height of the pulses from the OPC. The PHA was used both in the calibration of the OPC with latex aerosols, and in the measurements of drop size for monodisperse salt nuclei at 100% humidity. The latex spheres were obtained from Dow Chemical, Midland, Michigan, and were 0.945 μm diameter polystyrene, and 2.02 μm diameter polyvinyltoluene. The manufacturer's calibration curve for the OPC (response on ordinate, size on abscissa) was shifted up or down to agree with these two calibration data points. It will be seen that the isothermal technique gives quite good results with such calibration of the OPC.

*Nuclear Data Inc., Golf and Meachan Roads, Schaumberg, Illinois 60162.

7. Results of the Nucleation Experiments

Fig. 7 shows a plot of selected data from the temperature sweep procedure. The ordinate shows the count, C , of nuclei with $S_c < S$, normalized with respect to the maximum count obtained during the temperature sweep. The abscissa shows the operating supersaturation, S , of the CFD. Data is shown for aerosols with three different size settings of the classifier, namely, $D_1 = 0.022, 0.05$, and $0.10 \mu\text{m}$. Data for aerosols produced by both generating techniques are shown and are distinguished.

The value of S at $C=0.5$ is taken to be S_c . The values of S at $C=0.8$ and $C=0.2$ are denoted $S_{0.8}$ and $S_{0.2}$, respectively. Let ΔS be defined by the equation:

$$2 (\Delta S) = S_{0.8} - S_{0.2} \quad (2)$$

An electrostatic classifier and CFD having infinite resolution would give a step function in Fig. 7 for a truly monodisperse aerosol. Bearing this in mind, $\Delta S/S_c$ can be seen to be a measure of the combined resolution of the classifier and the CFD.

Table 1 shows all of the temperature sweep data for aerosols produced by condensation. The first column shows D_1 , the size setting of the classifier. The second column shows Q_3 , the filtered air flow rate in the classifier. The classifier aerosol flow rate was always 0.1 times Q_3 . The third column shows the dew point of the air supply to the aerosol generator (Fig. 1). In cases where the dew point is below -21°C , the air supply was from the dry-air-supply-system of the University of Missouri cloud simulation chamber

facility. In these cases the dew point was measured with a Cambridge Systems* Model 992-C1 dew point hygrometer. In cases where the dew point is higher, the air supply was room air, and on the basis of sporadic sling psychrometer measurements, the dew point was estimated to be $10^{\circ}\text{C} \pm 3^{\circ}\text{C}$. The fourth column in Table 1 shows which CFD was used. Recall that CFD #1 has a Royco OPC and CFD #2 has a Climet OPC. The fifth column shows S_c , and the last column shows $\Delta S/S_c$, with ΔS defined by eq. 2.

Table 2 is similar to table 1, but is for aerosols from the evaporation generator. Comparing tables 1 and 2, it can be seen that for $D_1 = 0.022 \mu\text{m}$, both aerosols give the same average value of S_c , namely, $S_c = 1.08\%$. For $D_1 = 0.050 \mu\text{m}$, the condensation aerosol shows $S_c = 0.337\%$, and the evaporation aerosol shows $S_c = 0.315\%$. This difference is in the direction which would indicate an energy barrier for dry NaCl in accord with the hypothesis of section 1. However, in view of the fact that the difference is less than the scatter in S_c shown by each aerosol, we interpret the difference to be statistically insignificant. At $D_1 = 0.10 \mu\text{m}$, the condensation aerosol shows $S_c = 0.127\%$, and the evaporation aerosol shows $S_c = 0.112\%$, which again is a difference in such a direction as to indicate an energy barrier. However, the difference is again judged to be so small as to be statistically insignificant.

Now focusing attention on the average values of $\Delta S/S_c$, it can be seen from tables 1 and 2 that $\Delta S/S_c$ increases as D_1 increases. Qualitatively, this is to be expected because the resolution of both the classifier and the CFD is best for the small particles. For the

*Cambridge Systems, Inc., 50 Hung Street, Newton, Mass. 02158.

classifier, this is because as D_1 increases, R decreases (Fig. 2). For the CFD, this is because for larger D_1 , there is increased difficulty in distinguishing the haze nuclei from the active nuclei (Alofs, 1978).

The overall average of $\Delta S/S_c$ is 0.075 for the data of tables 1 and 2. It is interesting to consider how much of $\Delta S/S_c$ is due to the classifier versus that which is due to the CFD. Assuming the classifier is behaving ideally, it would have a triangular transfer function, Ω , such that $\Delta Z/Z_p = 0.1$ (Section 3). Integrating Ω with respect to Z , one obtains a cumulative transfer function, β . The value of β is zero for $Z < Z_p - \Delta Z$, rises nonlinearly with Z in the range from $Z_p - \Delta Z$ to $Z_p + \Delta Z$ and is unity for $Z > Z_p + \Delta Z$. The value of Z at $\beta = 0.2$ is denoted $Z_{0.2}$, and at $\beta = 0.8$ is $Z_{0.8}$. Then it can be shown that $Z_{0.8} - Z_{0.2} = 0.74 \Delta Z = 0.074 Z_p$. In analogy to eq. 2, let ΔZ_c be defined by the equation:

$$2 (\Delta Z_c) = Z_{0.8} - Z_{0.2} \quad (3)$$

Thus $\Delta Z_c = 0.037 Z_p$. By consulting a mobility table for singly charged particles, it can be determined that a 3.7% change in mobility corresponds to about a 2.0% change in particle diameter in the size range 0.01 μm to 0.10 μm . Now consulting the Köhler equations, it can be determined that a 2% change in particle size corresponds to a 3.5% change in S_c . Thus the value of $\Delta S/S_c$ attributable to an ideal classifier is $\Delta S/S_c = 0.035$. This then shows that about half of the average experimental value of $\Delta S/S_c$ is due to other considerations, either non ideal behavior of the classifier, or the resolution of the CFD. Incidentally, it should be pointed out that the

scatter in the value of $\Delta S/S_c$ is very large, and the reason for this scatter is unknown. It would not seem to be due to wandering of the aerosol stream in the CFD from the midplane, as this would cause both $\Delta S/S_c$ and S_c to go up, whereas the data shows no such correlation.

Before leaving tables 1 and 2, it is noted that Q_3 , the classifier filtered air flow rate, did not noticeably influence S_c . This gives some confidence in the classifier flowmeters, voltmeters, and aerodynamic flow. It is also noted that S_c did not depend on which of the two CFD was used. From table 1, it can be seen that the dew point of the air supply for the condensation generator did not influence S_c .

Fig. 8 shows the average value of S_c from table 1 and table 2, plotted as a function of D_1 . The error bars denote the maximum scatter in S_c from these tables. Also shown on Fig. 8 are the results of the isothermal mode experiments. The straight line in Fig. 8 is the theoretical result given by Köhler equations. This line has the equation:

$$D_1 = 0.0232 S_c^{-2/3} \quad (4)$$

Eq. 4 was not obtained from the Köhler equations, but instead was obtained by carefully measuring the coordinates of the line in Fig. 8 of the paper by Gerber *et al.* (1977). Moreover, eq. 4, agrees very well with Table X in the article by Hañel (1976). It can be seen from Fig. 8 that the experiments are in good agreement with the Köhler theory.

8. Summary

The nucleation experiments with monodisperse NaCl aerosols showed good agreement with the Köhler theory relating the critical supersaturation, S_c , to dry size. Aerosols produced by condensing NaCl showed nearly the same S_c as those produced by evaporating aqueous NaCl solution droplets. This indicates that dry NaCl particles present no additional energy barrier for nucleation above that of NaCl particles which have retained water. These results also indicate that there is no significant contamination of the evaporated aerosol by surface active materials during the course of our experiments. The fact that the evaporation aerosol particles are cubical crystals and the condensation aerosols are amorphous spheres is shown to make little or no difference in the nucleation threshold.

The investigation also gives insights into the performance of the equipment used. The commercial electrostatic classifier gave internally consistent results when the flow rates were varied. The pattern of salt deposits observed when cleaning the classifier showed angular non-uniformity, indicating that the aerodynamics of the inlet system could be improved. As to the resolution of the classifier, the ideal value for the quantity $\Delta S/S_c$ is 0.035. The average value of $\Delta S/S_c$ measured with the continuous flow thermal diffusion chamber (CFD) was 0.075, but it is not known how much of this $\Delta S/S_c$ is due to the resolution of the classifier versus how much is due to the TDC.

The CFD was operated in the isothermal mode for monodisperse

NaCl aerosols of 0.13, 0.2 and 0.4 μm diameter. Good agreement with the Köhler equations was obtained when the Royco and Climet optical particle counters were calibrated with latex aerosols.

ACKNOWLEDGEMENTS

The major encouragement for developing the aerosol generation facility was provided by J. L. Kassner, Jr. The condensation aerosol generator has been under development for some five years at this laboratory. The first work on it was done by S. Shahriari, with successive contributions by J. Podzimek and J. F. Stampfer.

The recent financial support for this work has been from two grants: Grant NSF-ATM75-21421 from the Atmospheric Sciences Section, National Science Foundation; and Grant ONR-N00014-75-C-0182 from the Office of Naval Research.

REFERENCES

1. Alofs, D. J., 1978: Performance of a dual range cloud nucleus counter. J. Appl. Meteor., 17, 1286-1297.
2. Cooke, D. D., and M. Kerker, 1975: Response calculations for light-scattering aerosol particle counters. Appl. Optics, 14, 734-739.
3. Derjaguin, B. V., I. S. Kurghin, L. A. Rosenzweig, and V. A. Fedoseyev, 1971: Study of passivation of condensation growth of water and salt solutions. Aerosol Sci., 2, 261-274.
4. Espenscheid, W. F., E. Matijevic and M. Kerker, 1964: Aerosol studies by light scattering. III Preparation and particle size analysis of sodium chloride aerosols of narrow size distribution. J. Phys. Chem., 68, 2831-2842.
5. Fuchs, N. A., 1964: The Mechanics of Aerosols. Pergamon Press, London, 408 pp.
6. Fuchs, N. A., and A. G. Sutugin, 1966: Generation and use of monodisperse aerosols. Aerosol Science, C. N. Davies, ed., Academic Press, New York, 468 pp.
7. Gerber, H. E., W. A. Hoppel, and T. A. Wojciechowski, 1977: Experimental Verification of the theoretical relationship between size and critical supersaturation of salt nuclei. J. Atmos. Sci., 34, 1836-1841.
8. Hänel, G., 1976: The properties of atmospheric aerosol particles as functions of the relative humidity at thermodynamic equilibrium with the surrounding moist air. Advances in Geophysics, Vol. 19, H. E. Landsberg and J. Van Mieghem, eds., Academic Press, New York, 312 pp.
9. Hoppel, W. A., 1978: Determination of the aerosol size distribution from the mobility distribution of the charged fraction of aerosols. J. Aerosol. Sci., 9, 41-54.
10. Kerker, M., 1975: Laboratory generation of aerosols. Adv. Colloid. Interface Sci., 5, 105-172.
11. Kitani, S. and S. Ouchi, 1967: Preparation of Monodisperse aerosols of sodium chloride. J. Colloid. Interface Sci., 23, 200-202.
12. Knight, C. A., 1971: A note on the action of hygroscopic cloud nuclei. J. Atmos. Sci., 28, 1296-1297.
13. Knutson, E. O., and K. T. Whitby, 1975: Aerosol classification by electric mobility: apparatus, theory, and applications. J. Aerosol Sci., 6, 443-451.

14. Liu, B. Y. H., and D. Y. H. Pui, 1974a: A submicron aerosol standard and the primary, absolute calibration of the condensation nuclei counter. J. Colloid Interface Sci., 47, 155-171.
15. Liu, B. Y. H., and D. Y. H. Pui, 1974b: Equilibrium Bipolar Charge Distribution of Aerosols. J. Colloid Interface Sci., 49, 305-312.
16. Liu, B. Y. H., R. N. Berglund, and J. K. Agarwal, 1974: Experimental studies of optical particle counters. Atmos. Environ., 8, 717-732.
17. Liu, B. Y. H., D. Y. H. Pui, A. W. Hogan, and T. A. Rich, 1975: Calibration of the Pollak Counter with Monodisperse Aerosols. J. Appl. Meteor., 14, 46-51.
18. Matijević, E., W. F. Espenscheid and M. Kerker, 1963: Aerosols consisting of spherical particles of sodium chloride. J. Colloid Sci., 18, 91-94.
19. May, K. R., 1973: The Collison nebulizer: description, performance and application. J. Aerosol Sci., 4, 235-243.
20. Podzimek, J., and A. N. Saad, 1975: Retardation of condensation nuclei growth by surfactant. J. Geophys. Res., 80, 3386-3392.
21. Pruppacher, H. R., and J. D. Klett, 1978: Microphysics of Clouds and Precipitation. D. Reidel Pub. Co., Dordrecht, 714 pp.
22. Winkler, P., and C. Junge, 1972: The growth of atmospheric aerosol particles as a function of humidity. J. Rech. Atmos., 6, 617-638.

AD-A102 679

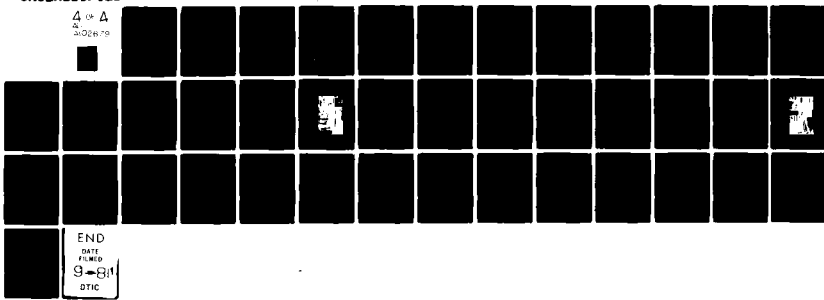
MISSOURI UNIV-ROLLA GRADUATE CENTER FOR CLOUD PHYSICS--ETC F/G 4/2
MARINE FOG STUDIES - FOG SIMULATION PROGRAM. (U)

N00014-75-C-0182

NL

UNCLASSIFIED

A or A
4
M08479



END
DATE FILMED
9-81
DTIC

TABLE 1. Data from nucleation experiments with
aerosol from the condensation generator.
See text for definition of terms.

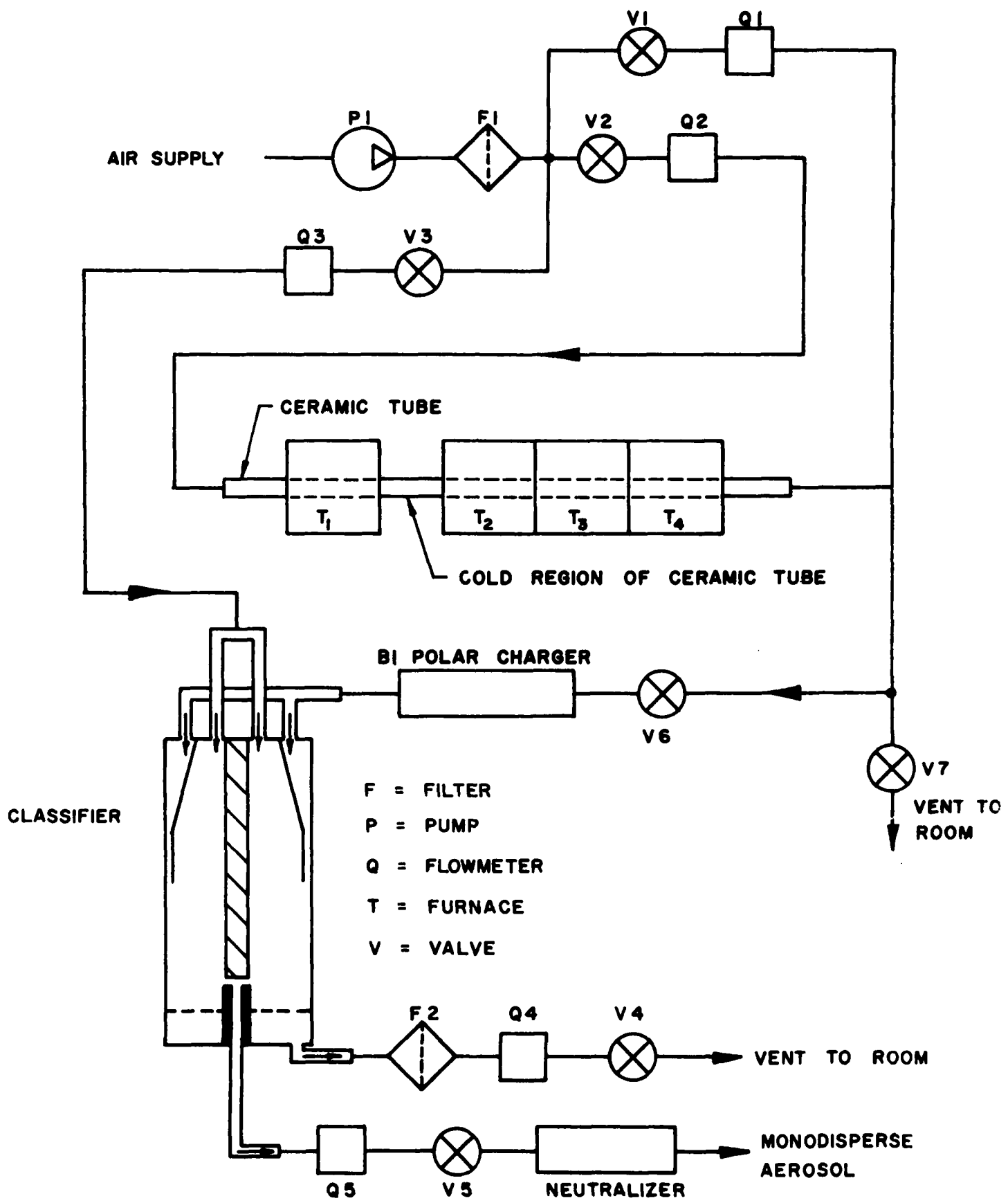
<u>D₁</u> <u>μm</u>	<u>Q₃</u> <u>l.min.⁻¹</u>	<u>DEW POINT</u> <u>°C</u>	<u>CFD</u> <u>#</u>	<u>DATE</u> <u>1978</u>	<u>S_c</u> <u>%</u>	<u>ΔS</u> <u>S_c</u>
0.022	20	10±3	2	08/31	1.09	0.031
0.022	20	10±3	2	09/28	1.10	0.068
0.022	20	-21	2	11/15	1.10	0.036
0.022	6	-38	2	12/15	1.05	0.046
0.022	6	10±3	2	12/15	1.05	0.046
				AVERAGE	1.08	0.045
0.050	20	10±3	2	08/04	0.32	0.094
0.050	20	10±3	2	09/07	0.35	0.078
0.050	6	10±3	2	10/11	0.33	0.075
0.050	6	10±3	2	10/13	0.35	0.071
0.050	20	10±3	2	11/30	0.34	0.044
0.050	20	-37	1	12/07	0.33	0.091
0.050	20	10±3	1	12/07	0.34	0.074
				AVERAGE	0.337	0.075
0.10	6	10±3	1	10/20	0.110	0.146
0.10	6	10±3	2	11/29	0.135	0.066
0.10	6	10±3	2	11/29	0.125	0.120
0.10	20	10±3	2	11/29	0.130	0.096
0.10	6	-35	2	12/08	0.125	0.080
0.10	6	10±3	2	12/08	0.135	0.140
				AVERAGE	0.127	0.108

TABLE 2. Data from nucleation experiments with
aerosol from the evaporation generator.
See text for definition of terms.

<u>D₁</u> <u>μm</u>	<u>Q₃</u> <u>l.min.⁻¹</u>	<u>CFD</u> <u>#</u>	<u>DATE</u> <u>1978</u>	<u>S_C</u> <u>%</u>	<u>ΔS</u> <u>S_C</u>
0.022	20	2	10/18	1.10	0.068
0.022	6	2	11/21	1.00	0.035
0.022	6	1	11/21	1.15	0.046
0.022	6	1	11/21	1.15	0.046
0.022	6	2	11/21	1.00	0.035
			AVERAGE	1.08	0.046
0.050	20	2	10/19	0.33	0.106
0.050	20	2	10/24	0.33	0.061
0.050	20	1	10/24	0.31	0.076
0.050	20	1	10/24	0.28	0.054
0.050	20	1	10/24	0.30	0.100
0.050	6	2	10/24	0.33	0.046
0.050	6	2	11/22	0.29	0.035
0.050	6	1	11/22	0.35	0.086
			AVERAGE	0.315	0.071
0.10	20	2	10/04	0.110	0.082
0.10	6	2	11/21	0.110	0.136
0.10	6	2	11/22	0.115	0.10
0.10	6	2	11/22	0.115	0.10
			AVERAGE	0.112	0.105

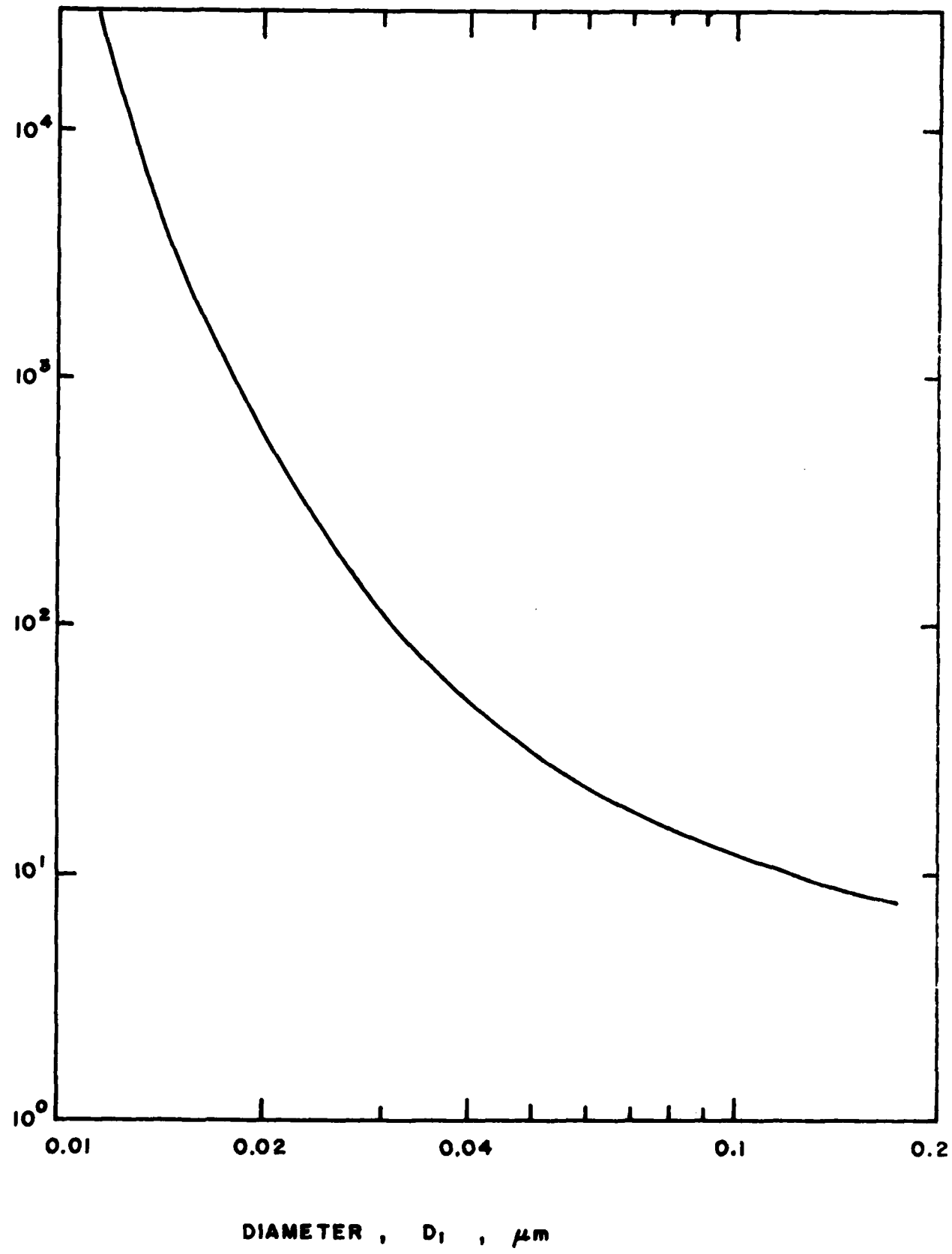
FIGURE CAPTIONS

1. Schematic of the condensation aerosol generator
2. The calculated ratio R of singly charged particle concentration divided by doubly charged particle concentration, both at the output of the classifier. The diameter D_1 is the size of the singly charged particles. The assumption, $N_1 = 4N_2$, is included, as described in the text.
3. Schematic of the evaporation aerosol generator.
4. The effect of varying Q_2 on the size distribution. $Q_1 = 2.0$, $Q_3 = 20$, $Q_6 = 2 \text{ l}.\text{min.}^{-1}$. $T_1 = 735$, $T_2 = 871$, $T_3 = 825$, $T_4 = 783^\circ\text{C}$.
5. The effect of varying T_3 and T_4 on the size distribution. $Q_1 = 1.0$, $Q_2 = 1.5$, $Q_3 = 20$, $Q_6 = 2 \text{ l}.\text{min.}^{-1}$. $T_1 = 732$, $T_2 = 871^\circ\text{C}$.
6. The effect of varying T_1 on the size distribution. $Q_1 = 2$, $Q_2 = 1.5$, $Q_3 = 20$, $Q_6 = 2 \text{ l}.\text{min.}^{-1}$. $T_2 = 870$, $T_3 = 822$, $T_4 = 781^\circ\text{C}$.
7. Selected data from the temperature sweep experiments.
8. Average values of S_C measured in the nucleation experiments, versus dry size of the monodisperse NaCl aerosols.



R, RATIO OF CONCENTRATIONS AT CLASSIFIER OUTPUT,

SINGLY CHARGED %
DOUBLY CHARGED



COMPRESSED
AIR

DRYER

PRESSURE
REGULATOR

F3

G1

Q9

VENT TO ROOM

V9

F4

IMPACTOR

DILUTION AIR

Q7

V7

Q8

V8

DIFFUSION DRYER

COLLISION
ATOMIZER

P2

V10

F5

ROOM AIR

VII

Q3

V6

BI POLAR
CHARGER

CLASSIFIER

F = FILTER

G = PRESSURE GAGE

Q = FLOWMETER

V = VALVE

F2

Q4

V4

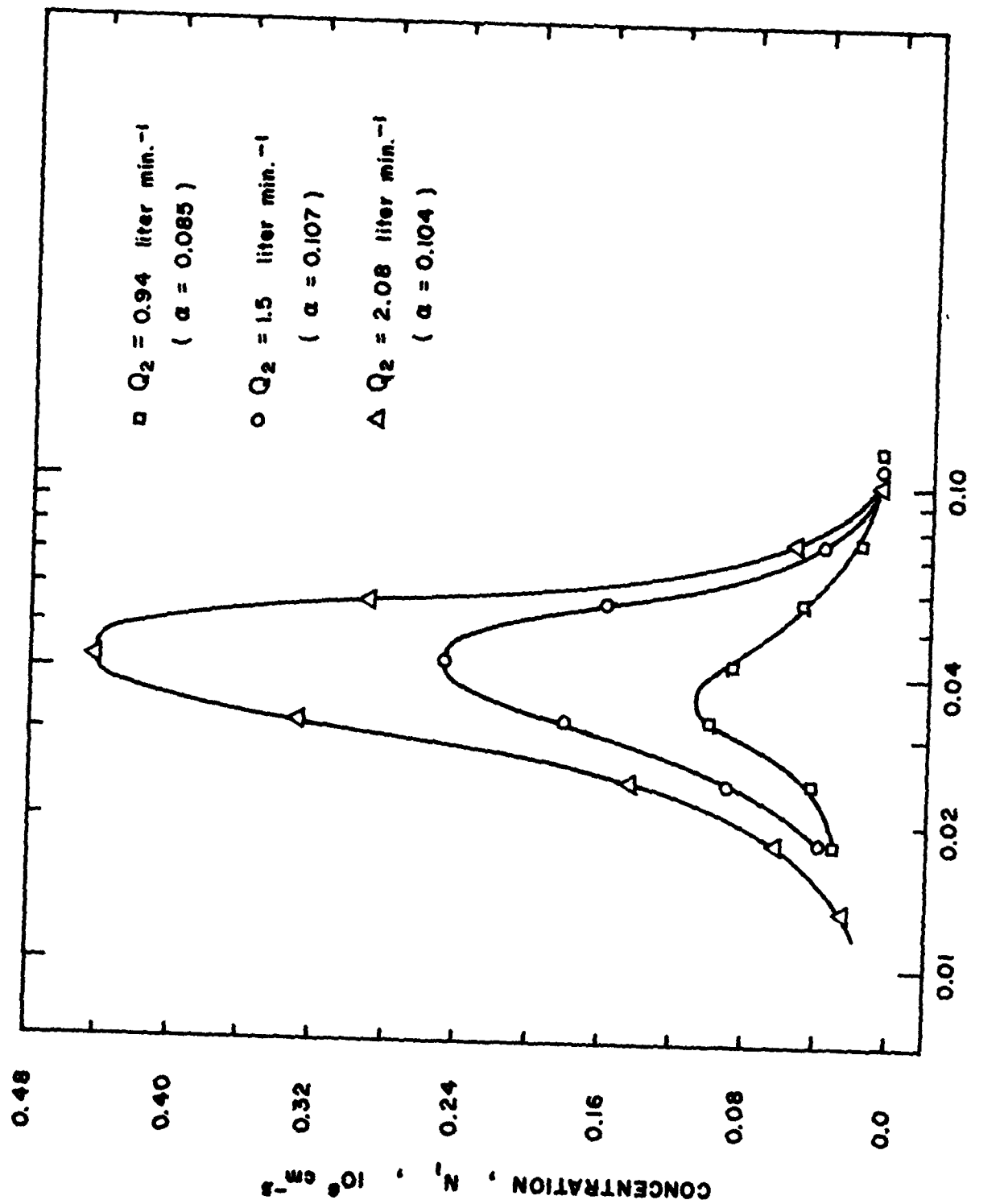
VENT TO ROOM

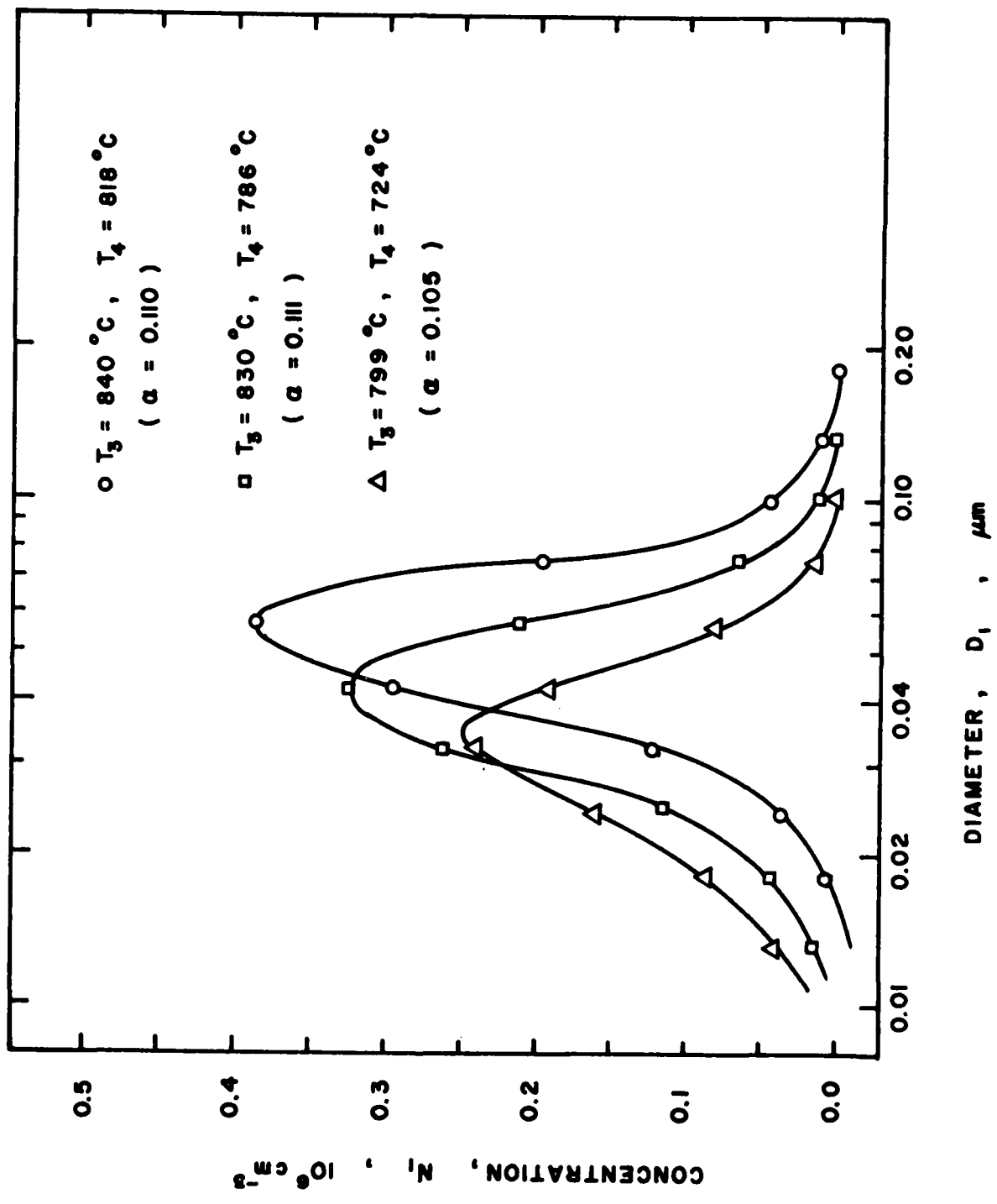
Q5

V5

NEUTRALIZER

MONODISPERSE
AEROSOL





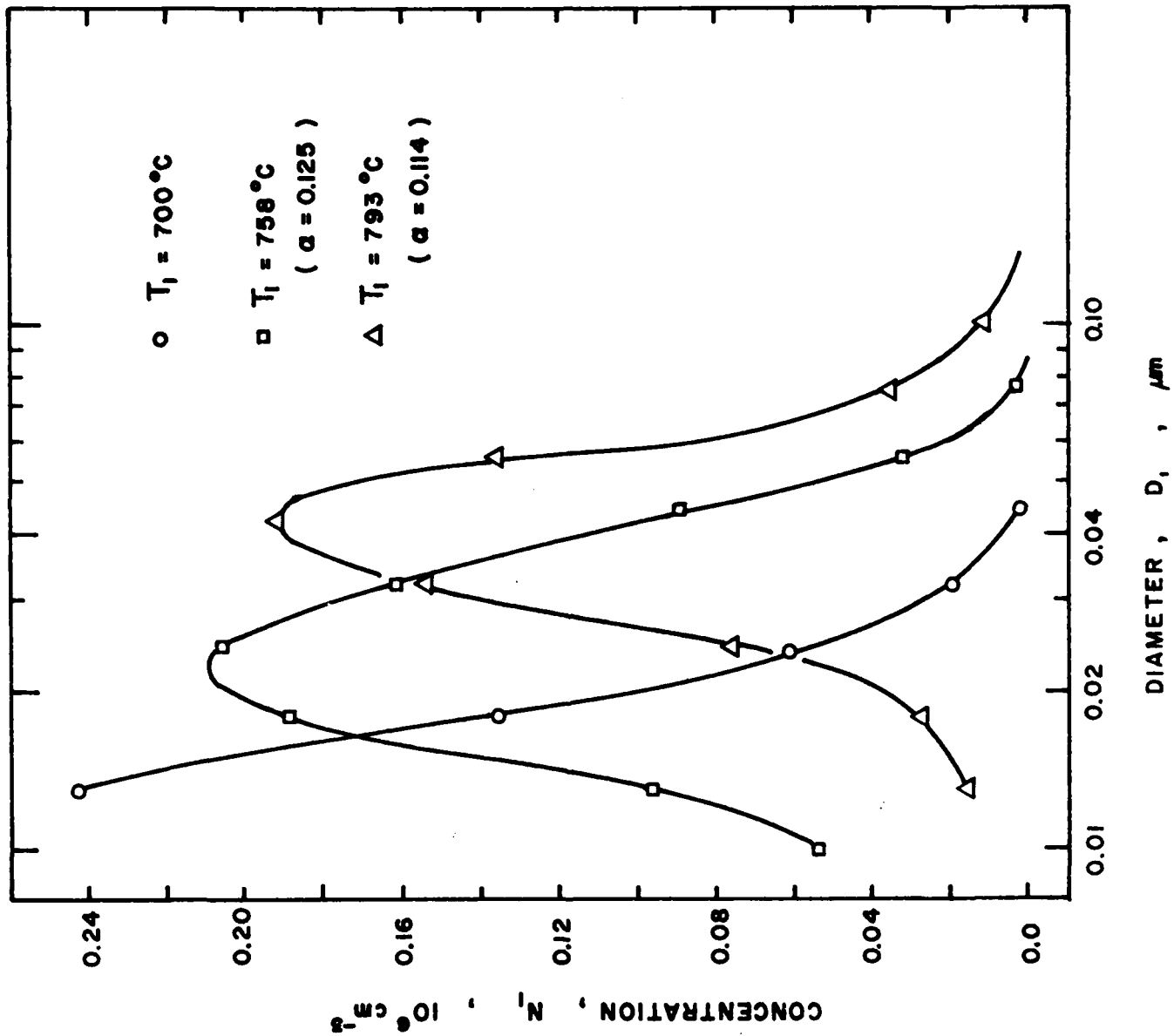
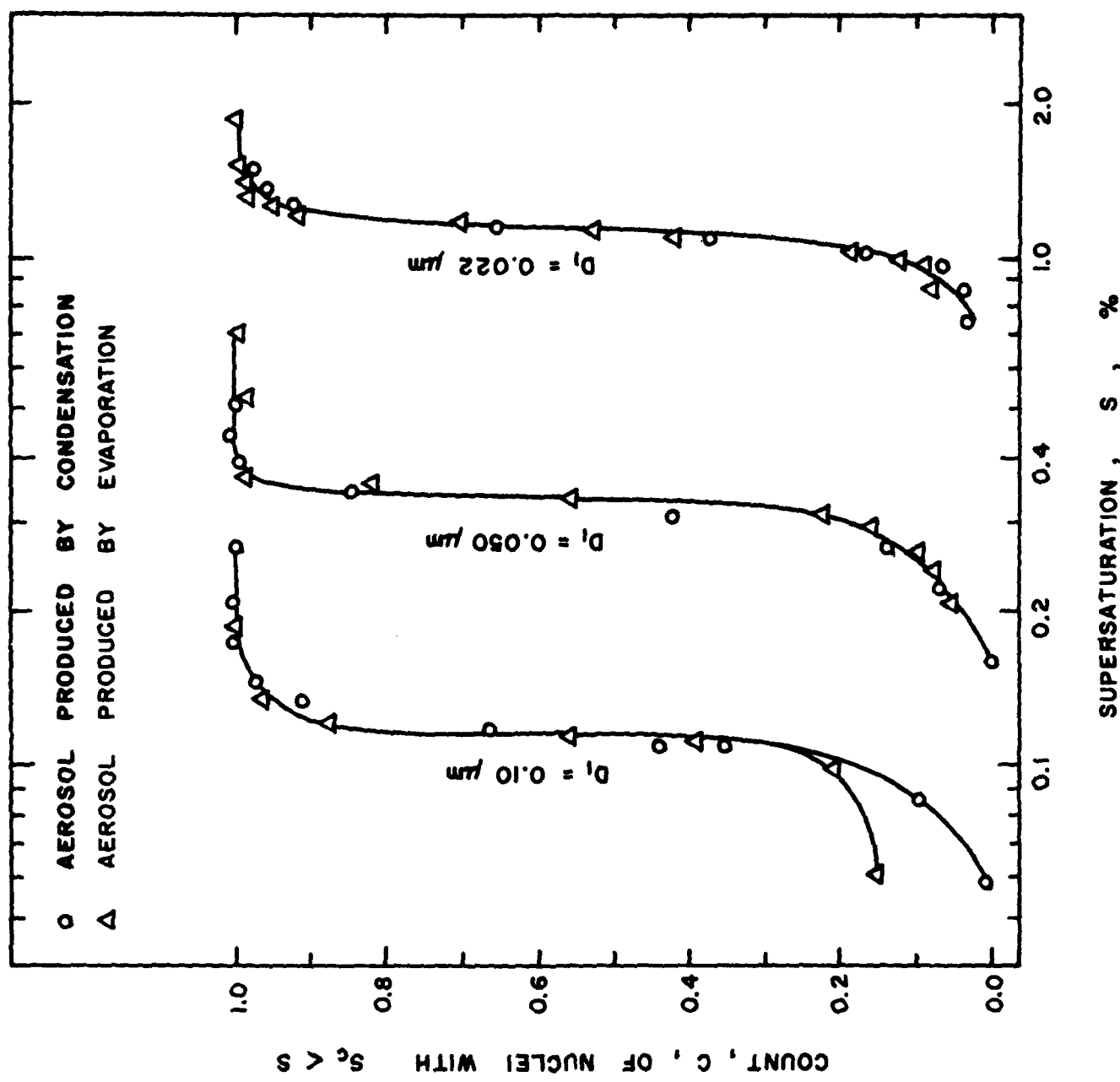
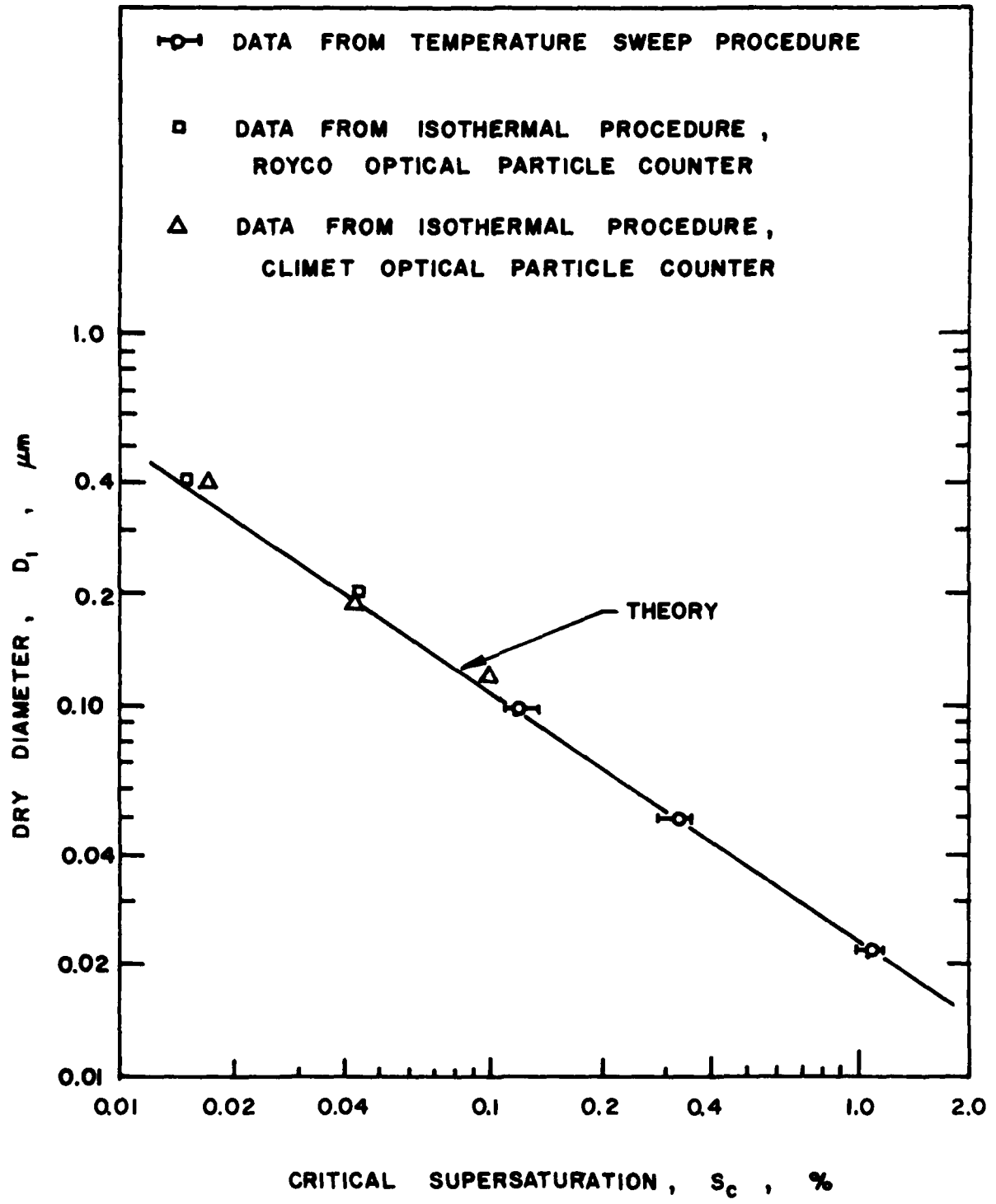


Fig. 7





APPENDIX I
NUCLEATION EXPERIMENTS ON SILICA AEROSOLS

D. J. Alofs and M. B. Trueblood

November 1979

Because silica (SiO_2) is so plentiful in the earth's crust and because the surface of silica particles is expected to have a monolayer of hydrated water, a program was started in May 1979 to determine the critical supersaturation spectra of silica aerosols.

To generate the silica particles, a chemical reaction described by Stober et al (1978)* is used. The reaction involves the hydrolysis of alkyl silicates in alcoholic solutions, in the presence of ammonia which acts as a catalyst. The reaction produces monodispersed spherical particles of amorphous silica, the size being determined by the chemical concentrations and the type of alcohol used.

The resulting suspension of silica particles is atomized to produce the test aerosol. In some cases the suspension was boiled for about one hour to remove most of the dissolved NH_3 . After atomizing the aerosol passes through an electrostatic classifier to improve the monodispersity and select the particle size. The activation supersaturation spectra is then measured by the continuous flow thermal diffusion chamber (Alofs, 1978)**.

Figure 1I shows the results of experiments using furnace drying. The line labeled "Kelvin Equation" is the theoretical relation for an unsoluble aerosol with zero contact angle. The line labeled " $\theta=5^\circ$ " is for an insoluble aerosol with a 5° contact angle with water. The line for NaCl is included for perspective.

The circle data points are for furnace temperatures below

*Stober et al.: "Controlled Growth of Monodisperse Silica Spheres in the Micron Size Range", *J. of Col. & Interface Science* 26, pp. 62-69 (1968).

**Alofs, D. J.: "Performance of a Dual Range Cloud Nucleus Counter", *J. Appl. Meteor.*, 17, pp. 1286-1297 (1978).

733°C. For furnace temperatures below 430°C the critical supersaturation decreased unless the solution was boiled to drive off the alcohol and ammonia. The behavior is consistant with the presence of an unsoluble component proportional to the surface area of the particle. Moreover, the data shows the number of ions in the droplet formed in the cloud chamber is calculated to exactly equal the number of water molecules in a monolayer of hydrated water on the silica particle. This number is also equal to half the number of surface silicon molecules. We have designated this behavior "soluble monolayer". We still do not fully understand this behavior.

The triangle data was taken for furnace temperatures of 790°C. The critical supersaturations are above the Kelvin equations and correspond to a contact angle of 5°. However, SiO_2 collects water of hydration by hydrogen bonding, so a nonzero contact angle is unexpected. Again the effect is not fully understood and further studies are needed.

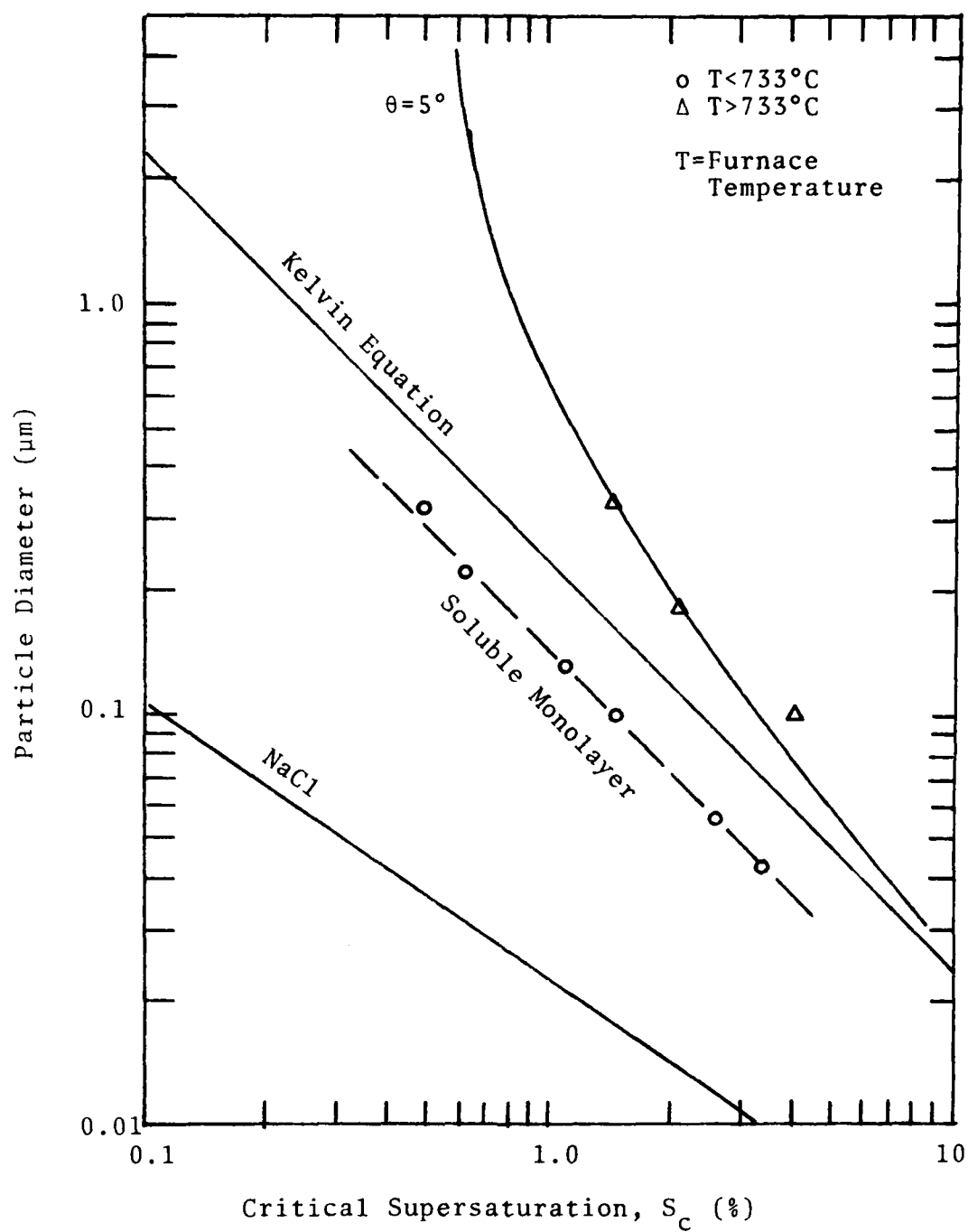


Figure 11. Critical Supersaturation Spectrum for Silica Aerosol Using Furnace Drying.

APPENDIX J

6

A Computer Data Acquisition and Control System for
an Atmospheric Cloud Chamber Facility

D. E. HAGEN, K. P. BERKBIGLER,* J.L. KASSNER, JR., and D. R. WHITE
Graduate Center for Cloud Physics Research, University of Missouri, Rolla, MO 65401

Reprinted from ACS SYMPOSIUM SERIES, No. 57
MINICOMPUTERS AND LARGE SCALE COMPUTATIONS
Peter Lykos, Editor
Copyright 1977 by the American Chemical Society
Reprinted by permission of the copyright owner

A Computer Data Acquisition and Control System for an Atmospheric Cloud Chamber Facility

D. E. HAGEN, K. P. BERKBIGLER,* J.L. KASSNER, JR., and D. R. WHITE

Graduate Center for Cloud Physics Research, University of Missouri, Rolla, MO 65401

The Graduate Center for Cloud Physics Research is a multi-disciplinary research center devoted primarily to the study of the microphysical processes active in cloud and fog. The research tools from the disciplines of physics, chemistry, mechanical engineering, and electrical engineering are employed in this effort. Special emphasis is placed on laboratory experiment and theoretical work, complimented by some field measurement activity.

The purpose of this paper is to describe the hybrid mini/macro computer system that is used to support one of our experimental laboratory facilities, the cloud simulation chamber. The minicomputer is dedicated to serve the data acquisition and control needs of the chamber and is not used for general purpose batch job processing. It is just one of many peripheral subsystems used to support the cloud simulation chamber. The chamber and its peripherals are devoted to "classic" academic research and as a result are in a continuing state of evolution. This discussion will emphasize the present state of development of the computer/chamber system, with some discussion given to the near future plans for the system.

The cloud simulation facility which is supported by the computer system is shown in the block diagram in Fig. 1 and in the photograph in Fig. 2. At the heart of the system is the cloud simulation chamber. It is an expansion cloud chamber, one of the longest used and more important tools in the cloud physics laboratory. In this device a sample of moist aerosol

* Present address: Sandia Laboratories, Livermore, Ca. 94550.

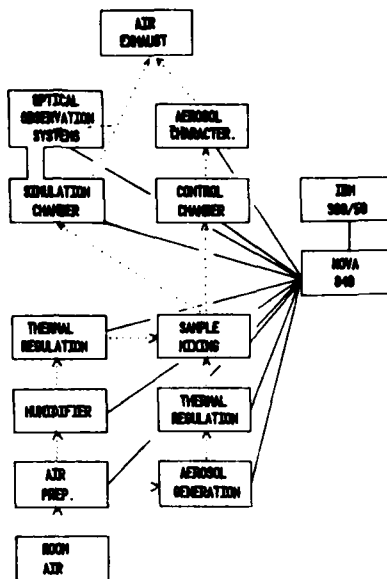


Figure 1. Cloud simulation chamber facility block diagram. ··· air flow; — data flow and control.

laden air is cooled by expansion. The air becomes supersaturated with respect to water and the water vapor condenses out on certain categories of the particulates to form a cloud which can then be studied. The expansion chamber is supported by a variety of peripheral systems. An air preparation system provides a supply of clean dry air. A bank of humidifiers raises the vapor content of the air to 100% relative humidity at a precisely known temperature. Aerosol generators provide a stable and predictable aerosol to serve as condensation nuclei. The control chamber allows for extensive analysis of the sample gas and its aerosol at the initial simulation chamber conditions during the time the cloud is being formed in the simulation chamber. The cloud in the simulation chamber can be observed by several optical systems: light attenuation, laser doppler shift (1), Mie scattering, photography, and visual observation by telescope. The aerosol characterization (critical activation supersaturation spectrum) is accomplished with a variety of techniques: electric aerosol analyzer (2), continuous flow thermal

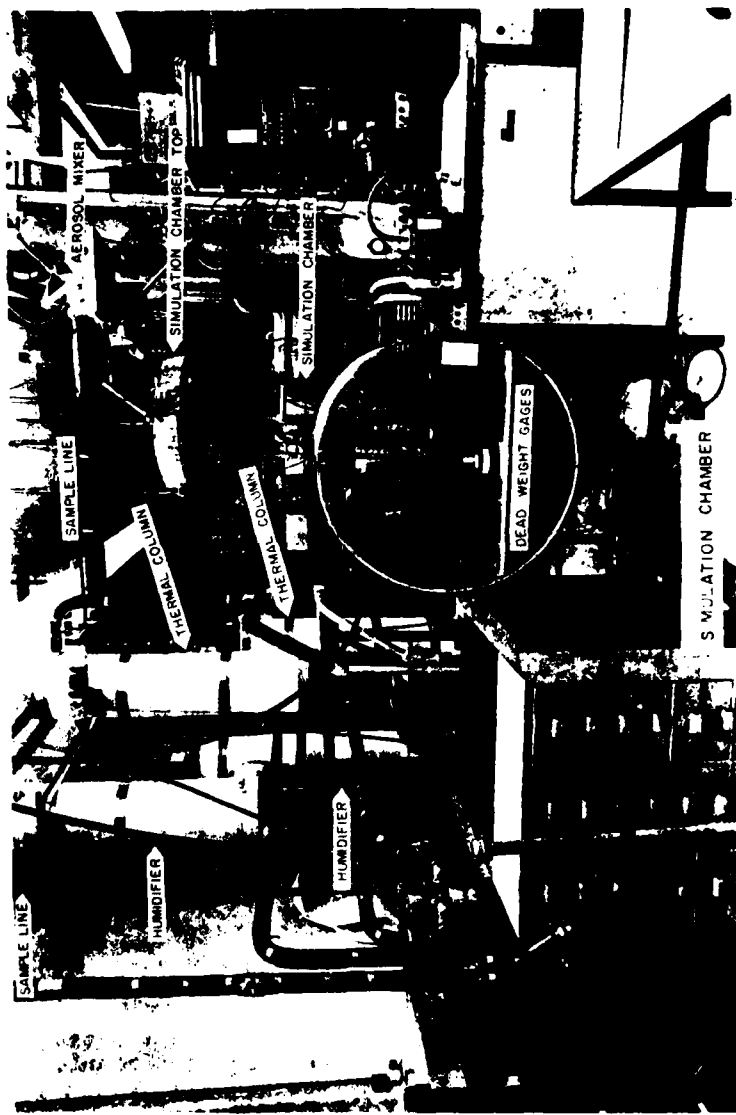


Figure 2. Cloud simulation chamber facility photograph.

diffusion chamber (3), Laktinov Chamber (4), and a Gardner counter.

A major limitation of expansion cloud chambers results from wall effects (5). The ordinary Wilson expansion cloud chamber cools and supersaturates the gas by means of a rapid expansion which is approximately adiabatic, but the chamber walls, whose heat capacity is very high in comparison to the gas, remain at their initial temperature. Heat from the walls flows into the gas and reduces the supersaturation, destroys the adiabaticity of the expansion, and leads to errors in one's knowledge of the evolving thermodynamics. Furthermore, evaporation occurs at all wet surfaces. Our simulation chamber has the unique feature of cooling the chamber walls in unison with the gas to remove this wall effect. The wall cooling is accomplished by thermoelectric modules (6) sandwiched between the chamber's interior and an external heat sink. Control of the gas and wall temperatures is one of the major real-time tasks of the computer system. The control loop is complicated by the fact that the gas temperature cannot be directly measured with sufficient accuracy (5), (7). Instead it is calculated from thermodynamics (5) and drop growth theory and measurements of pressure and liquid water content.

The set of equations governing these processes are given below:

$$\dot{T} = \frac{(nRT/P)\dot{P} - (L+\beta T)\dot{r}}{c_p + s(r_0 - r)}, \quad (1)$$

$$\dot{a}_j = \frac{D_p [S - S_j^* (a_j)]}{a_j + \lambda}, \quad (2)$$

$$r = r_0 - \frac{\pi}{s} \rho_L \sum_j N_j (a_j^3 - a_{0j}^3), \quad (3)$$

where T denotes temperature,

n denotes the number of moles of gas,

R denotes the universal gas constant,

P denotes pressure,

L denotes the latent heat of vaporization of water, it is temperature dependent,

β denotes the coefficient in the linear dependence of the specific heat of moist air on its mixing ratio, ie. $\beta = dc_p/dr$.

- r denotes the mixing ratio for the moist air, ie. the number of grams of water vapor contained in one gram of dry air,
 r_0 denotes the initial mixing ratio,
 c_p denotes the specific heat of moist air, it is temperature, pressure, and mixing ratio dependent,
 s denotes the specific heat of liquid water, it is temperature dependent,
 a_j denotes the radius of a cloud drop in family j ,
 j denotes the drop family, the cloud is broken down into a set of families based on the amount of condensation nuclei material contained within the drops,
 D denotes an effective diffusion constant, it is temperature and pressure dependent,
 ρ denotes the equilibrium vapor density of water, it is temperature dependent,
 S denotes the ambient supersaturation ratio, it depends on temperature, pressure, and mixing ratio,
 S_j^* denotes the equilibrium supersaturation ratio for a drop in family j with radius a_j , it is temperature dependent,
 λ denotes the kinetic coefficient in droplet growth theory, it is temperature and pressure dependent,
 ρ_L denotes the density of liquid water,
 N_j denotes the number of droplets of family j in our sample (those contained in one gram of dry air),
 a_{0j} denotes the initial radius of drops in family j .

The dot denotes differentiation with respect to time. Eq. (1) describes the thermodynamic evolution of the system, and Eq. (2) describes the diffusional growth of the cloud drops. Eq. (2) represents a set of equations, one for each cloud drop family. Normally a system of 10 to 30 families is included in the problem. Equations (1) and (2) are coupled through Eq. (3). The gas temperature calculation involves the numerical solution of this set of coupled differential equations.

The steps involved in a typical experiment are as follows. First a large sample of moist aerosol-laden air is prepared and used to thoroughly flush the chamber. The chamber is sealed and a stilling period is allowed for air motion to die down and equilibrium to be reached. During this time the initial temperature, pressure, relative humidity, and aerosol characteristics are determined. After the stilling period a slow expansion is performed, which simulates the expansion experienced by ascending air parcels in the real atmosphere, and the evolution of the resulting cloud is observed. The observations are then compared with theory during the post-mortem analysis.

In the near future our computer system will be used to support a second cloud simulation chamber facility as well as the present one. NASA is planning to put an Atmospheric Cloud Physics Laboratory (ACPL) on board Skylab in 1980. The ACPL will be patterned after our cloud simulation chamber facility. In support of the ACPL NASA has constructed a prototype facility, called the Science Simulator, which contains most of the hardware shown on Fig. 1. The NASA Ground Based Functional Science Simulator will be located at our research center and will be supported by the same computer system that services our simulation chamber. The Science Simulator will be used to: train the astronauts who will operate the ACPL, test new pieces of equipment before they are incorporated into the ACPL, and aid in the preparation of experiments for the ACPL.

Data acquisition is one of the computer's primary real-time duties. The simulation chamber and its peripheral subsystems generate a variety of analog and digital data. Approximately 100 temperature points are measured throughout the system, with analog temperature signals derived from transistor thermometers, (9), thermocouples, and thermistors. Other analog signals are generated by air flow meters, a pressure transducer, a valve position indicator, a photomultiplier tube, a silicon photodiode, and several voltages from the wall temperature controllers. Digital data sources are a Hewlett Packard quartz crystal thermometer, a laser scattering counter, optical particle counters, and an external digital clock. In total the computer system services 152 analog data inputs, 128 from the UMR simulation chamber, and 32 from the NASA Science Simulator; and 80 bits of digital input data, 48 from the UMR system, and 32 from the NASA system.

Control is the computer's other real-time responsibility. Numerous air flow control valves are involved in the system shown in Fig. 1, and these are all digitally controlled. The NASA chamber's analog data input hardware has an external multiplexer built into it, and it is digitally controlled through our digital output unit. Both chambers have camera/flash optical systems under digital control. The continuous flow diffusion chamber requires analog temperature control and digital control for its optical particle counters.

During the expansion we want the gas and wall temperatures to track each other accurately in order to minimize wall effects. Causing this to happen is our most difficult control problem. Because of its high heat capacity and slow response time the wall temperature is made to track a pre-determined time profile. The desired time dependent wall temperature signal is generated by the NOVA and output through its D/A. The entire wall is broken down into 28 individually controlled sections. The sectionalization of the chamber aids in reducing thermal differences from place to place on the surface of the chamber. These are isolated from one another with 28 linear analog isolators. During the experiment we then measure the wall temperature and the thermodynamic parameters that determine the gas temperature, calculate the gas temperature, and then control the gas pressure so as to keep the gas at the wall temperature at all times.

We have two distinct systems available for the gas temperature control during the expansion. The first is a hybrid digital/analog controller (10). Here the gas temperature is approximated by the sum of a dry adiabatic temperature term plus a latent heat term due to condensed cloud droplets. The dry adiabatic temperature is calculated via a small analog computer. The latent heat term is calculated digitally and the result is output through a D/A channel. The two temperature components are then summed with an analog summation amplifier, compensated analog, and then the result is used to drive a three-way (chamber, high pressure reservoir, low pressure reservoir) rotary valve driven by a servo motor. This hybrid system was the earliest to be put into operation; however, it suffers from the usual difficulties with analog systems, drift and inaccuracy. Also its range of accurate operation limited it to relatively small expansions, those with a temperature change of 2°C or less. Much larger expansions are desired.

The second gas temperature controller, now being completed is a purely digital system, with the computer doing all of the pressure-temperature calculations and control compensation. Fig. 3 contains a block diagram of the control scheme. P denotes pressure, T_{wall} denotes the measured wall temperature, and the X's denote other measured parameters which vary from experiment to experiment. A discrete time optimal tracking technique is used. The control signal is sent through the digital output system to a stepper motor driving a three-way rotary valve. The number from the digital output is sent to a specially designed interface which then emits that number of pulses at 900 Hz to the stepper motor.

Several reasons were behind the decision to use digital data acquisition and control rather than the combination manual-analog systems used on previous fast expansion chambers (11). First of all, the accuracies required in the control related computations are beyond those available with analog transfer function generators. In order to take full

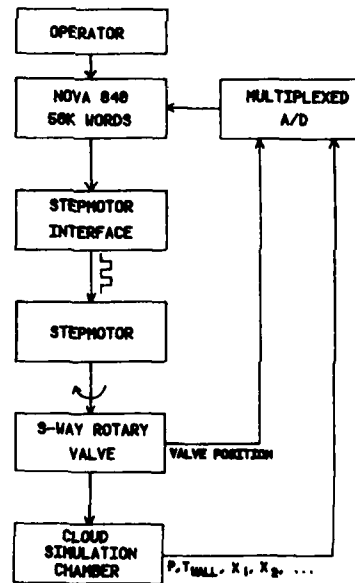


Figure 3. Expansion control loop block diagram

advantage of the accuracies of the wall temperature and the chamber pressure measurements, the gas temperature should be calculated to an accuracy of 0.001 °C. Analog devices could not meet this requirement. Furthermore, the cost of the less accurate analog system is comparable to that of the digital system if not more expensive. The cost of the digitizing equipment must be included in either approach since the data has to be in digital form in order to be stored and analyzed. Moreover the multiplexing capability of the digital system reduces the overall cost considerably.

Another major advantage of the digital system is its versatility. The simulation chamber can be used for a wide variety of experiments. With a computer based control and data acquisition system the nature of the experiment can be changed substantially by making only simple software changes to the computer program, with little or no hardware changes. Such changes are faster and less expensive than analog hardware changes and readjustments. This feature greatly increases the versatility of the chamber and increases the number of experiments which the chamber can perform per unit time. It also makes it easier for more than one experimenter to use the chamber.

Computer System

Figure 4 shows a block diagram of the computer system used for cloud chamber support. Fig. 5 shows a photograph of the computer system. The NOVA 840 system is dedicated to our two cloud chamber facilities and is not used for the batch processing of general jobs. The cable link is a hard wire 19.2 K-baud link to the UMR IBM 360/50 through the UMR mini-network (12). The IBM 360/50 features 524, 288 bytes of core storage, 5 IBM 2314 Disk Drives, 2 IBM 2415 magnetic tape units, 2 IBM 1403N1 printers, an IBM 2540 card reader/punch, an IBM 2501 card reader, and an IBM 2701 transmission control unit for data transmission lines to the University of Missouri IBM 370/168 and 370/158 computers. The IBM 370 is not used for the direct real time support of our cloud simulation chamber effort. It is used for general modelling, software development, and the experiment's post-mortem analysis.

Our NOVA minicomputer system was acquired over a period of several years at a total cost of \$73,500.

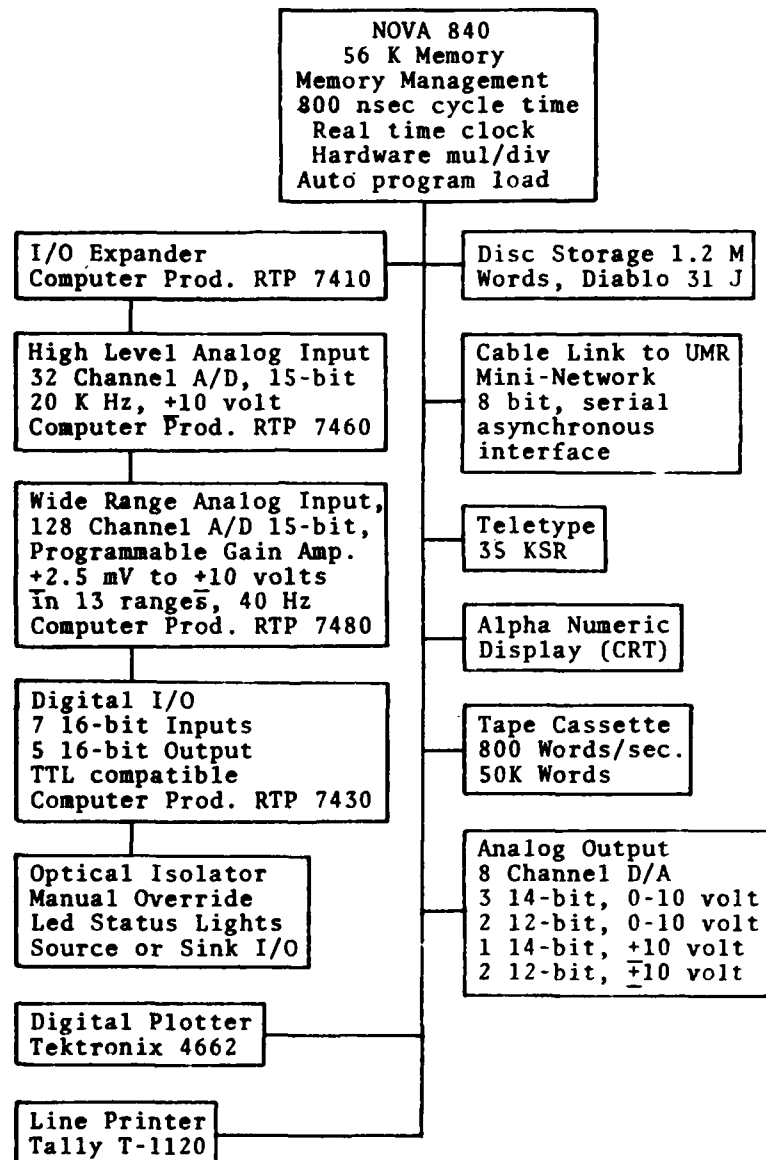


Figure 4. Computer system block diagram

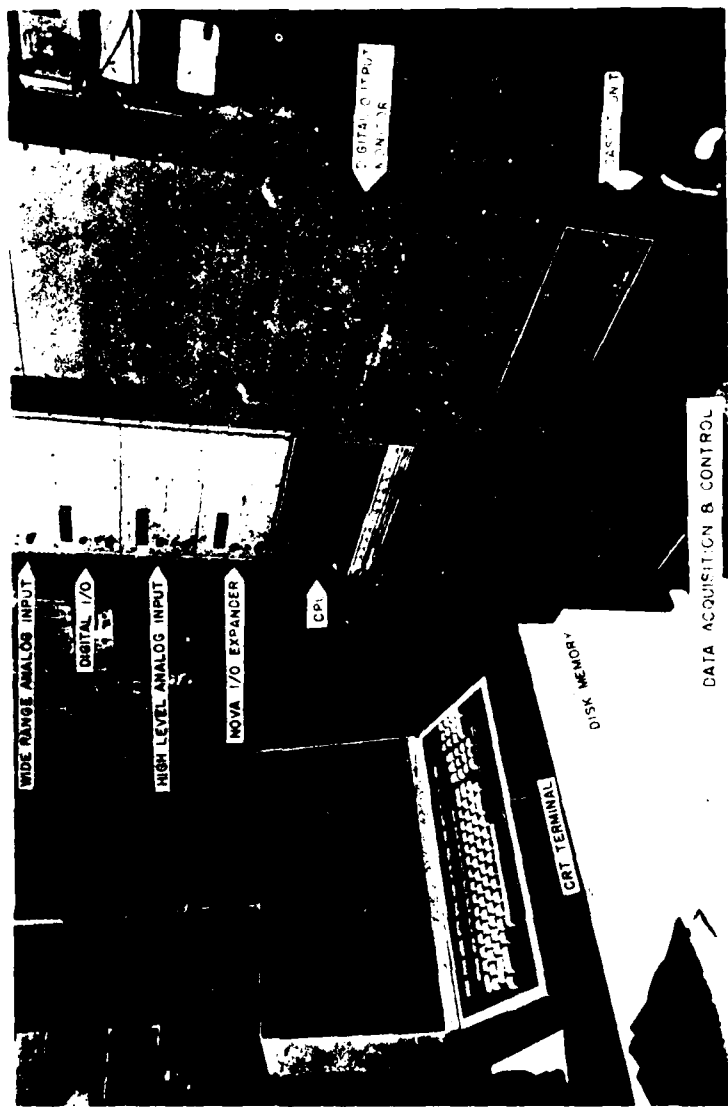


Figure 5. Computer system block diagram.

Maintenance is handled by our Center's electrical engineering staff at a cost of approximately \$100/month. The computer system has proven quite reliable. In its 2½ years of operation it has rarely caused the shutdown of the cloud chamber facility. Our campus operates ten of the NOVA 800 series mini-computers. A staff member in the electrical engineering department handles the more sophisticated repair and interfacing problems for all the NOVAs on campus. The optical isolators attached to the digital I/O are homemade units that cost about \$3500.

The NOVA's operating system is RDOS (Real time disc operating system). The memory management and protection option divides the computer into three partitions that are hardware protected from each other. The operating system resides in one, and two independent programs can be run in a time sharing mode in the other two partitions. Hence, we can run the two cloud chambers simultaneously, or run one chamber and edit programs for the other, etc. The partitioning feature has proven quite useful. Our cloud chamber support programming is done in Fortran, Basic, and Assembler. Most of the chamber operation programs are in Fortran, all of the subroutines which handle our peripherals (A/D, D/A, etc.) are in Assembler and are Fortran callable.

The IBM 360/50 services the entire UMR campus and handles both batch jobs and real time service of the mini-network. It is a \$1,000,000 machine with a \$2,000/month maintenance cost. It uses the OS 360 MVT Rel. 21 operating system and the mini-network is accessed with the BTAM method. All of our usage of the IBM 360 is done under Fortran.

Computer System Role in Expansion Control

There is a distinct division of labor between the NOVA and the IBM 360 during an experiment. The 360 is involved in Chamber operation because we need to calculate the gas temperature (the gas temperature cannot be directly measured with sufficient accuracy due to condensation on the sensors (5,7)) in order to properly control the experiment (make the gas temperature track the wall temperature). The gas temperature is calculated via a numerical cloud model that solves a set of simultaneous differential equations (Eqs. (1-3)), describing the thermodynamics and cloud droplet growth. This cloud model is too large and runs too slow for the NOVA to handle.

Inputs to the cloud model are the initial temperature (T_0), pressure (P_0), supersaturation ratio (S_0), the aerosol's critical supersaturation spectrum, and the pressure vs. time ($P(t)$) profile during the experiment. The output from the cloud model is the time dependent temperature, $T(t)$, plus drop sizes and other thermodynamic information. Ideally the cloud model should be run in real time using the initial conditions and aerosol characterization measured just before the expansion plus the measured real time pressure profile as inputs. However this is not practical for a machine of the NOVA's size and speed. Instead we use a "perturbation" type of approach. The NOVA collects the initial thermodynamic and aerosol starting conditions. We know in advance the approximate pressure profile that will occur during the experiment since our goal is to make the gas track the wall temperature, and this defines a pressure profile. The wall temperature profile is predetermined to the extent that we can make the walls track a desired temperature profile. The cloud model is (Eqs. (1-3)) is run on the 360 for the measured initial conditions and the expected pressure profile. The resulting temperature profile is approximately what will occur during the actual experiment. All we need to calculate in real time is the deviation from this anticipated behavior due to deviations in the other measured parameters during the experiment. To accomplish this the IBM 360 performs a functional fit; the gas temperature is expressed as a simple function of measured parameters. Various options are available for which parameters are used (liquid water content, mixing ratio, light attenuation, pressure, etc.) depending on the type of experiment. These functional fits are found to be quite accurate (on the order of 0.001°C) but are valid only for the exact experiment for which they were calculated. They must be recalculated for each experiment. The 360 transmits the results of the functional fit back to the NOVA. This information is then used in the NOVA for its time control calculations. Since simple functions were used in the functional fit they can be evaluated in real time on the NOVA.

The following list summarizes the steps taken by the two linked computer systems in order to accomplish an experiment.

- 1) The NOVA oversees the preparation of the experiment and the measurement of the initial conditions of the system (T_0 , P_0 , S_0 , and aerosol).
 - 2) The information taken in step 1 plus the expected pressure profile, $P(t)$, is transmitted from the NOVA to the IBM 360.
 - 3) The cloud model is then run on the IBM 360, yielding the temperature profile $T(t)$.
 - 4) A functional fit is performed on the IBM 360, yielding $T(P, x_1, x_2, \dots)$, ie. temperature as a function of the measurable parameters P , x_1, x_2, \dots . P denotes pressure, and x_1, x_2, \dots the other measurable parameters selected for this experiment.
 - 5) The function $T(P, x_1, x_2, \dots)$ is transmitted from the IBM 360 to the NOVA.
 - 6) The NOVA uses the function $T(P, x_1, x_2, \dots)$ for its real time control calculations during the experiment, as shown in Fig. 3.
- Steps 3 and 4 are run on the IBM 360 during the stilling period following the flushing of the chamber with the aerosol-laden moist air.

Cloud Simulation Chamber Program

In this section we describe the computer program that runs on the NOVA and oversees the cloud chamber operation during an experiment. The program is written in Fortran and makes extensive use of Data General Fortran's multitasking feature. During an experiment various activities (take temperature data, take laser data, output wall temperature control signal, etc.) must be done periodically. The multitasking feature allows each activity to be designated as a task, each with its own priority and frequency of execution. Various tasks can be active simultaneously. They compete for system resources based on need and priority.

The overall simulation chamber software is too large to fit into the available core, so it is broken down into four programs corresponding to four consecutive phases of experimental activity: preparation of the chamber, closing of the chamber, the expansion, and the post-expansion clean-up. Chaining is used to automatically transfer from one program to the next; upon completion of its duties the

phase one program deletes itself, causes the phase two program to be loaded into core from disc, and begins its execution, and so on down the line.

PART 1 - Preparation. This program collects input information from the operator via the CRT keyboard that defines the experiment to be done. Questions are displayed on the CRT and the operator responds. Then the program reads disc files containing the desired wall temperature profile and the cloud model functional fit result, $T(P, X_1, X_2, \dots)$.

Up to this point in time a manual chamber flush with dry air has been in progress. All of our valves that control air flow have a manual override. The computer now switches valve control digital output bits to the dry flush position and asks to have all the valves changed from manual to computer control. Then at the operator's signal, the computer initializes a chamber flush with moist aerosol-laden air, and it takes periodic data readings (temperature, light scattering, etc.) and stores the results on the disc and displays them on the CRT. When the operator decides that the flush is sufficient, he signals the computer and it then chains to the phase 2 program.

PART 2 - Closing of the chamber. Here the computer takes one set of thermometer readings, stores them on the disc, and displays them on the CRT. Then the temporal length of the wet flush is recorded, the chamber valves are closed, and the stilling period begins. During this time the initial readings (T_0, P_0, S_0 , aerosol, etc.) are taken and transmitted to the IBM 360. When the 360's cloud model results are received and the operator signals that he is ready for the expansion to begin, the program chains to the phase 3 program.

PART 3 - Expansion. This phase of the experiment is handled with multitasking. PART 3 activates five tasks and then simply waits for the duration of the expansion to pass. TASK 1 takes periodic wall temperature and gas pressure readings, TASK 2 takes periodic laser (Mie and Doppler) light scattering data, TASK 3 displays current information on the CRT, TASK 4 outputs an updated wall temperature control signal, and TASK 5 outputs an updated gas temperature control signal. When the time allotted for the expansion elapses, the computer aborts all five tasks and chains to the phase 4 program.

PART 4 - Post-expansion. Under this phase the computer re-opens the chamber and begins a chamber

flush with clean dry air for a given amount of time. Disc data files resulting from this experiment are secured for the post-experiment analysis.

Independent programs are then run on the NOVA after the experiment to perform some analysis on the raw data stored on disc files. They produce written listings and graphical output that records the experimental data in permanent form. Then some of the raw data files are transmitted to the IBM 360 via the mininetwork link and are stored on cards. The subsequent post-mortem analysis using the cloud model and other physics or chemistry models for the process under study are performed on the IBM 360 or the IBM 370 as batch jobs.

Acknowledgement

This work was supported by the Office of Naval Research, ONR-N00014-75-C-0182, and by the National Aeronautics and Space Administration, NAS8-31849.

Abstract

The Graduate Center for Cloud Physics Research operates an experimental cloud simulation chamber facility designed for the study of atmospheric micro-physics and chemistry. The Marshall Space Flight Center is constructing a miniaturized version of this facility as a ground based science simulator in support of an Atmospheric Cloud Physics Laboratory which is planned for the Space Shuttle. These two facilities are supported by a hybrid NOVA 840 - IBM 360/50 computer system for data acquisition and control purposes.

Literature Cited

1. Hagen, D. E., Hale, M. H., and Carter, J., Proc. Electro-Optical Systems Design Conf., Anaheim, CA, 1975, p. 373.
2. Whitby, K. T., Liu, B. Y. H., Husar, R. B., and Barsic, N. J., J. Colloid Interface Sci., (1972), 39, 136.
3. SInnarawalla, A. M. and Alofs, D. J., J. Appl. Meteor., (1973), 12, 831.
4. Lakinov, A. G., English Translation Atmos. and Oceanic Phys., (1972), 8, 382.
5. Kassner, J. L. Jr., Carstens, J. C., and Allen, L. B., J. Atmos. Sci., (1968), 25, 919.
6. "Thermoelectric Handbook," Cambridge Thermionic Corp., Cambridge, Mass., 1972

7. Kassner, J. L. Jr., Carstens, J. C., and Allen, L. B., *J. Recherches Atmospheriques*, (1968), 3, 25.
8. Carstens, J. C., Podzimek, J., and Saad, A., *J. Atmos. Sci.*, (1974), 31, 592.
9. Pease, R. A., *Instruments and Control Systems*, (1972), 45, (6), 80.
10. Hagen, D. E., Tebelak, A. C., and Kassner, J. L. Jr., *Rev. Sci. Instrum.*, (1974), 45, 195.
11. Allen, L. B., "An Experimental Determination of the Homogeneous Nucleation Rate of Water Vapor in Argon and Helium," Ph. D. Dissertation, University of Missouri-Rolla, 1968.
12. Beistel, D. W., Mollenkamp, R. A., Pottinger, H. J., de Good, J. S., and Tracey, J. H., in "Computer Networking and Chemistry," ACS Symposium Series 19, (1975), ed. by P. Lykos, p. 118.

APPENDIX K

Reprinted from JOURNAL OF APPLIED METEOROLOGY, Vol. 18, No. 8, August 1979
American Meteorological Society
Printed in U. S. A.

A Numerical Cloud Model for the Support of Laboratory Experimentation

DONALD E. HAGEN

Physics Department and Graduate Center for Cloud Physics Research, University of Missouri, Rolla 65401
(Manuscript received 25 August 1978, in final form 24 March 1979)

ABSTRACT

A numerical cloud model is presented which can describe the evolution of a cloud starting from moist aerosol-laden air through the diffusional growth regime. The model is designed for the direct support of cloud chamber laboratory experimentation, i.e., experiment preparation, real-time control and data analysis. In the model the thermodynamics is uncoupled from the droplet growth processes. Analytic solutions for the cloud droplet growth equations are developed which can be applied in most laboratory situations. The model is applied to a variety of representative experiments.

1. Introduction

This laboratory has been deeply involved in the study of the microphysical processes active in cloud and fog with special emphasis on laboratory work. A substantial facility (Kassner *et al.*, 1973) has been developed for simulating cloud processes (see Fig. 1). The basic element in the facility is a cooled-wall expansion cloud chamber, and it is supported by a variety of subsystems, e.g., aerosol generators, aerosol characterizers, air preparation system and cloud observation systems. Control and data acquisition support is handled by an on-line NOVA 840 minicomputer system (Hagen *et al.*, 1977) which has access to an IBM 360/50 through the UMR minicomputer network (Brustel *et al.*, 1975). The cooled-wall feature (the chamber walls are cooled at the same rate that the expansion cools the gas) allows adiabatic cloud processes to be studied in their natural time frame; it is not necessary to accelerate the process in order to finish the experiment before wall effects interfere. The present chamber, 0.61 m high, is a prototype and its experiments are limited by sedimentation. A taller 2.7 m version is planned.

A wide range of cloud processes are amenable to investigation by this facility. The initial phase of our experimental program will be devoted to warm cloud microphysics, e.g., aerosol activation, cloud formation, diffusional droplet growth, Ostwald ripening and collisional coalescence. The cloud chamber can operate down to -40°C so ice nucleation and growth problems can be studied. Clouds can be made to specification for studying their optical properties, scavenging and chemical reactions.

NASA is preparing an Atmospheric Cloud Physics Laboratory (Smith *et al.*, 1976) (ACPL) facility for use aboard Spacelab to take advantage of the low-

gravity environment in orbit. This facility is essentially a miniaturized version of our cooled-wall expansion cloud simulation chamber facility. The range of experiments envisioned is broad and is similar to the range of experiments suited to our terrestrial facility.

These types of experimental facilities have an obvious need for cloud modeling support to describe the physical processes occurring within the experimental chambers. There are a variety of numerical cloud models in existence (Cotton, 1975) but these are primarily oriented toward theoretical studies which give what we might call strategic support to this area of cloud physics. There is also a need for direct tactical support for the laboratory effort. Such a cloud model is first needed to help prepare experiments. This involves selection of the initial conditions, type of expansion and aerosol which are needed to produce the type of cloud desired for study. The second need for tactical support concerns cloud chamber control. The control system must, via the cloud model, determine the value of the pressure which will cause the gas temperature to equal that of the walls at the current time. Direct gas temperature measurements are not practical here (Kassner *et al.*, 1968). The effects of drop growth must be included. This requires the cloud model to be run in real time on a computer tied to the experimental facility. In most theoretical problems, the pressure versus time profile, such as that corresponding to a constant updraft, is a known function input to the model and temperature versus time is the output. For this tactical support, just the opposite is usually needed. The temperature profile is input and the pressure profile is output. The third type of support is the post experiment analysis. It is here that theory and experimental results meet to search for common ground.

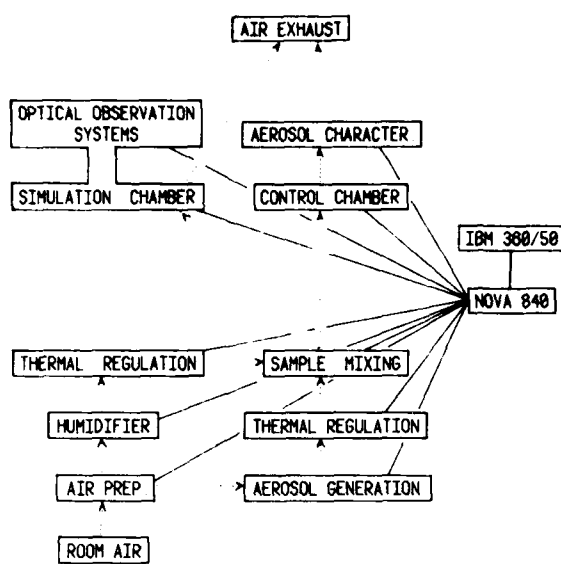


FIG. 1. Cloud simulation chamber facility block diagram: dotted lines, air flow; continuous lines, data flow and control.

A prime requirement of the numerical cloud model used for tactical chamber support is computational speed. First of all, in order to participate in chamber control, the cloud model must be able to run in real time. Here the concern is more than just the monetary cost of the computer time, since the speed of the model can limit the range of experiments amenable to the facility. Furthermore, the model needs to run fast enough to make it feasible to include phenomena not ordinarily included in the normal thermodynamics plus drop growth cloud models. Phenomena needed for direct experimental support would include heat diffusion from the walls into the gas (no control system is perfect), the effects due to gravitational sedimentation of the cloud drops (producing inhomogeneities in temperature, drop size spectrum and water vapor density), Mie light scattering off the cloud drops, the Doppler frequency shift (Hagen *et al.*, 1975) of this scattered light (for size spectrum measurement), light attenuation, the evolution of ice when it is involved in the experiment, collision coalescence and scavenging.

Another attribute of the tactical support cloud model is that it should have the adaptability to accommodate newly measured parameters as they become available during the course of the program. In particular, substantial efforts are currently being expended to develop methods for obtaining real-time cloud drop size spectrum measurements. When these are developed, the cloud model module which calculates the evolution of the drop size spectrum can be replaced by a module which takes the measured data and converts them into the size spectrum.

The measurement and control systems of the simulation chamber are accurate to about 0.02°C in temperature and 0.16 mb in pressure. The optical systems for drop size measurement are good to about $0.2 \mu\text{m}$. The computations in the support cloud model need to be somewhat better than this level of accuracy.

The tactical cloud model should be well documented in the literature. A large number of investigators from a wide variety of laboratories are envisioned as users of the ACPL facility. Many will be familiar with one or two components of the facility but few will be familiar with all of its components. The cloud model used for the direct support of the expansion chamber is one component that should be well documented.

The numerical cloud model should be able to handle different types of expansions, rather than just those corresponding to constant updraft, so that a wide variety of experiments can be modeled. The ultimate goal of the cloud chamber facility is to study cloud microphysics. In order to emphasize certain phenomena of interest, it will be necessary to perform expansions in which the pressure and temperature vary in ways which do not occur in nature. Such behavior can cause problems for the numerical routines if they are not sufficiently flexible.

The purpose of this paper is to describe the formulation of a numerical cloud model designed for the direct support of a laboratory cloud chamber facility. The model presently performs the thermodynamics, droplet growth and light attenuation parts of the problem, and was designed to provide the capability for future inclusion of other interesting phenomena such as heat diffusion, sedimentation, Mie scattering, etc. In the numerical solution, the thermodynamics and the droplets growth equations are uncoupled. The model is used to analyze a set of "typical" experiments suitable for an expansion cloud chamber facility. It is found that the model is capable of real-time performance on a macro computer system.

2. Cloud-model equations

We consider a closed system consisting of one gram of dry air plus r grams of water vapor which occupies a volume v , which varies with time. As the water condenses into liquid it remains in the system. The water vapor mixing ratio r also changes with time. We assume the moist gas obeys the ideal gas law

$$\rho = (1+r)R_m T, \quad (1)$$

where ρ denotes the total pressure, R_m the gas constant for moist air and T the temperature.

For this system, the first law of thermodynamics takes the form

$$dQ = du + pdv, \quad (2)$$

where dQ denotes an increment of heat added to the system and du an incremental change in internal

energy of the gas. We assume that the cooled-wall feature of the facility prevents the flow of heat into the sample parcel of moist air from the walls. The only two contributions to dQ come from the latent heat release by the condensing water and the heat released by the liquid drops as they are cooled. With this, (1) and (2) can be combined to yield

$$\dot{p} = v^{-1}[(1+\eta r)c_{pd} + c_w(r_0-r)]\dot{T} + v^{-1}(L+c_p,T)\dot{r}, \quad (3)$$

where

$$v = (1+r)R_m T / p = (1+r/\epsilon)R_d T / p.$$

The dot refers to differentiation with respect to time, c_{pd} and c_p , denote the specific heats (per gram) at constant pressure of dry air and water vapor, $\eta = c_{pw}/c_{pd}$, c_w is the specific heat of liquid water, L the latent heat of condensation of water, R_d the gas constant for dry air, ϵ the ratio of the molecular weight of water vapor to that of dry air and r_0 denotes the initial value of r . Numerical values are taken from the *Smithsonian Meteorological Tables* (List, 1971).

In order to evaluate p as a function of time, one needs to know r as a function of time. This can be determined from the measurement of the droplet size spectrum if that is done, or it can be evaluated from droplet growth theory. For the growth theory case, we make use of the linearized version of droplet growth theory (Carstens *et al.*, 1974; Carstens, 1979), i.e.,

$$\dot{a} = D_{eff}\rho_{sat}(S - S^*)/(a + l)\rho_w, \quad (4)$$

where

$$1/D_{eff} = [1 - r/(\epsilon + r)]/D + LB/KR_a T,$$

$$l = D_{eff}(l_a LB/KR_a T + l_b/D),$$

$$l_a = (1 - \alpha/2)K(\gamma - 1)(8\pi T/R_a)^{1/2}/[\alpha p(\gamma + 1)],$$

$$l_b = (1 - \beta/2)D(2\pi/R_a T)^{1/2}/\beta,$$

and where

a	drop radius
$\rho_{sat}(T)$	saturation water vapor density over a flat surface
S	supersaturation ratio, the ratio of the water vapor pressure over the equilibrium vapor pressure above a plane water surface
$S^*(a)$	equilibrium supersaturation ratio over a droplet of radius a
D	diffusion coefficient of water vapor in air
B	slope of the $e_s(T)$ curve [$= de_s/dT$]
e_s	saturation vapor pressure
L	latent heat of condensation for water
K	thermal conductivity of moist air
α	thermal accommodation coefficient
β	condensation coefficient
γ	specific heat ratio of moist air
R_a	gas constant for dry air
R_v	gas constant for water vapor
ρ_w	density of liquid water.

The equilibrium supersaturation ratio $S^*(a)$ is given by the commonly used Köhler expression (Byers, 1965; Low, 1969)

$$S^* = 1 + b_1/a - b_2/a^3, \quad (5)$$

where b_1 is the curvature term and b_2 the solubility term. More elaborate forms for S^* (Low, 1969) could be used, but were not felt to be necessary at this time.

The cloud drop spectrum is broken down into a number of families based upon the amount of dissolved salt. In practice this information comes from the activation supersaturation spectrum of the aerosol as measured in the continuous flow thermal diffusion chamber. All of the members of a given family behave identically and are described by (4). The droplet growth equations feed back to the thermodynamics through the mixing ratio r :

$$r = r_0 - (\frac{1}{3})\pi\rho_w \sum_{j=1}^J N_j (a_j^3 - a_0^3), \quad (6)$$

where r_0 is the initial mixing ratio, N_j the number of drops in family j (number per gram of dry air, not the number per unit volume), a_0 , the initial radius of a drop in family j , and there is a total of J families in the system. The supersaturation ratio is dependent on r through

$$S = [p/e_s(T)]/(1 + \epsilon/r), \quad (7)$$

where $e_s(T)$ is the equilibrium vapor pressure over a flat surface at temperature T .

The slope B of the $e_s(T)$ curve is temperature dependent and should be evaluated at the temperature T_d of the drop which is slightly different from the ambient temperature (Carstens, 1979; Fukuta and Walter, 1970). T_d is determined by (Carstens, 1979)

$$T_d = T + LD(1 + r/\epsilon)[Se_s(T) - e_s(T_d)](a + l_a)/KR_a T(a + l_b).$$

We have a subroutine to solve this equation for T_d and account for it in (4) but we rarely invoke it because the effect is negligibly small for low supersaturations and it increases the computation time by about 20%. Since T_d depends on a it has to be recalculated for each drop family. In the droplet growth experiment (Section 4) inclusion of the drop temperature changes the gas temperature less than 3×10^{-4} K and the drop sizes by less than 5×10^{-4} μm .

The evolution of the cloud is governed by the set of $J+1$ differential equations (3) and (4), coupled through (6) and (7), by the initial conditions (temperature, pressure, mixing ratio and aerosol), and by the temperature versus time profile. The numerical solution of these equations is discussed in the next section.

3. Numerical solution of the cloud model

We assume that initially the aerosol is in equilibrium with the moist air sample. Each aerosol family is at the stable equilibrium size given by the intersection of its Kohler curve and the initial relative humidity. The numerical problem consists of following the evolution of this cloud in time as described by (3) and (4).

As discussed above, the thermodynamic and the droplet growth equations are solved in an uncoupled fashion. A basic idea used here is that often the droplet growth processes occur on a much faster time scale than the thermodynamic processes. During a certain short period of time or time step, the thermodynamic parameters may be treated as linear functions of time during the droplet growth calculations. After the droplet growth calculations, the coupling between drop growth and the thermodynamics is accounted for and then the thermodynamic equation is processed through the time step.

The size of this time step is controlled by the non-linearity of the thermodynamic variables p (pressure), T (temperature) and S (supersaturation ratio). We consider p first. Let Δp denote the expected range of p during the experiment. The time step h is selected such that if β (the second derivative with respect to time) is constant then the error with respect to the linear approximation that builds up in time h will be equal to $\Delta p/10^4$. Hence

$$h = (2\Delta p/10^4 \beta)^{1/2}. \quad (8)$$

We determine β from the immediate past history of p . A similar calculation is carried out for T and S . The minimum of the three time steps is chosen for the time step used in the cloud model calculations. As a check on this choice of a step size the droplet growth experiment (Section 4) with the pressure profile used as input was run twice, once with 10^4 in Eq. (8) and once with 10^6 which gave a smaller time step. The maximum temperature difference was 3×10^{-5} °C and the maximum difference in drop radius 9×10^{-4} μm. These differences are negligible. Reasonable upper and lower bounds are set for the range of values that will be used for the time step. Note that this is a dynamic technique for selecting the time step. When events move fast, the step gets small; when events move more leisurely, the time step gets large.

The sequence of events during a given time step, from t_{i-1} to t_i , is as follows. At time t_{i-1} it is assumed we know everything about the system: T_{i-1} , p_{i-1} , r_{i-1} , $(a_j)_{i-1}$ for every j , etc. At time t_i we know T , since the wall temperature is both predetermined and directly measurable; we want to determine p . To accomplish this, the value of r at time t_i is needed. If the cloud drop size spectrum is measured, then it can be evaluated from (6). If not, then the drop size

spectrum at t_i is calculated by drop growth theory, i.e., Eq. (4). For the calculation, we assume that the parameters $D_{eff} \rho_{sat}$, S and l can be linearly extrapolated in time based on their behavior in the previous time step. Then a becomes a function of t for $t_{i-1} \leq t \leq t_i$; and a_i at time t_i can then be evaluated. For this task, the IMSL¹ subroutine DVOGER, a variable step program utilizing Gear's method of solving differential equations, is used. This is repeated for each family j , and then r is calculated via (6).

Then the temperature and mixing ratio are assumed to be linear functions of time for $t_{i-1} \leq t \leq t_i$. This makes p become a known function of t via (3) and the value of p at time t_i can be computed with the routine DVOGER. With this, any other relevant parameter can be calculated for time t_i , and the next time step can be taken.

A major part of computational time is spent on the droplet growth calculations. Special effort has been made to optimize this task by employing analytical solutions where practical. One situation where this is possible and, in fact, necessary, is the case where the droplet is smaller than critical size and the slope of its Kohler curve is very steep. A numerical problem arises here because any numerical solution for the droplet radius a has some acceptable uncertainty δa . If the Kohler curve is steep, i.e., dS^*/da is large, then the "apparent" growth rate due to a displacement δa in a ,

$$\dot{a} = D_{eff} \rho_{sat} (dS^*/da) (\delta a) / \rho_w (a + l), \quad (9)$$

can become larger than the actual growth rate due to the change in S with time,

$$\dot{a} = \dot{S}/(dS^*/da) = a^2 \dot{S} / (3b_2/a^2 - b_1). \quad (10)$$

When the growth rate in (9) exceeds that in (10), the numerical solution is unstable. When this situation occurs, the Kohler curve is so steep that the growing droplet tracks the supersaturation and remains very close to equilibrium with it (Carstens, 1974; Brown and Arnason, 1973). The solution is to not use a numerical solution but rather solve

$$S = S^*(a) \quad (11)$$

for a . This can be done when the following conditions are met:

1. $a < a_{critical}$ (corresponds to a maximum in the Kohler curve)
2. Eq. (9) exceeds (10)
3. $S < S_{critical}$ (corresponds to a maximum in the Kohler curve)
4. $|a_{eqi} - a_{previous}| < 20\delta a$.

Condition 3 results from the requirement that the solution of (11) be real and not complex. a_{eqi} denotes

¹ International Mathematical & Statistical Libraries, 7500 Bellaire Blvd., Houston, TX, 77036.

the solution of (11) and a_{previous} denotes the solution found at the last time step. Condition 4 results from the requirement that the actual growth rate must be significantly less than that given by (9). When these conditions are met, the solution of (11) can be used as the solution to the growth problem. This saves considerable computer time and avoids an unstable numerical problem.

Another situation where time savings can be made is when the drop gets large. When

$$a > a_{\text{critical}} + 2 \mu\text{m}, \quad (12)$$

the Köhler term S^* becomes only weakly dependent on drop size and the significant a dependence in (4) resides in the $a+l$ term. We may take advantage of this and obtain an analytic solution for the growth. Eq. (4) can be written in the form

$$\begin{aligned} d(a+l_e)^2/dt &= f(t) \\ &= 2D_{\text{eff}}\rho_{\text{sat}}(S-S^*)(a+l_e)/\rho_w(a+l), \end{aligned}$$

where $l_e = 3l_{i-1}/2 - l_{i-2}/2$. When inequality (12) is satisfied for the i th time step, f is only weakly dependent on a and can be approximated as a linear function of time. Hence we can write

$$d(a+l_e)^2/dt = c_1 + c_2(t - t_{i-1}), \quad (13)$$

where

$$\begin{aligned} c_1 &= f(t_{i-1}), \\ c_2 &= [f(t_{i-1}) - f(t_{i-2})]/(t_{i-1} - t_{i-2}). \end{aligned}$$

The solution of (13) is

$$a_i = [(a_{i-1} + l_e)^2 + c_1(t_i - t_{i-1}) + \frac{1}{2}c_2(t_i - t_{i-1})^2]^{1/2} - l_e.$$

The droplet experiment (Section 4) with the pressure profile used as input was run twice: with and without this approximation. The maximum differences in temperature and drop radius were 8×10^{-5} K and 1×10^{-4} μm , respectively. These errors are acceptable.

Eq. (4) needs to be solved numerically only when the droplet is near the activation regime. When it is far from this regime, the above analytical solutions can give the drop size with much less computer time.

Even when the cloud is in the activation regime, the number of differential equations that need to be solved numerically can be greatly reduced. A common situation, particularly for cloud chamber laboratory work, is that during activation the ambient supersaturation is substantially above the equilibrium supersaturations for many of the drop families. Often when this occurs, the behavior of one drop family will be similar to that of its neighboring families. The differential equations of growth need to be solved numerically only for a few droplet families. The growth of the rest can be calculated analytically from the growth of the numerically solved families, while still taking the distinct characteristics of the different families into account.

We consider the ratio of the droplet growth equations (4) for two neighboring families:

$$da/dt = (a_{j-1} + l) \times [1 - (S_j^* - S_{j-1}^*)/(S - S_{j-1}^*)]/(a + l). \quad (14)$$

This equation describes the growth of family j in terms of the behavior of the preceding family; a_{j-1} rather than t is treated as the independent variable. The dependence on D_{eff} and ρ_{sat} drops out. If the evolution of family $j-1$ over the time interval t_{i-1} to t_i is known, then we can calculate the growth of family j from (14).

When the ambient supersaturation is well above the equilibrium supersaturations of drops with similar characteristics, the term

$$(S_j^* - S_{j-1}^*)/(S - S_{j-1}^*) = \Delta \quad (15)$$

is small. If this small term is neglected, the solution of (14) for a_j in terms of a_{j-1} is trivial.

The effect of Δ can be accounted for in the following way. Assume that $a_{j-1,i-1}$ (a_{j-1} at time t_{i-1}) is known. If we let $u = a + l$, then (14) can be written

$$du/dt = (u_{j-1}/u_j)(1 - \Delta), \quad (16)$$

where Δ is known at time t_{i-1} . We then solve (16) for $u_{j,i}$ by holding Δ constant at the value Δ_{i-1} . This yields an approximate value for $u_{j,i}$ and hence $a_{j,i}$. Using this value, we calculate an approximate value Δ'_i for Δ at time t_i . We then assume Δ is a linear function of u_{j-1} , i.e.,

$$\Delta = \Delta_{i-1} + s(u_{j-1} - u_{j-1,i-1}), \quad (17)$$

where s denotes the slope

$$s = (\Delta'_i - \Delta_{i-1})/(u_{j-1,i} - u_{j-1,i-1}).$$

The solution of (16) using (17) for Δ yields

$$\begin{aligned} a_{j,i} &= \{(u_{j-1,i})^2 + [(u_{j-1,i})^2 \\ &\quad - (u_{j-1,i-1})^2](1 - \Delta_{i-1} + su_{j-1,i-1}) \\ &\quad - (\frac{2}{3})s[(u_{j-1,i})^3 - (u_{j-1,i-1})^3]\}^{1/2} - l. \quad (18) \end{aligned}$$

This yields an analytic expression for $a_{j,i}$ good to first order in the change in the small term Δ .

Approximation errors are likely to aid constructively in this process of solving for a_j in terms of a_{j-1} which itself was solved for in terms of a_{j-2} , etc. A limit has to be placed on the distance one gets from the droplet family whose growth was determined by the numerical solution of (4). The error associated with the family j calculation can be estimated by the difference between the final $a_{j,i}$ given by (18) and the approximate $a_{j,i}$ given by (18) with $s=0$. This error is summed from family to family starting from the last family to be solved for numerically. When the error reaches the value used for the requested accuracy from the numerical differential equation routine, then the next family is solved for numerically rather than

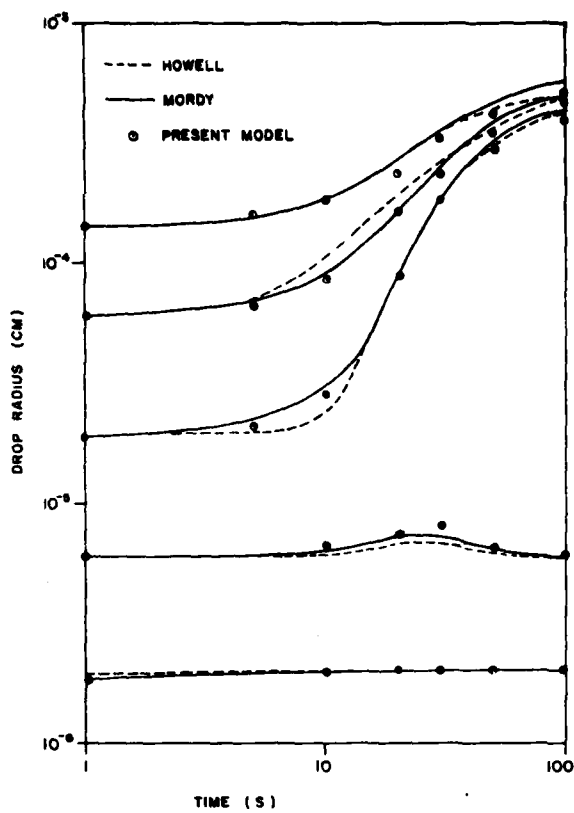


FIG. 2. Comparison of droplet growth results for Howell's test case I.

by this analytic technique in (18), and the cycle is then repeated. If Δ is not small, then one knows in advance that the influence of s will be relatively large since the two families will have different characteristics, and so this analytic technique will not be particularly useful. $\Delta=0.1$ has been found to be a good upper limit on the range of Δ for which (18) is a useful formula for a_{ij} . The droplet growth experiment (Section 4) with the pressure profile used as input was run twice: with and without this approximation. The maximum differences in temperature and drop radius were 3×10^{-5} K and 7×10^{-4} μm , respectively. These errors are negligible.

4. Results

Numerical simulations have been done (Howell, 1949; Mordy, 1959) for the case of a cloud forming experiment involving a polydispersed aerosol and a constant updraft. As a check on our model we ran this experiment on our program and found good agreement with these previous results. A comparison of our results with those of Mordy and Howell for Howell's test case I are shown in Fig. 2.

The numerical cloud model now is applied to a variety of typical experiments suitable to this type of cloud chamber facility. Some of the experiments involve expansion profiles which do not simulate natural cloud evolution but rather involve strongly time-dependent expansion rates designed to emphasize the phenomena under study. Here we demonstrate that the program can function under these varied expansion profiles and does so in real time. Three types of experiments are treated: cloud formation, droplet growth and Ostwald ripening.

The objective of the cloud forming experiment is to simulate convective cloud formation by producing an adiabatic expansion with constant expansion rate, using an aerosol whose critical supersaturation spectrum is accurately known. The properties of the resulting cloud (the final drop count primarily, along with the size spectrum if available) will then be compared with theory. Here the pressure versus time profile is predetermined and is an input to the model; the temperature profile is output. A virtue of this experiment is that it is relatively insensitive to the initial relative humidity of the sample gas. This is so because at a fixed expansion rate the same peak supersaturation is reached for a wide range of initial relative humidities. The input parameters for the model are the initial conditions ($T_0=20^\circ\text{C}$, $p=965$ mb

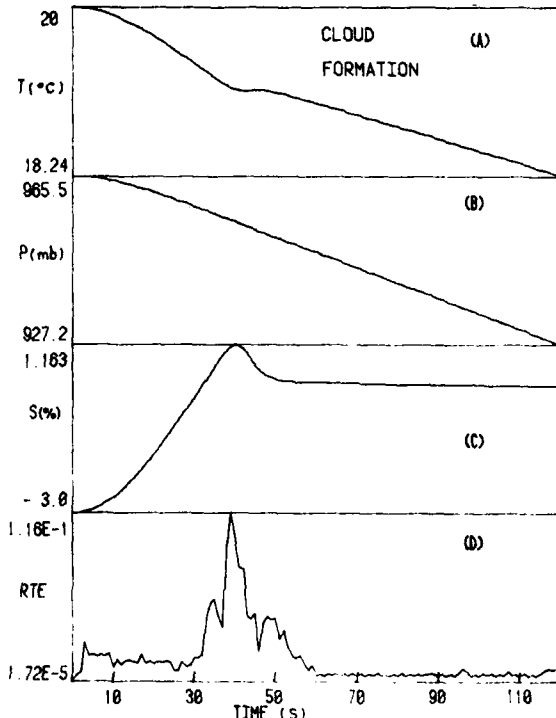


FIG. 3. Time variations of temperature ($^\circ\text{C}$), pressure (mb), supersaturation (%), and real-time efficiency for cloud formation experiment.

and $S_0=0.97$), the aerosol critical supersaturation spectrum [$n(S) = (1 \times 10^7 \text{ cm}^{-3})(S-1)^2$], and the expansion rate ($\dot{p} = -0.33 \text{ mb s}^{-1}$). The aerosol is divided into 14 families between 0.1 and 1.4% critical activation supersaturations. The pressure profile, which is an input variable for this experiment is shown in Fig. 3b. The output parameters from the cloud model are shown in Figs. 3 and 4. The temperature profile shows a kink near $t=40 \text{ s}$ as the transition is made from a dry adiabat to a wet adiabat. Aerosol activation occurs here and the supersaturation profile reaches a maximum as vapor depletion begins to occur.

Since the speed of calculation is important for real-time applications we now consider performance. Curve d on Fig. 3 shows a parameter RTE (real time efficiency) that contains information about the speed of the calculation in comparison to the actual speed of the experimental processes. It is defined as the ratio of the computer time needed to evaluate an increment of experiment divided by the simulated elapsed time for that increment. It is plotted linearly. When this ratio is less than 1, the computer is fast enough to keep up with the experiment in real time, otherwise it is slower than real time. This parameter is obviously machine dependent. Our on-line computer, a NOVA 840, does not have a hardware floating point unit and as a result cannot be used for real-time calculations yet. Steps are presently underway to obtain a floating point unit. These calculations were

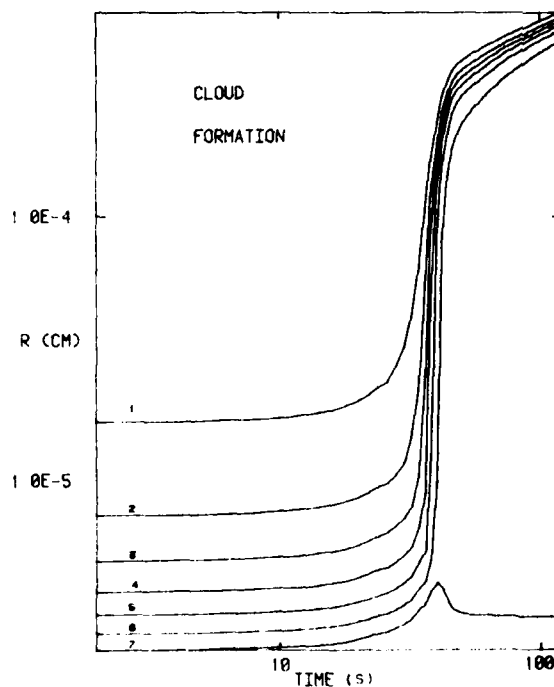


FIG. 4. Time variation of cloud drop size (radius) for selected drop families. Cloud formation experiment.

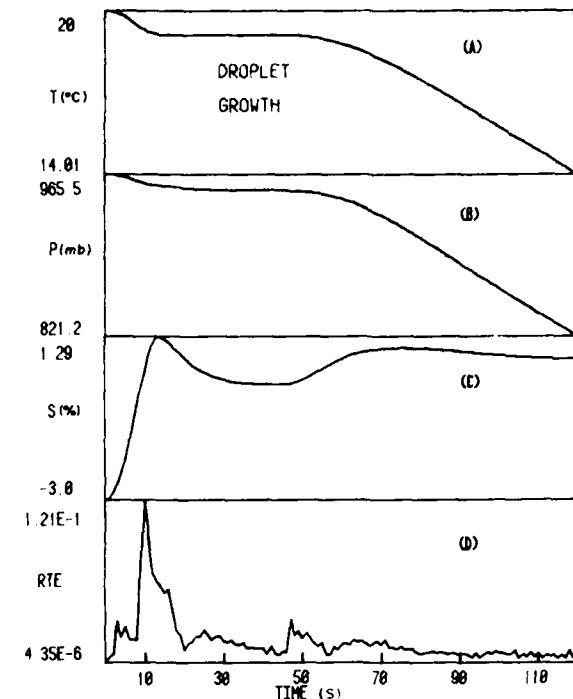


FIG. 5. Time variations of temperature ($^{\circ}\text{C}$), pressure (mb), supersaturation (%), and real-time efficiency for droplet growth experiment.

carried out on an IBM 370-168. Eventually, we plan to do some real-time cloud model calculations on our on-line NOVA 840.

The RTE curve on Fig. 3 shows that the cloud model is able to run in real time since the RTE is everywhere less than 1. It reaches a maximum, $\text{RTE} \approx 0.1$, near $t=40 \text{ s}$, the point where activation occurs. The computer slows down here because there is a maximum amount of computational activity—the time increments are small and the largest number of equations require numerical rather than analytic solution here.

The results of the cloud droplet size calculations are shown on Fig. 4. As usual in condensational growth models, the width of the droplet size distribution narrows with time.

A second experiment concerns the measurement of droplet growth rates. The basic concept of this experiment is to produce a monodisperse cloud, subject it to a high and well-known supersaturation, and then measure its growth rate. The droplet size measurements are performed by means of Mie light-scattering techniques. The input parameters to the model are the initial conditions ($T_0 = 20^{\circ}\text{C}$, $p_0 = 965 \text{ mb}$, and $S_0 = 0.97$), the aerosol (NaCl with Gaussian dry size distribution, mean radius $0.02 \mu\text{m}$, half-width $0.002 \mu\text{m}$, concentration 608 cm^{-3} , and divided into 12 families), and the temperature profile shown in

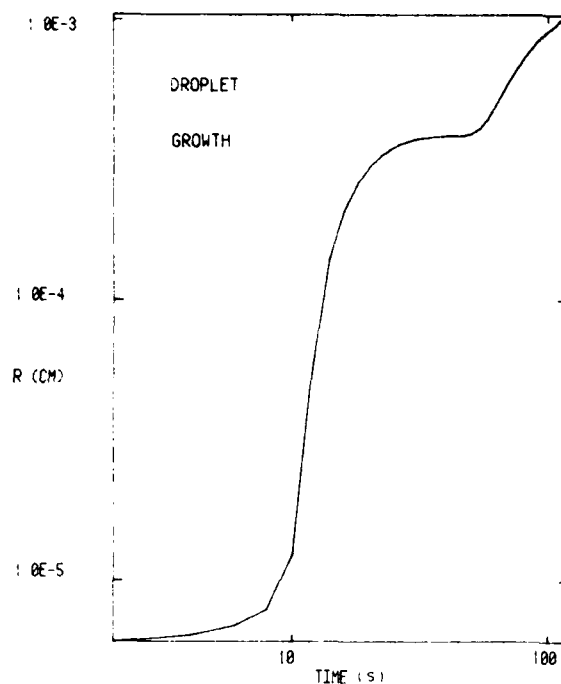


FIG. 6. Time variation of cloud drop size (radius) for the monodispersed cloud in the droplet growth experiment.

Fig. 5a. The aerosol corresponds to that which can be produced with a NaCl generator and an electric aerosol classifier (Liu and Pui, 1974). The expansion consists of a fast expansion during the first 14 s which produces a supersaturation sufficient to activate all of the aerosol and activate it all at nearly the same time. This is followed by a period of constant temperature during which the cloud drops can grow to observable size. Then the expansion is resumed to provide supersaturation for droplet growth at observable droplet sizes.

The output parameters for this experiment (pressure, supersaturation and RTE) are shown in Fig. 5. The droplet size for the monodisperse cloud is shown in Fig. 6. The half-width of the cloud droplet size distribution when the mean size is 1 μm is 0.11 μm , which is sufficiently narrow for Mie scattering size measurements. Measurements can be made for small droplet sizes, $a \leq l$, to determine the accommodation coefficients, and for larger drop sizes, $a > l$, to determine the effective diffusion coefficient in the same experiment. The cloud model calculations are real time; for this case, the computer is faster than the cloud process by a factor of at least 8.

The next type of experiment concerns the mechanism of Ostwald ripening (Dunning, 1973). In this experiment, a cloud is produced which has a definite size distribution. Then the temperature is either held constant or permitted to change only slowly, so that

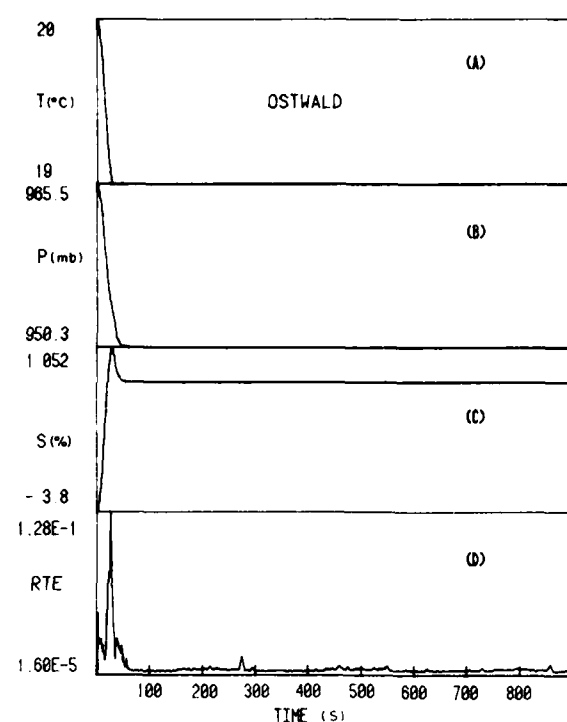


FIG. 7. Time variations of temperature ($^{\circ}\text{C}$), pressure (mb), supersaturation (%) and real-time efficiency for Ostwald ripening experiment.

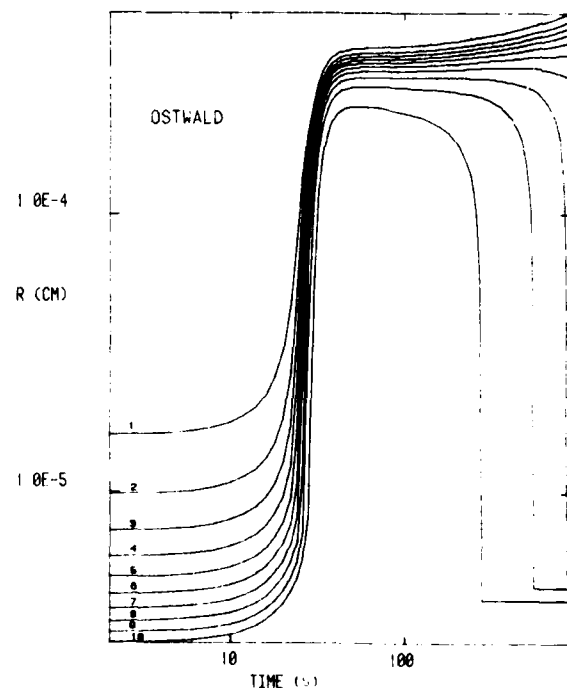


FIG. 8. Time variations of cloud drop size (radius) for selected drop families. Ostwald ripening experiment.

the supersaturation is reduced by the growing drops. Eventually, the supersaturation will fall between the equilibrium supersaturation of the small drops and that of the large drops. We then observe the growth of the large drops at the expense of the small ones. This is a potential drop size distribution broadening mechanism. It is interesting here because the cloud spends considerable time in the activation/de-activation regime and the cloud model must handle both growth and evaporation. The input parameters for the cloud model are the initial conditions ($T_0=20^\circ\text{C}$, $p_0=965 \text{ mb}$ and $S_0=0.96$), the aerosol is the same as that used in the cloud forming experiment, and the temperature profile is given by (see Fig. 7)

$$T(t) = \begin{cases} 19.5 + 0.5 \cos(\pi t/30)^\circ\text{C}, & 0 < t < 30 \text{ s} \\ 19^\circ\text{C}, & 30 < t < 900 \text{ s.} \end{cases}$$

The results are as follows (see Figs. 7 and 8). The peak supersaturation of 1.05% is reached at $t=29 \text{ s}$. This activates the aerosol and the growing drops deplete the supersaturation. The smallest drop family begins to evaporate at $t=55 \text{ s}$ and deactivates at $t=290 \text{ s}$. Progressively larger families then deactivate in turn. The Ostwald ripening process should be observable. At $t=55 \text{ s}$, the drop concentration is 1000 cm^{-3} ; at $a \approx 3 \mu\text{m}$ and at $t=900 \text{ s}$ it is down to 490 cm^{-3} at $a \approx 4 \mu\text{m}$. The computer is able to keep up with the Ostwald ripening process as shown in Fig. 7. Small peaks occur on the RTE curve whenever a droplet family deactivates (e.g., $t=290 \text{ s}$ and 550 s) due to extra computational activity at these times. The cloud model is able to handle the simultaneous growth and evaporation of competing cloud drop families.

Acknowledgment. This work was supported by the National Science Foundation under Grant NSF-ATM 75-16900, and by the National Aeronautics and Space Administration under Contract NAS8-31849.

REFERENCES

- Beistel, D. W., R. A. Mollenkamp, H. J. Pottinger, J. S. de Good and J. H. Tracey, 1975: Computer networking at UMR. *Computer Networking and Chemistry*, P. Lykos, Ed., ACS Symposium Series, No. 19 [Library of Congress QD 39.3.E46C64].
- Brown, P. S., and G. Arnason, 1973: Efficient numerical integration of the equation governing droplet growth by condensation. *J. Atmos. Sci.*, **30**, 245-248.
- Byers, H. B., 1965: *Elements of Cloud Physics*. University of Chicago Press, 191 pp. (see pp. 33-37).
- Carstens, J. C., 1979: Drop growth in the atmosphere by condensation: application to cloud physics. *Advances Colloid Interface Science*, Vol. 10, Academic Press, 285-314.
- , J. Podzimek and A. Saad, 1974: On the analysis of the condensational growth of a stationary cloud droplet in the vicinity of activation. *J. Atmos. Sci.*, **31**, 592-596.
- Cotton, W. R., 1975: Theoretical cumulus dynamics. *Rev. Geophys. Space Phys.*, **13**, 419-448.
- Dunning, W. J., 1973: Ripening and aging processes in precipitates. *Particle Growth in Suspensions*, A. L. Smith, Ed., Academic Press, 36 pp. (see pp. 3-28).
- Fukuta, N., and L. A. Walter, 1970: Kinetics of hydrometeor growth from a vapor-spherical model. *J. Atmos. Sci.*, **27**, 1160-1172.
- Hagen, D. E., G. M. Hale, and J. Carter, 1975: Laser doppler method for cloud droplet size spectrum. *Proc. Electro-Optical Systems Design Conf.*, Anaheim, Laser Institute of America, 373-379.
- , J. L. Kassner, Jr., K. P. Berkbigler and D. R. White, 1977: A computer data acquisition and control system for an atmospheric cloud chamber facility. *Minicomputers and Large-Scale Computations*, P. Lykos, Ed., ACS Symposium Series, No. 57, 77-93 [Library of Congress QD 39.3.E46 M56].
- Howell, W. E., 1949: The growth of cloud drops in uniformly cooled air. *J. Meteor.*, **6**, 134-149.
- Kassner, J. L., Jr., J. C. Carstens and L. B. Allen, 1968: Analysis of the heat and vapor propagation from the walls of the Nolan, Pollak, and Gardner type condensation nucleus counter. *J. Atmos. Sci.*, **25**, 919-926.
- , J. Podzimek, J. C. Carstens and D. R. White, 1973: The cloud simulation program at the University of Missouri-Rolla. *Proc. VIII Int. Conf. Nucleation*, Leningrad, USSR, Int. Union Geodesy Geophys., 308-317.
- List, R. J., 1971: *Smithsonian Meteorological Tables*. Smithsonian Institution Press, 527 pp.
- Liu, B. Y. H., and D. Y. H. Pui, 1974: A submicron aerosol standard and the primary, absolute calibration of the condensation nuclei counter. *J. Colloid Interface Sci.*, **47**, 155-171.
- Low, R. D., 1969: A generalized equation for the solution effect in droplet growth. *J. Atmos. Sci.*, **26**, 608-611.
- Mordy, W., 1959: Computations of the growth by condensation of a population of cloud droplets. *Tellus*, **11**, 16-44.
- Smith, R., J. Anderson, B. Schrick and C. Ellsworth, 1976: An atmospheric cloud physics laboratory for the space laboratory. *Preprints Int. Conf. Cloud Physics*, Boulder, Amer. Meteor. Soc., 655-629.

